2021

Plasmonic core-multi-shell nanomaterials for improving energy efficiency and sensing

---

https://hdl.handle.net/2144/41916

Boston University

BOSTON UNIVERSITY

COLLEGE OF ENGINEERING

Dissertation

PLASMONIC CORE-MULTI-SHELL NANOMATERIALS FOR IMPROVING ENERGY EFFICIENCY AND SENSING

by

AMARTYA DUTTA

B.S., University of Calcutta, 2012
M.S., Indian Institute of Technology, Kanpur 2014

Submitted in partial fulfillment of the

requirements for the degree of

Doctor of Philosophy

2021

Approved by

First Reader

Chen Yang, Ph.D.
Associate Professor of Electrical and Computer Engineering
Associate Professor of Chemistry
Associate Professor of Materials Science and Engineering

Second Reader

Luca Dal Negro, Ph.D.
Professor of Electrical and Computer Engineering
Professor of Materials Science and Engineering
Professor of Physics

Third Reader

Roberto Paiella, Ph.D.
Professor of Electrical and Computer Engineering
Professor of Materials Science and Engineering

Fourth Reader

Xi Ling, Ph.D.
Assistant Professor of Chemistry
Assistant Professor of Materials Science and Engineering

“The secret of getting ahead is getting started. The secret of getting started is breaking your complex overwhelming tasks into small manageable tasks, and then starting on the first one.” – Mark Twain

DEDICATION

To my parents Avijit and Debjani. Your unwavering love, encouragement and wisdom helped me to push forward to greater heights in the pursuit of science

ACKNOWLEDGMENTS

First and foremost, I would like to express my sincere gratitude to my advisor, Professor Chen Yang. She has been an amazing mentor, guiding me at every roadblock and always encouraging to think of new ideas to move ahead. She has helped me develop an independent way of thinking and her advice on my research and my career path ahead have helped shape me as a researcher. I would also like to thank my graduate committee members Professor Luca Dal Negro, Professor Roberto Paiella and Professor Xi Ling for all their guidance and insightful discussions.

I sincerely thank Professor Luca Dal Negro, for all the insightful discussions regarding core multishell nanoparticles and the physics which guides the plasmonic properties of such nanostructures. I would like to thank Professor Roberto Paiella for his advice and insight on the application of core multishell nanowires towards improving White LED efficiency. I would also like to thank Professor Ji-Xin Cheng for his advice and guidance in understanding the application of core multishell nanoparticles in Raman spectroscopy.

I sincerely thank Mr. Paul Mak for his support in the opto-electronic facility and for always patiently helping at every technical hurdle; special thanks to all the help he gave in setting up the lab. I would also like to thank Dr. Alexey Nikiforov for patiently teaching me about TEM and being there whenever I ran into a problem, and for all the fun conversations which I had with him. I would also like to thank Ms. Anlee Krupp for teaching me about the various instruments in the Precision Measurement Laboratory and for providing a solution to every question asked.

I would like to specially thank Yuyao Chen, who has worked with me on the core multishell nanoparticle project, and for simulating all the fields and resonances for these particles as well as Au nanoparticles which was used in hematite. I would also like to thank Sean Gorsky for his help in getting the dark field spectra for the core multishell nanoparticles. Special thanks to Dr. Cheng Zhong who worked with me in developing the core multishell nanoparticles and helped me in getting all the Raman spectra using these nanoparticles. Special thanks to Dr. Sarath Ramadurgam who worked closely with me on the core multishell nanowire project and helped me through various problems.

I sincerely thank all my labmates-Brian Pihuleac, Katherine Hansen and Melissa Cardona, all of whom worked with me collaboratively in multiple projects and in setting up the lab; Yimin Huang, Linli Shi, Nan Zheng and Ran Cheng, working with whom I learned something new every time.

I would like to express my special thanks to my fiancée Amrita Basu, whose support and encouragement helped me strive for more every day. I am thankful for all the adventures and fun we have had together and look forward to many more. I am also grateful for all the support which I received from my family both here and back home. Finally, I would like to express my thanks to all my friends, special shoutout to Aruni, Avishek, Shayoree, with whom there were multiple chats which would always make me feel better, as well as the Purdue family who helped make a home away from home.

PLASMONIC CORE-MULTI-SHELL NANOMATERIALS FOR IMPROVING ENERGY EFFICIENCY AND SENSING

AMARTYA DUTTA

Boston University, College of Engineering, 2021

Major Professor: Chen Yang, Ph.D., Associate Professor of Electrical and Computer Engineering, Associate Professor of Chemistry, Associate Professor of Materials Science and Engineering

ABSTRACT

In recent times, plasmonics has been a hallmark in improving optoelectronic device performance as well as in improving sensing. Confining light in dimensions below the diffraction limit and subsequently converting the incident photons into localized charge-density oscillations called localized surface plasmons, optical enhancements of the local fields by many orders of magnitude is possible. This dissertation explores the use of such surface plasmon resonances in core multishell nanostructures and demonstrates the values of such structures in energy harvesting and sensing. Additionally, it also shows the use of emerging plasmonic materials like metal nitrides (TiN, ZrN) instead of traditional plasmonic materials (Au, Ag) in the nanostructure designs.

Utilizing the localized surface plasmon resonance (LSPR) in metallic components of core multishell nanowires, calculations of the local density of states as a measure of emission were made using a Green’s function method, while the absorption and scattering were simulated using the Mie formalism. Combining both the absorption and the emission, the quantum efficiency of white LEDs was calculated and the optimal material/dimensions for maximal performance was determined for different phosphor components in a white

LED. Additionally, the use of ZrN as a plasmonic cloak for noise cancellation in Si photodetectors is shown and the performance is compared with an Au cloak. Using the developed methodology, it is proved that ZrN cloaks can outperform Au cloaks in a certain region of the visible spectrum, showing the benefit of using such plasmonic systems in place of traditional materials. The fabrication of the different components of the core multishell nanowires is also presented, and in particular, fabrication of ultra-thin (sub-10 nm) plasmonic TiN is achieved.

Utilizing plasmon hybridization, a tunable double resonance feature is observed in Au/SiO_2/Au core shell shell (CSS) nanoparticles, which have been then demonstrated to improve the photocatalytic performance in hematite. In particular, the double resonance peak allows absorption of light beyond the band gap of hematite and subsequent conversion into photocurrent through hot electron injection. Comparison has been made with Au nanoparticles, and it has been shown that the CSS nanoparticles outperform Au nanoparticles significantly. These CSS nanoparticles have also been used for bioimaging, in particular for Raman spectroscopy, with strong results at high densities of the nanoparticles. Utilizing stronger scattering SiO_2/Au Nanoshells, it has been possible to work towards single particle imaging of molecules and demonstration of this phenomenon has been shown here through the use of coherent Raman scattering spectroscopy.

TABLE OF CONTENTS

LIST OF TABLES

LIST OF FIGURES

LIST OF ABBREVIATIONS

ALD	Atomic Layer Deposition
CMS	Core Multi Shell
CS	Core Shell
CSS	Core Shell Shell
EQE	External Quantum Efficiency
FOM	Figure of Merit
IQE	Internal Quantum Efficiency
LDOS	Local Density of States
LSPR	Localized Surface Plasmon Resonance
NP	Nanoparticle
NS	Nanoshell
NW	Nanowire
PF	Purcell Factor
SP	Surface Plasmon
SPR	Surface Plasmon Resonance
TE	Transverse Electric
TM	Transverse Magnetic
WLED	White Light Emitting Diode

CHAPTER ONE: INTRODUCTION

Section One: Motivation

In recent years, plasmonics, which explores the confinement of electromagnetic fields in dimensions on the order of or smaller than the wavelength, has been a major hallmark in improving the efficiency of opto-electronic devices and sensors. In particular, surface plasmons (SPs), which are based on interaction processes between electromagnetic radiation and conduction electrons at metallic interfaces or in small metallic nanostructures, have been of particular interest due to the enhanced optical near field in sub-wavelength dimension provided[1-6]. Depending on their dimensions, the plasmon response exhibited by metal nanostructures can be tuned and subsequently utilized for enhancing absorption, increasing light scattering, resonantly transferring energy to generate electron-hole pairs in a surrounding material and for providing hot electrons[7]. Additionally, semiconductor (dielectric) materials have also drawn considerable attention due to their dimension dependent optical absorption and emission[8-9]. When the optical excitation of the semiconductor materials is combined with the localized surface plasmon resonances (LSPRs) of metals in conformal core multi-shell (CMS) nanostructures, unique optical properties arise which can be used in various photonic applications.

This dissertation focuses on two such conformal CMS nanostructures, namely, CMS nanowires (NWs) and CMS nanoparticles (NPs). In particular, the work focuses on the application of CMS NWs in two applications-improving the efficiency of White Light Emitting Diodes (WLEDs) and improving the signal to noise ratio in silicon-based photodetectors. By identifying the correct dimensions and materials of each component of the CMS NWs, it is possible to improve the efficiency of these devices over that of current traditional devices. The use of emerging plasmonic materials like TiN and ZrN instead of traditional metals like Au, Ag would also help in stronger responses of the CMS NWs used. For the CMS NPs, the two applications which have been focused upon are: improving the photo-electrocatalytic response of semiconductor electrodes and improving the Raman response of small molecules using single NPs. By varying the dimensions and the number of layers used, the optical response of the CMS NPs can be controlled with high precision to strongly influence the system under consideration.

Section Two: Nanoplasmonics-An outlook

In nanoplasmonics, light is typically confined in dimensions below the diffraction limit (which typically is half the width of the wavelength of light being used) by converting the incident photons into localized charge-density oscillations, which are the SPs, in metal nanostructures, which then serve as nanoscale analogs of antennas. The resonance frequencies of these oscillations are sensitive to the material, dimensions and dielectric environment of the nanostructures, allowing for a large variety of possible optical properties and applications[10-13]. This dependence on particle size and the dielectric environment has been shown extensively for both plasmonic films and plasmonic nanostructures. Figure 1.1 gives such an example for Au nanoparticles (NPs). Figure 1.1(a) and 1.1(b) show the electric field distributions for a 20 nm Au NP and a 50 nm Au NP respectively in a dielectric environment of air (n=1). The plasmon resonances of the two particles due to difference in size is 520.1 nm and 535.1 nm respectively. Though the

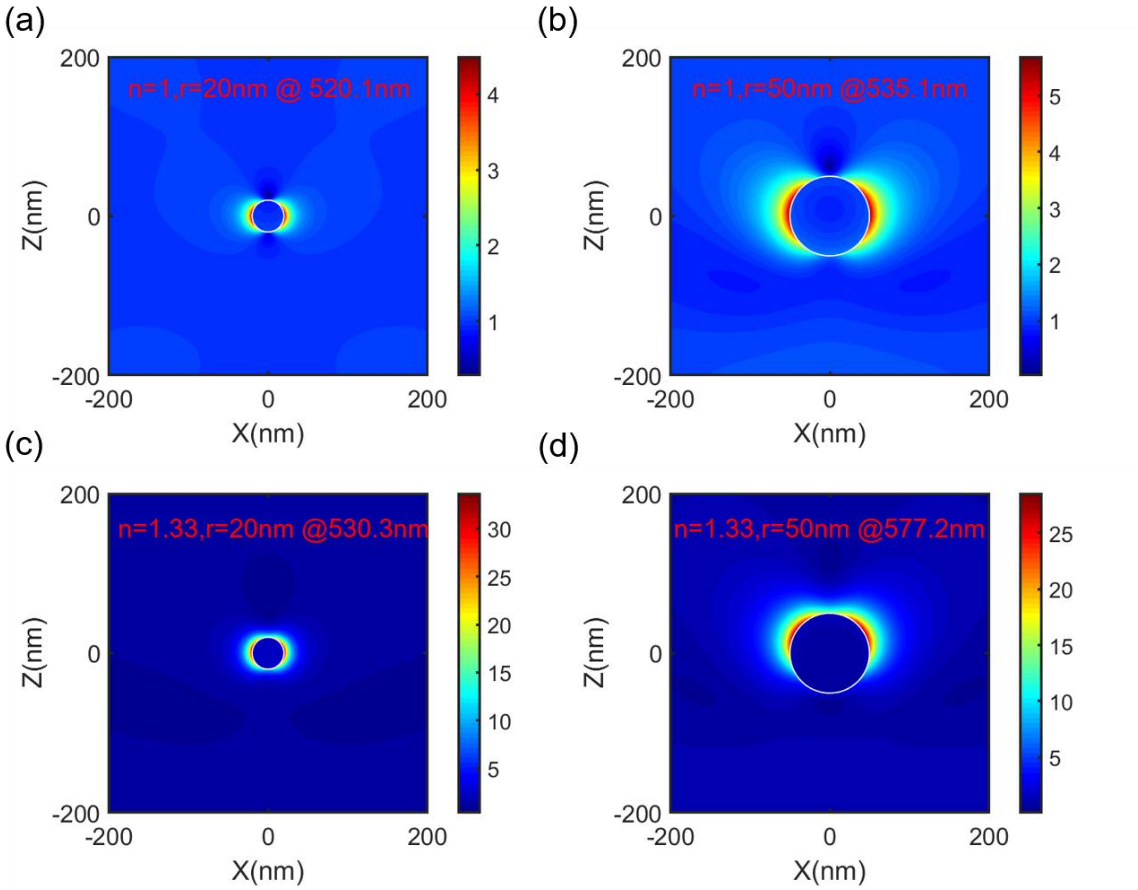

Figure 1.1: Electric fields of Au NPs. n is the refractive index of the surrounding medium (n=1 is and n=1.33 is water), r is the radius of the Au NP, and the plasmon resonance wavelength is given following @.

maxima of the electric fields are similar in magnitude, the electric fields extend a much further distance from the surface for the 50 nm Au NP. Figure 1.1(c) and 1.1(d) show the electric field distributions for a 20 nm Au NP and a 50 nm Au NP respectively in a dielectric environment of water (n=1.33). It is evident that the fields are not only stronger in magnitude compared to a dielectric environment of air, but the field distribution is also different. Additionally, the plasmon resonances are quite different from the values in air, being 530.3 nm for the 20 nm NP and 577.2 nm for the 50 nm NP. This figure thus gives an example of how sensitive the resonance frequency oscillations are to the dimensions and the dielectric environment.

By tuning the frequencies of these oscillations, the local field enhancements and subsequent enhancement in optical properties can be used for various applications. For example, by using a nanoplasmonics array, highly directional emission of light with a 60-fold enhancement for solid state lighting devices has been demonstrated[14]. Incorporation of plasmonic nanostructures for light trapping in thin film organic photovoltaic devices has helped push the power conversion efficiency of these devices to much greater than 10%, due to increase in light harvesting by as much as 70% using plasmonic nanoparticles[15]. Muench et. al. demonstrated an enhanced graphene photodetector which utilized Au films for telecom wavelengths operating at zero dark current[16]. Additionally, there is a large dependence of the plasmonic properties on the geometry of the nanostructures. For example, though the local resonance fields are primarily dipolar for gold nanospherical structures, for nanostructures with sharper features the fields are focused at the sharper contour edges like the corners for nanocubes, the tips for nanostars, etc. This feature has been utilized extensively over the last decade, particularly in bio-imaging and nanoscale microscopy, where it becomes important to detect molecules at very low concentrations[17-20].

Section Three: Uniqueness of plasmonic core-multi-shell nanostructures

Though the optical properties of plasmonic nanostructures can be tuned by changing the dimension and the dielectric environment, it is generally difficult to tune the wavelengths of plasmonic nanoparticles to high wavelengths in the infra-red (IR) region without using complicated aggregations or structures, which makes them unusable for applications requiring such wavelengths. Additionally, semiconductor nanostructures have been of great interest due to their dimension dependent absorption and emission. However, their inherent optical properties are very weak, and use of some other structures to improve absorption/emission is necessary for practical applications.

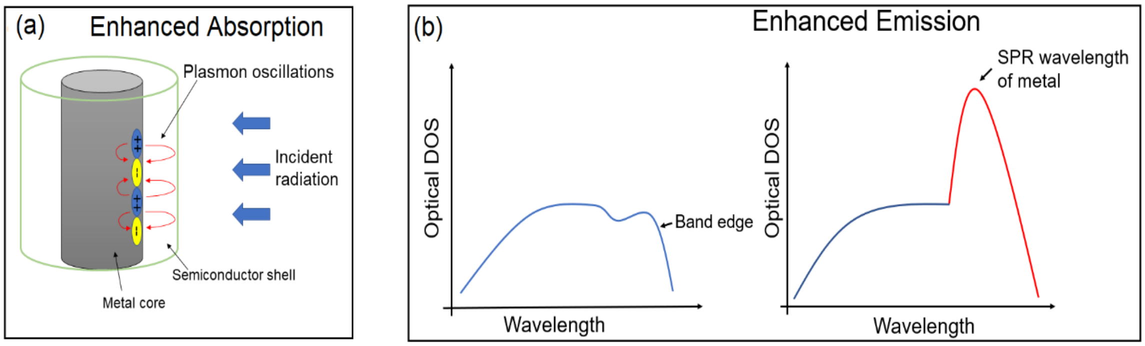

Figure 1.2: Schematic of the improved absorption and emission. (a) Enhancement of absorption in the shell due to plasmon resonance results in greater electric fields. The positive and negative signs in the metal core indicate regions of higher and lower electron concentrations respectively. (b) Enhancement of emission from the semiconductor due to increase of the optical DOS in the region of plasmon oscillations

Use of core-multi-shell (CMS) nanostructures, where a conformal coating of metal-semiconductor layers is present, is one way in which the optical properties can be manipulated. It has been shown that using a plasmonic core and a semiconductor shell, the optical properties of the semiconductor nanostructure can be enhanced significantly[21-23]. Fig. 1.2 shows the schematic for such a core-shell (CS) nanowire. Figure 1.2(a) shows enhancement of absorption in the outer semiconductor shell due to greater electric fields resulting from plasmon resonance of the inner metallic core, when the incident wavelength coincides with the resonance wavelength. Figure 1.2(b) illustrates enhancement of

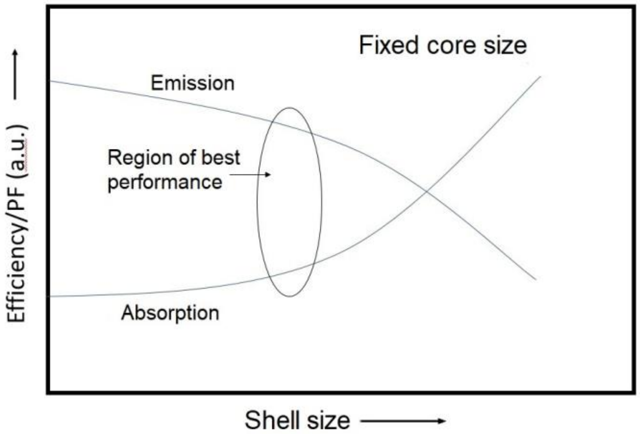

Figure 1.3: Dependence of absorption and emission of a CS nanostructure as a function of the dimensions of the shell, keeping the core radius fixed

emission in the semiconductor due to increase of the optical density of states (DOS) in the region of plasmon oscillations, when in the CS NW, the metal provides a SPR peak close to the emission wavelength of the semiconductor. The core size and shell thickness of CS NWs can be individually controlled to tune the absorption and emission performance, utilizing the plasmon resonance. Figure 1.3 shows the schematic for the importance of choosing the optimal dimensions for maximum efficiency. Keeping the core radius fixed, as the shell size is increased, the absorption efficiency improves due to increase in the absorption cross-section. At the same time, however, the emission, characterized by a number called the Purcell Factor (PF), decreases due to the spreading of the optical DOS. It is necessary to choose the correct dimensions in between which would lead to maximum efficiency.

Addition of another shell to such a metal-semiconductor CS nanostructure leads to a core-shell-shell (CSS) nanostructure, which introduces new optical properties due to plasmon hybridization. Basically, by sandwiching a semiconductor layer within two

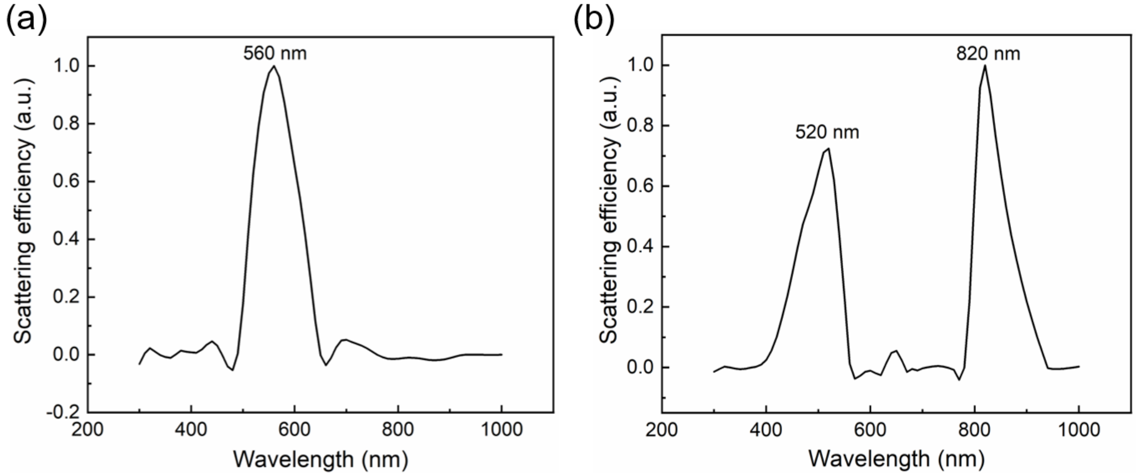

Figure 1.4: (a) Scattering efficiency of a 40 nm radius Au NW (b) Scattering efficiency of a Fe_2O_3/Au/Fe_2O_3 CSS NW with inner core of 40 nm radius, inner shell thickness of 20 nm and outer shell thickness of 20 nm.

metallic layers to create a metal-semiconductor-metal CSS nanostructure or a metallic layer between two semiconductor layers to create a semiconductor-metal-semiconductor CSS nanostructure, two separate interactions occur at the metal-semiconductor interfaces, which subsequently lead to a double resonance feature in a manner similar to molecular orbital theory, and this phenomena has been coined plasmon hybridization. This unique double resonance feature can be utilized to excite simultaneously multiple features in the application under concern. Additionally, by tuning the dimension of each layer involved, the 2nd peak can be tuned to higher wavelength values, a feature which cannot be achieved with traditional single layer plasmonic nanostructures. Figure 1.4 shows a representative example of the two cases, with (a) showing the scattering efficiency of a 40 nm radius Au NW, and (b) showing the scattering efficiency of a Fe_2O_3/Au/Fe_2O_3 CSS NW with dimensions of 40 nm/20 nm/20 nm with respect to the core radius/inner shell thickness/outer shell thickness. It can be seen that though the Au NW has only a single resonance peak at 560 nm, the CSS NW has two resonance peaks at 520 nm and 820 nm. These peaks are quite sensitive to the dimensions of each layer and can be shifted significantly, close to 1000 nm and even beyond. Under this configuration, it becomes relevant for multiple applications especially in biology, including photothermal cancer therapy, biosensing, etc., which require higher wavelength excitations in order to avoid tissue damage. This feature can also be extended to other nanostructures. Table 1 shows some examples of the variation of the peaks by changing the dimensions of the different layers of the Fe_2O_3/Au/Fe_2O_3 CSS NW.

Core radius (nm)	Inner shell thickness (nm)	Outer Shell thickness (nm)	Peak 1 (nm)	Peak 2 (nm)
20	20	20	430	720
40	20	20	520	820
80	20	20	560	900
20	40	20	540	680
20	80	20	600	670
20	20	40	550	740
20	20	80	630	800

Table 1.1: Variation of plasmon resonance peaks with dimensions for a Fe_2O_3/Au/Fe_2O_3 CSS NW

Section Four: Metal nitrides as emerging plasmonic materials

While the majority of plasmonics research has focused on noble metals such as gold and silver, today there is a need to replace these traditional materials with alternatives to make commercially viable plasmonic devices. Metal nitrides have proven to be one such class of materials which are among the most promising due to many physical properties such as their thermal stability, high melting point and compatibility with a wide number of substrate materials. The optical properties are also unique compared to traditional plasmonic metals. When compared to traditional plasmonic metals like Au and Ag, metal nitrides like TiN and ZrN have a plasmonic resonance which is located within a similar range, but the resonance is broad over wavelength, which is beneficial for a number of applications. The optical losses of the metal nitrides are also very low in the visible range due to reduced carrier concentrations[24-25]. However, at longer wavelengths, this advantage is lost. For instance, Au NPs have the imaginary part of the dielectric constant (which determines the optical losses of a material) ranging from 2-6 in the range of 400-550 nm, while TiN's values are between 3.5-5 over that same wavelength range[26]. However, between 1000-1500 nm, the imaginary part of the dielectric constant varies from 3-10 for Au and between 10-18 for TiN, indicating significantly greater optical losses. Also, unlike traditional plasmonic metals, the optical properties of the metal nitrides are variable and their plasmon resonance has been demonstrated from the near-IR region to the visible region. The wide range of substrate compatibility of the metal nitrides such as MgO, Alumina, Silicon, is another advantage of the metal nitrides over traditional plasmonic metals. Finally, crystalline TiN and ZrN can be easily fabricated and integrated into available CMOS technology with very little surface roughness. All the aforementioned conditions make metal nitrides good candidates to be used as the metallic components in lieu of traditional plasmonic metals.

Section Five: Outline

Chapter 1 introduces the novel optical properties of CMS nanostructures and provides a brief motivation towards using them in opto-electronic devices as well as in biological applications. It also motivates using emerging plasmonic materials such as metal nitrides instead of traditional plasmonic materials.

Chapter 2 provides a Green’s function method for rigorous derivation of the Purcell Factor (PF) of CMS NWs, which can be used directly as an indication of the emission from CMS NWs. Appendix A provides the codes used for this simulation. Combining this with previously explored Mie absorption theories, the application of CMS NWs towards improving efficiencies of opto-electronic devices like WLEDs and photodetectors, is explored. Additionally, fabrication of ultra-thin plasmonic TiN films for use in lieu of traditional plasmonic materials is also shown in detail.

Chapter 3 provides a fabrication method and characterization of CMS NPs and shows the advantage of using these particles in improving the photoelectrocatalytic (PEC) activity of hematite. It also shows detailed analysis and comparison with Au NPs to show the advantages of using such NPs.

Chapter 4 describes using these CMS NPs to improve sensing, in particular focusing on ultra-fast imaging at the single particle level.

Finally, Chapter 5 summarizes the work done in this dissertation and describes some broader outlooks and applications with the CMS nanostructures described here.

CHAPTER TWO: CMS BASED OPTO-ELECTRONIC DEVICES

Section One: Green's function for computing emission of CMS NWs[27]

The CMS NWs are modeled as cylinders with infinite length and with the incident light perpendicular to the axis. Because the emission is being considered radially, LSPRs can be sustained along the circumferential direction in the NWs of infinite lengths. To calculate the local density of states (LDOS) and Purcell factor (PF), a Green's function approach has been utilized[28]. As it is due to the recombination of an electron and a hole at the band gap of the semiconductor, the emission can be described as arising due to the electric and magnetic fields emitted by a dipole. The electric field due to a dipole is the Green's function solution to Maxwell's equations. The complete solution account for the orientation of the dipole is defined as a 2D Green's tensor[29-30]. This tensor can be used to calculate the local density of states, and consequently, the PF. The PF calculated here is obtained starting from Fermi's golden rule and is in the low coupling regime[31]. The following shows the methodology for deriving the equations for CS NWs. The same principles can be extended for additional shells.

There are two distinct regimes for coupling of the surface plasmons. In the first regime, when the system has both the length and the width comparable to the wavelength of light, there would be strong coupling of both the localized surface plasmon resonances (LSPRs) along the length of the system as well as the surface plasmon polaritons (SPPs) with the TM modes. In the second regime, when the system is a NW with the NW diameter being much smaller, and the NW length being much greater than the wavelength of light, the LSPRs cannot exist along the axial direction and the SPPs get attenuated even if the coupling condition is met. Here, we are working in the second regime, with high aspect ratios where L>50D.

Solution to Maxwell's Equations in Free Space

Maxwell's Equation in SI units for fields with $e^{-i\omega t}$ time dependence and source terms (ρ_s and J_s) are given as:

$$\nabla \cdot E = \frac{\rho_s}{\epsilon}$$
$$\nabla \cdot H = 0$$
$$\nabla \times E = i\omega\mu H$$
$$\nabla \times H = -i\omega\epsilon E + J_s$$

The electric and magnetic fields can be written as:

$$(\nabla^2 + k^2)E = \nabla\left(\frac{\rho_s}{\epsilon}\right) - i\omega\mu J_s \tag{1}$$
$$(\nabla^2 + k^2)H = -\nabla \times J_s \tag{2}$$

Here, $k = \omega\sqrt{\varepsilon\mu}$ is the wavenumber. For a dipole source located at r_s, the source terms are as follows:

$$\rho_s = 0$$
$$J_s = j_s\delta(r - r_s)$$

The Green's function for the inhomogeneous Helmholtz equation is given as:

$$(\nabla^2 + k^2)G(r, r_s) = \delta(r - r_s) \tag{3}$$

$$G(r, r_s) = \frac{1}{4i}H_0^{(1)}(k|r - r_s|) \tag{4}$$

where k represents the wave vector, while r and r_s indicate the field and source positions respectively. In 2D, the hankel function of the first kind represents the Green's function.

$$\nabla \times ((\nabla^2 + k^2)G(r, r_s)) = \nabla^2(\nabla \times G(r,r_s)) + k^2(\nabla \times G(r,r_s))$$

$$\Rightarrow (\nabla^2 + k^2)\,(\nabla \times G(r,r_s)) = \nabla \times \delta(r - r_s) \tag{5}$$

The electric and magnetic fields due to a dipole source (E^S and H^S) can be calculated from the Green's function.

$$\begin{aligned} E(r) &= -i\omega\mu \int_S J_s G(r,r_s)dS \\ E^S(r) &= -i\omega\mu j_s G(r,r_s) = -\frac{\omega\mu j_s}{4} H_0^{(1)}(k|r-r_s|) \end{aligned} \tag{6}$$

$$\begin{aligned} H(r) &= -\int_S J_s(\nabla \times G(r,r_s))dS \\ H^S(r) &= -j_s(\nabla \times G(r,r_s)) = -\frac{j_s}{4i}\nabla \times H_0^{(1)}(k|r-r_s|) \end{aligned} \tag{7}$$

Here, j_S represents the current density due to the source, while ω and μ represent the frequency of the radiation and the permeability of the space, respectively. For transverse magnetic (TM) radiation where the electric field is parallel to the nanowire axis ($\hat{z}$), the electric field along $\hat{z}$ represents the source fields. For transverse electric (TE) radiation where the magnetic field is parallel to the nanowire axis, the dipole can be oriented along $\hat{x}$ and $\hat{y}$, and the magnetic field along $\hat{z}$ can be used to simplify solving the 2D equations. The source terms are as follows:

$$E_z^{S_z} = -\frac{\omega\mu j_s}{4} H_0^{(1)}(k|r-r_s|)\hat{z}$$

$$H_z^{S_x} = -\frac{kj_s}{4i} H_1^{(1)}(k|r-r_s|)\sin(\theta)\,\hat{z}$$

$$H_z^{S_y} = \frac{kj_s}{4i} H_1^{(1)}(k|r-r_s|)\cos(\theta)\hat{z} \tag{8}$$

Here, $\theta = \arg(r - r_S)$, and due to the magnetic field along $\hat{z}$ for $\hat{x}$ and $\hat{y}$ dipoles, the corresponding electric fields have components along both $\hat{x}$ and $\hat{y}$.

The electric fields for the TE case can then be calculated as:

$$E^{S_x} = \frac{i}{\omega\epsilon}\left[\nabla \times H_z^{S_x}\right] = \frac{i}{\omega\epsilon}\left[\frac{\partial H_z^{S_x}}{\partial y}\hat{x} - \frac{\partial H_z^{S_x}}{\partial x}\hat{y}\right] \tag{9}$$

$$\begin{aligned} E^{S_x} &= -\frac{\omega\mu j_s}{8}\Big[\Big(H_0^{(1)}(k|r-r_s|) + H_2^{(1)}(k|r-r_s|)\cos(2\theta)\Big)\hat{x} \\ &\quad + \Big(H_2^{(1)}(k|r-r_s|)\sin(2\theta)\Big)\hat{y}\Big] \\ E^{S_y} &= -\frac{\omega\mu j_s}{8}\Big[\Big(H_0^{(1)}(k|r-r_s|) - H_2^{(1)}(k|r-r_s|)\cos(2\theta)\Big)\hat{x} \\ &\quad + \Big(H_2^{(1)}(k|r-r_s|)\sin(2\theta)\Big)\hat{y}\Big] \end{aligned} \tag{10}$$

The 2D Green's tensor is obtained from the electric field due to dipoles oriented along $\hat{x}, \hat{y}$ and $\hat{z}$ directions. The terms can be read as: $E_z^{S_z}$ is the electric field for a source dipole oriented in the $\hat{z}$ direction (S_Z) along $\hat{z}$.

$$G^E(r, r_s, \omega) = \begin{bmatrix} G_{xx} & G_{xy} & 0 \\ G_{yx} & G_{yy} & 0 \\ 0 & 0 & G_{zz} \end{bmatrix} = -\frac{1}{i\omega\mu}\begin{bmatrix} E_x^{S_x} & E_y^{S_x} & 0 \\ E_x^{S_y} & E_y^{S_y} & 0 \\ 0 & 0 & E_z^{S_z} \end{bmatrix} \tag{11}$$

The local density of states or LDOS can be obtained from Green's tensor as follows:

$$\rho(r_s, \omega) = -\frac{2\omega}{\pi c^2} Im[Tr\left(G^E(r, r_s, \omega)\right)] \tag{12}$$

The emission rate due to a dipole of strength μ can be computed from the LDOS as follows:

$$\gamma = \frac{2\omega}{\hbar\varepsilon}|\mu|^2 \rho(r_s, \omega) \tag{13}$$

The dielectric constants as a function of wavelength have been obtained from nanohub[32]. As we are using the total dielectric functions of the metals involved, the optical losses arising from the plasmonic metals are included through the inclusion of the imaginary part of the dielectric constant in the calculations. The Purcell factor (PF) can then be defined as the ratio of emission rate in the presence of scatters to that in free space.

$$\mathrm{PF} = \frac{\gamma}{\gamma_0} = \frac{\rho(r_s,\omega)}{\rho_0(r_s,\omega)} \tag{14}$$

LDOS for Core-Shell Nanowires

- Dipolar source in TM polarization

For an electric dipolar source along $\hat{z}$, the electric field ($\vec{E} = V^E\hat{z}$) is the solution to equation (1):

$$(\nabla^2 + k^2)\, V^E = -i\omega\mu j_s\delta(r - r_s) \tag{15}$$

Here V^E is a "scalar potential" that satisfies the Helmholtz equation in the absence of any sources. By making the assumption that the magnitude of the source $j_s = \frac{1}{i\omega\mu}$, from equation (4) we obtain $V^E = G_{zz}$. The field at (r,φ) due to a dipole source at (r_s,β) along $\hat{z}$ in the absence of scatterers is given by:

$$Vs_z^E = \frac{1}{4i}H_0^{(1)}(k|r - r_s|) \tag{16}$$

Using Graf's addition theorem:

$$Vs_z^E = \sum_m B_{m,z}^E X_m(kr)e^{im\phi}$$
$$B_{m,z}^E = \begin{cases} \frac{1}{4i}H_m^{(1)}(kr_s)e^{-im\beta} & r < r_s \\ \frac{1}{4i}J_m(kr_s)e^{-im\beta} & r > r_s \end{cases}$$
$$X_m(kr) = \begin{cases} J_m(kr) & r < r_s \\ H_m^{(1)}(kr) & r > r_s \end{cases} \tag{17}$$

- LDOS for TM polarization

The electric field in the absence of sources is a solution to the Helmholtz equation and can be expressed as a summation of Bessel and Hankel functions. By adding the contribution due to the dipolar source within the shell using the expression defined in equation (17), the electric field inside and outside the nanowire can be written as follows:

$$V^E_{z,ext} = -\sum_m \{A_m H^{(1)}_m(kr)\} e^{im\phi}$$

$$V^E_{z,shell} = \sum_m \{B^E_{m,z} X_m(kr) + C_m J_m(kr) + D_m H^{(1)}_m(kr)\} e^{im\phi}$$

$$V^E_{z,core} = \sum_m \{E_m J_m(kr)\} e^{im\phi}$$

Here the coefficients A_m, C_m, D_m and E_m can be obtained by applying the boundary conditions at each interface. The tangential fields (E_z and H_φ) at each interface are continuous which gives the following set of linear equations:

$$\begin{pmatrix} -H^{(1)}_m(k_0 b) & -J_m(k_2 b) & -H^{(1)}_m(k_2 b) & 0 \\ -\frac{1}{\eta_0} H^{(1)\prime}_m(k_0 b) & -\frac{1}{\eta_2} J'_m(k_2 b) & -\frac{1}{\eta_2} H^{(1)\prime}_m(k_2 b) & 0 \\ 0 & -J_m(k_2 a) & -H^{(1)}_m(k_2 a) & J_m(k_1 a) \\ 0 & -\frac{1}{\eta_2} J'_m(k_2 a) & -\frac{1}{\eta_2} H^{(1)\prime}_m(k_2 a) & \frac{1}{\eta_1} J'_m(k_1 a) \end{pmatrix} \begin{pmatrix} A_m \\ C_m \\ D_m \\ E_m \end{pmatrix} = \begin{pmatrix} B^E_{m,z} H^{(1)}_m(k_2 b) \\ \frac{1}{\eta_2} B^E_{m,z} H^{(1)\prime}_m(k_2 b) \\ B^E_{m,z} J_m(k_2 a) \\ \frac{1}{\eta_2} B^E_{m,z} J'_m(k_1 a) \end{pmatrix}$$

Here, $\eta_i = \sqrt{\mu_i/\varepsilon_i}$ is the wave impedance. The electric field and in turn the LDOS for TM polarization can be obtained by solving these linear equations.

- Dipolar source in TE polarization

For an electric dipolar source oriented along $\hat{u}$, where $u = x$ or y, the magnetic field ($\vec{H} = V^H \hat{z}$) is the solution to

$$(\nabla^2 + k^2) V^H = \frac{1}{i\omega\mu} \hat{z}.[\nabla \times -\hat{u}\delta(r - r_s)] \tag{18}$$

Here V^H is a “scalar potential” that satisfies the Helmholtz equation in the absence of any sources. The Green’s tensor in equation (11) can be evaluated by solving equation (18).

The field at (r,φ) along $\hat{z}$ due to a dipole source at (r_s,β) along $\hat{x}$ or $\hat{y}$ in the absence of scatterers is given by:

$$Vs^H_{z,x} = \frac{1}{i\omega\mu}\hat{z}.[\nabla \times \hat{x}\frac{1}{4i}H_0^{(1)}(k|r-r_s|)] = -\frac{1}{4}\sqrt{\frac{\epsilon}{\mu}}H_1^{(1)}(k|r-r_s|)\sin(\theta)$$

$$Vs^H_{z,y} = \frac{1}{i\omega\mu}\hat{z}.[\nabla \times \hat{y}\frac{1}{4i}H_0^{(1)}(k|r-r_s|)] = \frac{1}{4}\sqrt{\frac{\epsilon}{\mu}}H_1^{(1)}(k|r-r_s|)\cos(\theta)$$

Using Graf’s addition theorem:

$$Vs^H_{z,x} = \sum_m B^H_{m,x}X_m(kr)e^{im\phi}$$

$$B^H_{m,x} = \begin{cases} -\frac{1}{8i}\sqrt{\frac{\epsilon}{\mu}}\{H^{(1)}_{m+1}(kr_s)e^{-i(m+1)\beta} + H^{(1)}_{m-1}(kr_s)e^{-i(m-1)\beta}\} & r < r_s \\ -\frac{1}{8i}\sqrt{\frac{\epsilon}{\mu}}\{J_{m+1}(kr_s)e^{-i(m+1)\beta} + J_{m-1}(kr_s)e^{-i(m-1)\beta}\} & r > r_s \end{cases}$$

$$Vs^H_{z,y} = \sum_m B^H_{m,y}X_m(kr)e^{im\phi}$$

$$B^H_{m,y} = \begin{cases} \frac{1}{8}\sqrt{\frac{\epsilon}{\mu}}\{H^{(1)}_{m+1}(kr_s)e^{-i(m+1)\beta} - H^{(1)}_{m-1}(kr_s)e^{-i(m-1)\beta}\} & r < r_s \\ -\frac{1}{8}\sqrt{\frac{\epsilon}{\mu}}\{J_{m+1}(kr_s)e^{-i(m+1)\beta} - J_{m-1}(kr_s)e^{-i(m-1)\beta}\} & r > r_s \end{cases}$$

(19)

Here $X_m(kr)$ is defined the same as in equation (17).

- LDOS for TE polarization

The magnetic field, similar to the previous case, in the absence of sources is a solution to Helmholtz equation and can be expressed as a summation of Bessel and Hankel functions. By adding the contributions due to the dipolar source along $\hat{x}$ within the shell using the expression defined in equation (19), the magnetic fields inside and outside the nanowire are:

$$
\begin{aligned}
V^H_{z,ext} &= -\sum_m \{A_m H^{(1)}_m(kr)\} e^{im\phi} \\
V^H_{z,shell} &= \sum_m \{B^H_{m,x} X_m(kr) + C_m J_m(kr) + D_m H^{(1)}_m(kr)\} e^{im\phi} \\
V^H_{z,core} &= \sum_m \{E_m J_m(kr)\} e^{im\phi}
\end{aligned}
$$

Only the source term changes if the dipole is oriented along $\hat{y}$. The coefficients A_m, C_m, D_m and E_m can be obtained by enforcing continuity of tangential fields (H_z and E_φ) at each interface which can be expressed as the following set of linear equations:

$$
\begin{pmatrix}
-H^{(1)}_m(k_0 b) & -J_m(k_2 b) & -H^{(1)}_m(k_2 b) & 0 \\
-\eta_0 H^{(1)'}_m(k_0 b) & -\eta_2 J'_m(k_2 b) & -\eta_2 H^{(1)'}_m(k_0 b) & 0 \\
0 & -J_m(k_2 a) & -H^{(1)}_m(k_2 a) & J_m(k_1 a) \\
0 & -\eta_2 J'_m(k_2 a) & -\eta_2 H^{(1)'}_m(k_0 a) & \eta_1 J'_m(k_1 a)
\end{pmatrix}
\begin{pmatrix} A_m \\ C_m \\ D_m \\ E_m \end{pmatrix}
=
\begin{pmatrix}
B^E_{m,x} H^{(1)}_m(k_2 b) \\
\eta_2 B^E_{m,x} H^{(1)'}_m(k_2 b) \\
B^E_{m,x} J_m(k_1 a) \\
\eta_2 B^E_{m,x} J'_m(k_2 a)
\end{pmatrix}
$$

Here, $\eta_i = \sqrt{\mu_i / \varepsilon_i}$ is the wave impedance. The magnetic field can be obtained by solving these linear equations which can be used to obtain the electric field and in turn the LDOS. The electric field for TE polarization is:

$$
\begin{aligned}
E^{TE} &= -\frac{1}{i\omega\epsilon}\left(\nabla \times V^H_z\right) = \frac{i}{\omega\epsilon}\left(\frac{1}{r}\frac{\partial V^H_z}{\partial\phi}\hat{r} - \frac{\partial V^H_z}{\partial r}\hat{\phi}\right) \\
E^{TE}_{ext} &= -\frac{i}{\omega\epsilon}\sum_m A_m \left(\frac{im}{r} H^{(1)}_m(kr)\hat{r} - k H^{(1)\prime}_m(kr)\right) e^{im\phi}
\end{aligned}
$$

$$E^{TE}_{shell} = \frac{i}{\omega\epsilon}\sum_m \{B^H_{m,x}\left(\frac{im}{r}X_m(kr)\hat{r} - kX'_m(kr)\hat{\phi}\right) + C_m\left(\frac{im}{r}J_m(kr)\hat{r} - kJ'_m(kr)\hat{\phi}\right)$$
$$+ D_m\left(\frac{im}{r}H^{(1)}_m(kr)\hat{r} - kH^{(1)\prime}_m(kr)\hat{\phi}\right)\}e^{im\phi}$$
$$E^{TE}_{core} = \frac{i}{\omega\epsilon}\sum_m E_m\left(\frac{im}{r}J_m(kr)\hat{r} - kJ'_m(kr)\hat{\phi}\right)e^{im\phi}$$

The sum of the electric fields along $\hat{x}$ and $\hat{y}$ when the source is respectively oriented along those directions gives the trace of Green's tensor for TE polarization.

Section Two: Mie Scattering and Absorption of CMS NWs

The NWs are modeled as cylinders of infinite length with the incident light perpendicular to the NW axis. Using Mie formalism developed for cylinders with and without a shell, rigorous solutions to Maxwell's equations are obtained and thus the scattering efficiency, and the absorption efficiency of individual layers and of the total nanowire can be calculated[33-35]. The scattering efficiencies were calculated for wires under unpolarized light with the nanowires being smaller than the wavelength of light in the radial direction. The total scattering efficiency of the CMS NWs can be calculated from the Mie coefficients a_n and b_n as follows:

$$Q^{(TM)}_{sca} = \frac{2}{k_0 r}\{\textstyle\sum_{n=-\infty}^{+\infty}(\left|a_n^{(TM)}\right|^2 + \left|b_n^{(TM)}\right|^2)\} \tag{20}$$

$$Q^{(TE)}_{sca} = \frac{2}{k_0 r}\{\sum_{n=-\infty}^{+\infty}(\left|a_n^{(TE)}\right|^2 + \left|b_n^{(TE)}\right|^2)\} \tag{21}$$

Here, k_0 is the wave number of the incident light in the medium, and r is the total radius of the NW considered. The total scattering efficiency for the unpolarized light can then be calculated as the average of the scattering from the TE and TM counterparts:

$$Q_{sca} = \frac{1}{2}\left\{Q_{sca}^{(TM)} + Q_{sca}^{(TE)}\right\} \tag{22}$$

The absorption efficiency for the TM and TE waves were calculated by first evaluating the extinction efficiency, and then using both the scattering efficiency and the extinction efficiency as follows:

$$Q_{ext}^{(TM)} = \frac{2}{k_0 r}\{\sum_{n=-\infty}^{+\infty} Re(b_n^{(TM)})\} \tag{23}$$

$$Q_{abs}^{(TM)} = Q_{ext}^{(TM)} - Q_{sca}^{(TM)} \tag{24}$$

$$Q_{ext}^{(TE)} = \frac{2}{k_0 r}\{\sum_{n=-\infty}^{+\infty} Re(a_n^{(TE)})\} \tag{25}$$

$$Q_{abs}^{(TE)} = Q_{ext}^{(TE)} - Q_{sca}^{(TE)} \tag{26}$$

$$Q_{abs} = \frac{1}{2}\left\{Q_{abs}^{(TE)} + Q_{abs}^{(TM)}\right\} \tag{27}$$

We further evaluated the absorption efficiency within individual layers, which is the ratio of the power absorbed over the power incident per unit length of the wire, and can thus be calculated for each layer by setting the integration limits appropriately:

$$\eta_i^{(TM)} = \frac{k_0}{2rE_0^2} \iint Im\{\epsilon(r)\} \left| (E_r^{(TM)})^2 + (E_\phi^{(TM)})^2 + (E_z^{(TM)})^2 \right| r\, dr d\phi \tag{28}$$

$$\eta_i^{(TE)} = \frac{k_0}{2rE_0^2} \iint Im\{\epsilon(r)\} \left| (E_r^{(TE)})^2 + (E_\phi^{(TE)})^2 + (E_z^{(TE)})^2 \right| r\, dr d\phi \tag{29}$$

$$\eta_i = \frac{1}{2}\left\{\eta_i^{(TM)} + \eta_i^{(TE)}\right\} \tag{30}$$

Here, E_0 is the magnitude of the incident field on the wire, and E_r, E_Φ and E_z can be calculated from the Mie coefficients.

Section Three: Plasmonic CMS NWs for White LEDs (WLEDs)

WLEDs and their disadvantages

WLEDs, compared to traditional illumination, have higher efficiencies, longer lifetimes and are also environmentally friendly. They are being used as replacements for conventional fluorescent and incandescent lamps, as well as for improving performances in displays, detectors and optical communications[36-39]. Current technology uses a blue LED with integrated phosphor systems, which absorb the blue light and re-emit green/red/yellow[40-42]. The most popular commercially used phosphor is yellow-emitting cerium-doped yttrium aluminum garnet [$(Y_{1-x}Ce_x)_3Al_5O_{12}$ or YAG:Ce)], which, along with an InGaN-based blue LED, is used in WLEDs. Such phosphors are often used in the powder form dispersed in a polymer matrix[43]. They suffer from a few disadvantages. The polymer matrices such as silicones or epoxies in which the phosphor remains dispersed have low thermal conductivity and thus prevent efficient heat dissipation, limiting the phosphor performance due to thermal degradation[44]. Such particles are also highly scattering and may lead to significant backscattering losses[45]. The particles do not provide good absorption due to a small absorption cross section for incident blue light. Current commercial WLEDs have a luminous efficacy up to 150 lm/W, but with a trade-off on color rendering index of 70%. To work towards the US Department of Energy target of a luminaire of 200 lm/W, it is necessary to develop new structures and designs for phosphors for WLEDs with high efficiency and better color rendering[46].

Quantum dots have been successfully demonstrated as phosphors to improve the efficiency[47-49]. Importantly, core-shell (CS) QDs, due to increased confinement of the electron and hole pair in the core because of the presence of the shell and passivation of the dangling bonds on the surface of the core semiconductor[50], further enable the improvement. It has been shown that there is a significant improvement in the performance of CS QD-based LEDs over current LEDs[51-52]. However, despite having strong emission characteristics, CdSe based CS QDs showed absorbance of 0.2-0.4 at the wavelength of 470 nm[53-55]. Such low absorbance leads to a poor value of the internal quantum efficiency (IQE).

CS NWs as phosphors to improve WLED performance

CS NWs are a group of new materials to achieve improved external quantum efficiency (EQE) in the phosphors through improving both IQE and photon extraction efficiency (EXE). It has been shown that when scaled for volume differences, the absorbance cross section of nanowires is at least an order of magnitude greater than those of QDs[56]. Therefore, CS nanowires are expected to show improved absorption and emission compared to CS QDs. Enhancement provided by the plasmonic property enables utilizing a thin semiconductor where photons generated will be close to the surface and hence can be extracted more easily, leading to improved EXE. We have studied the PFs for different semiconductors (CdSe, CdTe, GaP, CdS) as well as Ce-doped YAG by combining them with the plasmonic metals (Au, Ag, Cu, Al) and varying the dimensions of the core metal/semiconductor shell nanowire, and compared these to the corresponding bare semiconductor NW. We also demonstrated the tunability of both absorption and emission of the nanowires with respect to the core/shell dimensions. Subsequently, by combining the PF with the absorption, we defined the EQE, and hence, compared the performances of different CS nanowires with a bare semiconductor nanowire. Based on the comparison, we predicted the dimension and material combination for which the performance will be the most improved over that of the bare nanowire.

Once we can calculate both the absorption and the emission, we can compute the overall performance of the nanowire using the EQE. The EQE is defined as:

$$EQE = \int_{r_1}^{r_2} 2rdr\,\gamma(r,\omega_{em}) \int_0^{2\pi} d\emptyset \left[\chi(r,\emptyset)\frac{\lambda_{inc}}{hc} I_{inc}\right] \tag{31}$$

where γ (r, ω_{em}) was defined in equation (13) with ω_{em} being the frequency at the emission wavelength, r_1 and r_2 being the inner and outer boundaries of the shell, I_{inc} is the strength of the incident radiation at λ =470 nm (blue LED), taken to be 100 mW/cm^2, and h is

Planck's constant. Here, we assume the photon extraction efficiency to be 1.0. As it is difficult to know the dipole moments inside the semiconductor precisely, we evaluate the EQE per unit dipole moment, namely, $\frac{EQE}{|\mu|^2}$.

To evaluate the emission characteristics of the NWs, the spatial PF of the bare NW and CS NWs have been computed. Figure 2.1 (a) gives a comparison of the spatial distribution of the Purcell Factor (PF) for nanowires of total radii 25 nm. Here, we compared the properties of a bare CdSe nanowire (black solid line), Au/CdSe (red solid line) and Ag/CdSe (blue solid line) CS nanowires. PF values were taken at the emission of 710 nm, corresponding to the band gap wavelength of CdSe, where the dipole emission is expected to be the greatest. Figure 2.1 (a) plots the logarithmic PF as a function of the radial position. As the shell is the emitter, we looked at the emission along the radial direction of the shell only. All the nanowires show PF peaks at the shell-air interface at the position 25 nm. In addition, the CS nanowires show peaks at the core-shell interface at the position 10 nm. The peaks imply the presence of an interface in the material in the radial direction and arise due to increase in the electric fields across the interface as a result of a decreasing permittivity. The PF drops as we move away from the nanowire for positions >25 nm, and gradually approaches unity indicating the LDOS approaches its value in free space. Significantly, the emission of both Au/CdSe and Ag/CdSe CS NWs (red and blue lines) is greater than that of the bare semiconductor NW (black line) over the entire position range of the shell. Specifically, Au/CdSe and Ag/CdSe CS nanowires show similar PF peak values of approximately 175 at the position 25 nm, while the bare CdSe NW has a lower value of about 115, indicating there is a 52% increase in the Purcell factor for the CS nanowires.

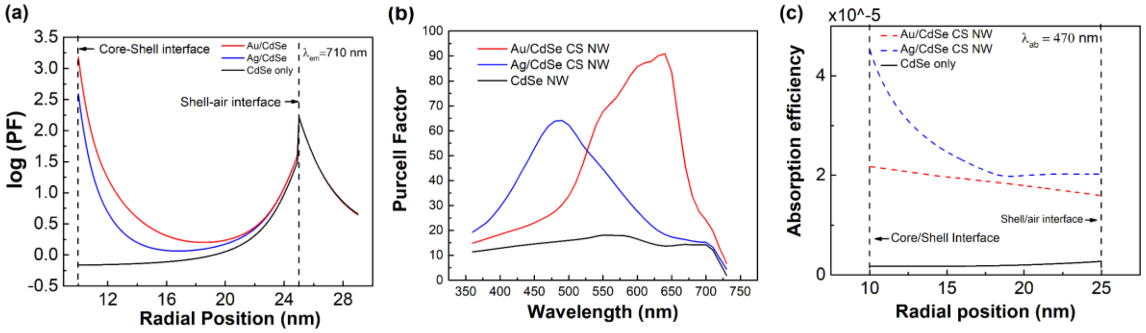

Figure 2.1: (a) Spatial variation of the logarithmic of the PF. (b) Average PF variation as a function of wavelength. (c) Spatial absorption efficiency for a bare CdSe nanowire (black), a Au/CdSe CS NW (red) and a Ag/CdSe CS NW (blue), respectively. The core radius and shell thickness are 10 nm and 15 nm respectively for the CS structures.

The improvement in the PF values is also seen for other CS nanowires studied with different combinations of metals and semiconductors, with improvements as high as 22 times at the shell-air interface for a Ag/GaP NW emitting at 550 nm, relative to a bare GaP

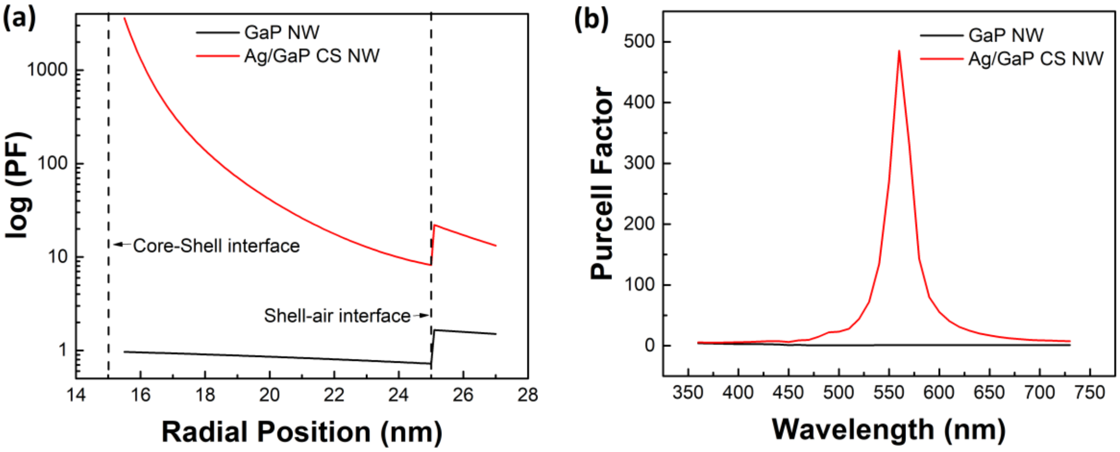

Figure 2.2: (a) shows a plot of the logarithmic PF as a function of the radial position in the nanowire. Comparisons have been made for a bare GaP nanowire of 25nm radius, and a CS Ag/GaP NW of core/shell radius 15 nm/10 nm. (b) shows the averaged PF as a function of wavelength for the same two nanowires.

NW (Figure 2.2 (a)). The main reason for the improved PF values is the enhancement in the TE and TM dipole electric fields in the shell, which lead to better emission.

In addition, the PF value depends on the metal being used. At the core-shell interface the Au/CdSe CS NW shows a PF value which is 3.87 times higher than that for the Ag/CdSe CS NW. For a certain portion of the shell close to the core-shell interface, PF is slightly greater for Au/CdSe than that of Ag/CdSe. The fact that the performance of the Au/CdSe CS nanowire is better than that of Ag/CdSe CS nanowire can be attributed to the fact that the plasmon resonance of Au is nearer to the emission wavelength of CdSe (710 nm) than Ag, and hence leads to a stronger response.

In order to study how the PF of the nanowire varies as a function of the wavelength, we plotted the averaged PF as a function of wavelength for different nanowires in Figure 2.1 (b). The averaged PF was obtained as a ratio between the integrated LDOS over the shell range of the nanowire and the integrated free space LDOS over the same range. Clearly, over the wavelength range studied, CS NWs show greater PF values compared to the bare CdSe NWs. Ag/CdSe CS NW has a peak at around 480 nm and the Au/CdSe NW shows a PF peak at 640 nm. These peak positions correspond to the plasmon resonance peaks of the metals respectively, leading to increased PF values at the corresponding wavelength. Specifically, Ag/CdSe CS NW has a peak PF value of 64 at a wavelength of 480 nm and Au/CdSe CS NW has a peak PF value of 90 at a wavelength of 640 nm, indicating a 3.5-fold improvement and a 5-fold improvement, compared to the maximum PF value of 18 obtained from the bare CdSe NW at 550 nm. We also examined the PF as a function of the wavelength for Ag/GaP CS NWs considered as a green emitter

(Figure 2.2 (b)). The Ag/GaP CS NW shows a PF peak value of 330 at 570 nm, compared to the PF peak value of 2.72 obtained from the bare GaP NW at 670 nm. Collectively, our results demonstrate that presence of metals improve the dipole emission characteristics of the CS NWs over that of the semiconductor NWs.

It is critical to evaluate emission as well as absorption to determine the overall performance of phosphors. We evaluated the absorption of the NW phosphors at the relevant blue LED incident wavelength of 470 nm. Figure 2.1 (c) shows the absorption efficiency along the radial direction in the shell range for Au/CdSe (red dashed line), Ag/CdSe (blue dashed line) and CdSe (black solid line) nanowires. The spatial absorption for both CS NWs is found to be better than the CdSe nanowire over the entire shell range. Specifically, Au/CdSe and Ag/CdSe nanowires show absorption peak values of 2.2×10^{-5} and 4.5×10^{-5} respectively, at the core-shell interface corresponding to 26.5 times and 55.7 times that of the CdSe NW. Notably, the Ag/CdSe CS nanowire always shows a better absorption spatially compared to the Au/CdSe CS NW, which is attributed to the fact that the plasmon resonance of Ag/CdSe peaks present at 480 nm is closer to the incident wavelength at which we are considering absorption.

Thermal radiation can reduce the enhancement in the emission described above, and it is important to compare the thermal losses arising in the NWs in order to choose the optimum design. The intensity of thermal radiation per unit projected area, per unit solid angle, per unit frequency is given by:

$$I=v_gU/4\pi \tag{32}$$

where v_g is the group velocity, and U is the energy density of radiation, defined by:

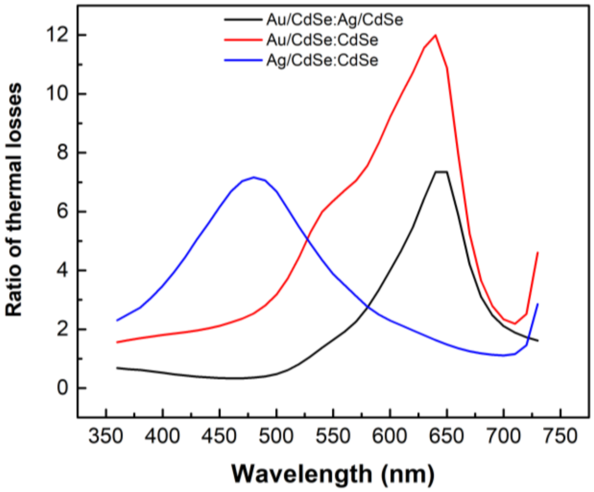

Figure 2.3: Ratio of the thermal losses of a Au/CdSe NW and a Ag/CdSe NW (black), a Au/CdSe NW and a bare CdSe NW (red), and a Ag/CdSe NW and a bare CdSe NW (blue), as a function of wavelength. The dimensions of the CS NWs are 10 nm/15 nm, while that of the bare CdSe NW is 45 nm.

$$U = D(\omega)\hbar\omega N(\omega,T) \tag{33}$$

where D(ω) is the density of states, and N(ω,T) is the mean occupation number of the photons[57]. Taking the temperature (*T*) to be constant, the mean occupation number *N(ω,T)* is equal at each frequency. Figure 2.3 plots the ratio of the thermal loss intensities I from equation (32) of a Au/CdSe CS NW with a Ag/CdSe CS NW, a Au/CdSe CS NW with a bare CdSe NW and a Ag/CdSe CS NW with a bare CdSe NW, as a function of wavelength. The CS NWs have a radius of 10 nm and shell thickness of 15 nm, while the bare CdSe NW has a radius of 45 nm. Here, the group velocity has been taken to be approximately constant for all the CdSe-based NWs. It shows that the ratio for Au/CdSe and Ag/CdSe CS NWs at first decreases, and then increases to a peak at 650 nm, and then decreases again. Both the initial decrease and the peak at 650 nm can be understood from the consideration that the thermal radiation is proportional to the density of states, which for the Ag/CdSe

CS NW shows a peak at 480 nm, and for Au/CdSe CS NW shows a peak at 640 nm. However, at the band gap emission wavelength of CdSe at 710 nm, the ratio is 1.8, implying that there is minimal difference with respect to thermal losses. The bare CdSe NW has a low thermal loss because it has low density of states compared to the CS NWs, as can be seen from Figure 2.1 (b).

It is expected that varying the core radius and the shell thickness will tune the PF and absorption efficiency in the CS NW. We aim at identifying the optimal core radius and shell thickness to achieve maximum absorption at 470 nm and maximum PF at the bandgap of the semiconductor chosen. Here we plotted the contour plots of TE absorption, TM absorption and PF as functions of the core metal radius and wavelength, for a Au/CdSe CS NW with shell thicknesses of 10 nm (Figure 2.4(a)-(c)) and 50 nm (Figure 2.4(d)-(f)), respectively. Figures 2.4(a) and 2.4(b) compare the absorption efficiencies under TE incidence and TM incidence respectively, varying core thicknesses and wavelengths for a fixed shell thickness of 10 nm. Figure 2.4(a) shows the TE absorption exhibits high values at lower wavelengths, showing the greatest values ranging from 0.3-0.65 at 300 nm. However, the value at the incident wavelength of 470 nm is low, ranging from 0.07 at low core thicknesses to 0.26 at high core thicknesses. On the other hand, the TM absorption in Figure 2.4(b) shows high values for a wide range of wavelengths from 300-550 nm, with values ranging from 0.6-0.9 for core radii of 10-20 nm. In particular, at 470 nm, the absorption efficiencies have values of 0.7-0.8 for these core radii. As these values are much higher than the TE absorption values for the incident wavelength, we conclude the TM absorption will dominate the absorption characteristics of these NWs. Figures 2.4(c) and 2.4(d) show a similar trend for the 50 nm thick shell nanowires. The TM absorption dominates the TE absorption, showing values from 1.25 to 1.40 for the 470 nm wavelength at core radii values of 10-25 nm, while the TE absorption shows values of 0.5-0.6 at the same wavelength.

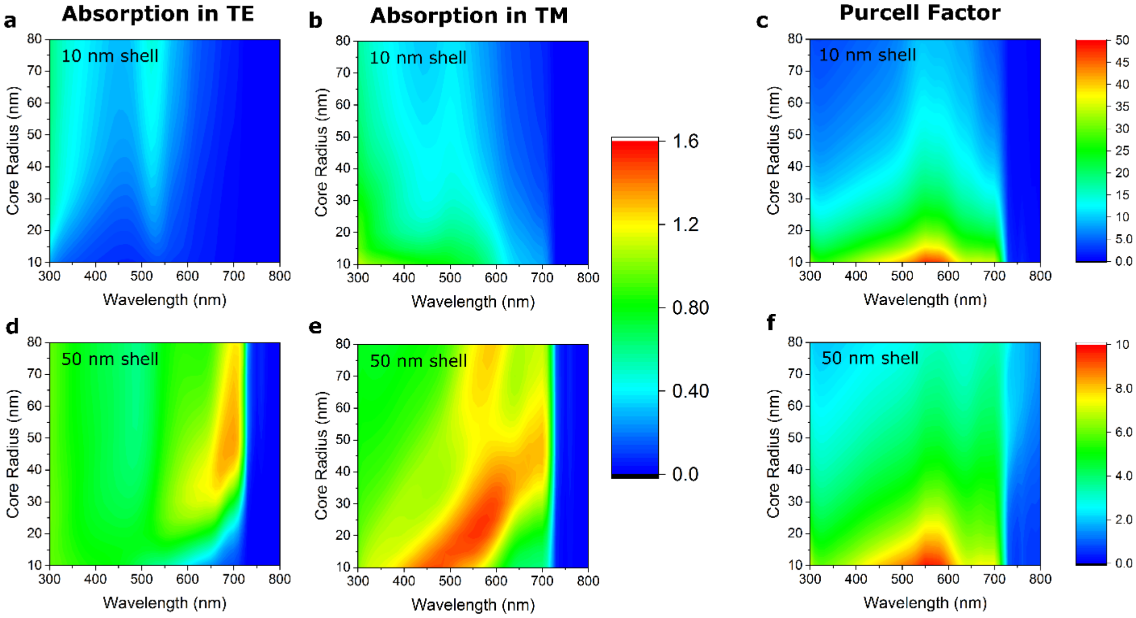

Figure 2.4: (a),(b), (d), (e) show the tunability of the absorption efficiency of a Au/CdSe CS structure of fixed shell sizes. (a) and (b) show how the absorption efficiency varies with core radius and wavelength for a fixed shell thickness of 10 nm under TE and TM incidence respectively, while (d) and (e) show the same for a fixed shell thickness of 50 nm. (c) and (f) show the tunability of the PF as functions of the core thickness and wavelength, at a point 0.5 nm away from the shell edge, for shell thicknesses of 10 nm and 50 nm respectively.

Figures 2.4(c) and 2.4(f) compare the emissions from a 10 nm shell CS structure with that of a 50 nm one, at a point 0.5 nm away from the shell edge. It can be seen that the NWs show their maximum values (~10 for 50 nm shell thicknesses and ~50 for 10 nm shell thicknesses) for lower values of the core thickness (~15-20 nm), at around 550 nm. The PF peak cannot be shifted, in general, to the emission wavelength of 710 nm by varying the core and shell dimensions as can be seen from the figures. The TE and TM cases have not been shown here separately; but the TE emission always dominates the TM emission, and it is the TE properties which are prominent in the emission characteristics. When studying them separately, we have seen that the peak TM emissions go to as low as 330 nm and to as high as 710 nm (band gap of CdSe) by varying the core radii, but the TE peaks do not show such a huge shift (shift from 440 nm-590 nm). One notable thing about the emission characteristics is that the peak PF value at this point drops sharply as we increase shell thickness. This is because the emitting states are spread across a wider radial thickness, and the density of states at any point decreases; hence the emission from any point will also considerably decrease. These results imply that the optimal design of the phosphors by varying their dimensions has to be based on both absorption and emission, as the absorption shows high values for greater shell thicknesses, while the PF shows high values for smaller shell thicknesses. To this end, we calculated EQE (equation (31)), as a parameter to characterize the overall performance, taking both absorption and emission

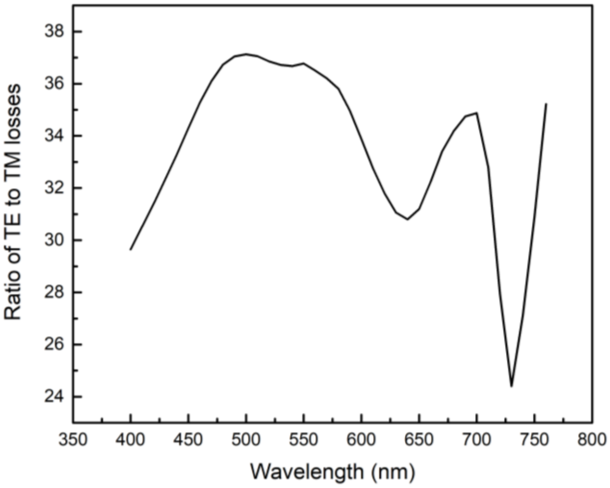

Figure 2.5: Ratio of the TE to TM losses as a function of wavelength for a Au/CdSe NW of dimensions 10 nm/15 nm.

into account. Figure 2.5 compares the ratio of the optical losses due to TE polarized and TM polarized emissions as a function of wavelength, for a Au/CdSe CS NW of dimensions 10 nm/15 nm. It can be seen that the losses due to TE polarized emission are much stronger than those due to the TM polarized emission, with the ratio being about 30 at the band-gap emission wavelength. As the TE characteristics dominate the emission properties of the NW, it is expected that the optical losses due to the metal would also be high for TE polarized emission in comparison to TM polarized emission.

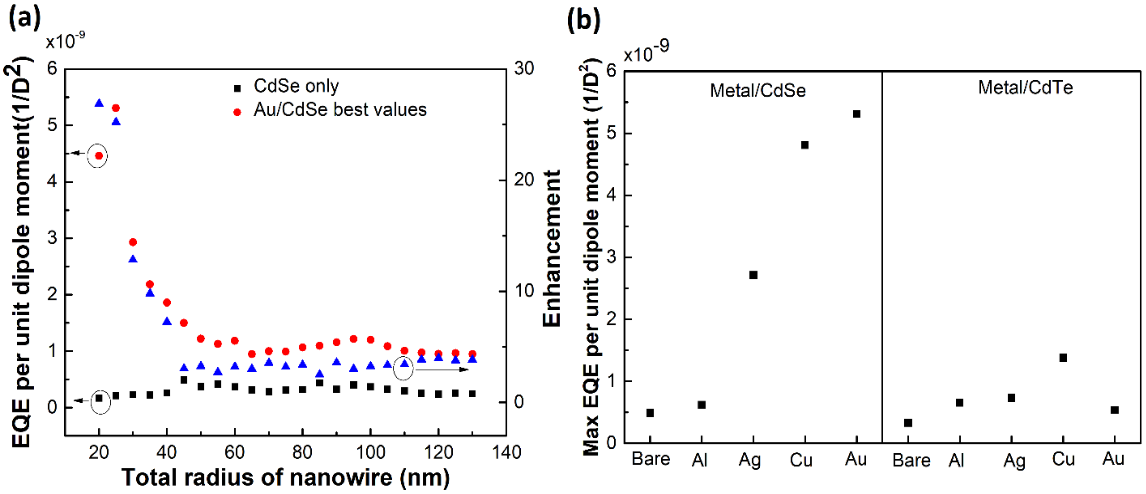

Figure 2.6: (a) EQE per unit dipole moment as a function of the total radius of nanowires. The black squares represent a bare CdSe nanowire, while the red circles show the best values for a Au/CdSe CS nanowire. Blue triangles represent the ratio of Au/CdSe CS NW EQE and CdSe NW EQE, considered as the enhancement factor. (b) The best EQE values identified considering different metals along with the optimal core/shell dimensions for the CdSe and CdTe based CS nanowires. The dimensions from left to right for CdSe (in nm) are 45, 50/40, 10/15, 10/10, 10/15, and 50, 35/25, 40/15, 10/10 and 30/25 for CdTe.

Figure 2.6(a) gives the EQE per unit dipole moment as a function of the total radius of the nanowire for a CdSe NW (black squares) and a Au/CdSe NW (red circles). The absorption has been taken to be at 470 nm wavelength, while the emission is at the CdSe band gap (710 nm). For the Au/CdSe CS nanowires, the EQE value plotted for each value of the total radius is the optimized EQE, based on varying the core radius and shell thicknesses while maintaining the total radius accordingly. The range of Au metal core radius considered is from 10 to 80 nm, and the range of the CdSe shell thickness is from 10 to 50 nm, at 5 nm intervals.

Clearly, the EQE of a Au/CdSe NW at any total radius is always better than that of a CdSe nanowire with the same total radius. The EQE of the CdSe NW is almost constant, increasing only slightly to a peak value of 4.9×10^{-10} per Debye^2 at around the radius of 45 nm. Au/CdSe NW shows a peak of 5.31×10^{-9} per Debye^2 at a total radius of 25 nm (10 nm/15 nm structure), followed by a decrease to almost a constant value around 9.5×10^{-10} per Debye^2. The enhancement, defined as the ratio between Au/CdSe CS NW EQE and CdSe NW EQE and illustrated by the blue triangles, decreases from the maximum value of 28 at the total radius of 20 nm to a steady value around 3.5 at radii larger than 45 nm.

Figure 2.6(b) summarizes the best EQE values obtained from nanowires studied as red phosphors based on CdSe and CdTe combined with different metals. In all cases, CS nanowires show a better maximum EQE value. The best performance of all the nanowires studied is the Au/CdSe CS structure (10 nm/15 nm), which shows a 10.8 times improvement over the best value for CdSe nanowire (45 nm diameter). The best combination for CdTe nanowire is Cu/CdTe (10 nm/10 nm), showing an enhancement of 4.18 over that of the bare semiconductor NW. It can be seen that the thin thicknesses actually give higher values of EQE, and comparing with Figure 2.4, we conclude that the PF dominates the absorption efficiency in the final EQE value of the NW. The current work does not take into account the presence of non-radiative states at the metal-semiconductor interface. However, Chance, et. al. have shown through their calculations that for an emitting dipole located near a metal interface (metal films considered are Au, Cu, Ag, Al), the probability of non-radiative energy transfer and the emission lifetime of an emitter decrease as the thickness of the metal film decreases[58]. They showed that for a Ag film, for maximum radiative emission, the Ag film should be approximately 10 nm thick, which is the approximate thickness of the metal layer we obtained from our calculations. Additionally, the presence of surface traps in the outer shell can negatively affect the emission properties, and therefore negatively impact the LED performance. These surface traps can be passivated by coating with ultra-thin materials of a larger bandgap. For CdSe, for example, ZnSe with a bandgap of 2.8 eV can be used to passivate CdSe surface traps[59]. By keeping the thickness of the films below 2 nm, emission of the CdSe shell should not be affected by this additional layer.

The above conclusions can be also drawn for phosphors emitting in other wavelength regions. The detailed results are plotted in Figure 2.7 with yellow-emitting YAG and green-emitting GaP based NWs. The best performing metals and dimension combinations for each of these semiconductors are listed in Table 2.1, along with the optimal enhancement relative to the bare nanowires. GaP and CdS show enhancement ratio values of EQE per dipole moment to be more than 1000 relative to the bare structure. Both the absorption and emission wavelengths for these structures are close to the plasmon resonance wavelength of Ag, which combined with the intrinsic low PF and absorbance of the bare semiconductor NWs, lead to large EQE enhancement.

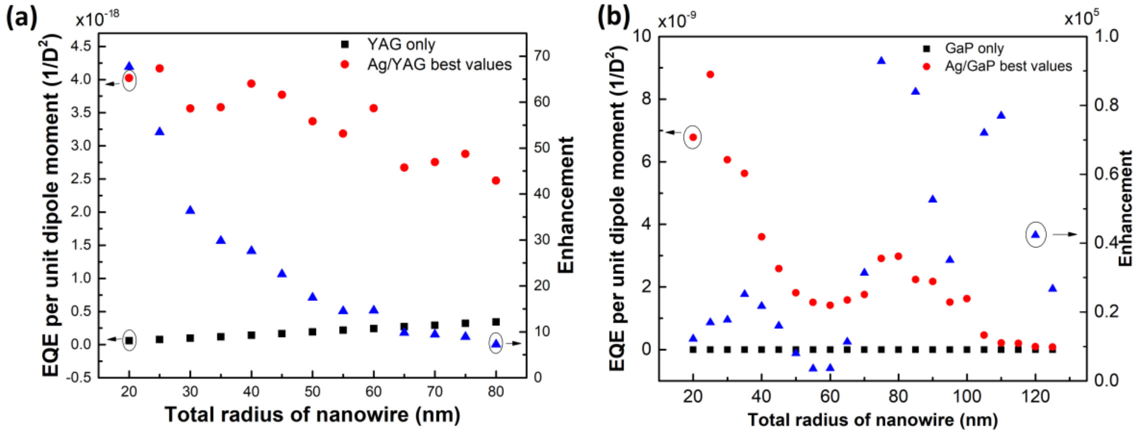

Figure 2.7: (a) shows the EQE per unit dipole moment as a function of the total radius of the nanowire. The black squares represent a bare YAG nanowire, while the red circles show the best values for a Ag/YAG structure. By best value, it means that combination of core and shell thicknesses which add up to the given total radius, and which shows the highest EQE value. The blue triangles show the enhancement at a particular radius of the EQE value of the CS structure over that of the bare nanowire. (b) shows the same for a bare GaP NW, and a Ag/GaP CS NW.

To compare directly the EQEs of CS nanowire phosphors to QD phosphors, we would need electric birefringence measurements to obtain the dipole moments of the nanowires. Therefore, for the theoretical studies, we here compare the simulated absorbance and the emission. The absorbance showed by CdSe based QDs are in the range of 0.2-0.4[53-55], for absorption of blue light at a wavelength of 470 nm. For CdSe-based nanowires, the absorption efficiencies are in the range of 0.6-0.9. For emission, Canneson and co-workers showed PF values as high as 60 for CdSe/CdS nanocrystals emitting at 660 nm[60]. In comparison, the PFs exhibited by the CdSe-based CS NWs vary from about 40 to 80 and are hence in the same order as that of QDs. Thus, combining these two factors, though the PF of the CS NWs is comparable to that of QDs, we believe that the much-improved absorption will lead to an improved EQE value of the CS NWs over the QDs.

Color	Semiconductor	Emission wavelength (nm)	Best metal	Core/Shell dimensions (nm)	Enhancement of EQE per dipole moment
Red	CdSe	710	Au	10/15	10.83
	CdTe	820	Cu	10/10	4.18
Green	CdS	510	Ag	10/15	1406
	GaP	550	Ag	15/10	15866
Yellow	YAG	570	Ag	10/15	12.2

Table 2.1: Best material combinations and dimensions for red/green phosphors. Enhancement of EQE per dipole moment of the CS NWs is measured as the improvement over bare semiconductor nanowires.

The absorbance reported for Ce-doped YAG powder is around 0.25-0.3[61], while for a Ag/YAG CS NW of core radius 10 nm and shell thickness 15 nm, the absorbance is 0.53. Using plasmon resonance, the maximum enhancement of emission over a bare YAG film has been 11 times[62]. In comparison, the greatest enhancement for the CS Ag/YAG NW compared to the bare NW is around 17.

CSS NWs as phosphors to improve WLED performance

The core shell concept can be extended to core-shell-shell (CSS) structures, enabling further improvement. Specifically, using a semiconductor-metal-semiconductor core-shell-shell structure, high PF values can be generated at the semiconductor core-metal inner shell interfaces, and the thin inner shell thickness will allow these to influence the PF

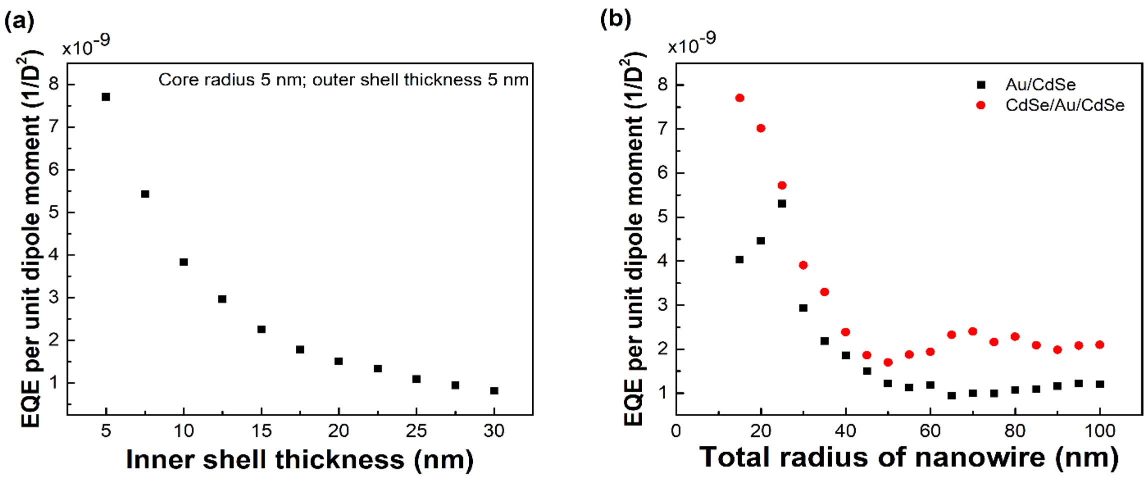

Figure 2.8: (a) plots the EQE per unit dipole moment as a function of the inner shell thickness for CdSe/Au/CdSe CSS NWs, keeping the core radii and outer shell thicknesses fixed at 5 nm and 5 nm respectively. (b) compares the EQEs of CS Au/CdSe and CSS CdSe/Au/CdSe NWs as a function of the total radius of the NWs.

values of the outer shell, correspondingly leading to further improved EQE values. To identify the configuration which gives the highest value of EQE per dipole moment, we varied the core, inner shell and outer shell thicknesses at intervals of 2.5 nm each. Notably, for a fixed core and outer shell thickness, there was a significant improvement in the EQE values towards lower inner shell thicknesses. Specifically, figure 2.8 (a) shows a CdSe/Au/CdSe CSS NW, with the core radius and outer shell thickness being fixed at 5 nm and 5 nm respectively. As the inner Au shell thickness is lowered, the calculated EQE per dipole moment starts showing a sharp increase from around 12.5 nm, going to as high as 7.73×10^{-9} per Debye^2 for a thickness of 5 nm. This value is showing an enhancement of 1.6 times over that of the best performing Au/CdSe CS NW, and a 17-time enhancement over the bare CdSe NW. The sharp increase in the EQE at such small shell thicknesses is

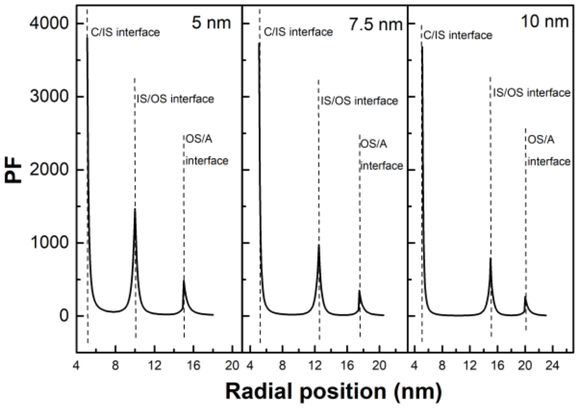

Figure 2.9: Comparison of the PF as a function of the radial position for CSS CdSe/Au/CdSe NWs. The core and outer shell thicknesses are fixed at 5 nm, and from left to right, the inner shell thicknesses are 5 nm, 7.5 nm and 10 nm respectively. C means core, IS means inner shell, OS means outer shell and A means air.

due to the high LDOS and high PF right at the core-inner shell interface, which can propagate through the inner shell to boost the PF of the outermost shell, provided the inner shell is thin enough to allow the penetration. For thicker inner shells, the electric fields cannot penetrate the inner shell to reach the outer shell. PF values for CSS NWs with different inner shell thickness were studied, supporting the discussion above (figure 2.9). Results confirmed that the PF at the interface of the inner and outer shell decreases from a value of ~1500 for the 5 nm thick Au shell to ~1000 and ~800 for the 7.5 nm and 10 nm thick Au shells respectively, though PF is the same at the core-inner shell interface for all three at ~4000. The inner shell thickness also affects the value of the PF at the outer shell-air interface, which is 481, 348 and 264 for the 5 nm, 7.5 nm and 10 nm thick Au shells respectively.

We also compared the performances of CS Au/CdSe NWs (black) and CSS

CdSe/Au/CdSe NWs (red) in Figure 2.8 (b), given a total radius. It can be seen that for a fixed total radius of the NW, there is always a CSS NW which outperforms the CS NW. Such optimal CSS NWs were often found to be the structures with 5 nm-7.5 nm Au shell thicknesses, consistent with the conclusion from figure 2.8 (a). The concept of multiple shell structures can be further to include more thin shells. Due to the similar underlying concepts, a CdSe/Au/CdSe/Au/CdSe is expected to perform better than a CdSe/Au/CdSe NW. However, the amount of improvement will go down sharply, as more layers are involved, as the fields from inner semiconductor layers would have to penetrate greater thickness to reach the outermost shell.

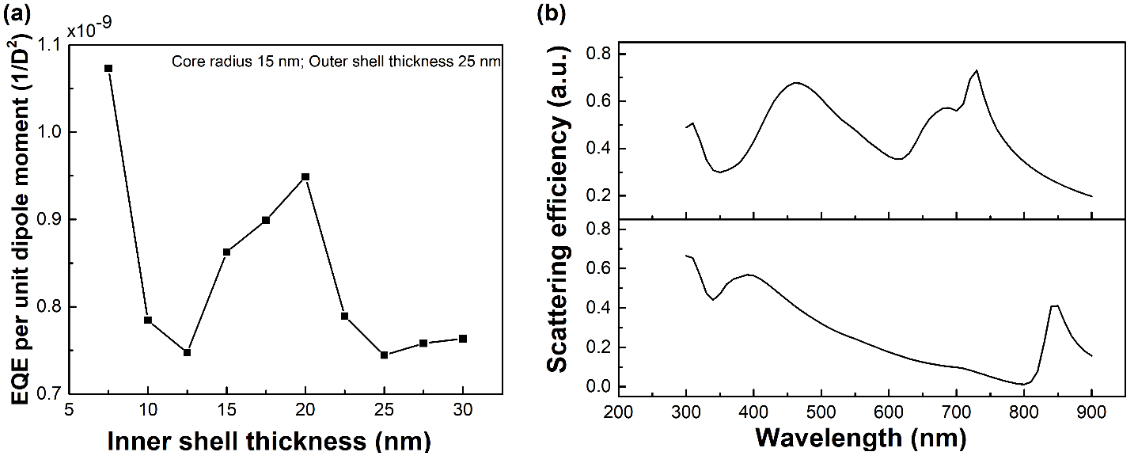

Figure 2.10: (a) plots the EQE per unit dipole moment as a function of the inner shell thickness, for CdSe/Ag/CdSe CSS NWs, keeping the core radii and outer shell thicknesses fixed at 15 nm and 25 nm respectively. (b) The scattering efficiency as a function of wavelength of a CdSe/Ag/CdSe CSS NW for the electric dipolar n=1 Mie mode, under TE polarized light. Top panel is a CSS NW with a core radius of 15 nm, inner shell thickness of 20 nm and outer shell thickness of 25 nm, while the Bottom panel is a CSS NW with a core radius of 15 nm, inner shell thickness of 7.5 nm and outer shell thickness of 25 nm.

In addition, plasmon hybridization was previously shown to allow the plasmon oscillations to show two resonant peaks in the CSS structures. By tuning the dimensions of the different layers in the CSS structures, it was shown that an improved absorption can be expected if bringing the resonant peaks close to the absorption wavelengths[63-64]. Here we explore the role of plasmon hybridization in the application of CSS NWs for phosphors. Figure 2.10 (a) plots the EQE per unit dipole moment of a CdSe/Ag/CdSe CSS NW with the fixed core radius and outer shell thicknesses being 15 nm and 25 nm respectively, as a function of the inner Ag shell thickness. The shell thickness has been varied from 7.5 nm to 30 nm, at intervals of 2.5 nm. The EQE shows two local maxima, including a peak value of 1.073×10^{-9} per Debye^2 at a thickness of 7.5 nm and a second peak value of 0.95×10^{-9} per Debye^2 at the Ag shell thickness of 20 nm. Figure 2.10 (b) shows the scattering efficiency of the CdSe/Ag/CdSe CSS NW as a function of wavelength for the electric dipolar Mie resonance mode (n=1). The top panel is plotted for the CSS structure giving the peak at 20 nm in Figure 2.10 (a), which has a core of 15 nm radius, an outer shell thickness of 25 nm, and the inner shell thicknesses of 20 nm, respectively. This CSS NW shows two peaks with comparable peak values that correspond to the electric plasmon oscillations at 470 nm matching with absorption wavelength and 720 nm overlapping with emission wavelength, respectively. This result confirms that double peaks overlapping with absorption and emission leads to an expected high value of the EQE per dipole moment, as seen with the second peak in figure 2.10 (a). Significantly, figure 2.10 (b) bottom panel plots the scattering efficiency for the CSS CdSe/Ag/CdSe NW giving the first peak in the figure 2.10 (a), with core radius, inner shell thickness and outer shell thickness of 15 nm, 7.5 nm, and 25 nm. As shown in figure 2.10 (b) the scattering efficiency of this CSS NW shows two peaks at 390 nm and 840 nm respectively, away from the 470 nm absorption and 710 nm emission of the nanowire. It is thus concluded that the highest EQE value is primarily due to small thicknesses of the inner shell as discussed above. The effect of the thin inner shell outperformed the improvement resulting from the plasmon hybridization.

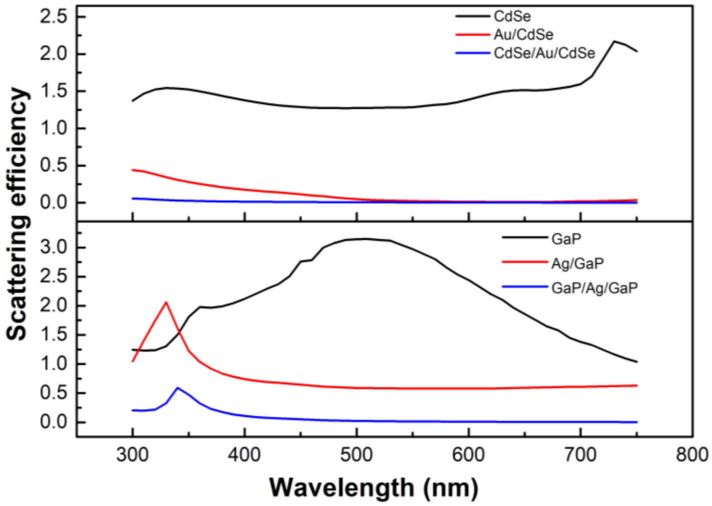

Figure 2.11: Comparison of the scattering efficiency as a function of the total wavelength for red and green emitting nanowires. The scattering efficiency has been calculated using the Mie formalism. Top panel is for a red-emitting CdSe-based NW, with the radii of the bare CdSe NW being 45 nm, the CS Au/CdSe NW having dimensions of 10/15 nm, and the CSS CdSe/Au/CdSe NW having dimensions of 5/5/5 nm. Bottom panel is for a green-emitting GaP-based NW, with the radii of the bare GaP NW being 25 nm, the CS Ag/GaP NW having dimensions of 15/10 nm, and the CSS GaP/Ag/GaP NW having dimensions of 5/5/5 nm.

To compare the scattering profiles of the NWs, we compare the scattering efficiencies as functions of wavelengths (Figure 2.11). The dimensions of the NWs chosen are those showing the greatest EQE values for given specific structures. The top panel compares the scattering efficiencies of a bare 45 nm radius CdSe NW, with a CS Au/CdSe NW of core radius of 10 nm and shell thickness 15 nm, and a CSS CdSe/Au/CdSe NW of core radius 5 nm, inner shell thickness of 5 nm and outer shell thickness of 5 nm. It shows that the scattering decreases gradually as we include more shells in the NWs, resulting in the scattering from the CSS NWs being negligible compared to the bare CdSe NW. The bottom panel, which compares the scattering efficiencies of a bare 25 nm GaP NW, with a CS Ag/GaP NW of core radius of 15 nm and shell thickness 10 nm, and a CSS GaP/Ag/GaP NW of core radius/inner shell thickness/outer shell thickness of 5/5/5 nm, also shows the CSS NW shows the least scattering. Thus, the scattering profile demonstrates that in addition to the CSS NWs showing the greatest EQE values when compared to CS and bare semiconductor NWs, they also have the lowest scattering losses among these three structures, making them the ideal candidates for use as phosphors.

Emerging plasmonic materials in CMS NW phosphors

Using emerging plasmonic materials as the metallic component in place of traditional plasmonic metals can enhance the performance of the CMS NW phosphors further. Figure 2.12 shows the plots of the EQE per unit dipole moments for CS and CSS NWs using metal nitrides like ZrN and TiN as the metallic components for a red emitting phosphor. Figure 2.12 (a) shows that the best performing ZrN/CdSe NW and the best performing TiN/CdSe NW show 1.9 times and 4.6 times improvement over a Au/CdSe CS NW respectively at a total radius of 20 nm for the NW. Figure 2.12 (b) shows that a Si/TiN/CdSe NW shows a 4.25 times improvement over a CSS Si/Au/CdSe NW at a total radius of 20 nm. Here, Si was used as the core material taking fabrication feasibility into consideration, where fabricating a Si NW is much easier than fabricating a CdSe NW.

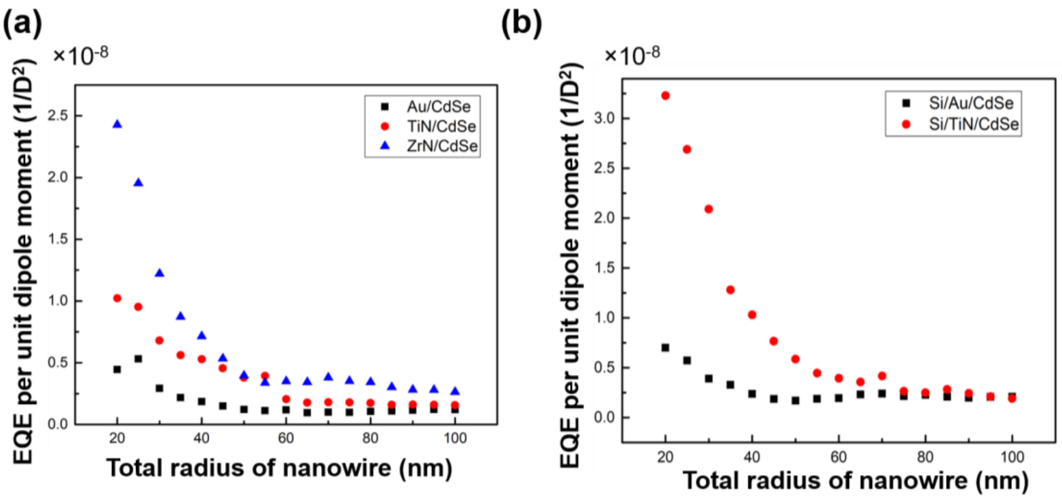

Figure 2.12: (a) shows the EQE per unit dipole moment as a function of the total radius of the nanowire. The black squares represent a CS Au/CdSe NW, the red circles show the best values for a CS TiN/CdSe NW structure, while the blue triangles show a ZrN/CdSe CS NW. (b) shows the same for a CSS Si/Au/CdSe NW (black square) and a CSS Si/TiN/CdSe NW (red circle).

Table 2.2 shows the best material combination and dimension for each kind of phosphor (red, yellow and green) as well as the optimal dimensions for CS and CSS NWs.

Type of Phosphors	Semiconductor (color)	Emission wavelength (nm)	Best material combination	Best Dimensions (nm)*	EQE per unit dipole moment ($1/D^2$)
CS NW	CdSe (red)	710	Au/CdSe	10/15	5.31×10^{-9}
	CdS (green)	510	Ag/CdS	10/15	7.58×10^{-8}
	YAG:Ce (yellow)	570	Ag/YAG:Ce	15/10	4.17×10^{-19}
CSS NW	CdSe (red)	710	CdSe/TiN/CdSe	10/5/5	3.65×10^{-8}
	CdS (green)	510	CdS/Ag/CdS	5/5/5	3.34×10^{-7}
	YAG:Ce (yellow)	570	YAG/Ag/YAG	5/5/25	1.25×10^{-18}

Table 2.2: Best performing CS/CSS NW phosphors for red/green/yellow emission, with the EXE taken to be 1.0. Calculations were done using dimensions rounded to 5 and 10 nm.

WLED efficiency estimation

We estimate the theoretical EQE of the proposed CS and CSS NW phosphors to be 0.51 and 0.69, respectively. Specifically, to estimate the EQE values and the luminous efficacy, we consider a 5 μm long Au/CdSe CS NW phosphor and a 5 μm long CdSe/Au/CdSe CSS NW phosphor. We use the theoretically calculated values of the EQE per dipole moment to estimate the luminous efficacies. The best performing NW phosphors for the CS and CSS NW phosphors have EQE per dipole moment values of 3.72×10^{-9} per Debye^2 and 2.55×10^{-8} per Debye^2 respectively based on equation (31), assuming that (1) the "unscreened" dipole moment is increasing linearly as functions of both the diameter and the length, (2) the dipole moment goes to zero when either the length and diameter of the NW is zero and (3) the dipole moments due to the length and the diameter can be added independently of each other to get the final dipole moment value. Based on experimental dipole moment data of CdSe nanorods from Li *et. al.*[65] we estimate the dipole moment of the abovementioned CS NW with shell thickness of 15 nm to be 1.1×10^4 Debye. Such large values of the dipole moments are justified, as these are different from the molecular dipole moments and have been shown to have high values for other nanorod systems[66]. We have so far assumed the EXE to be 1 for the phosphors for ease of calculation. Practically, the EXE is lower. Based on the reported value range, the average EXE of the phosphors can be taken to be 0.7[67-69]. Therefore, taking that into account, the EQE for the CS NW is 0.51, and 0.69 for the CSS NW. The luminous efficacy η_L and the Phosphor Conversion Efficiency (*PCE*) for phosphors are given by:

$$\eta_L = WPE \times PCE$$

$$PCE = LE \times EQE \times PE \tag{34}$$

where *WPE* is the Wall Power Efficiency of the blue LED component, and *LE* is the Lumen Equivalent of the blue LED, and *PE* is the Packing efficiency. With the *PE* having a value of 0.9 for the high-power domed LED design[70], and *LE* having a value of 453 mW for an OSRAM Golden Dragon package LB W5SM with emission at $\lambda = 467\ nm$, **w**e estimate luminous efficacy values of 195 lm/W and 260 lm/W respectively, for the CS and CSS NW phosphors.

Section Four: Plasmonic CMS NWs for Si photodetectors[71]

Visible light Si photodetectors and cloaking to improve performance

Photodetectors are utilized in many applications including sensing, and imaging. In the pursuit of scaling device size while maintaining high responsivity, short response time, and high photoconductive gain, semiconducting nanostructures, especially nanowires, have been shown to be promising [72-74]. Semiconductor nanowires (NWs) show high light sensitivity due to the large surface area to volume ratio, as well as high photoconductive gain due to surface state promoted charge separation. Silicon is one of the most common visible light photoconductive materials due to its common use in electronics[73] and the resulting highly developed fabrication technology[75-76]. When silicon-based nanoscale photodetection devices perform in the near field of the observed object, they are disturbed by noise introduced due to light scattered by the sensor itself [73, 77-78].

An effective method proposed to reduce field disturbance from light scattering by the photodetector itself is cloaking, where a shell is placed over the detector and cancels the scattering due to the electromagnetic fields from the sensor, ideally over a desired range of wavelengths[77, 79-80]. Therefore scattering cancellation was found to be an optimal cloaking strategy to improve the signal/noise ratio[81]. The schematic of the principle of cloaking is shown in Figure 2.13, where a shell (green) over a detector (grey) reduces the scattering from the detector thereby reducing noise. Plasmonic cloaks, which achieve scattering cancellation due to their negative permittivity resulting in a local polarization vector antiparallel to that of the cloaked sensor, have been shown to be advantageous [81-82]. Plasmonic cloaking is found to be particularly advantageous in the near-infrared, visible, and ultraviolet regions, where plasmonic materials possess the desired negative real permittivity values required to act as cloaks [77, 83-84]. Another advantage of plasmonic cloaks is that it allows cloaking to occur without affecting the capacity to sense external fields. Plasmonic cloaks have been shown theoretically capable of achieving scattering cancellation of spheres [84-85] and cylinders [82]. In the solution to Maxwell's equations, for both spheres[84] and cylinders[82] within the quasi static limit, where the object is smaller than

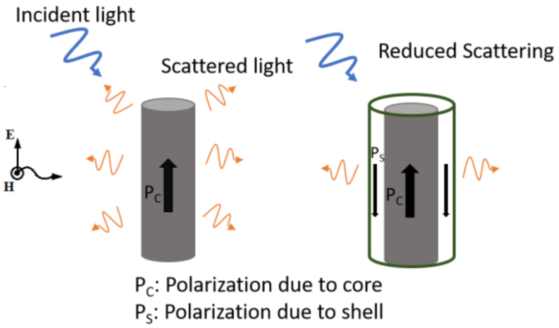

Figure 2.13: Schematic of cloaking to reduce scattering from a photodetector

the wavelength of light, the electric dipole is the dominant scattering term, and can be cancelled by a thin shell with a real permittivity less than the permittivity of free space, resulting in plasmonic cloaking. In the case of one-dimensional nanostructures, *Fan et al*.[86] showed that a gold overcoat could be engineered to suppress the light scattering of a silicon nanowire photodetector in the visible region at around 600 nm, under TM-polarized white light. It was observed that the scattering was reduced by over two orders of magnitude at the cloaking resonance. However, design including metals, especially Au, has challenges of incompatibility with Si fabrication. New plasmonic materials and designs more compatible with Si industrial processing are in need for greater scattering cancellation over the desired range of wavelengths and minimal interference with the absorption of a photosensor. Transition metal nitrides are a good alternative because of their comparative permittivities in the visible range, ease of fabrication and integration with nm-level precision, compatibility with CMOS technology enabling lower fabrication costs, easy integration and upscaling in mainstream industrial electronic devices, and exceptional mechanical properties.

One such example of a transition metal nitride is ZrN. The optical properties of ZrN largely depend on the growth conditions and it was shown to become metallic when the growth allows it to be non-stoichiometric due to nitrogen deficiency [87]. Such metallic ZrN fits a Drude-Lorentz model, resulting in dielectric functions describing metallic behavior, and a cross-over wavelength defined as the real part of the permittivity crossing zero, in the blue wavelength region of the visible spectrum [88]. Furthermore, Lalisse et al. found that ZrN to have better plasmonic properties for near-field applications than gold through their figure of merit, the Faraday number, which determined ZrN nanoparticles to be 1.5 times better than Au nanoparticles, making it a better plasmonic material used to enhance the optical near field [89]. These properties make ZrN an ideal candidate to act as a plasmonic cloak for photosensors in the visible region.

Polarization and Figure of Merit (FOM) for evaluating performance

The total scattering efficiency for unpolarized light was calculated as shown in equation (22). In the quasi-static limit, normal incident TE and TM polarized light produce scattering due to contributions from lower order multipoles (up to dipolar contributions) [90]. We confirmed the lack of higher order multipole contributions using a case example of a 28 nm diameter Si NW with a 10 nm Au shell (Figure 2.14 (a)), which shows quadrupole contributions to the scattering are 3 orders of magnitude less than dipole contributions, and octupole contributions are 8 orders of magnitude less than dipole contributions. Similar

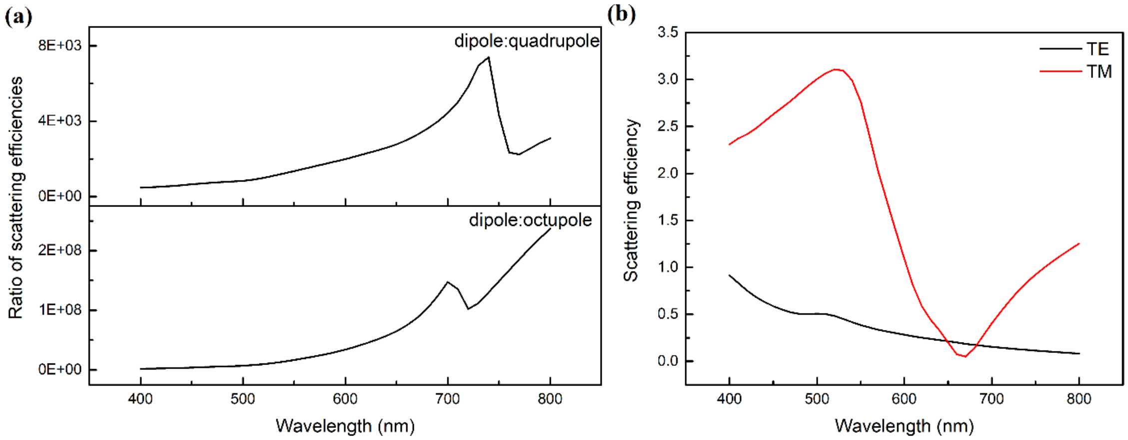

Figure 2.14: (a) Comparison of ratios of dipolar to quadrupolar scattering efficiencies (top) and dipolar to octupolar scattering efficiencies (bottom). (b) Comparison of TE and TM scattering efficiencies as functions of wavelength for a 28 nm radius Si NW with a 10 nm Au shell.

features were confirmed in other dimensions calculated. The TM modes dominate the scattering efficiency in such wires (Figure 2.14 (b)). The total scattering efficiencies were normalized by dividing the efficiencies by the highest efficiency value from the bare silicon nanowire with an identical diameter to the Si core in the cloaked structures.

The addition of the shell to the bare NW introduces one additional degree of freedom and can be manipulated to cancel the effect of the dominant scattering term, the dipole term. The effectiveness of this shell in cancelling out the scattering term, and hence acting as a reliable cloak, can be evaluated by calculating its polarization vector antiparallel to that of the core and hence its dipole moment. The polarization is given by:

$$P = D - \varepsilon_0 E = \left(\varepsilon_j - \varepsilon_0\right) E \tag{35}$$

Here, ε_j and ε_0 are the permittivities of the material and free space respectively, and E is the electric field calculated from Mie formalism, following a similar methodology as that described by our previous work. The dipole moment p per unit length can be obtained by integrating the polarization over the entire cross-section of the cloaking shell:

$$p = \int dA\left(\varepsilon_j - \varepsilon_0\right) E \tag{36}$$

The total absorption efficiency as well as the absorption efficiency in each individual layer can be calculated as shown in equations 23-27 and 28-30 respectively. We calculated the ratio of the absorption to scattering efficiency and use the ratio of that from a cloaked core-shell NW system over that of a bare Si NW as a figure of merit (FOM).

$$FOM = \frac{(\eta_i)_{c,cloaked}/(Q_{sca})_{cloaked}}{(\eta_i)_{bare}/(Q_{sca})_{bare}} = \frac{(\eta_i)_{c,cloaked} \times (Q_{sca})_{bare}}{(\eta_i)_{bare} \times (Q_{sca})_{cloaked}} \tag{37}$$

where $(\eta_i)_{c,cloaked}$ is the absorption in only the Si core and $(Q_{sca})_{cloaked}$ is the overall scattering in the cloaked system, while $(\eta_i)_{bare}$and $(Q_{sca})_{bare}$represent the same in a bare Si NW. For an ideal cloaked sensor, the scattering of the cloaked NW ($(Q_{sca})_{cloaked}$) should correspond to a minima at the wavelength where the bare Si NW scattering is a maxima ($(Q_{sca})_{bare}$). At the same time, the cloaking shell should not prevent absorption in the core, so that the absorption in the core ($(\eta_i)_{c,cloaked}$) is sufficiently high for it to act as a photosensor.

The dimensions considered in this study are from 10 nm-50 nm radii for the Si NW or the Si core in the cloaked core-shell structure, and from 1 nm-50 nm for the shell thicknesses. These dimensions were chosen based on feasibility of fabrication of the different components of the cloaked system, with the radii for Si NWs chosen being the most common dimensions fabricated, and the thickness of the shell being controlled with a nm-level precision using various techniques [87, 91].

ZrN for cloaking Si photodetectors

To compare the cloaking ability of a ZrN shell on a Si NW with a traditional plasmonic material such as Au, contour plots of the total scattering efficiency, as functions of the core Si NW radius and the cloaking shell thickness, were plotted in the visible wavelength region between 400-700 nm, at 50 nm intervals. Figure 2.15 (a) and Figure 2.15 (b) plot such contours at two example wavelengths of 500 nm and 650 nm. Results

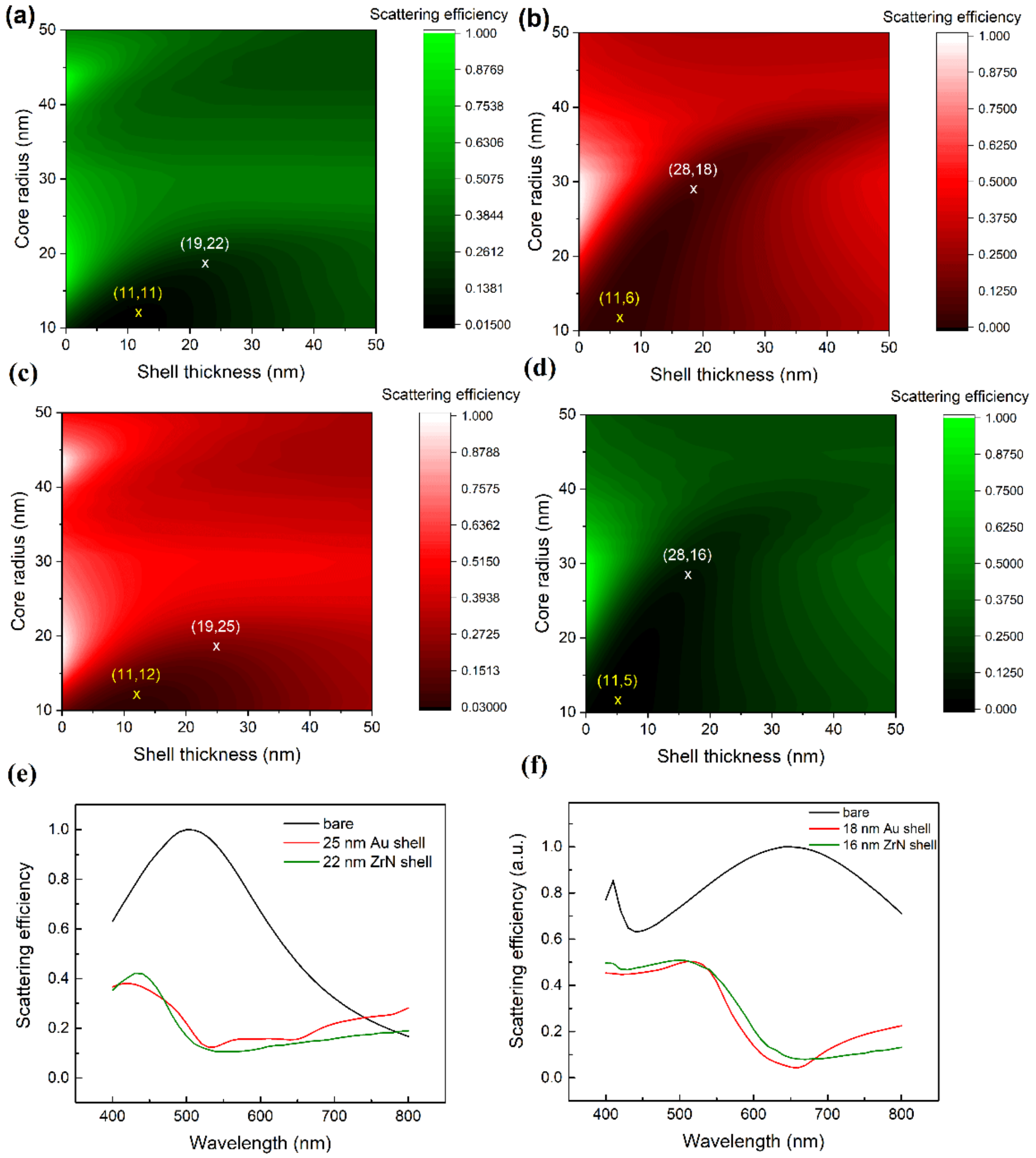

Figure 2.15: Scattering efficiency under unpolarized illumination as functions of the core radius and shell thickness. (a) Contour for ZrN cloaks, and (c) Au cloaks at a wavelength of 500 nm. (b) Contour for Au cloaks and (d) ZrN cloaks at a wavelength of 650 nm. Yellow and white crosses refer to the dimensions for lowest scattering efficiency and greatest scattering cancellation respectively, with the two numbers in the parentheses referring to core radius and shell thickness, in the unit of nanometer, respectively. (e) Scattering efficiency under unpolarized illumination for a 19 nm (radius) bare Si NW (black), with a 25 nm Au shell (red), and with a 22 nm ZrN shell (green). (f) Scattering efficiency under unpolarized illumination for a 28 nm (radius) bare Si NW (black), with a 18 nm Au shell (red), and with a 16 nm ZrN shell (green).

for other wavelengths are included in Figure 2.16. Figure 2.15 (a) plots the scattering efficiency at 500 nm as a function of the Si core radius and the ZrN shell thickness. All scattering efficiencies were normalized to the highest scattering efficiency identified in the data set. This contour shows lower scattering efficiencies occur for small core radius and shell thickness, with the lowest scattering being 0.02 at a core radius of 11 nm, and a shell thickness of 11 nm. This contour provides an opportunity to systemically study the scattering at various dimensions for different cloaking materials at a given wavelength. For instance, a contour plot where Au is used as the cloaking shell at 500 nm is shown in Figure 2.15 (c). Comparing the lowest scattering efficiencies obtained from contour plots for all wavelengths, we found that ZrN cloaks with optimized dimensions are capable to perform better than Au cloaks particularly in the wavelength range of 400-500 nm. This is the rationale we present the plot at 500 nm for ZrN cloaking structures here. Similarly, Au cloaks perform better in the wavelength range of 600-700 nm, so we use 650 nm as the example for Au cloaking structure.

Specifically, the contours also allow us to identify the dimensions of the cloak which provide greatest scattering cancellation to a given Si NW at a particular wavelength. At 500 nm wavelength, a bare Si NW with a radius of 19 nm shows a maximum scattering compared to other bare Si NWs (Figure 2.15 (a), and Fig. 2.15 (e) black). The ZrN shell could provide further reduction of the scattering and we identified that the ZrN shell with a 22 nm thickness shows the lowest scattering specifically for this Si core (Figure 2.15 (a)). Similarly, a 25 nm thickness was identified for the most effective Au cloak for this Si core (Figure 2.15(c)). A comparison for the scattering cancellation in these two structures, the

Si (19 nm radius)/ZrN (22 nm thickness) NW and the Si (19 nm radius)/Au (25 nm thickness) as a function of wavelength is summarized and presented in Figure 2.15(e). Clearly, it also confirms that ZrN (Figure 2.15 (e), green) and Au (Figure 2.15 (e), red) cloaks with the specific thicknesses both effectively reduce the maximum scattering of the bare Si NWs at 500 nm (Figure 2.15 (e) black). In addition, this ZrN cloak also shows a consistent effective cancellation, greater than the Au cloak (Figure 2.15 (e), red), throughout the visible wavelength region from 470 nm to 800 nm (Figure 2.15 (e), green). Though the scattering efficiency values are relatively close for the ZrN cloak and the Au cloak, the better compatibility with the CMOS technology and easier integration with Si systems, as mentioned earlier, make ZrN a superior cloaking material.

Notably, the scattering cancellation behaviors by cloaks are highly dependent of the working wavelength. This can be evident from an analysis performed for the wavelength of 650 nm. Figure 2.15 (b) plots the scattering efficiency at 650 nm as a function of the Si core radius and the Au shell thickness. In Figure 2.15 (b), the lowest value of scattering efficiency is 0.002 at a core radius of 11 nm, and a shell thickness of 6 nm. A ZrN shell, at this wavelength however, has a value of 0.004 at a core radius of 11 nm and shell thickness of 5 nm (Figure 2.15 (d)), which is greater than that of the Au cloak. To find out the dimensions for the greatest scattering cancellation at 650 nm, the bare Si NW of radius 28 nm was identified as the bare NW with the highest scattering efficiency. The greatest scattering cancellations for a Au shell and a ZrN shell for this core are 0.05 (18 nm thickness) and 0.08 (16 nm thickness) respectively. At 650 nm, the Au shell provides greater scattering cancellation compared to a ZrN shell. Figure 2.15 (f) plots the scattering efficiency as a function of wavelength, for these structures, i.e. the bare Si NW with a 28 nm radius, the core-shell NWs with an 18 nm Au shell (red) and a 16 nm ZrN shell (green). It can be seen that the performance of the Au-cloaked and the ZrN-cloaked NWs are similar, up till the wavelength of 540 nm, after which the Au shell provides a greater scattering cancellation till a wavelength of 680 nm.

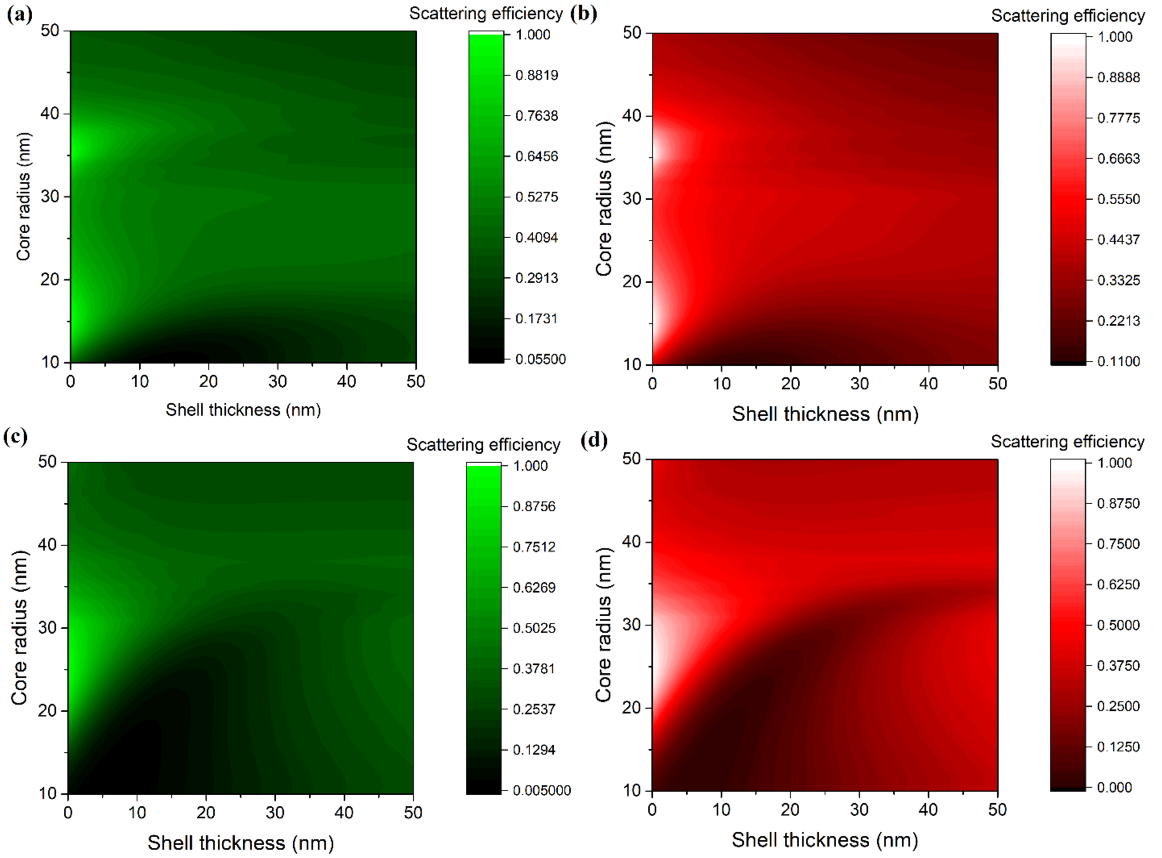

Figure 2.16: Scattering efficiency contour plots under unpolarized illumination as functions of the core radius and shell thickness for a (a) ZrN cloak at a wavelength of 450 nm, (b) Au cloak at a wavelength of 450 nm, (c) ZrN cloak at a wavelength of 600 nm and (d) Au cloak at a wavelength of 600 nm.

Figure 2.16 (a) and 2.16 (b) compare the contour plots at 450 nm, while Figure 2.16 (c) and Figure 2.16 (d) compare the contour plots at 600 nm. At 450 nm, the highest scattering efficiency for bare Si is for a 15 nm radius Si NW, for which the greatest scattering cancellation is with a 24 nm ZrN shell (0.16) and a 22 nm Au shell (0.24). At 600 nm, a 25 nm radius Si NW has the highest scattering efficiency for which an 18 nm ZrN cloak (0.10) and a 16 nm Au cloak (0.06) give the greatest scattering cancellations. From our observations of the contour plots, we can thus conclude that there are two wavelength regimes: 1) between 400-500 nm, where there is always a ZrN shell which provides better performance in terms of scattering compared to a Au shell, and 2) between 600-700 nm, where there is always a Au shell which provides better performance in terms of scattering compared to a ZrN shell. In between these two wavelength regions, at 550 nm, the scattering efficiencies provided by a ZrN shell and a Au shell are similar in magnitudes.

To gain insight on what guides the differences in scattering cancellation, the polarization vector is plotted at the wavelength corresponding to greatest scattering cancellation for the optimized systems studied in Figure 2.15 (c) and Figure 2.15(d). The goal of plasmonic cloaking is to reduce the dipolar scattering and is measured by the response of the polarization vector (P) (equation (35)). For the core where $\varepsilon_j > \varepsilon_0$, dipolar fields are induced by the local field as a result of exciting the electric field (E). This is cancelled by placing a shell which has $\varepsilon_j < \varepsilon_0$, and ideally negative. Thus, its resulting polarization vector is antiparallel to that of the core, cancelling the original dipole moment of the core itself, and thus scattering. Therefore, the greatest scattering cancellation is caused when the polarization in the shell (P_{shell}) at any given wavelength is equal in magnitude but opposite in sign to the polarization in the core (P_{core}). Figure 2.17 (a)

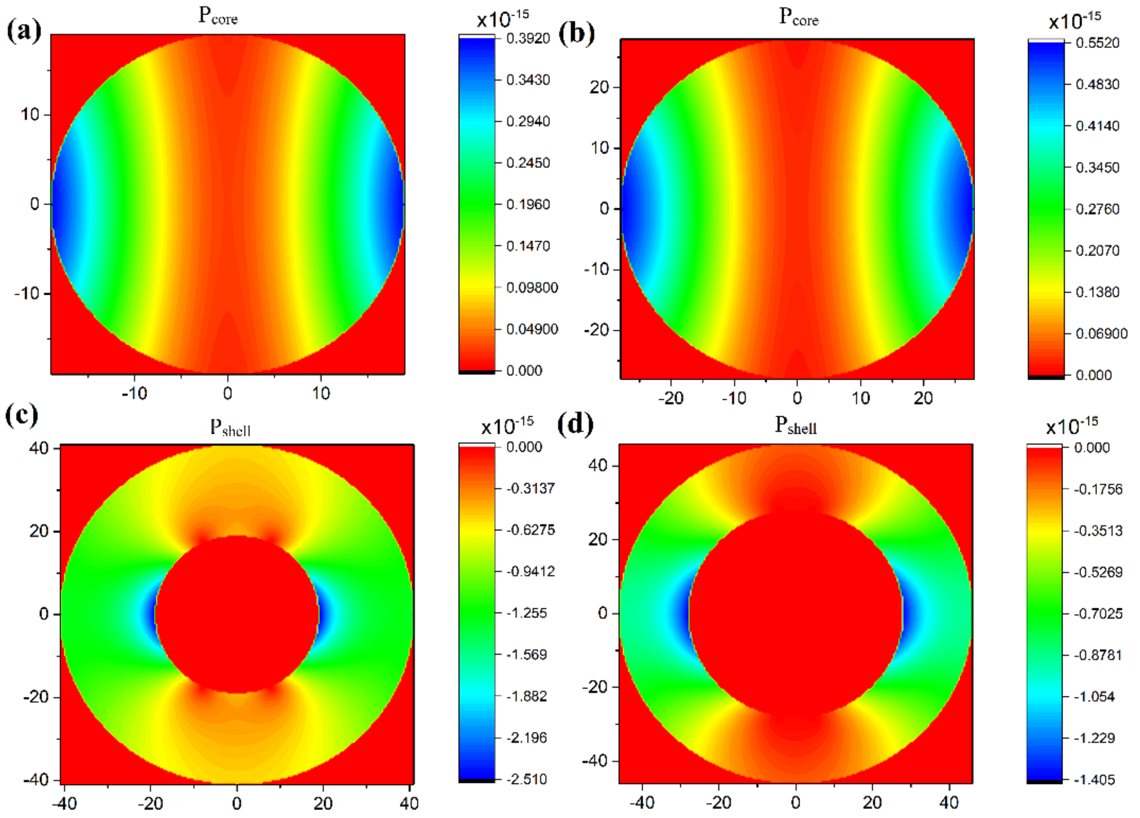

Figure 2.17: (a) Polarization for a 19 nm Si core NW at 500 nm, (b) Polarization for a 28 nm Si core NW at 650 nm, (c) Polarization for a ZrN cavity with inner radius 19 nm and thickness of 22 nm at 650 nm, (d) Polarization for a Au cavity with inner diameter 28 nm and thickness of 18 nm at 650 nm.

corresponds to the polarization vector for a 19 nm radius Si NW, while Figure 2.17 (c) corresponds to a ZrN wire cavity whose inner diameter is 19 nm and thickness is 22 nm, surrounded by air, at the wavelength of 500 nm. Figure 2.17 (a) and Figure 2.17 (c) show that the polarization vectors for the Si core and the ZrN cavity are almost equal and opposite, with the maximum values of the magnitudes of the polarization vectors being within an order of difference, and the ratio of the magnitudes of the averaged polarization in the core to that in the shell being 0.7. In contrast, at the same wavelength, a Au cavity (Figure 2.18 (a)) with an inner radius of 19 nm and a thickness of 25 nm, has a maximum can be concluded that the better matching between P_{core} and P_{shell} leads to greater scattering cancellation for a ZrN-cloaked NW in comparison to a Au-cloaked NW, at this wavelength.

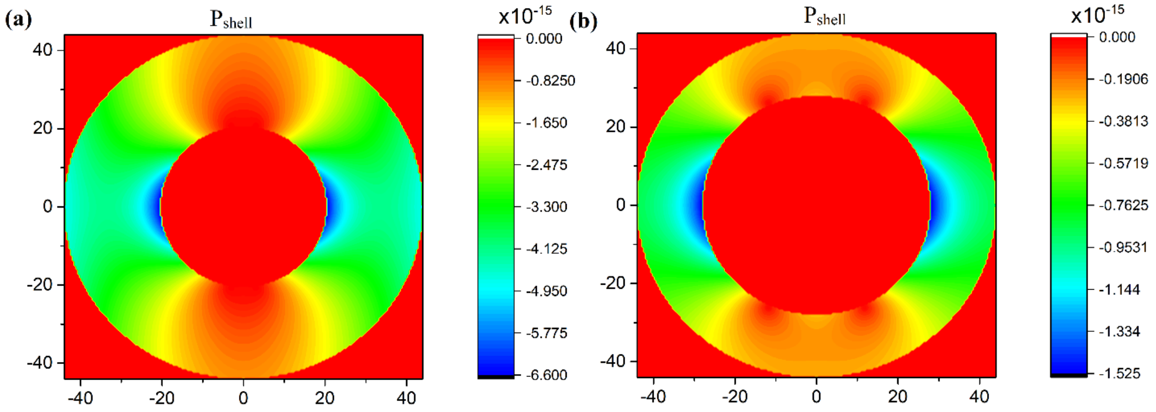

Figure 2.18: (a) Polarization for a Au cavity with inner radius 19 nm and thickness of 25 nm at 500 nm, (b) Polarization for a ZrN cavity with inner diameter 28 nm and thickness of 16 nm at 650 nm.

A similar conclusion can also be stated for the better performance of Au at a wavelength of 650 nm. Figure 2.17 (b) and Figure 2.17 (d) plot the polarization contours for a 28 nm radius Si NW, and an 18 nm thick Au cavity of inner radius 28 nm surrounded by air, while Figure 2.18 (b) plots a ZrN cavity of thickness 16 nm and inner radius 28 nm. The maximum value of the magnitude of the polarization for the Au cavity is only two times greater than that of the Si core, with the ratio of P_{core} to P_{shell} being 0.95. The close matching of the polarization vectors leads to a very high scattering cancellation and therefore a very low scattering efficiency value of 0.05 as shown in Figure 2.15 (b). Figure 2.18 (b), on the other hand, shows the maximum value for a 16 nm ZrN cavity being about 8% greater than that of the Au cavity, and the ratio of P_{core} to P_{shell} being 0.83. This leads to a slightly higher scattering efficiency value of 0.08. Thus, it can be concluded that the polarization of the shell being antiparallel to the polarization of the core with almost matching magnitudes plays a crucial role in scattering cancellation.

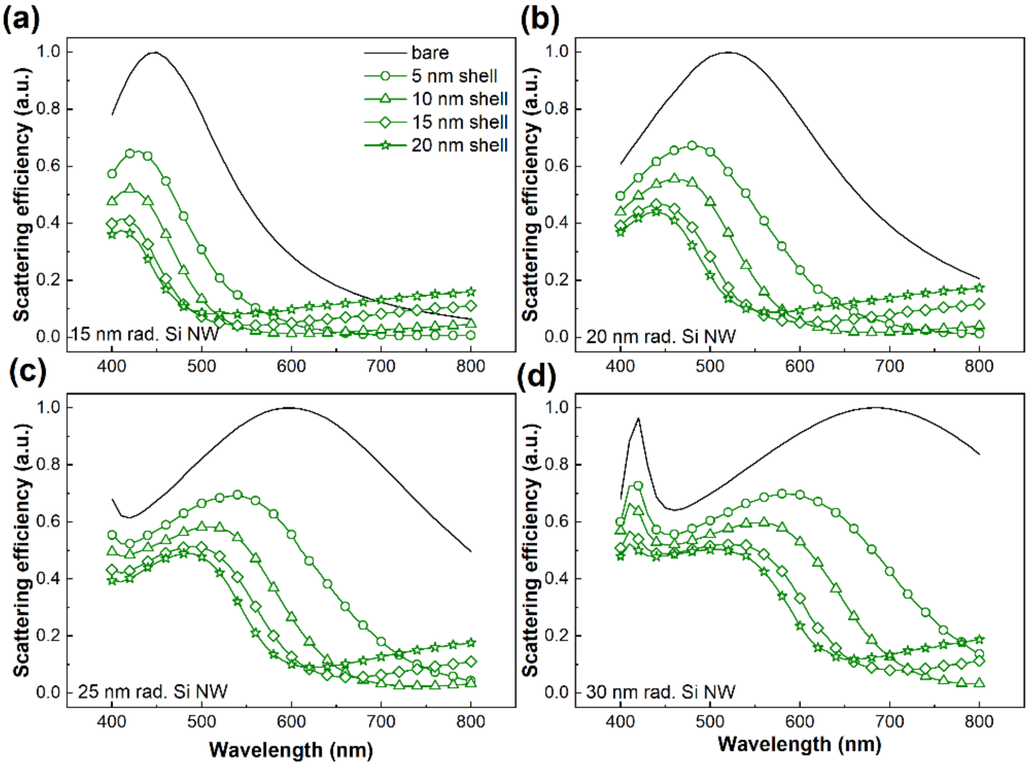

Figure 2.19: Normalized scattering efficiencies under unpolarized illumination as a function of wavelength plotted for bare Si NW (black), and ZrN shell thicknesses of 5, 10, 15 and 20 nm (green) for (a) 15 nm radius silicon nanowire and core, (b) 20 nm radius silicon nanowire and core, (c) 25 nm radius silicon nanowire and core, and (d) 30 nm radius silicon nanowire and core. The legend for all labels is in (a).

To further understand the design of Si NW based photosensors, we analyzed the scattering efficiency for various Si NW core diameters and ZrN shell thicknesses (Figure 2.19). For each core diameter, the scattering peak of the cloaked NW (green) decreases over all visible light wavelengths compared to that of the bare wire (black) as the shell thickness increases from 5 to 20 nm. As seen in the 15 nm radius Si NW case (Figure 2.19 (a)) where the bare Si NW has a scattering peak at 450 nm, two features are observed in the presence of the ZrN shell. First, the scattering peak blue shifts by 20 nm, 30 nm, 40 nm and 50 nm with shell thicknesses of 5, 10, 15 and 20 nm respectively. The blue shift is likely a consequence of increasing the total NW diameter, as previously demonstrated [92-94]. Second, as ZrN shell thickness increases, the value of the scattering maxima decreases while at the same time, the minima also start increasing. Therefore, at wavelengths below 500 nm, a 20 nm ZrN shell results in the best cloaking for this radius. However, at higher wavelengths above 600 nm, the 20 nm ZrN shell is no longer the best choice due to increase in the scattering efficiency. In this wavelength region, a 5 nm or a 10 nm ZrN shell would be more beneficial for scattering reduction for this radius of the silicon NW.

To explain the increase in the scattering at higher wavelengths for thicker ZrN shells, Figure 2.20 (a) plots the ratio of the magnitudes of the averaged polarization in the core to that in the shell as a function of wavelength for a 15 nm radius Si NW core with a 5 nm thick ZrN shell and a 20 nm thick ZrN shell. It can be seen that the Si/5 nm ZrN NW has a high ratio initially, implying that the Si core is dominating the scattering. Subsequently, the ratio starts decreasing until it is closest to 1 at 670 nm, which is where the minima of the scattering peak is. After this, the ratio goes below 1, and the ZrN shell starts controlling the scattering, due to a stronger polarization. As the 5 nm ZrN shell has a low scattering by its own (Figure 2.20 (b)), the scattering efficiency remains low in the wavelength region 670-800 nm. For the Si NW/20 nm ZrN shell, Figure 2.20 (a) shows that the ratio of P_{core} to P_{shell} crosses 1 at 480 nm, which correlates to the minima in Figure 2.19 (a). Additionally, the polarizations are more closely matched initially compared to the Si NW/5 nm ZrN shell, which is the reason for the smaller peak scattering efficiency values. However, the ratio drops below 1 faster than that for the 5 nm ZrN shell, and the

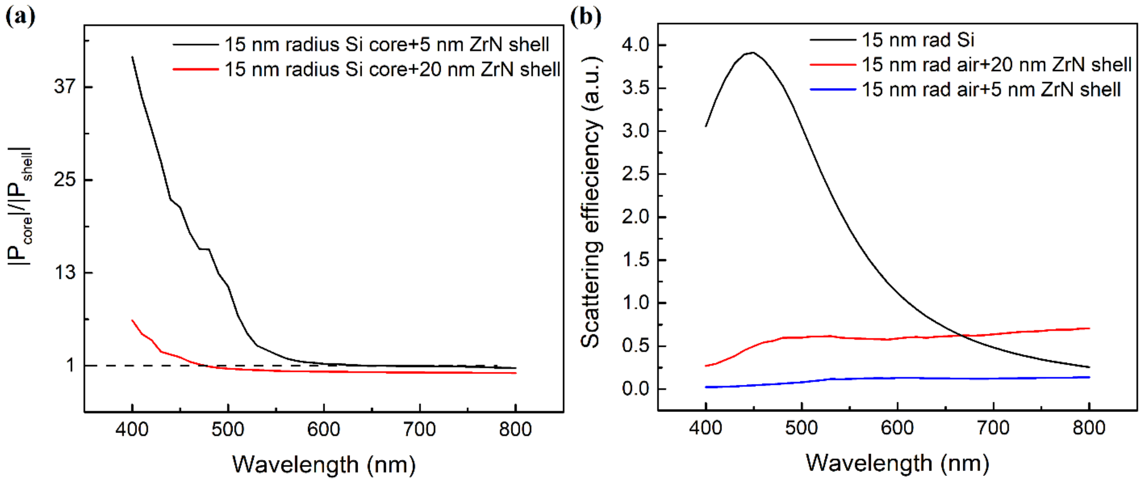

Figure 2.20: (a) Ratio of averaged polarization in the core to that in the shell for a 15 nm radius core Si NW with a 5 nm ZrN shell and a 20 nm ZrN shell, (b) Scattering efficiency as a function of wavelength for a 15 nm radius Si NW, a 5 nm thick ZrN cavity with inner radius 15 nm and a 20 nm thick ZrN cavity with inner radius 15 nm.

20 nm ZrN shell starts dominating the scattering, which combined with its own high scattering (Figure 2.20 (b)) leads to higher values of the scattering efficiency after the minima at 480 nm. These trends of blue-shifting the scattering peak, reduced scattering as ZrN shell thickness is increased, and increased scattering after the scattering minima are also observed over the core radius range of 20-30 nm (Figure 2.19 (b)-2.19 (d)). This is why it is important to optimize the shell thickness to get the greatest scattering cancellation at a given wavelength.

The Si NW core radius also impacts on both the photosensor performance and cloaking efficiency of the ZrN shell. The scattering spectrum of a bare Si NW is diameter dependent. The scattering peak red-shifts dependent on the Si NW diameter: 450, 520, 600, and 680 nm for Si NW radii of 15, 20, 25 and 30 nm respectively. For a given ZrN thickness, for example 10 nm, the wavelength at which the scattering efficiency approaches zero (defined as less than scattering efficiency of 0.1) also red-shifts with the peak as the radius of the Si NW core increases. Therefore, the Si NW cores with different radii have differences in the cloaking efficiency and this is why the same ZrN shell thickness would not provide the greatest scattering cancellation for different radii of the core.

A reduction in scattering efficiency is not the only parameter to determine the performance of the photosensor. Absorbance of the incident electromagnetic radiation is also a determining factor [95]. The absorption efficiencies of a bare Si NW and a cloaked Si NW are presented in Figure 2.21. Figure 2.21 (a) compares the efficiencies of the optimized Si/ZrN NW (with respect to greatest scattering cancellation at 500 nm, with the core radius and shell thickness of 19 nm and 22 nm respectively), to that of the optimized Si/Au NW, with core radius and shell thickness of 19 nm and 25 nm respectively. It shows that the Si/ZrN system (solid green line) improves absorption for the whole wire over that of the bare Si NW (black line), on an average by 2.4 times at lower wavelengths (up to 550 nm) and as much as 10 times in the longer wavelength region (650 nm-800 nm). There is a reduction in the absorption efficiency of just the Si core in the Si/ZrN system (green dashed line) on average by 40% from that of the bare NW at wavelengths up to 550 nm, with the shell contributing to the rest of the absorption. Similar features are also seen for the Si/Au system, where the Si/Au system (solid red line) improves absorption of the whole wire over that of the bare NW (solid black line) on an average by as much as 3 times at lower wavelengths (up to 520 nm), and about 2 times between 600-750 nm. The absorption efficiency of just the Si core in the Si/Au system (red dashed line) is comparable to that of

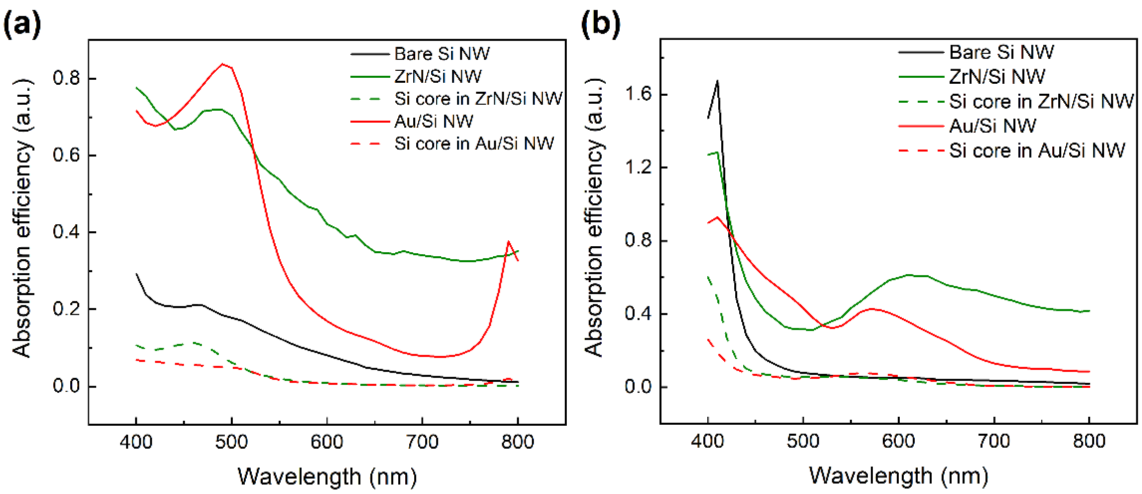

Figure 2.21: Normalized absorption efficiencies under unpolarized illumination as a function of wavelength plotted for (a) 19 nm radius bare (black), 22 nm ZrN shell cloaked (solid green) and 25 nm Au shell cloaked (solid red) silicon NWs. The figure also includes the efficiencies in the core of the corresponding NWs (dashed line), (b) 28 nm radius bare (black), 16 nm ZrN shell cloaked (solid green), 18 nm Au shell cloaked (solid red) silicon NWs. The figure also includes the efficiencies in the core of the corresponding NWs (dashed line).

the core in the Si/ZrN system, with the Si core in the latter absorbing slightly better in the wavelength region of 400-500 nm. We acknowledge that due to the larger value of the imaginary part of the dielectric constant of ZrN as compared to Au in the wavelength region greater than 500 nm, the loss in the ZrN shell due to generation of evanescent waves is expected to be greater than that of Au. Notably, in the wavelength region (400 nm-500 nm) ZrN has a lower value of the imaginary part of the dielectric constant and hence lower losses, and ZrN is found to outperform Au with respect to the FOM defined in equation (37) as shown later, thereby establishing that it is a superior cloak in the region of 400 nm-500 nm.

Figure 2.21 (b) shows the efficiencies of the optimized (with respect to greatest scattering cancellation at 650 nm) Si/ZrN NW, with core radius and shell thickness of 28 nm and 16 nm respectively, with that of the optimized Si/Au NW, with core radius and shell thickness of 28 nm and 18 nm respectively. Similar features are observed. The cloaked systems absorb better than the bare NW. The absorption in the core decreases, with that in the Au cloaked system and in the ZrN cloaked system being similar. The observed absorption in the silicon core of the ZrN cloaked nanowire indicates that non-negligible fields are able to penetrate to the silicon core, resulting in absorption for photocurrent generation.[95] Fan et. al. experimentally observed strong absorption in a Au-cloaked Si NW and thus photocurrent generation similar to that of a bare nanowire.[86] Our simulation results are reasonably close to their simulated absorption data (peak absorption efficiency around 0.9 at 570 nm), showing an absorption efficiency of 0.9 at 560 nm for the 20 nm thick Au-cloaked Si NW of 50 nm diameter. We have assumed here an ideal generation of charges, so that every photon absorbed by the Si core leads to an excited electron-hole pair. Our results show that the absorption in the Si is decreased in the cloaked system compared to the bare Si NWs, which is not favorable. The overall performance of the photosensor shall be evaluated based on combining absorption and scattering.

To evaluate the overall photosensor performance of the cloaked NWs, we calculated the FOM using the definition in equation (37), which calculates the enhancement in the ratio of absorption efficiency to the scattering efficiency of the cloaked NW over that of the bare Si NW. A higher FOM indicates that the probed field is less disturbed by the light scattered by the photosensor itself, and/or more absorption is achieved by the photosensor, together resulting in a better signal/noise ratio in the photosensor signal. Figure 2.22 (a) shows the contour plot of the FOM as functions of the core radius and the

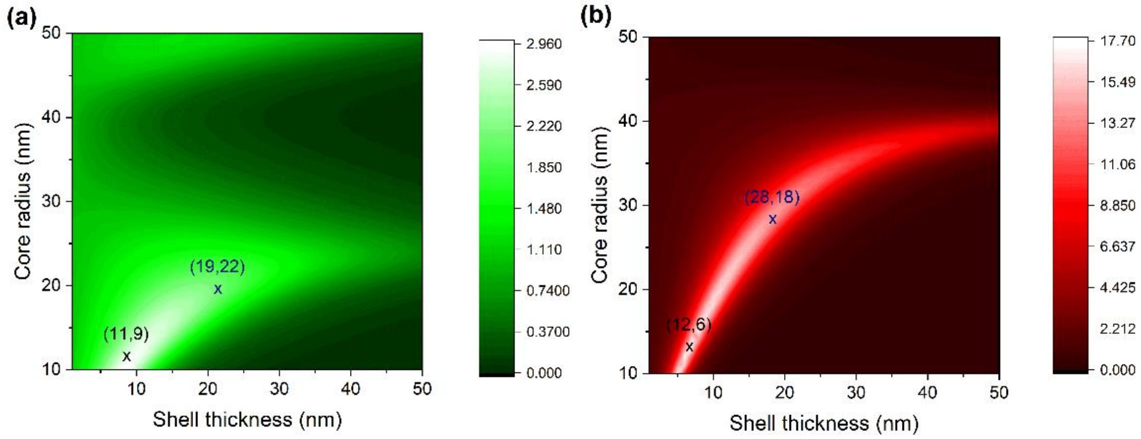

Figure 2.22: FOM contour plots as functions of core radius and shell thickness for (a) a ZrN cloak at 500 nm wavelength, and (b) a Au cloak at 650 nm wavelength. Black and blue crosses refer to the dimensions for highest FOM and FOM for the optimized system in Fig. 1 with respect to scattering cancellation respectively, with the two numbers in the parentheses referring to core radius and shell thickness respectively.

shell thickness, at 500 nm, for ZrN. The highest FOM at this wavelength was found to be 2.95, provided by a 11 nm radius Si core NW with a 9 nm thick ZrN cloak. In comparison, Figure 2.23 (a) shows the contour plot of the FOM for Au at 500 nm. The highest FOM for Au is 1.86 for a 11 nm radius Si/9 nm Au shell system, which is about 60% less than the highest FOM value for ZrN at this wavelength.

Similar dominance of a ZrN shell over a Au shell is also observed in the wavelength regime of 400-500 nm. After 550 nm, in the wavelength regime of 600-700 nm, the Au shell performs better than ZrN. Figure 2.22 (b) and Figure 2.23 (b) are comparing the highest FOM for 650 nm based on the contour plots. For the Si/Au (Figure 2.22 (b)), the highest FOM value is 17.69 for a 12 nm radius Si NW with a 6 nm thick Au shell, which is 2.7 times greater than the highest FOM identified for ZrN (Figure 2.23 (b)) found in the

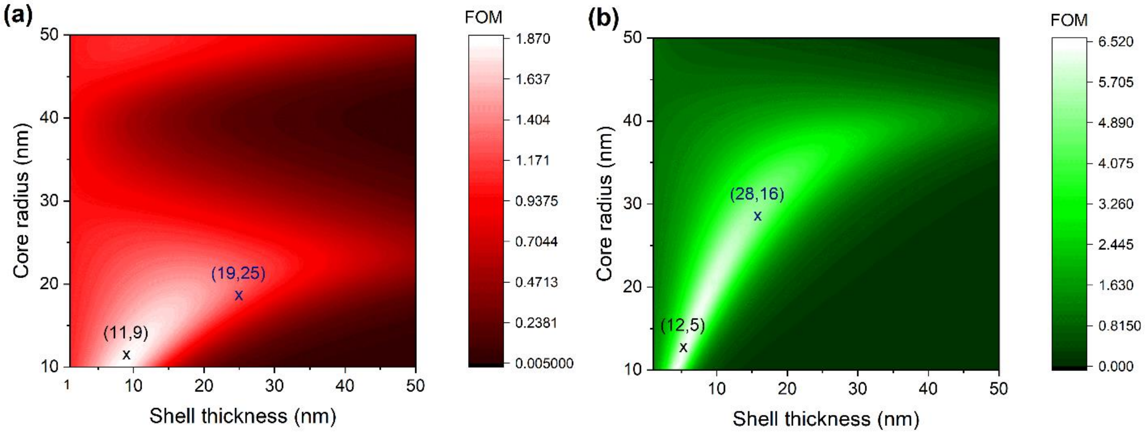

Figure 2.23: FOM contour plots as functions of core radius and shell thickness for (a) a Au cloak at 500 nm wavelength, and (b) a ZrN cloak at 650 nm wavelength. Black and blue crosses refer to the dimensions for highest FOM and FOM for the optimized system in Fig. 1 with respect to scattering cancellation respectively, with the two numbers in the parentheses referring to core radius and shell thickness respectively.

structure of 12 nm radius Si NW/5 nm thick ZrN shell. Therefore, when it comes to overall performance of Si NW based photosensors in the visible regime, we notice two definite regions: 1) lower wavelength regime of 400-500 nm where ZrN cloaks will result in better performance than Au cloaks, and 2) higher wavelength regime of 600-700 nm where Au cloaks will be better compared to ZrN cloaks. Table 2.3 summarizes the optimal cloak material and material thickness, as well as the Si NW core radius, for the highest FOM. We notice that between 700 nm and 800 nm, bare Si NWs have very low scattering (between 0.05 and 0.3), therefore the cloaking strategy by either ZrN or Au would not be effective in improving the performance. Additionally, from a fundamental point of view, we notice that the system which shows the greatest scattering cancellation in Figure 2.15 does not necessarily display the highest FOM. This implies that despite having a high scattering cancellation, the absorption in these systems is not high. The FOM value of the for the cloaked ZrN system in Figure 2.15 (19 nm Si core/22 nm ZrN shell) at 500 nm wavelength is 2.24, which is much lower than the value of 2.95 shown by the 11 nm core Si/9 nm ZrN shell system. Similar observations are also made at other wavelengths, as well as for the Au/Si NW systems, signifying that for best performance, both the absorption and the scattering need to be taken into consideration.

Photosensor wavelength (nm)	Si NW radius for highest scattering (nm)	Cloak material for highest FOM	Corresponding cloak thickness (nm)	Scattering efficiency	FOM
400	11	ZrN	7	0.45	1.04
450	15	ZrN	16	0.23	1.65
500	19	ZrN	18	0.17	2.38
550	22	Au	18	0.09	6.18
600	25	Au	18	0.05	10.73
650	28	Au	16	0.06	12.92

Table 2.3: Optimal cloak materials and dimensions for highest FOM values at different wavelengths. Note at 550 nm, Au was chosen here as the cloaking shell which gives the highest FOM. ZrN performs comparably with a FOM of 6.04 for a 17 nm ZrN shell.

Our observations of the scattering cancellation and the FOM give us an important way of predicting the properties of a plasmonic cloak. Figure 2.24 plots the real (solid lines) and imaginary permittivities (dashed lines) of ZrN (green) and Au (red) in the visible region. From Figure 2.24, we see that in the region between 400-500 nm, the real part of the dielectric constant (ε_1) for ZrN is slightly lower than that for Au, implying that in this region it is slightly more metallic. At the same time, the optical loss, indicated by the imaginary part of the dielectric constant (ε_2) for ZrN is much lower than that for Au. Thus, ZrN acts as a better plasmonic cloak in the region of 400-500 nm. Conversely, the same reason can also be argued for the better performance of Au compared to ZrN in the region of 600-700 nm.

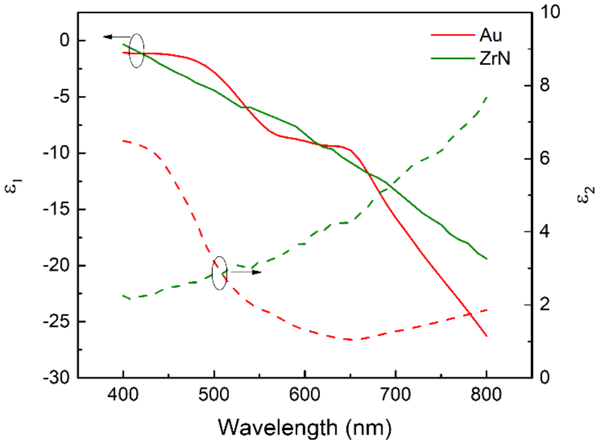

Figure 2.24: Comparison of the real (solid lines) and imaginary parts (dashed lines) of the dielectric constants for Au (red) and ZrN (green).

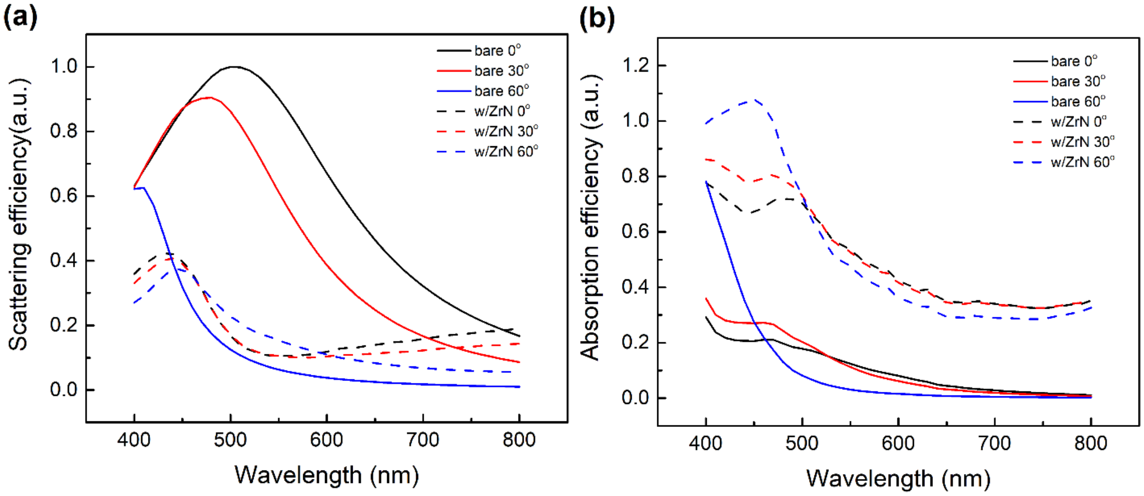

Figure 2.25: (a) Scattering efficiency and (b) Total absorption efficiency of a bare 19 nm Si NW (solid lines) and a 19 nm Si NW with a 22 nm ZrN shell (dashed lines) at angles of incidence of 0^o, 30^o, and 60^0.

All the calculations so far were done under normal incidence of light (taken as 0^o with respect to the normal). Figure 2.25 shows the dependence of the scattering efficiency and the absorption efficiency on the angle of incidence for a bare 19 nm Si NW and a 19 nm Si NW with a 22 nm ZrN shell. Though the scattering by the bare NW decreases with increase in the angle of incidence, at the same time its absorption decreases. For the ZrN-cloaked NW, the scattering is almost independent of the angle of incidence, but the total absorption, as well as the absorption in the core increases. So, it is expected that the ZrN cloak will still show an improved FOM for different angles of incidence.

Section Five: Fabrication of Plasmonic CMS NWs

Each component of the CMS NW was fabricated separately, according to the requirements from theory. They can then be combined together to form the desired CMS NWs.

Fabrication of the core

- Fabrication of the metal core

The Lithographically Patterned Nanowire Electrodeposition (LPNE) method was chosen for the fabrication of the metal NWs[96]. This method allows fabrication of long NWs lying on a transparent substrate (length parallel to the horizontal surface) based on photolithography with potential for cost effective large-scale production. Figure 2.26 (a) shows the fabrication steps involved, taking Au as an example. The first step is depositing a sacrificial layer of Ni on a glass substrate by e-beam evaporation. The height of the NW is controlled by the height of the Ni layer. This is followed by spin-coating positive photoresist (PR) onto the Ni layer. Then, photolithography is performed to get patterned PR strips of 1 μm width, separated by 1 μm, on top of the Ni layer. Then, a Ni etchant (0.8 M HNO_3) is used, and by varying the etching time an undercut can be achieved underneath

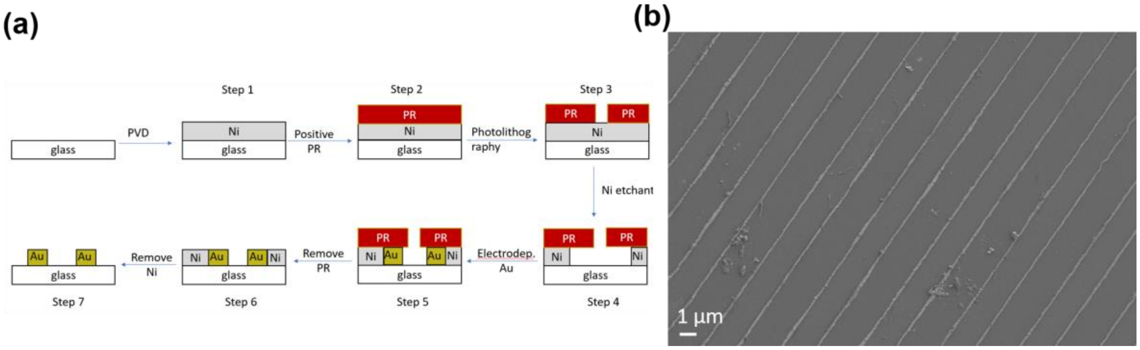

Figure 2.26: (a) Schematic of the LPNE method using Au as an example (b) LPNE deposited Au NWs

the PR layer. Then, Au is electrodeposited on the Ni layer using a 3-electrode setup, where the electrolyte is a 6 mM solution of $AuCl_3$ and the counter-electrode and reference electrodes are a Pt wire and Saturated Calomel Electrode (SCE) respectively. The electrodeposition time is used to control the width of the nanowires deposited. The last two steps involve a sequential removal of the PR and the Ni layers using acetone and 0.8 M HNO_3 respectively, finally leaving us with Au nanowires lying horizontally on the glass substrate. To keep the symmetry of the NWs simulated, the width and height of the NWs were approximately kept the same. To deposit Ag NWs, a Ag layer instead of Ni was deposited in step 1 using e-beam evaporation. After photolithography, in step 4, an etchant of 18% NH_4OH and 4% H_2O_2 was to etch silver. The etching time was varied to control the thickness of the Ag layer. Finally, the PR layer was removed using acetone, to form horizontal Ag NWs lying on the glass substrate. Figure 2.26 (b) shows the results of fabrication of Au NWs using this method. The Au NWs used in this example are around 40-60 nm in width and lengths around 100 µm. The height of the wires is 30 nm, and the average spacing between the wires is 2.5 µm.

- Fabrication of the Si NWs

The fabrication of Si NWs was done using a chemical vapor deposition (CVD) method previously developed in the group using Au seeds on a Si substrate, and using a mixture of silicon tetrachloride ($SiCl_4$) and H_2 gas for the growth[97].

Fabrication of the ultra-thin plasmonic TiN films[98]

Emerging plasmonic materials can be used as both the inner metallic shells for the CSS NWs for WLEDs as well as the cloak for Si photodetectors. However, for WLEDs, the inner metallic layer needs to be sub 10 nm for maximal enhancement. The following Atomic Layer Deposition was used to develop ultra-thin plasmonic TiN, and a similar methodology can also be developed for plasmonic ZrN.

- Methodology

The TiN films were synthesized in a Gemstar XT plasma enhanced atomic layer deposition system (Arradiance). Argon (99.999%, Airgas) is used as a carrier and purging gas. All steps of the TiN film synthesis are carried out in the ALD reaction chamber under vacuum at 250 °C. TiN thin films are grown directly onto the MgO and Si <100> substrates.

Similar to a previously established methods to produce metallic TiN[99-101], Tetrakis(dimethylamido) titanium(IV) (99%, Strem Chemical), known as TDMATi, is used as the titanium precursor and heated to 65 °C to increase its vapor pressure. TDMATi is exposed to the chamber for 1000 milliseconds, followed by a 10 second purge under 110 sccm argon. The chamber next is exposed to 300 W NH_3:Ar plasma (10 sccm:100 sccm, respectively) for 20 seconds, followed by a 10 second purge under 110 sccm argon. This completes one cycle, which is repeated until the desired thickness is reached.

For samples that undergo post-deposition hydrogen plasma treatment, the substrates are kept inside the ALD chamber at 250 °C. The samples are repeatedly exposed to 5 second intervals of 300 W H_2 plasma balanced in argon. This is repeated 600 times for a total exposure time of 50 minutes to hydrogen plasma.

- Characterization

X-ray reflectivity (XRR) is performed using a D8 Discover X-Ray System (Bruker) with a copper k-alpha source. Thickness is first measured from the raw data using a Fourier transform method. This thickness is used to develop a model using Diffrac.Suite LEPTOS Software, which is fit to the raw data to extract the thickness, roughness and density of TiN films for various cycle numbers. Optical characterization was done using variable angle spectroscopic ellipsometry (J. A. Woollam Co., Inc) from wavelengths of 400 to 1200 nm and angles of 65º, 70º and 75º. This data is modeled with a Drude-Lorentz function with one Lorentz operator, as demonstrated previously over this wavelength range,[102] to obtain the real (ε_1) and imaginary (ε_2) values of permittivity.

- Results

Atomic layer deposition is performed by repeating exposures of TDMATi and NH_3 plasma, which makes up one cycle and the growth rate is expected to be linear over cycle number. Figure 2.27 (a) confirms this linear growth rate, which is calculated from the slope as 0.097 ± 0.0038 nm per cycle (or approx. 9.7 nm per 100 cycles). The optical properties of the as-prepared TiN are measured using Spectroscopic Ellipsometry (SE), and the influence of TiN thickness (Figure 2.27 (b)) for TiN films that are 42 and 11 nm are observed. SE reveals the real and imaginary parts of the dielectric function (ε_1 and ε_2) over the range 400-1200 nm. MgO is selected as the substrate here due to its near-perfect lattice match with TiN: both are cubic crystal systems with lattice constants of 4.241 Å for TiN, 4.213 Å for MgO[103].

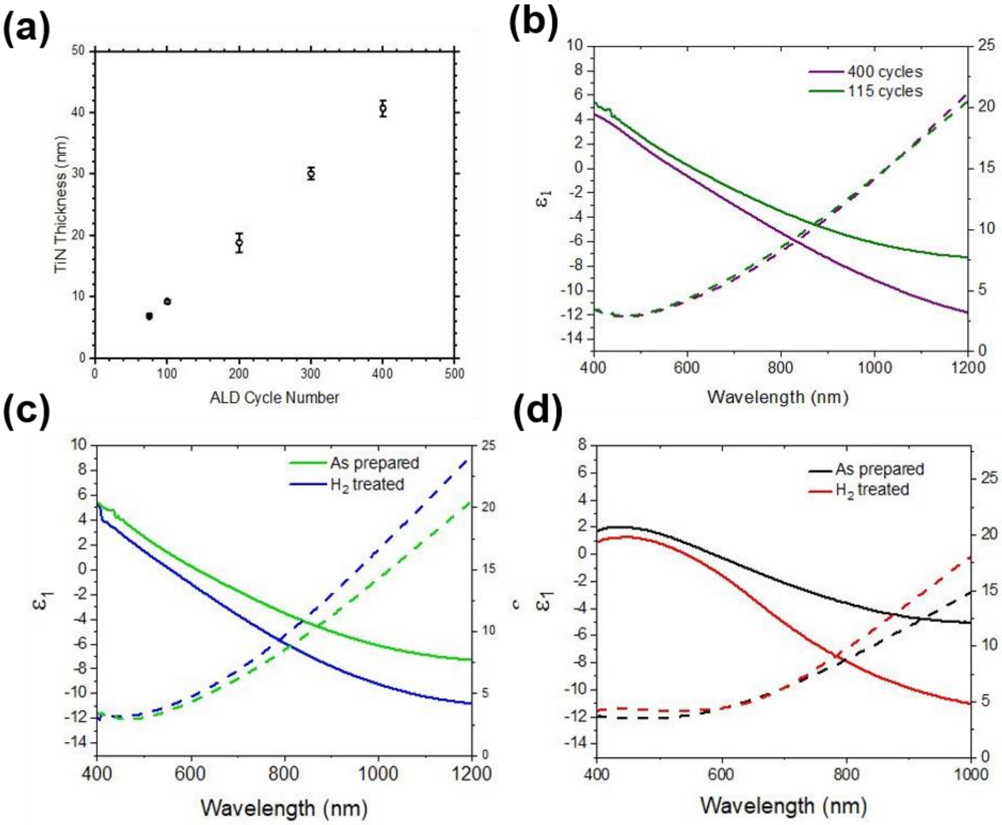

Figure 2.27: (a) TiN thickness as a function of ALD cycle number. (b) Real (solid line) and imaginary (dashed line) values of permittivity (optical constants) for TiN on MgO, TiN film thickness are 42 (purple) and 11 (green) nm. (c) Real (solid lines) and imaginary (dashed lines) values of permittivity of ultra-thin TiN (100 cycles) on MgO as prepared (green) and after hydrogen plasma anneal (blue). (d) Real (solid line) and imaginary (dashed line) values of permittivity for ultra-thin TiN on Si <100> substrate as prepared (black) and after hydrogen plasma treatment (red)

First, it is observed that the ε_2 values for the TiN films are similar for both thicknesses, indicating that the TiN films has similar optical losses. For TiN thin and ultra-thin films, ε_2 reaches a minimum value of approximately 2.9 at the wavelength 465 nm. Second, it is observed that the slope of ε_1 is negative for both TiN samples, indicating the TiN is optically metallic. Thicker TiN film is more metallic, especially in the higher wavelength region of 800-1200 nm. The plasmon wavelength, defined as $\varepsilon_1(\lambda)=0$, is located at 574 nm for TiN prepared by 400 cycles. The ultra-thin film shows a comparatively red-shifted plasmon resonance of 613 nm, which has been seen previously in ultra-thin TiN.[102] This demonstrates that TiN of various thicknesses produced by this PE-ALD method has tunable, visible light plasmon resonances for thin films on the order of 40 nm and 10 nm.

Unique from traditional plasmonic metals, TiN has variable optical properties in the near-IR and visible regions. One method of tuning the optical properties is through high-temperature annealing in vacuum, which results in a down-shift in ε_1 and may reduce ε_2. However, high temperature anneals are not ideal for all applications, and therefore a having a low-temperature post-deposition treatment to achieve varied optical properties is advantageous. One alternative to high temperature annealing is plasma post-treatment, which has been demonstrated previously with ALD metal films to modify the surface and decrease resistance.[104] Herein, we study the effect of a post-deposition hydrogen treatment on ultra-thin TiN thin films (11 nm). This hydrogen treatment occurs at the same temperature as the TiN deposition, 250 °C, using a 300 W H_2 plasma balanced in argon, repeating a five second exposures to the plasma for a total of 50 minute exposure time.

To observe how the post deposition hydrogen plasma treatment affects the optical properties, we plot the dielectric functions of as-prepared TiN and H_2 plasma treated TiN

(Figure 2.27 (c)). The hydrogen plasma treated TiN (blue) has a plasmon resonance of 554 nm, a 59 nm blue-shift compared to the as-prepared sample. For comparison, it has previously been shown that the plasmon resonance of sputtered TiN films can be been blue shifted by 45 nm after annealing at 600° C and 71 nm at temperatures of 700° C.[105] Similarly, previous ALD syntheses have demonstrated plasmon wavelength blue shifts of 52 nm after post-deposition annealing at 600° C.[106] Therefore, the effect of a post deposition hydrogen plasma on the plasmon wavelength is similar to that of a high temperature anneal.

The ε_2 values are higher in the hydrogen treated sample: for instance, at a wavelength of 800 nm the value of ε_2 is 9.7 in the hydrogen treated sample and 8.2 in the as-prepared sample, and this difference only increases as in as the wavelength proceeds into toward the infra-red region. However, the values of ε_2 are similar at their respective plasmon wavelength. For hydrogen plasma treated TiN, the value of ε_2 at the plasmon wavelength is 4.04, while the as-prepared sample has an ε_2 value of 4.5. Therefore, taking both parts of the dielectric function into consideration, post deposition treatment with hydrogen plasma is an effective way to tune the optical properties of ultra-thin plasmonic TiN on MgO.

TiN's compatibility with silicon is another advantage of alternative plasmonic materials over gold or silver. However, unlike those traditional plasmonic metals, TiN has been demonstrated to have substrate-dependent optical properties, and therefore it cannot be assumed that the optical properties of TiN on one substrate will be identical to another.[25, 106-107] To confirm that ultra-thin TiN synthesized on silicon substrates via PE-ALD is plasmonic in the visible and near-IR region, the optical properties are studied from 400-1200 nm (Figure 2.27 (d)). It is observed that the as-prepared TiN (black) has plasmonic character on Si <100> for near-10 nm TiN. The slope of ε_1 in the visible region is similar to ultra-thin TiN on MgO in the region of 500-900 nm. Though the TiN shows dielectric behavior (a flattening of ε_1) at wavelengths over 900 nm. This is in part attributed to oxygen contamination in the TiN, and is consistent with previous findings of TiN thin films on silicon with oxygen contents between 10 and 25%.[108-109] The slope and position of ε_1 indicate a broad plasmon resonance centered at 586 nm, with a corresponding ε_2 value of 4.21. That the plasmon wavelength is red-shifted for TiN on Si compared to the plasmon wavelength of TiN on MgO is likely due to lattice mismatch between silicon and TiN.[106]

Film thickness (nm)	Substrate	plasma anneal	λ_{ps} (nm)
42	MgO	no	574
11	MgO	no	613
11	MgO	yes	554
11	Si	no	586
11	Si	yes	542
8	Si	yes	530

Table 2.4: Summary of the film thicknesses fabricated on different substrates and the subsequent plasmon responses.

Finally, Figure 2.27 (d) shows that TiN treated with hydrogen plasma (red) results in an increase in the metallic behavior of the thin film, as seen by an increase in the slope of ε_1 over wavelengths. Re(ε) for the plasma-treated TiN reaches a value of -11 at 1000 nm, significantly lower than the as-prepared TiN, which as a value of -5.1 at 1000 nm. This indicates that the hydrogen treated films are more optically metallic. For the H_2 plasma treated TiN, the plasmon wavelength is located at 542 nm, a 44 nm blue shift compared to the untreated film. At 542 nm, the value of ε_2 is 4.2, which is similar to ε_2 of the as-prepared film at its plasmon wavelength. Table 2.4 summarizes all the plasmon resonances (λ_{ps}) and the thicknesses of the different films fabricated. Thus, the ALD method allows development of ultra-thin plasmonic metal nitrides in accordance with theoretical requirements. Additionally, the ALD method allows conformal coating on NWs, as previously demonstrated in the group, making this method ideal for developing the plasmonic shells as desired.

Fabrication of the semiconductor phosphor films

The final component for the WLED CS/CSS phosphors is the semiconductor phosphor films like CdSe and CdS. Electrochemical deposition (ED) was used to deposit CdSe and CdS, and the method allows a conformal coating around metallic NWs, which can be used as the active electrode in the process. Pt electrode and a SCE electrode were used as the counter electrode and the reference electrode respectively. This is an inexpensive method for deposition of films. The electrolyte solution used is 0.05 M $Cd(NO_3)_2$ and 0.01 M SeO_2 for CdSe films will then be deposited for 1-5 min at a uniform voltage of -0.6 V vs. SCE. The electrolyte for CdS ED is 0.01 M $Cd(NO_3)_2$ and 0.35 M $Na_2S_2O_3$. The pH of the solution needs to be acidic (2~3) and this is achieved by adding a few drops of HCl to the electrolyte. The deposition voltage is around -0.6 V to -0.7 V vs

SCE electrode. Deposition time can be varied in a similar manner to get the desired thicknesses.

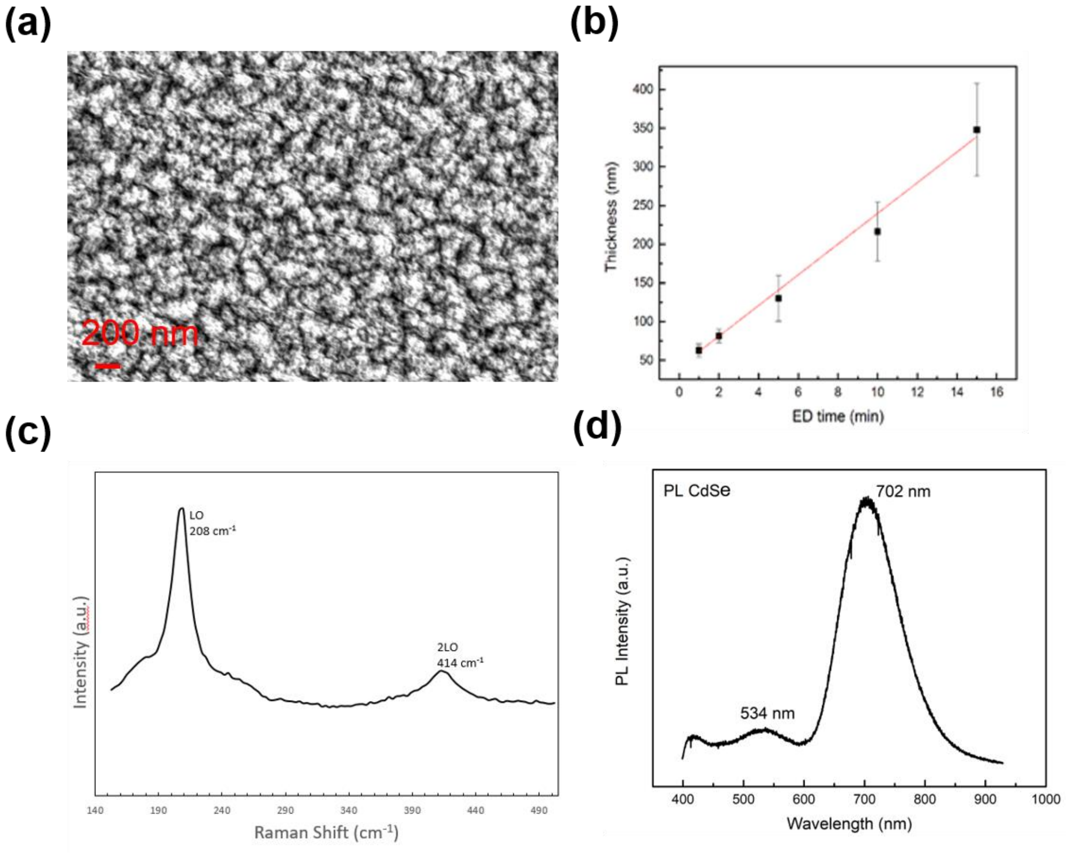

Figure 2.28: (a) SEM of a 1 min deposited ED film for CdSe. (b) Thickness as a function of ED time for CdSE films. (c) Raman spectroscopy and (d) CdSe Photoluminescence (PL) for a 1 min ED CdSe film.

Figure 2.28 (a) gives an SEM example of a CdSe film produced by 1 min of ED and annealed at 275^{o}C and shows the high crystallinity and quality of the film. Figure 2.28 (b) gives the thickness of the electrodeposited CdSe thin film as a function of the electrodeposition time. The thickness decreases linearly with decreasing time, as does the surface roughness. Figure 2.28 (c) gives the typical Raman spectra of a 1 min ED deposited

CdSe films on FTO-coated glass substrate, and the characteristic peaks at 208 cm^{-1} and 414 cm^{-1} shows the crystallinity of the films deposited. Figure 2.28 (d) gives the emission or the photoluminescence (PL) as a function of wavelength for the same CdSe film, showing the characteristic peak of a CdSe film around 702 nm. The strong emission peak shows the high quality of the film fabricated and shows its ideal for use as a red phosphor, matching the wavelength predicted from theory. Similarly, fabricated CdS films have a peak around 515 nm making them ideal for use as green phosphors.

CHAPTER THREE: PLASMONIC CSS NPs FOR ENHANCING PHOTOCATALYTIC ACTIVITY OF HEMATITE

Section One: Photoelectrocatalysis (PEC) and Hematite performance

The efficient and economical generation of Hydrogen (H_2) is promising towards developing a carbon-neutral society[110-111]. Among the strategies used for hydrogen generation, the photocatalytic method is particularly of interest as it is an environmentally friendly and near-zero carbon emission process[112]. Photoelectrochemical (PEC) water splitting using semiconductor electrodes has the advantage of offering a potential high Solar-to-Hydrogen (STH) efficiency and photocurrent density through a simple device architecture[113-114]. In the PEC process, however, though photocathodes have been successfully optimized with solar to hydrogen (STH) efficiencies of ~18-20%[115], the photoanode performance remains below desirable levels.[116] Various n-type photocatalytic materials have been investigated as the photoanode, including TiO_2,[117-119] $BiVO_4$,[120-122] WO_3,[123-125] $LaTiO_2N$,[126-128] TaON,[129-131] and $BaTaO_2N$.[132-134] Among them, hematite (α-Fe_2O_3) stands out for its favorable band gap energy of ~2 eV matching the water splitting voltage of 1.23V vs. RHE.[135-136], its high chemical and electrochemical stability under illumination in an electrolyte solution, non-toxicity, and abundance of the raw materials in the Earth's crust. Additionally, hematite has a high theoretical maximum solar-to-hydrogen (STH) efficiency of 15.3% at 1.23 V vs. RHE under 1 sun irradiation (100 mW/cm^2). These makes hematite a viable photoanode candidate to be optimized toward the benchmark 10% STH for practical applications.[121, 137] However, hematite suffers from poor oxygen evolution kinetics due to a large number of defect states, and poor charge separation efficiency due to a short excited-state lifetime (3–10 ps) and small hole diffusion length (2–4 nm).[138-141]

Various strategies have been developed to overcome these challenges. In addition to doping and nanostructuring widely explored, [142-145] plasmonic enhancement has received much attention a for developing new hematite photoanode systems. Ag, Au and Pt nanoparticles (NPs) when incorporated into the hematite photoanode systems have been demonstrated to provide noticeable improvement in photoanode performances.[146-148] When the plasmon response of the NPs is in resonance with the wavelength of the incident light in a wavelength region which is inside the band-edge of hematite enhanced absorption of light by the semiconductor nanostructures occurs from these NPs. Additionally, the energy released during the plasmonic relaxation process can be utilized by the carriers in the surface defect states to be promoted to the conduction band and participate in the reaction at the semiconductor-electrolyte interface. These help to overcome in large measure the before mentioned problems with carrier lifetime and potentially lead to higher PEC activity.[149-151]Au has a clear advantage over other plasmonic systems in that its plasmonic resonance falls around 550 nm, which lines up with the peak intensity of the solar spectrum.[152-155] These studies demonstrate that plasmonic nanoparticle systems are versatile, and easy to integrate with doped photoanode nanostructures and/or co-catalytic overlayers to push photocurrents to more useful levels. Notably, even using Au NPs, the photocurrent densities achieved are far from desirable. New materials, strategies and device architectures are still being sought to further improve the performance of hematite photoanodes.

Section Two: Plasmonic Au/SiO$_2$/Au CSS NPs

We design core-shell-shell (CSS) Au@SiO$_2$@Au nanoparticles and demonstrate them as a new and improved plasmonic system enhancing photocurrent density when incorporated into the hematite photoanode. Newly developed CSS NPs have gained attention as they provide two unique scattering peaks in the visible spectrum, as well as strong absorption in the longer wavelength peak for increased carrier generation.[156-157] Each peak can be optimized independently by changing the dimensions of the different layers for a specific plasmonic excitation/relaxation process, i.e. scattering/hot-electron injection or scattering/heating. These features give these CSS particles a unique advantage over pure plasmonic nanoparticles, where the particles are either strongly scattering (>20 nm diameter) or strongly absorbing (<20 nm diameter) leading to hot-electron injection. These nanoparticles have been used in a CSS NP-decorated ITO electrode as an open-circuit electrochemical cell to study the photo-oxidation of citrate ions, as well as for the strong heating effects for tumor treatment in mice. In our work, we design the CSS Au@SiO$_2$@Au NPs with dimensions optimized to improve the PEC activity of hematite through optimizing near-field scattering of the incident light to increase photoexcitation of carriers and absorption of light and subsequent injection of hot carriers. This has been achieved by calculating the field response of the CSS NPs using the rigorous Mie scattering theory[158]. The unique double peak response in the visible range and high tunability of the resonant electric fields, as well as control over the plasmonic excitation and relaxation pathways allow us to manipulate the photoanode-NP architecture for maximized photocurrent density and subsequently STH efficiencies.

Section Three: Synthesis and characterization methods

Chemicals used

All chemicals were purchased from Sigma-Aldrich unless otherwise mentioned. Ferric chloride hexahydrate (ACS reagent, 97%), sodium nitrate (ReagentPlus, 99%), tin (IV) chloride (98%), Ethanol (ACS reagent, 99.5%) and hydrochloric acid (1 N, BioReagent) were used for the synthesis of hematite on fluorine tin oxide (FTO) doped glass substrate (resistivity ~7 ohms/sq). Core-shell (CS) Au@SiO_2 NPs of desired dimensions were purchased from Nanocomposix, with 3-Aminopropyltrimethoxysilane (APTMS, 97%), hydroxylamine hydrochloride (ReagentPlus, 99%) and gold (III) chloride hydrate (99.995%) being used for CSS synthesis. For deposition of the Co-Pi overlayer, potassium phosphate monobasic (ACS reagent, 99%), potassium phosphate dibasic (ACS reagent, 98%) and cobalt (II) nitrate hexahydrate (ACS reagent, 98%) were used.

Synthesis of Sn-doped hematite

Hematite was synthesized by a hydrothermal method following reported protocols.[159-160] In brief, the fluorine-doped tin oxide (FTO) substrates were first cleaned with, in order, Toluene, Acetone and Isopropyl Alcohol. A portion of the FTO substrate surface was taped to avoid deposition in that region and kept bare for proper connection of the electrodes. The cleaned FTO substrates were then immersed in Ferric chloride solution

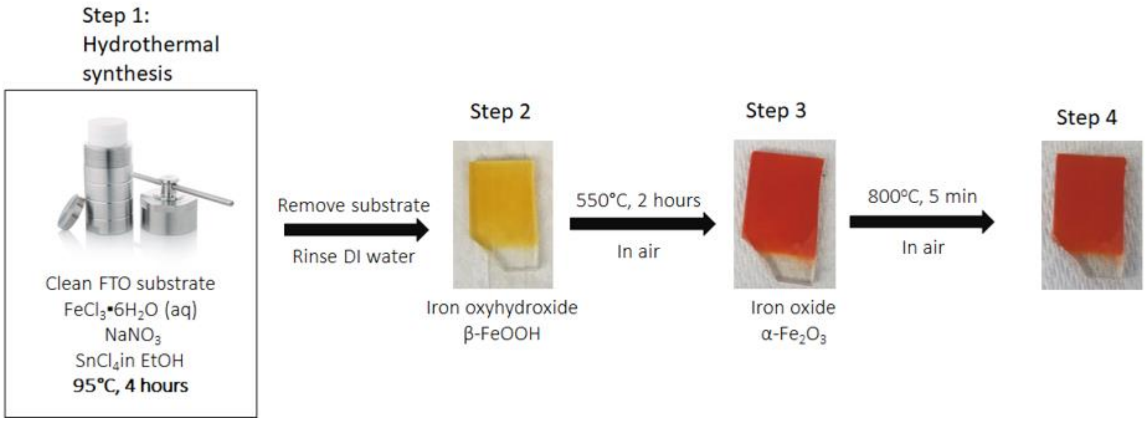

Figure 3.1: Step by step methodology for preparing hematite films

containing 10 mL ultra-pure water with 0.460 g $FeCl_3$, 0.935 g $NaNO_3$, 555 µL of 1% $SnCl_4$ in EtOH solution (Sn-dopant), and 300 mL 1 M HCl in an autoclave chamber, and the sealed chamber was then put in an oven at 100^{o}C for 4 hours. The solution level was kept below the level of the taped portion of the FTO substrates, to avoid contamination. This leads to the growth of β-FeOOH. The FTO substrates with the β-FeOOH were cleaned and the tape was removed. The portion revealed after the removal of the tape was thoroughly cleaned with acetone. The sample was then annealed in air in a tube furnace at 550 ^{o}C for 2 hours, followed by 5-minute annealing at 800 ^{o}C during which the β-FeOOH is converted into hematite (α-Fe_2O_3). The annealing temperature is a key factor for the crystallinity of the hematite. As the temperature increases from 550 ^{o}C to 800 ^{o}C, the crystallinity increases and the number of trap states decreases resulting in higher PEC activity[116, 161-162]. Above 800 ^{o}C, however the FTO substrate begins to break down, making higher temperatures impractical. To test the effects of our plasmonic NPs on hematite at different qualities, the annealing temperature was varied between 700 ^{o}C to 800 ^{o}C, as discussed later. The temperature was ramped at a rate of 2 degrees per minute. At the end of the annealing process the sample was allowed to cool down to room temperature.

Synthesis of CSS Nanoparticles

CSS NPs were prepared following a protocol similar to the one developed by the Halas group[157]. Two dimensions of commercial CS NPs were used as the inner structure of the CSS NPs based on simulation results, with the core radius/silica shell thicknesses being 10 nm/20 nm, and 25 nm/20 nm respectively. 100 µL of commercial CS NPs with desired Au core and SiO_2 shell layer thicknesses were incubated with 100 µL of APTMS for 4.5 hours at 4 ^{o}C. After that, the particles were centrifuged to remove excess APTMS, and diluted with 200 µL ultrapure water. To prepare Au seeds on the functionalized SiO_2 shell of CS NPs for the growth of the outer Au layer, a Duff solution, which consists of sub-3 nm Au seeds, was made[163]. 8 mL of the Duff solution was taken, and then, in order, 120 µL of a 1M NaCl solution and 200 µL of the functionalized CS NPs were added. This was left in the dark for 2 days to allow the Au seeded CS NPs to form. TEM images were taken of the Au seeded CS NPs to ensure that the Au seeds on the silica surface were sub-3 nm. This is critical to ensure uniform and smooth Au outer layer growth, as larger Au seeds can lead to aggregates of Au being deposited on the SiO_2 layer instead of a uniform Au shell.

For the CSS synthesis, 2 µL of the Au seeded CS NPs was diluted to 20 µL, and under a vortex, equal volumes of 25 mM hydroxylamine hydrochloride ($NH_2OH.HCl$) and 0.01% chloroauric acid ($HAuCl_4$) were added dropwise. For the purpose of making a 15 nm thick outer shell, 2 µL of $NH_2OH.HCL$ was added 15 times to make a total volume of

30 µL, followed by 2 µL of $HAuCl_4$ for 15 times with 10 second intervals to allow the reaction to complete, again making a total volume of 30 µL. The volumes of these components added in each step have a strong impact on the size and smoothness of the outer shell; larger volume addition leads to rough surfaces being formed as seen under an SEM [164]. Ten such prepared CSS NP samples were then combined to form the stock solution for preparation of the hematite-NP architecture. Figure 3.2 shows the results of the different steps involved in the synthesis process, as well as the extinction spectrum of each product formed. The CSS NP dimensions will be represented as ($r_1/d_2/d_3$) from hereon, where r_1 is the core radius, d_2 is the inner shell thickness and d_3 is the outer shell thickness.

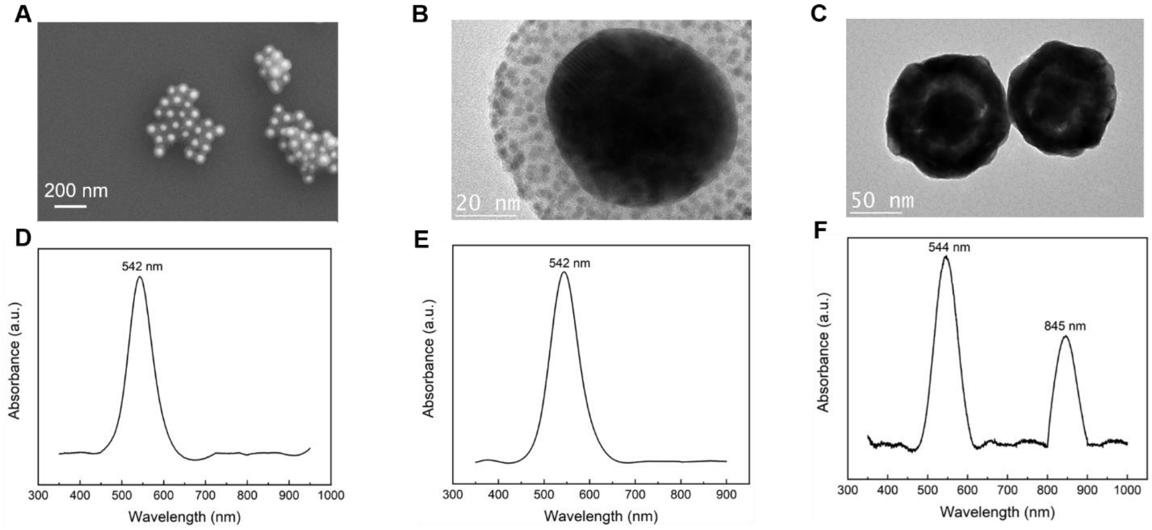

Figure 3.2: (A) SEM image and (D) Absorption spectrum of (25/20) CS NPs. (B) SEM image and (E) Absorption spectrum of (25/20) CS NPs with the Duff seeds. (C)SEM image and (F) Absorption spectrum of (25/20/15) CSS NPs.

Figure 3.3: (A) The two NPs (Au and Au/SiO_2/Au) used to compare Hematite performances, (B) NPs deposited on top of hematite, and (C) NPs embedded in hematite.

Preparation of hematite-nanoparticle photoanodes

Using two designs of NPs (Au NPs and CSS NPs, Figure 3.2A), two architectures were used for hematite photoanodes, a NP-embedded architecture and a NP-top-deposited architecture (Figure 3.3B and C). In the embedded architecture, it is important to compare the plasmonic NP incorporated hematite photoelectrode performance to the same sample of bare hematite. To this end, 100µL of 10^8 NPs/mL solution was drop cast onto the top quarter of the FTO glass substrate. The samples were then left under vacuum to promote an even deposition pattern. The samples were treated in this way 3 times to ensure an even dispersal of NPs, highly localized only on the top quarter of the FTO glass substrate. The presence of the NPs on the desired area of the FTO substrate and the absence of NPs on the untreated area was confirmed via dark field microscopy and SEM imaging. The density of CSS and Au NPs was estimated to be 100 NPs per 10 μm^2 from various SEM micrographs across multiple samples. The hematite was then grown following the protocol discussed above over the particles, effectively embedding the particles into the structure of the hematite nanocorals. To prepare the top-deposited samples, as grown hematite samples were immersed in a 10^8 NPs/mL NP solution for 24 hours, without any surface modification.

Deposition of the Co-Pi overlayer on hematite

A photodeposition method was used at 1-sun illumination.[142] Specifically, a solution of 0.5 $\times 10^{-3}$ M cobalt nitrate in 0.1 M potassium phosphate buffer at pH 7 was prepared, and a photodeposition carried out at 0.2 V versus Ag/AgCl for 300 s. A 3-electrode setup was used for the Co-Pi deposition, with a platinum cathode, Ag/AgCl reference electrode and the hematite as the photoanode for deposition.

Characterization of the CSS NPs and Hematite

SEM (Zeiss Supra55VP) images were taken to measure the diameters of the CSS NPs, as well as to study the surface morphology of the hematite-NP photoelectrodes and the surface distribution of the NPs on the hematite/FTO surface. TEM (FEI Tecnai Osiris) images were taken to characterize structurally the CSS NPs, as well as the CS NPs, Au-seeded CS NPs. The absorbance spectra of the samples were taken using a spectrophotometer (Agilent Cary5000).

Photocurrent measurements

A 3-electrode setup was used for the photocurrent measurements. For that purpose, the hematite samples were incorporated as photoanodes in the 3-electrode setup as follows. The portion of bare FTO (previously taped) of the sample was coated with Ag paint, and a clean piece of copper tape was attached to it. Care was taken to not make direct contact with the hematite and thus only record current flowing from the hematite into the FTO substrate. All samples were prepared with a 1 mm^2 active area while Epoxy covered the rest of the hematite surface. This was used as the working electrode with the other two electrodes being a Ag/AgCl reference electrode (Thermo-fisher) and a Pt counter electrode (Hanna Instruments). A 1 M NaOH solution was used as the electrolyte for water splitting. A 300 W Ozone-free Xenon lamp (Newport) was used as the solar simulator, and characterization was done under a 1-sun illumination condition. The photocurrent was measured as a function of voltage using a VersaSTAT4 potentiostat (Princeton Applied Research).

Section Four: Enhancement of PEC activity of Hematite using CSS NPs

To identify the optimal dimensions of the CSS NPs for the resonant behavior of CSS NPs with maximal electromagnetic field enhancement and rationalize how the CSS NPs can act as novel plasmonic systems to improve hematite performance, we simulated the extinction contours and electric field distributions of single CSS and Au NPs, respectively. Figure 3.4A shows an example of the extinction contours plotted as functions of the wavelength and inner core radius r_1 of the CSS NPs while d_2 and d_3 are fixed at 20 nm each. The key variable plotted here is the extinction field coefficient (Q_{ext}), which will give an indication of the intensity of the scattering and absorption coefficients. This, in turn, will determine the feasibility of use of these CSS NPs for enhancing the PEC activity of hematite. The increase in the intensity of Q_{ext} relative to the background (dark blue region) indicates the plasmon resonance peak edges, with the highest value in such a region indicating the peak location. The contours were plotted within the wavelength range of 400

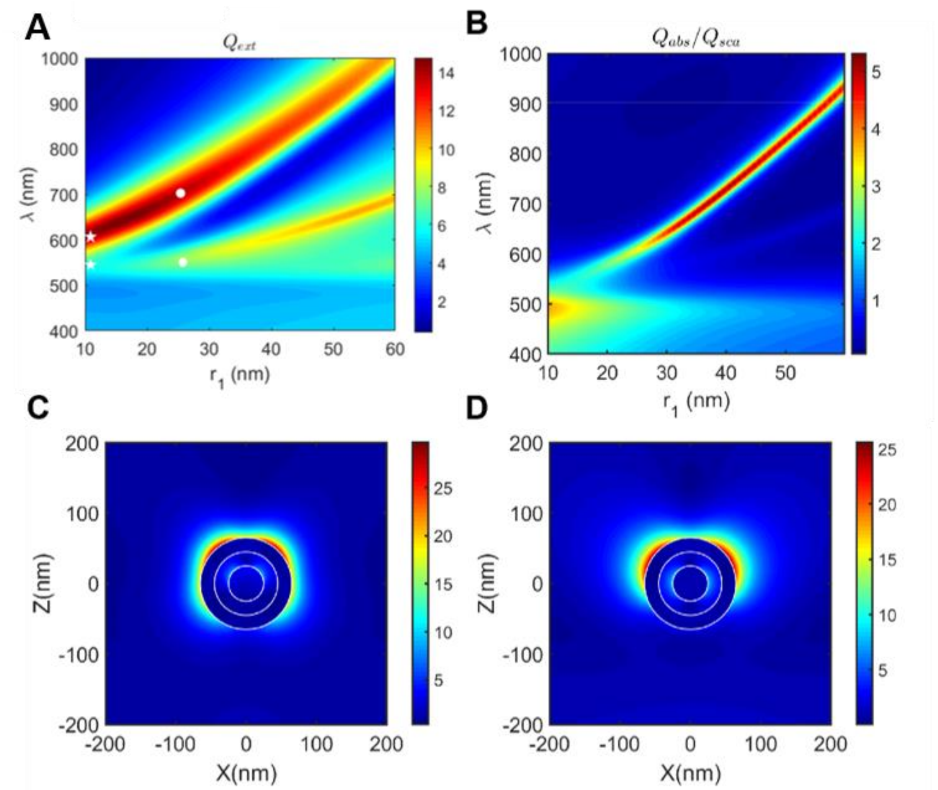

Figure 3.4: (A) Contour plot of the extinction spectrum as a function of wavelength and the core radius r_{1}, with the inner shell (d_2) and outer shell (d_3) fixed at 20 nm. White stars and white dots indicate the plasmonic resonance peaks of optimal dimensions identified, namely, CSS NPs of dimensions (10/20/20) nm and (25/20/20) nm respectively. (B) Ratio of the absorption to scattering coefficients for a CSS NP as a function of wavelength and the core radius (r_1) with d_2=20 nm and d_3=20 nm. (C) Field distribution at 540 nm and (D) field distribution at 710 nm, of a (25/20/20) nm CSS NP (corresponding to the white dots).

nm to 1000 nm to straddle the visible spectrum, and the dimension range for the CSS NPs was chosen to ensure that the plasmonic peaks at any given r_1 remained within the range of 400 to 1000 nm. When r_1>60 nm, the plasmonic peaks no longer remained in the visible spectrum and were not plotted for this purpose. The lower limit of r_1=10 nm in the contour plot was chosen keeping in mind synthesis feasibilities.

The contour plots clearly show the unique double plasmonic peak feature of the CSS NPs, which can be understood by looking at the contour plot at any particular value of r_1. For example, at r_1=25 nm, there are two regions where Q_{ext} is substantially larger than the background. The first region extends from 510 nm to 570 nm, with the highest value at 540 nm, which is identified as the first plasmonic resonance peak. The second range extends from 640 nm to 760 nm, with the highest value at 700 nm, which is identified as the second plasmonic peak. Hereon, we refer to the peak at the lower wavelength as the first peak and the peak at the higher wavelength as the second peak. Figure 3.4A shows that the first peak shifts from 540 nm to 700 nm as r_1 increases from 10 to 60 nm, while the second peak shifts from 600 nm to 1000 nm, which demonstrates the high tunability of the peaks, in particular the second peak. Using the field contours, the choice of the optimal CSS NP was made based on the following factors: 1) proximity of both the plasmonic peaks to the hematite bandgap, and 2) high intensities for both the peaks. CSS NPs with dimensions of (10/20/20) nm (peaks are shown by the white stars), and (25/20/20) nm, (peaks are shown by the white dots), were identified as the optimal configurations. These particles will be labeled as CSS10 and CSS25 respectively. CSS10 was chosen as an optimal configuration as the first plasmonic peak is at 540 nm and the second one at 600 nm. Thus, both the peaks are around the band edge of hematite (590 nm) and would directly be able to influence the optical properties of hematite through their near field scattering enhancement. CSS25, on the other hand, has the first plasmonic peak at 540 nm, which would be able to directly contribute optically to the hematite PEC activity. The second plasmonic peak is, on the other hand, located at 700 nm, which is outside the hematite band edge. However, the extinction coefficient has the highest value at this peak. Figure 3.4B shows the contour plot of the ratio of the absorption intensity to the scattering intensity of CSS NPs as functions of the wavelength and $r_{1.}$ It can be seen that at the second peak, the CSS NP is strongly absorbing, especially for values of r_1>25 nm. This, along with the high extinction coefficient value, implies that at the second plasmonic peak, the CSS NP would strongly absorb the incident light and correspondingly be capable of hot carrier generation, which can be injected into hematite. Thus, CSS 25 will be able to influence the electrical properties of hematite both optically (through the 540 nm peak) and electrically (through the 700 nm peak), justifying the choice as an optimal configuration. Figure 3.4A shows the variation of the extinction contours as a function of r_1 keeping d_2 and d_3 fixed. Extinction contours were also plotted by varying d_2 with r_1 and d_3 fixed, and by varying d_3 with r_1 and d_2 fixed, in order to arrive at the optimal configuration. Similar tunabilities and double resonance features were observed from these figures. Figure 3.5A plots a representative example with the extinction field contours plotted as functions of wavelength and d_2, with r_1=25 nm and d_3=20 nm, while Figure 3.5B plots a representative example with the extinction field contours plotted as functions of wavelength and d_3, with r_1=25 nm and d_2=20 nm.

To further investigate whether the CSS NPs presented additional potential benefits to the PEC activity of hematite, the spatial electric fields were simulated for the CSS NPs at each resonance peak wavelength identified in Figure 3.4A. Figure 3.4C and D show the

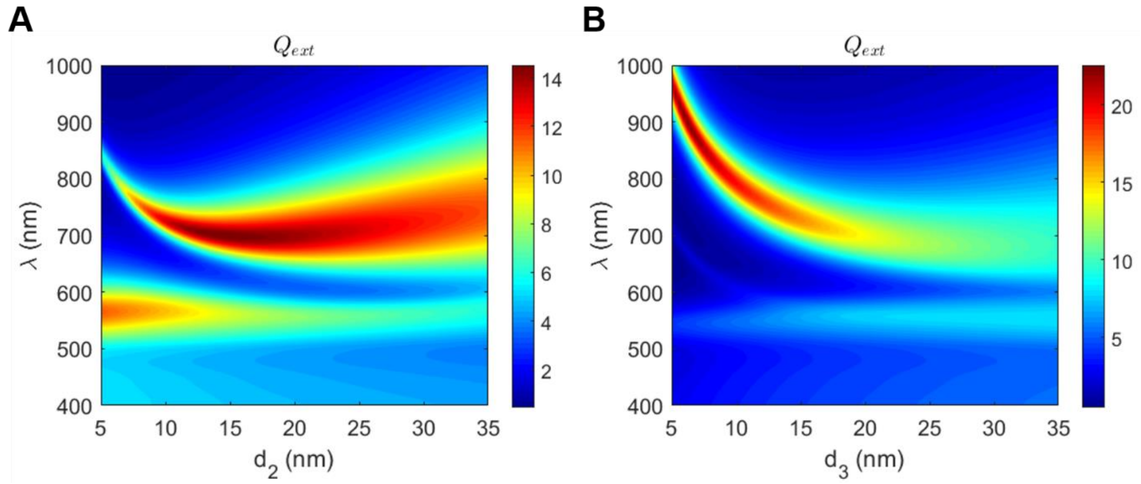

Figure 3.5: (A) Extinction contour plot as a function of wavelength and inner shell thickness (d_2) with r_1=25 nm and d_3=20 nm. (B) Extinction contour plot as a function of wavelength and outer shell thickness (d_3) with r_1=25 nm and d_2=20 nm.

fields of the first peak at a wavelength of 540 nm and at the second peak at a wavelength of 710 nm for a CSS25 NP. It can be seen that at the first peak, the electric field distribution corresponds to the excitation of a quadrupole mode, while the second peak corresponds to a dipole mode. Additionally, at both the peaks, the electric field distributions are uniform on the surface. The distance the electric fields extend before dropping to half of its maximum value is 20 nm from the surface for the first peak and 25 nm from the surface for the second peak. In addition, at the first peak, the electric field is more broadly distributed across the entire surface of the CSS NP, as compared to the second peak. This is because the quadrupolar moment starts contributing to the electric fields, and though it is weaker than the dipolar response, it is of the same order of magnitude. The quadrupolar fields are distributed across the surface of the NP as opposed to being restricted to only across the top half of the surface as for the dipolar fields, and this combined effect of the two fields leads to a more uniform distribution of the electric fields across the entire surface of the CSS NP. How these features potentially contribute towards photocurrent improvement can be rationalized as follows. Firstly, at the plasmonic excitation, near field scattering of incident light increases photo-excited carrier generation in hematite over a broad range extending to around 20 nm from the surface of the NPs. This effect is more notable at the first peak, as the peak is located within the hematite bandgap. We expect the contribution of the second peak through this effect to be minimal. Secondly, during the relaxation of these plasmons, the energy released can lead to hot carrier generation.[165] The stronger absorbing the peak is, greater is this effect. Figure 3.4B shows that at the second peak, the CSS NP absorbs the incident light strongly, and we expect the contribution through hot carrier generation of the second peak to be significant. Additionally, for NPs located near the semiconductor-electrolyte interface, the energy released during the relaxation can be transferred to charge carriers in the surface trap states, which can lead to their promotion to the conduction band and hence increase carrier charge density. Finally, the electronic energy released during relaxation can be converted to heat energy, which can be beneficial towards creating additional carriers.[7] As the heat fields are determined by the absorption, it is conceivable that these heat fields will also be broad and influence a large area of the hematite. Combining the unique effects of these features, it is clear that the CSS NPs present multiple benefits towards improving hematite performance which cannot be achieved using pure NPs.

To study the structure of the synthesized CSS NPs, electron microscopy images of the NPs were taken. Figure 3.6A shows a representative SEM image of the CSS25 NPs

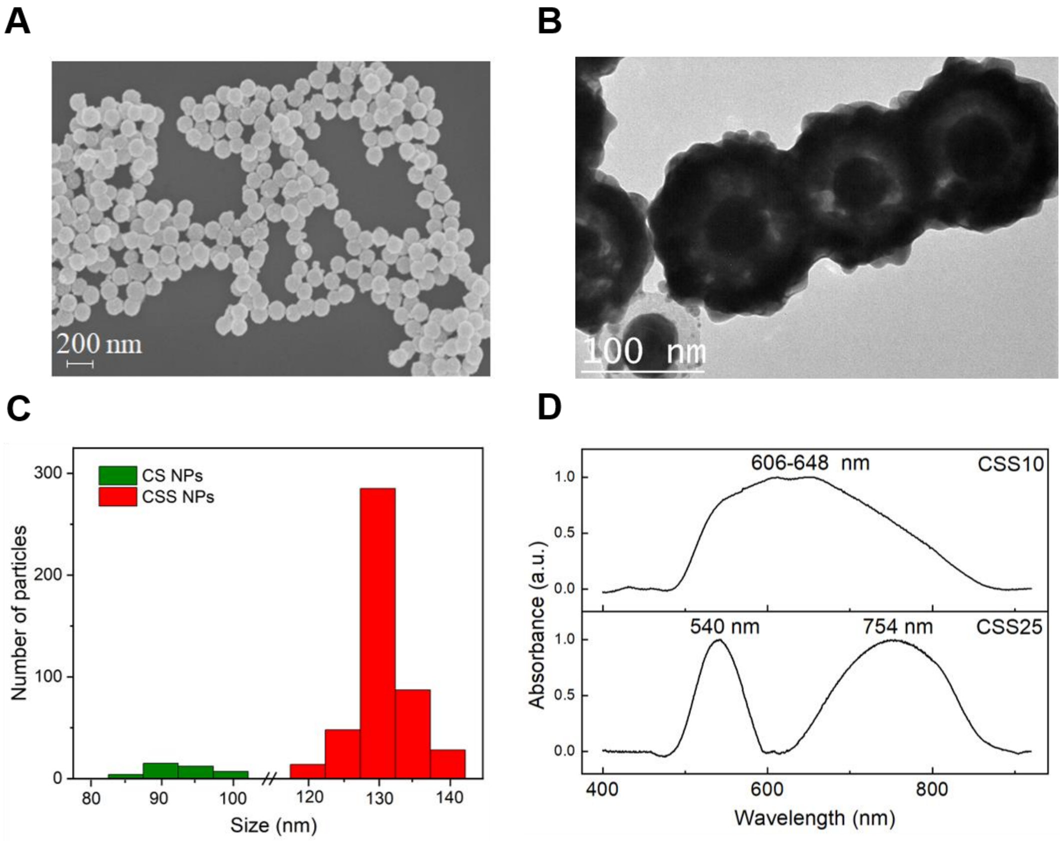

Figure 3.6: (A) SEM image and (B) TEM image of CSS25 NPs. (C) Histogram of the size distributions of CS and CSS25 NPs. (D) Absorption spectra of the CSS NPs. Here CSS10 and CSS25 refer to particles with core diameters of 20 nm and 50 nm respectively, with d_2=d_3=20 nm.

synthesized and dispersed on SiO_2/Si substrates. The overall diameter of a total of 500 NPs in the CSS product from 10 different batches (where a particle was taken to be a CSS NP if it has a diameter>105 nm) were averaged to be 130 nm ± 7 nm, consistent with the value of 130 nm from synthesis design, demonstrating successful synthesis. Figure 3.6B shows a TEM image of the same particles. The three different layers of the CSS particle can be seen in the TEM image. An analysis of ~100 particles using TEM shows the particles have an average dimension with a core diameter of 48±3.5 nm, d_2 of 19±2.8 nm, d_3 of 20±3.2

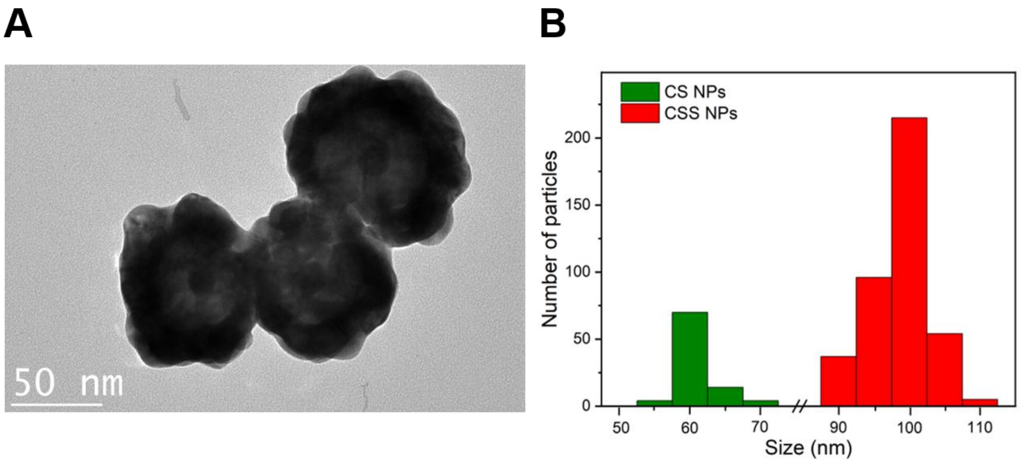

Figure 3.7: (A) TEM image of CSS10 NPs. (B) Histogram of the size distributions of CS and CSS10 NPs.

nm, which corresponds to an average overall diameter of 126 nm consistent with SEM measurement. The surface of the NPs shows an average roughness of ~3 nm. A separate analysis for the initial CS NPs, before functionalizing them with APTMS, showed an average diameter of 90 nm ± 5 nm. Figure 3.6C plots the histogram of the size distributions across the 500 measured CSS NPs. It can be seen that the majority of the CSS NPs have sizes corresponding to what is expected from the CSS NPs (~130 nm), with very few unreacted CS NPs across 500 NPs. The particles were considered to be CSS NPs if the size is between 120 nm and 140 nm and were considered to be CS NPs if the size is between 80 nm and 100 nm. We estimated that over 90% of the CS NPs were converted to CSS NPs following the synthesis method used. Similar control over the size for the CSS10 NPs is also evident form Figure 3.7. An analysis of the size of ~100 NPs for the CSS10 from TEM analysis shows the core diameter to be 19.17 ± 1.82 nm, d_2 to be 19.18 ± 1.92 nm, and d_3 to be 19.39 ± 2.99 nm. Figure 3.7B plots the histogram of the size distributions across 500 measured particles, and we estimate that over 80% of the CS NPs were converted to CSS

NPs following the synthesis method we used. Thus, the above results demonstrate the control over the synthesis steps for uniform CSS NPs in accordance to the dimensions optimized from theory with a high yield.

To validate the optical properties of CSS NPs experimentally, the extinction spectra were taken as a function of wavelength. Figure 3.6D plots the extinction spectra of CSS10 (top) and CSS25 (bottom) particles. It can be seen that the behavior of the particles closely resembles that predicted from calculation (Figure 3.4A, white stars for CSS10 and white dots for CSS25). The two peaks converge and form a broad peak over the range of 606-648 nm for the CSS10, and two distinct peaks of equal intensity are present at 540 nm and 754 nm respectively for the CSS25. The slight deviation from theoretical values noticed could be attributed to the deviation from the perfect spherical shape and dimensions used for the modeling, as seen from the TEM images. The deviation could also result from the slight mismatch of the fabricated inner layers when compared to the theoretically predicted values. Additionally, as the extinction measurement is an ensemble measurement of the nanoparticle solution, due to the variation of sizes in the ensemble, a broadening of the peaks can be seen. These results suggest the plasmonic response of the synthesized CSS NPs closely matches what was predicted from our theoretical model. This indicates that we have successfully synthesized CSS NPs in the optimal range for the enhancement of PEC activity in hematite based on the design and optimization provided by the simulation.

To demonstrate the enhancement of the photocurrent density of the hematite photoanode using these CSS NPs, we then fabricate the hematite nanocoral photoanodes incorporated with the CSS NPs and measure the photocurrent density characterizing their

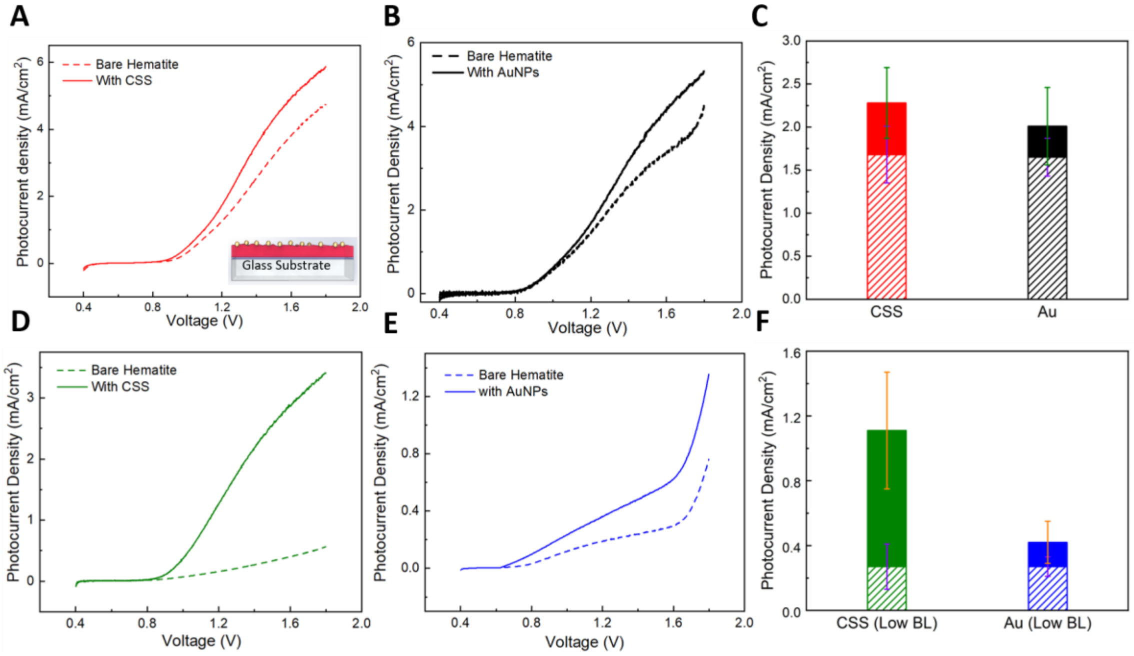

Figure 3.8: Photocurrent density as a function of voltage for (A) Bare hematite (red dashed) and CSS10 NP-deposited sample (red solid), (B) Bare hematite (black dashed) and 100 nm Au NP-deposited sample (black solid), (D) Bare Hematite at a low baseline (green dashed) and CSS10-deposited sample (green solid) and (E) Bare Hematite at a low baseline (blue dashed) and 100 nm Au NP-deposited sample (blue solid). Comparison of the average photocurrent densities of 5 samples at 1.23 V vs RHE for (C) Au-deposited (black) and CSS-deposited (red) samples, and (F) Au-deposited (blue) and CSS-deposited (green) samples at low baselines. Dashed region of bar represents bare sample, while solid section represents the improvement using the NPs.

PEC activity. We first present the results of the top-deposited NP-hematite architecture in Figure 3.8. In this architecture, the hematite nanocorals were grown and then immersed into a NP solution, leading to the NPs sitting on the surface of the hematite at the semi-conductor electrolyte interface. The concentration of the particles used for the deposition in both Au NP and CSS NP cases was 10^8 particles/mL for direct comparison. We estimate based on SEM micrographs a surface density of 100 NPs per 10 μm^2. This surface density

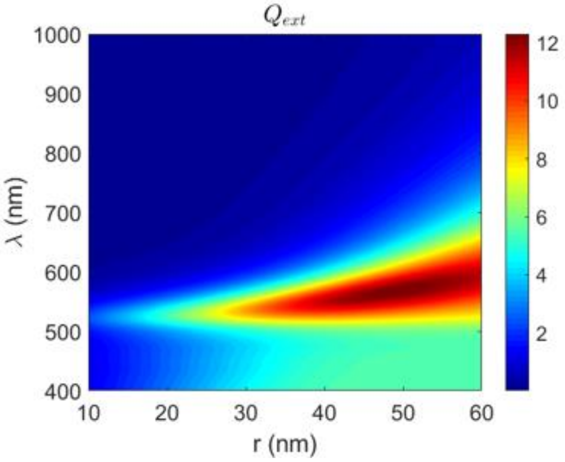

Figure 3.9: Extinction contour plot as a function of wavelength and radius of a Au NP.

was selected with cost considerations for an industrial design. Extinction contour plots for Au NPs (Figure 3.9) show that Au NPs with radii of 50 nm have the highest extinction coefficients and were chosen as the representative particles for comparison of performances with the CSS NPs after incorporation into hematite. Our initial testing results (Figure 3.10) show that the samples with CSS10 NPs show an average improvement of 0.6 mA/cm^2 whereas the samples with CSS25 NPs show an improvement of only 0.15 mA/cm^2. This is because scattering of the incident light using the near field enhancement of the CSS NPs and excitation of carriers from the surface trap states are the major contributors to the improvement in the photocurrent here, as detailed later. These effects will be more significant if the plasmonic peaks are closer to the hematite band edge. As CSS10 has plasmonic peaks more overlapping with the hematite band edge relative to CSS25 (Figure 3.6D and Figure 3.4A), CSS10 would lead to a greater improvement, as seen. Thus, 100 nm Au NPs and CSS 10 were selected as the main systems to compare for the top-deposited architecture. Figure 3.8A and 3.8B compare the J-V curves for representative CSS10 and

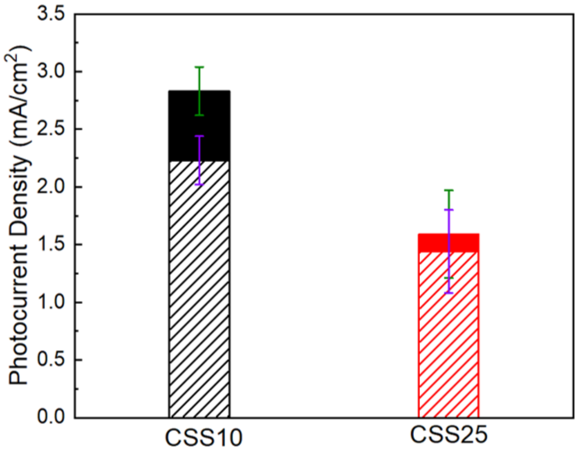

Figure 3.10: Comparison of the average photocurrent densities over 5 samples for CSS10 and CSS25 top deposited hematite.

100 nm Au NPs top-deposited hematite samples respectively. Figure 3.8A shows that using CSS NPs, the photocurrent density increases from 1.43 mA/cm^2 for the bare hematite (red dashed line) to 2.02 mA/cm^2 at 1.23 V vs RHE after the deposition with the CSS10 NPs (red solid line). This is an improvement of 0.59 mA/cm^2 from the bare hematite value. In comparison, Figure 3.8B shows that using Au NPs, the value improves from 1.61 mA/cm^2 for bare hematite (black dashed line) to 1.94 mA/cm^2 for the 100 nm Au NP-deposited sample (black solid line), which is an improvement of 0.23 mA/cm^2. Thus, the improvement using the CSS NPs was found to be greater than that of the Au NPs. To test the reproducibility of the improvement, the average of the photocurrent density at 1.23 V vs RHE from 5 samples of each type was taken and presented in Figure 3.8C. The dashed line shaded portions of the bars here represent the bare hematite samples, while the solid portions represent the improvement of the samples using the deposited NPs, black for Au NPs and red for CSS NPs. It is observed that the average value of the photocurrent density for the CSS NP-deposited sample increased from 1.68 ± 0.33 mA/cm^2 to 2.28 ± 0.41

mA/cm^2 with an increase of 0.6 mA/cm^2. In comparison, the Au NPs improved the value from 1.65 ± 0.22 mA/cm^2 to 2.01 ± 0.45 mA/cm^2 with an increase of 0.36 mA/cm^2, which is less than the average improvement using the CSS NPs. These results demonstrate the superiority of CSS system in comparison to plain Au NPs in this top-deposition configuration.

To test how robust the CSS NPs induced improvement in the top-deposited architecture was, and if it is independent of the hematite quality, testing was also performed on different hematite samples with a low photocurrent density baseline. For this purpose, the hematite was specifically annealed at 700^{o}C instead of 800^{o}C producing an expected lower photocurrent density. It has been suggested that under low annealing temperature condition, the performance of hematite deteriorates due to formation of a large number of surface trap states, which prevents the holes from reaching the semiconductor-electrolyte interface.[161] The results of the top-deposited NP-hematite architecture using the hematite prepared at 700 ^{o}C are plotted in Figure 3.8D-3.8F. Figure 3.8D-3.8F confirmed that the bare hematite shows an average baseline of 0.27 ± 0.06 mA/cm^2 at 1.23 V vs RHE as expected Figure 3.8D shows that using CSS NPs, the photocurrent density increases from 0.23 mA/cm^2 for the bare hematite (green dashed line) to 1.43 mA/cm^2 at 1.23 V vs RHE after deposition of CSS10 NPs (green solid line). This is a substantial improvement of 1.20 mA/cm^2 from the bare hematite value. In comparison, Figure 3.8E shows that using Au NPs, the value improves from 0.21 mA/cm^2 for bare hematite (blue dashed line) to 0.42 mA/cm^2 for the 100 nm Au NP-deposited sample (blue solid line), which is a 0.21 mA/cm^2 improvement. Figure 3.8F shows the average improvements obtained from 5 samples. The improvement using both CSS NPs and Au NPs is greater from a lower baseline (BL) hematite than a higher baseline one. This gives us some insight into the mechanism dominating the improvement in the top-deposited architecture. The CSS NPs, as previously hypothesized, can contribute to the photocurrent density of hematite by beneficial scattering, localized heating effects, and hot electron injection. While hot electron injection may still play a role, any heating effects will be much less in the top-deposited case, as the nanoparticles are in direct contact with the electrolyte solution, which will cause the dissipation of heat very quickly and prevent the majority of this heat from exciting carriers in the bulk. The scattering effect, however, still causes an increase in total light absorbed by the hematite. Although the NPs are on the surface of hematite, they scatter light into the higher refractive index material, favoring the hematite over the electrolyte solution. Additionally, the surface plasmons also can give energy during their decay to promote holes from the trap states to the conduction band and hence help in the water splitting process. In the hematite prepared with a lower annealing temperature, due to the greater number of surface trap states expected, the influence of the NPs is greater in the above-mentioned regard, and hence the photocurrent improvements are also larger. Thus, it can be concluded that the CSS NPs are more beneficial in terms of improving hematite performance in the top-deposited architecture when compared to Au NPs.

The top-deposited NPs cannot lead to generation of additional photoexcited pairs in the bulk as the field extent is insufficient to excite into the bulk with the NPs being only on the surface. Therefore, it is necessary to explore the embedded architecture and evaluate how the embedded architecture can improve the performance. Figure 3.11 plots the results

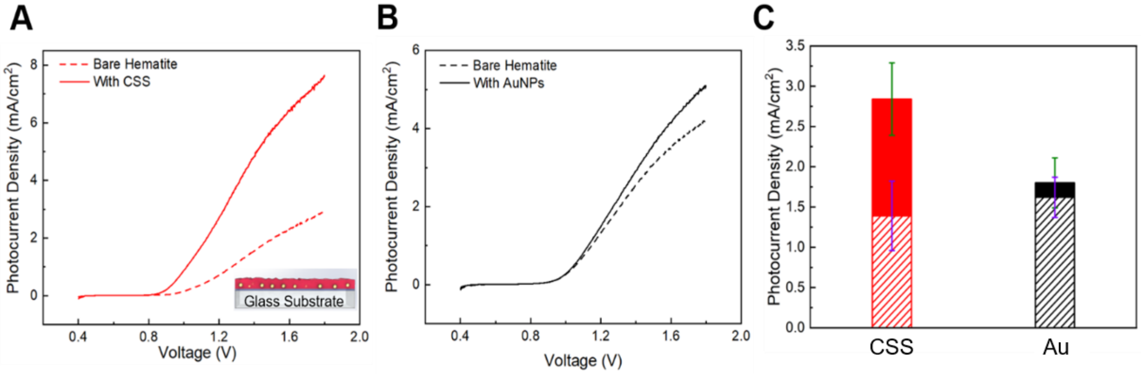

Figure 3.11: Photocurrent density as a function of voltage for (A) Bare hematite (red dashed) and CSS25 NP-deposited sample (red solid), (B) Bare hematite (black dashed) and 100 nm Au NP-deposited sample (black solid). (C) Comparison of the average photocurrent densities of 5 samples at 1.23 V vs. RHE for Au-deposited (black) and CSS-deposited (red) samples. Dashed region of bar represents bare sample, while solid section represents the improvement using the NPs.

of the embedded architecture, where the NPs were first deposited on the FTO and then hematite was grown on top. The photocurrent measurement of the bare hematite and plasmonically enhanced hematite were performed from the same grown sample. This allows direct comparison of the photocurrent with nanoparticles and without nanoparticles on the same grown hematite sample. The photocurrent measurements of the hematite-CSS and hematite-Au NP embedded structures were carried out. Based on our preliminary results (Figure 3.12), samples with CSS25 NPs showed an average improvement of 1.45 mA/cm^2 whereas samples with CSS10 NPs showed an average improvement of 0.22 mA/cm^2. Based on these results, CSS25 NPs were selected for optimization. Figures 3.11A and 3.11B compare the J-V curves for representative CSS25 and 100 nm Au NPs embedded hematite samples respectively. The concentration of the particles used for the embedding in both cases was 10^8 particles/mL for direct comparison. We estimate based on SEM

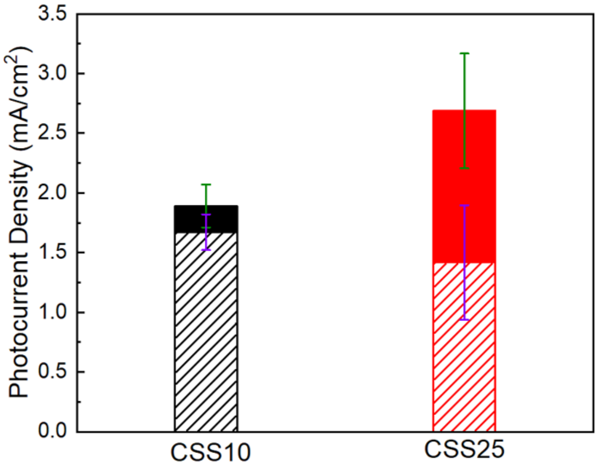

Figure 3.12: Comparison of the average photocurrent densities over 5 samples for CSS10 and CSS25 embedded hematite.

micrographs, a surface density of 100 NPs per 10 μm^2. Figure 3.11A shows that the photocurrent density increases from 0.82 mA/cm^2 for the bare hematite (red dashed line) to 3.0 mA/cm^2 at 1.23 V vs RHE after the deposition with the CSS25 NPs (red solid line). This is an improvement of 2.18 mA/cm^2 from the bare hematite value. In comparison, Figure 3.11B shows that the value improves from 1.51 mA/cm^2 for bare hematite (black dashed line) to 1.76 mA/cm^2 for the 100 nm Au NP-deposited sample (black solid line), which is only an improvement of 0.25mA/cm^2. It can be seen that, while the embedded 100 nm Au NPs provide a plasmonic enhancement to the bare hematite baseline, the embedded CSS 25 structure results in a substantial enhancement over bare hematite, a more than 3 times stronger increase than that from the Au NP plasmonic enhancement. Figure 3.11C shows the PEC results from five samples of embedded CSS 25 and five samples of embedded 100 nm Au NPs. All photocurrent densities are reported at 1.23 V vs RHE. The dashed shaded portion of the bar represent the bare sample, while the solid portions represent the improvement of the samples using the deposited NPs. The black bars are for

Au NPs, while the red bars are for CSS NPs. The average value of the photocurrent density for the Au NP-deposited sample increased from 1.62 ± 0.25 mA/cm^2 to 1.80 ± 0.31 mA/cm^2 which is an increase of 0.18 mA/cm^2. In comparison, the CSS NPs improved the photocurrent density from 1.39 ± 0.43 mA/cm^2 to 2.84 ± 0.45 mA/cm^2, which is an improvement of 1.45 mA/cm^2, more than 8 times greater than the average improvement using the Au NPs. This clearly demonstrates the superiority of the CSS25 NPs compared to plain Au NPs for the plasmonic enhancement of hematite in this architecture.

To understand why the CSS NPs are highly beneficial in the embedded configuration, we refer to the following points. Firstly, the CSS NPs have a broad near-field electric field distribution and as a result improved scattering effects at the resonance frequency. This allows each CSS NP to scatter incoming light over a much larger area, increasing the optical path length and dramatically increasing absorption within the hematite nanostructures. Essentially, light which has passed through the semiconductor is incident on the embedded. This light is then scattered back up through the semi-conductor and absorbed a second time. Thus, there is efficient light-harvesting with a relatively low concentration of NPs. Secondly, the second peak becomes beneficial here as it is strongly absorbing at resonance and can potentially lead to hot electron injection directly into hematite, leading to increase in the carrier density in the hematite bulk. So even though the second peak is outside the band gap of hematite, it can contribute indirectly to improvement of the photocurrent density. Finally, as the plasmonic heating effects relate directly with the near-field distribution, the CSS NPs produce much more intense heating effects upon relaxation of the localized surface plasmon. This heating effect has been demonstrated to

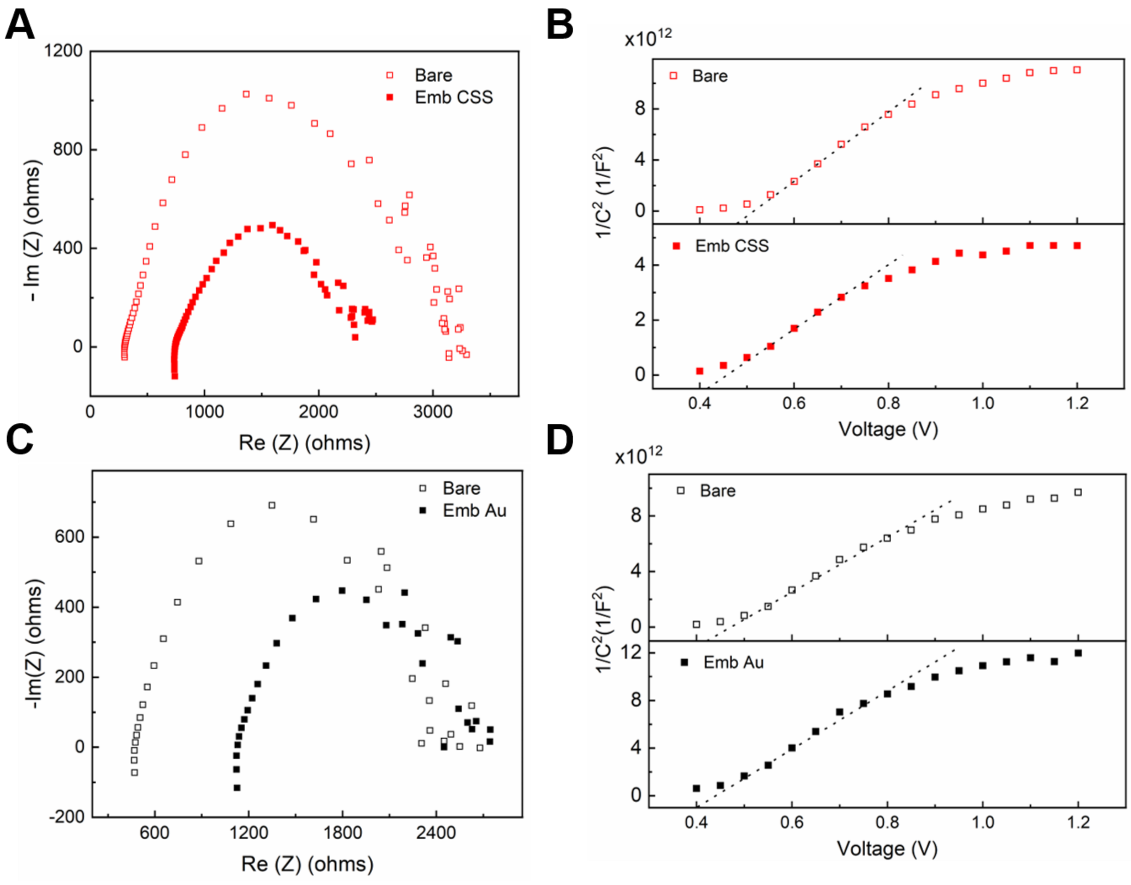

Figure 3.13: (A) shows the EIS spectroscopy data at 1.4 V vs RHE and (B) shows the Mott-Schottky plots for an embedded CSS-hematite photoanode. (C) shows the EIS spectroscopy data at 1.4 V vs RHE and (D) shows the Mott-Schottky plots for an embedded Au-hematite photoanode. Hollow and solid symbols represent the bare hematite and embedded NP-hematite respectively.

great effect in work from Halas et al.[165] This extreme localized heating of the CSS NPs can be strong enough to lead to improved charge carrier generation and separation in the hematite through increase in the localized temperature. 100 nm Au NPs, on the other hand, are strongly scattering with minimal absorption, as has been demonstrated earlier.[166] This small absorption cross section combined with a small field distribution results in a minimal contribution to the semiconductor through heating effects. As a result of beneficial scattering, hot electron injection and heating effects, the CSS NPs are much more advantageous to the performance of hematite in the embedded architecture when compared to Au NPs.

R/Ω CPE/F,n	R_s	R_{CT1} CPE1, n_1	R_{CT2} CPE2, n_2
Bare	52.75	371.43 $4.2x10^{-6}$, 0	2603 $4.33x10^{-6}$, 0.80
`	8.99	1310.3 $8.5x10^{-6}$, 0	1492 $1.61x10^{-5}$, 0.69
Bare	140	234.6 $1.45x10^{-6}$, 0	1245.6 $8.53x10^{-6}$, 0.89
Au emb	120	345.8 $8.32x10^{-6}$, 0.61	1023.4 $2.12x10^{-6}$, 0.70

Table 3.1: Fitted parameters for EIS data for Au NP embedded and CSS NP embedded samples

To further characterize and compare the performances of a CSS embedded sample and a Au embedded sample, Electro Impedance spectroscopy (EIS) and Mott-Schottky (MS) data were taken. Figure 3.13A and 3.13C compare the EIS data for a CSS25 NP embedded hematite sample and a 100 nm Au NP embedded hematite sample. The hollow and the solid symbols show the data for the bare hematite and the NP embedded hematite respectively. Figure 3.13A shows the EIS data for a CSS25 embedded sample at 1.4 V vs RHE, for which the photocurrent density has improved from 1.74 mA/cm^2 to 2.94 mA/cm^2. This is reflected in the EIS data, which shows the semicircle radius decrease by ~1.7 times for the CSS NP embedded sample (red solid) from the bare hematite (red hollow). Figure 3.14 shows the equivalent circuit used to analyze the impedances. Here, R_s means the sheet

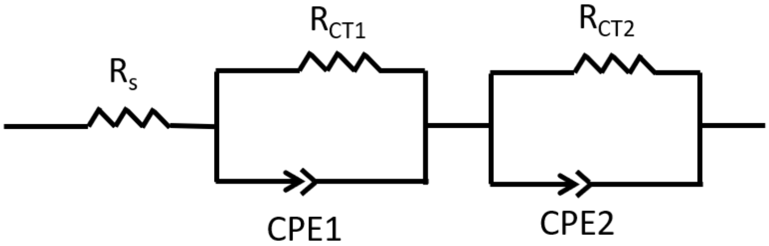

Figure 3.14: Equivalent circuit for EIS spectroscopy

resistance across hematite, and each R-C circuit represents one interface in the anode. CPE represents a constant phase element which is determined by a number $0<n<1$, where $n=0$ means a pure resistor and $n=1$ represents a pure capacitor. The largest of the R_{CT} values, which basically represents the highest resistance across any interface, will be for the hematite-electrolyte interface. A decrease of this value would imply easier transfer of holes from the hematite to the electrolyte, leading to a higher photocurrent density. Table 3.1 shows the fitted values obtained for the samples represented in Figures 3.13A and 3.13C. It can be seen for the CSS embedded hematite, R_{CT2} has the largest value of 2603 **Ω**, and represents the resistance at the hematite-electrolyte interface. This value decreases significantly to 1492 **Ω** and is the primary factor for the improvement in the photocurrent. At the same time, CPE2 also increases from 4.33×10^{-6} F to 1.61×10^{-5} F, and this trend is in agreement with observations made in literature for improvement in the photocurrent[167-168]. However, both R_{CT1} and CPE1 increase, which represents an increase in the impedances at the hematite-FTO interface. This increase is most likely due to the embedding of NPs on the surface of the FTO and growing hematite over these NPs, which leads to an increase in the resistances at the interface. Similar trends are also seen from Figure 3.13C, which represent the trends for a Au NP-embedded hematite sample. The photocurrent density increases from 2.21 mA/cm^2 to 2.61 mA/cm^2 at 1.4 V vs RHE, and this is also represented by a 20% decrease in the radius of the semicircle. The fitted values show a similar trend as the CSS embedded sample, with a decrease in the resistance at the hematite-electrolyte interface and an increase in the values at the hematite-FTO interface. However, the decrease in resistance at the hematite-electrolyte interface is much smaller than that for the CSS embedded sample, which explains the lower improvement using Au NP embedding.

Figure 3.13B and 3.13D show the Mott-Schottky (MS) plots for the CSS NP embedded hematite and Au NP embedded hematite respectively. The intercept of the linear portion of the graph gives us the flatband potential (V_{FB}) for the samples. For the CSS embedded sample (Figure 3.13B), V_{FB} decreases from 0.47 V for the bare sample to 0.41 V for the CSS embedded NP sample, while for the Au NP embedded sample (Figure 3.13D), it decreases from 0.42 V to 0.40 V. The greater decrease of the flatband potential for the CSS NP embedded hematite sample is further testament of the better improvement provided by CSS NPs for improving hematite performance when compared to Au NPs.

To demonstrate the contribution of both plasmonic peaks of the CSS NPs to the photocurrent, filter tests were performed to isolate the contribution of each peak to the photocurrent. Figure 3.15A and 3.15B represent the data for bare hematite and a typical CSS25 NP embedded hematite respectively. The photocurrent density improves from 0.77 mA/cm^2 for the bare hematite to 1.90 mA/cm^2 for the CSS NP embedded hematite. Figure 3.15A shows that using a 400 nm longpass (LP) filter, the photocurrent density decreases from 0.77 mA/cm^2, to 0.54 mA/cm^2, indicating significant absorption and photocurrent generation at wavelengths below 400 nm. Using a 400 nm-600 nm filter in conjunction

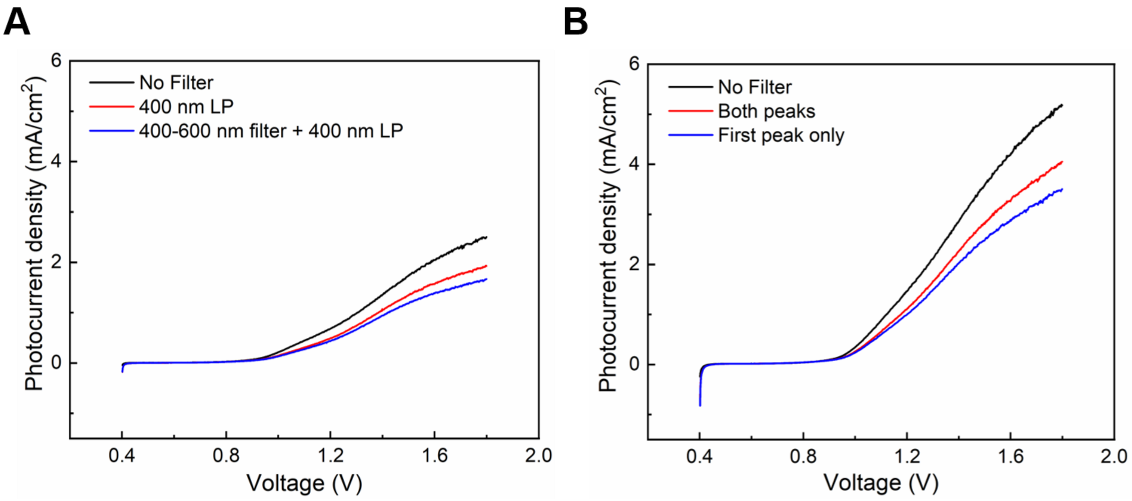

Figure 3.15: (A)Photocurrent density of bare hematite with no filter (black), with a 400 nm longpass filter (red) and with a 400 nm longpass filter and a 400-600 nm filter in conjunction. (B) Photocurrent density of a CSS embedded hematite sample with no filter (black), with a 400 nm longpass filter (red) and with a 400 nm longpass filter and a 400-600 nm filter in conjunction.

with the LP filter decreases the photocurrent density further to 0.50 mA/cm^2, which can indicate either an imperfection in the filter or small absorption in hematite beyond 600 nm. Figure 3.15B shows that the photocurrent density with no filter is 1.90 mA/cm^2, which decreases to 1.46 mA/cm^2 with a 400 nm LP filter and to 1.14 mA/cm^2 with a 400 nm-600 nm filter in conjunction with a 400 nm LP filter. The 400 nm LP filter has contributions from both the peaks to the photocurrent density, while using a 400 nm-600 nm filter blocks out absorption by the 2nd peak. The percentage change of the photocurrent density with the filter is 28%, which is calculated as the percentage difference at the water splitting voltage between the configuration with the 400 nm-600 nm filter and the LP filter, and only the LP filter. A similar calculation for the bare sample yields a percentage change of only 8%, which can arise from imperfections of hematite or the filter, as previously mentioned. The large difference clearly indicates that a large amount of light is absorbed by the plasmonic CSS NPs and either through hot carrier generation or through plasmonic heating, a significant contribution to the photocurrent density is made.

To demonstrate the versatility of our CSS/hematite heterostructured photoanodes and assess viability for further improvements, we treated our top-deposited and embedded samples with a cobalt phosphate (Co-Pi) co-catalytic overlayer. This strategy has also been shown to successfully improve photoanode performance reproducibly. The Co-Pi helps to reduce surface recombination and effectively mediates the photocatalytic process at the semiconductor-electrolyte interface. This results in lowering of the onset potential for the hematite photoanode, and a subsequent higher photocurrent at the water splitting voltage. Figure 3.16 shows the J-V curves for two representative samples before and after deposition of the Co-Pi overlayer. In Figure 3.16A, the bare hematite shows (black line) 1.59 mA/cm^2 at 1.23 V vs. RHE, and after top-deposition of CSS10 (red line) the photocurrent density increases to 2.04 mA/cm^2. With Co-Pi (green line), the final photocurrent density achieved is 3.40 mA/cm^2 at 1.23 V vs. RHE. This is a 1.7 times improvement after using a Co-Pi overlayer and an overall improvement of 1.81 mA/cm^2 from the bare hematite, which is a 2.1 times improvement. For the embedded sample in Figure 3.16B, the baseline hematite (black line) shows 1.27 mA/cm^2 at 1.23 V vs. RHE, and an improvement via embedded CSS25 (red line) is 3.04 mA/cm^2. With Co-Pi, a photocurrent density of 4.10 mA/cm^2 at 1.23 V vs. RHE is achieved. This is a 1.3 times improvement after treatment with Co-Pi, and an overall increase of 2.83 mA/cm^2, which is 3.2 times better when compared with the bare hematite. These results demonstrate the

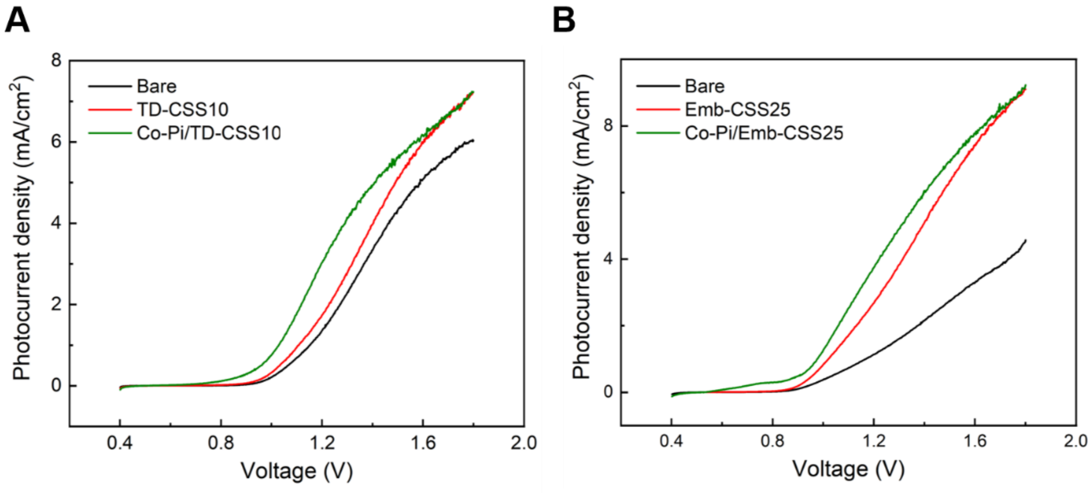

Figure 3.16: Photocurrent density as a function of voltage for (A) Bare hematite (black), top-deposited CSS10 NPs on hematite (red) and Co-Pi deposition on the CSS/hematite heterostructure (green), and (B) Bare hematite (black), embedded CSS25 NPs on hematite (red) and Co-Pi deposition on the CSS/hematite heterostructure (green).

versatility of the CSS/hematite system for use with other improvement strategies, such as co-catalysts which can help to push the photocatalytic activity of hematite to higher, towards closing the gap for large scale production of H_2.

CHAPTER FOUR: PLASMONIC CMS NPs FOR SENSING

Section One: Raman Spectroscopy as a tool for sensing

SPRs can significantly enhance the surface sensitivity of nanostructures and accurately detect the binding of target molecules at the surface, even at low concentrations, due to the large enhancements of the electric fields at the surface. This promotes the advent of SPR sensors, which are powerful tools for real-time supervising of interactions in biology and chemistry analysis[169-171]. The first use of SPR sensors was decades ago, when the benefit of using SPR sensors for sensing and gas detection was demonstrated[172-173]. Since then, it has been extensively used and studied for potential incorporation into medical devices for tumor detection, point of care devices, etc[3, 174-176].

Raman spectroscopy, which probes vibrational transitions, allows the label-free identification of a wide variety of molecules, thereby becoming a highly relevant tool in sensing[177-178]. Raman signals by themselves have a very small scattering cross section ($\sim 10^{-24}$ cm^2) which is much smaller than the fluorescence cross-section ($\sim 10^{-16}$ cm^2). Surface-enhanced Raman scattering (SERS) is the amplified Raman scattering by molecules adsorbed on metal surfaces, and it is widely believed that the EM field enhancements from localized excited surface plasmons is the primary factor leading to the enhancements. Locally created EM hotspots around surfaces, or at sharp corners of nanostructures can lead to enhancement factors (EFs) as high as 10^{10}, or even greater[20, 179-180]. However, a major disadvantage of Raman spectroscopy is that the time required to get an image is long (~several seconds) and such a long time of exposure to the excitation might be damaging for the tissue.

Coherent Anti-stoke's Raman Spectroscopy (CARS) is a third order non-linear optical process that uses multiple photons to excite molecular vibrations and produce a coherent signal. Typically, two light fields (a pump beam ω_P and a Stoke's beam ω_S) couple the molecule's ground state with its vibrationally excited state. This is done with a phase that is determined by the phase of the incident fields. The nonlinear polarization induced in the molecule thus oscillates with a well-defined phase at its onset, and, within the coherence time of the vibrational mode, the radiation that follows maintains a definite phase relation with the driving fields. The major advantages of CARS over SERS are: (1) constructive interference between the signal fields from individual Raman scatterers gives rise to strong and directional signals, and (2) the response of the vibrational modes can be time-resolved which in turn enables a direct look at the evolution of mutual coherences between different modes and between molecules in the ensemble[181]. The coherent amplification of the Raman response can be several orders of magnitude and subsequently this leads to much faster (~10^6-10^8) acquisitions of the response. As a result, CARS has become a very popular tool for bioimaging in the past few years[182-184]. Here, we present results for both SERS and CARS of plasmonic CSS NPs introduced in the last chapter, as well as nano-shells (NS), primarily focusing on single NP imaging.

Section Two: Plasmonic Au/SiO$_2$/Au NPs for fast sensing

The CSS NPs introduced in the last chapter have the unique property of two resonances in their spectrum. The 2nd resonance can be tuned to wavelengths between 600-1000 nm as shown in Figures 3.4 and 3.5. The advantage of this is that these plasmonic

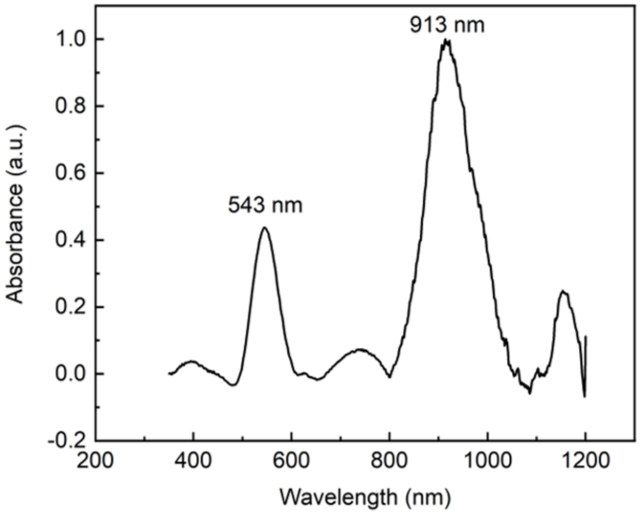

Figure 4.1: Absorbance spectra of CSS NPs with dimensions (25,20,15) nm.

resonances can be excited by NIR excitations, which are less detrimental to tissues. It is not possible to achieve such high plasmon resonances with traditional plasmonic NPs at the single particle level. Figure 4.1 shows the absorbance spectra of the CSS NPs used for the SERS and CARS measurements. From TEM analysis, the average dimensions of the core diameter, inner shell thickness and outer shell thickness are (48±3.5 nm, 17±2.8 nm, 15±3.2 nm). This has been achieved by varying the amount of $HAuCl_4$ added in the last synthesis step to the seeded (25,20) nm CS NPs. It can be seen that the second peak is much stronger than the first peak, and this is the plasmon resonance which will be used to excite the vibrational spectra.

Figure 4.2 shows the SERS and CARS measurements from a high-density CSS NP using 4-mercaptopyridine(4-mpy) as the molecule under consideration. The sample was prepared as follows. A cover glass substrate was immersed initially in 0.2% APTMS for 5 hours. The cover glass was then taken out and washed thoroughly to remove any loosely bonded molecules. 20 μL of the NPs colloid (~10^9 particles/mL) was then mixed with 10

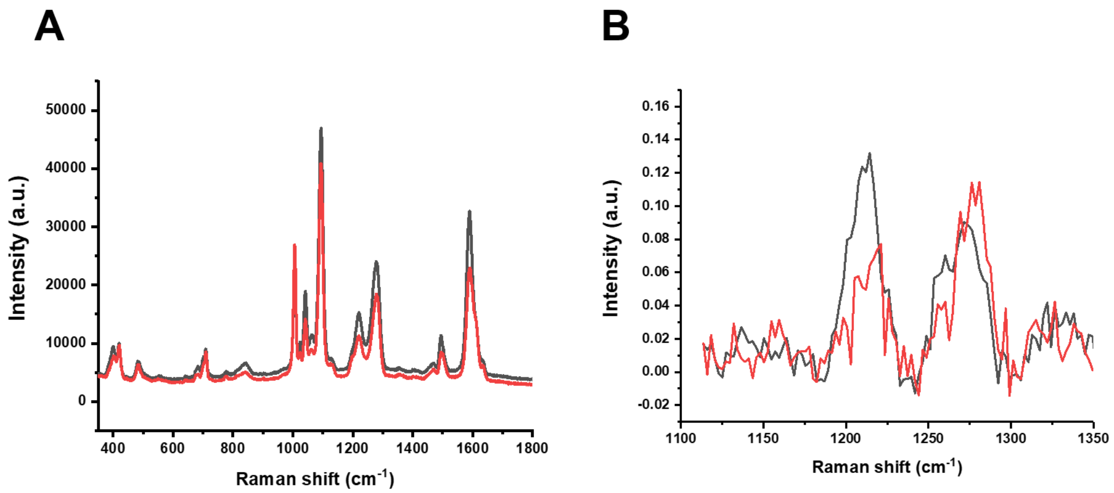

Figure 4.2: (A) SERS measurement and (B) CARS of 4-mpy molecule with high density of CSS NPs as plasmonic particles. Laser conditions for SERS were excitation of 785 nm, power of 1.5 mW and integration time of 10 seconds for SERS. Laser conditions for CARS were pump: 921 nm, 200 µW; Stoke's: 1040 nm, 200 µW.

µL of 57 µM 4-mpy solution and allowed to react overnight at 4°C to ensure complete adsorption of the molecules over the CSS surface. Then this was dropped on the glass substrate 5 µL at a time and dried in vacuum to form a high-density CSS NP aggregate. SERS measurement was taken using a Renishaw Raman Spectroscopy instrument, with a 785 nm laser excitation at 1.5 mW power and an integration time of 10 seconds.

Figure 4.2A shows two measurements of the 4-mpy Raman spectrum and shows that the characteristic peaks of 4-mpy are visible in the Raman spectrum. The 2nd peak absorbance for the CSS NPs is expected to be close to the laser excitation due to the dielectric environment being air which blue shifts the resonance peaks. This matching with the laser excitation will improve quite significantly the electric fields at the surface of the CSS NPs. The strongest of these peaks is at 1107 cm^{-1}, with an average baseline to peak value of ~40000 a.u. Other notable characteristic peaks of 4-mpy are at 1041 cm^{-1}, 1278

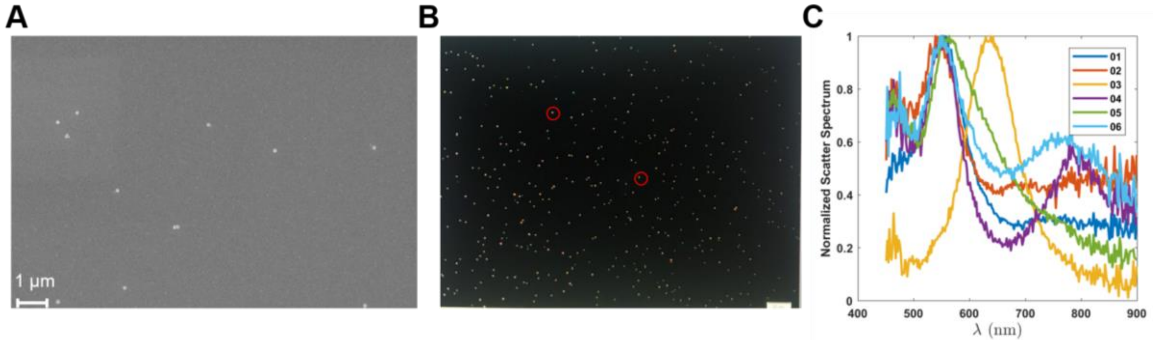

Figure 4.3: (A) SEM image of uniformly dispersed single CSS NPs. (B) Dark field image of the uniformly dispersed CSS NPs. (C) Single particle scattering spectroscopy of the particles in (B). Red circles in (B) indicate Measurement 04 and Measurement 06 in (C).

cm^{-1} and 1612 cm^{-1}. Of these the 1612 cm^{-1} peak is also strong, with an average baseline to peak value of ~25000 a.u. This conclusively proves that the CSS NPs are capable of generating SERS signals for 4-mpy at high densities.

Figure 4.2B shows the CARS signal for the same sample. The laser conditions were chosen so that the Raman peaks between 1150 cm^{-1} and 1350 cm^{-1} are visible. It can be seen that signals were obtained for the characteristic peaks at 1230 cm^{-1} and 1278 cm^{-1} at very high pump and probe powers, but for lower powers the signal was no longer detectable over the background noise. The acquisition time for this image was small compared to the integration time used in SERS, approximately around 0.1 sec. Thus, using high density CSS NPs, it was possible to detect 4-mpy molecules bound to its surface both in SERS and in CARS.

However, the goal is to move towards single particle detection. In that sense, the first objective is to create a uniform dispersion of single CSS NPs across the substrate and then reduce the density of these CSS NPs to move towards single particle imaging. Figure 4.3A shows the SEM of single particle dispersion on a cover glass substrate. To achieve this, the cover glass substrate was exposed to an oxygen plasma (100 sccm O_2, 250 W power, 5 minutes) which makes the surface hydrophilic and allows the NP droplets to spread uniformly across. The colloid of CSS NPs and 4-mpy was diluted 10 times from the previous stock solution, and 10 μL of the new solution was dropped onto the cover glass substrate. This was then blown off after 30 seconds with a N_2 air gun. This led to the uniform dispersion of single NPs as shown in the SEM image in Figure 4.3A. Analysis across 20 such images showed that about 75% of the NPs were singly distributed while the remaining 25% were aggregated in groups of two or greater. Figures 4.3B and 4.3 C show the dark field microscopy and dark field scattering spectroscopy of the same sample. Figure 4.3B shows the uniform dispersion of single NPs on a cover glass substrate, with the scale bar being 10 μm. Figure 4.3C shows the dark field scattering microscopy of 6 NPs. The red circles in Figure 4.3B indicate measurements 04 and 06 in 4.3C, which show the double peak feature of the CSS NPs. The peaks for these measurements are at 550 nm and 780 nm. The single peaks for the other particles indicate that the outer shell was not formed uniformly for these particles, leading to no plasmon hybridization peaks. There are two things which can be observed for the CSS resonance peaks: (1) the peak locations, especially for the 2nd peak, are different from that observed from the absorbance in Figure 4.1. This is mainly due to the fact that the dielectric medium for this setup is air, which has a relative permittivity of 1 (lower than the permittivity of 1.33 for water), and this results in a blue shift of the 2nd peak, which is more sensitive to the dielectric medium than the 1st peak. (2) The relative peak intensities are opposite to that in Figure 4.1. This can be explained by the fact that Figure 4.1 measures the absorbance, which is the sum of both

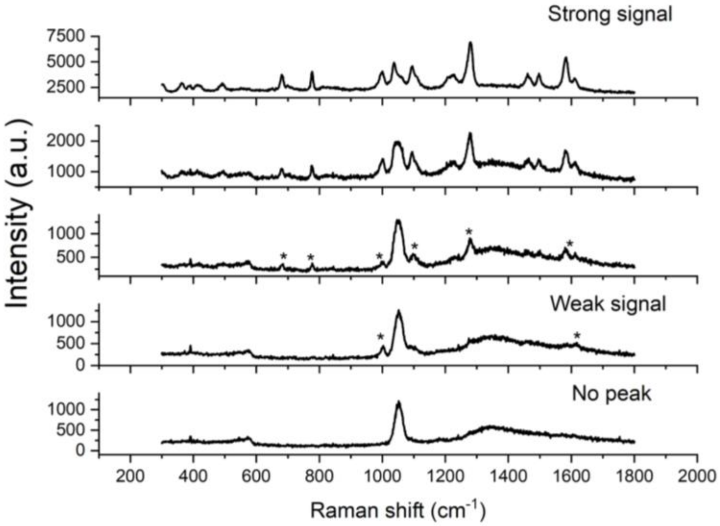

Figure 4.4: SERS measurement of 4-mpy molecules using low density CSS NPs. The amount of a 10^8 particles/mL solution added for measurement on the cover glass are 10 μL, 7.5 μL, 5 μL, 2.5 μL and 1 μL. Stars indicate characteristic peaks of 4-mpy.

scattering and absorption by the NPs, while Figure 4.3C measures only the scattering. It can be seen from Figure 3.4B that the 2nd peak is primarily absorbing, and as a result, the intensity is much lower as compared to Figure 4.1.

To measure the effectiveness of these NPs for single particle imaging, both SERS and CARS were performed on the above substrates. Figure 4.4 shows the SERS images taken as lower drop sizes of the colloid were added on to the cover glass substrate. As the laser spot size is very large for the SERS (~1 μm^2) and there is no way to image the particles at the time of taking a SERS measurement. The topmost panel shows a drop size of 10 μL, and the subsequent lower panels are 7.5 μL, 5 μL, 2.5 μL and 1 μL. The stars indicate the characteristic peaks of 4-mpy. As the drop sizes decrease, the intensity of the peaks also decreases, until there is no peak for the 1 μL drop. At the same time, the background

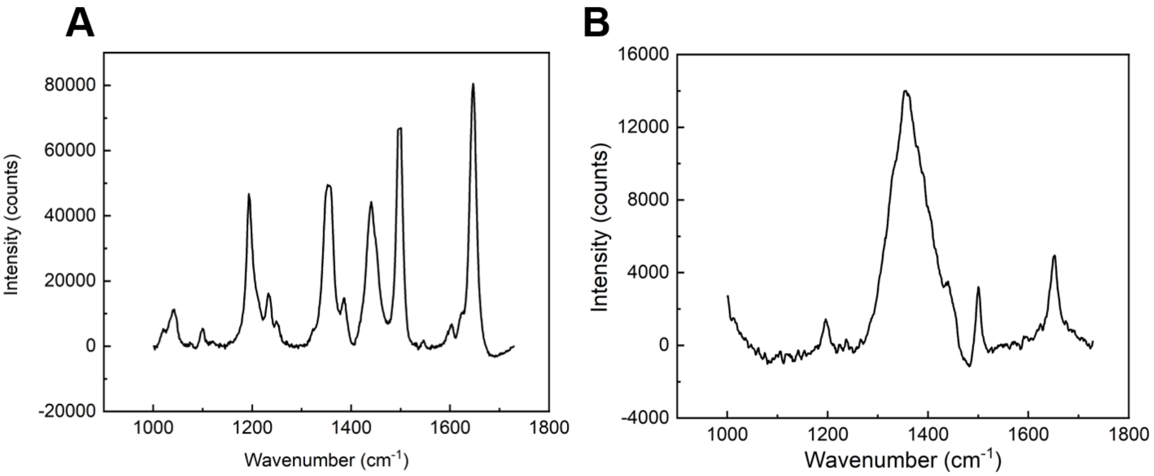

Figure 4.5: (A) SERS spectrum of Rh-800 molecules adsorbed onto CSS NPs which in turn have been dispersed in high density. Laser conditions: 785 nm wavelength, 339.5 µW, 10 s int. (B) Raman spectra of Rh-800 molecules. Laser conditions: Wavelength-785 nm, Power- 77.6E+3 µW, integration time-10 s.

fluorescence also keeps increasing in intensity and becomes the primary visible peak in the spectrum for the smallest drop size. CARS measurements (image not included) performed on these samples showed only noise, implying that the scattering was not strong enough from these monodispersed substrates to produce a measurable signal. This can be a combined effect of low scattering from the 2nd peak of the CSS NPs as well as the mismatch of the plasmon resonance with the pump and Stoke's beams.

To see if there is any change to the spectrum on using a molecule with different properties, Rhodamine 800 (Rh-800) was also used as a molecule for testing. The advantage of Rh-800 over 4-mpy is the larger polar surface area compared to 4-mpy and a peak absorbance around 700 nm, which is approximately where the CSS plasmon resonance is also located. Figure 4.5A shows the SERS spectra of Rh-800 molecules adsorbed onto CSS NPs. To prepare this substrate, 20 µL of the stock solution of CSS NPs was mixed with 10 μL of 85 μM Rh-800 and left for 24 hours at 4^{o}C. This was then dropped onto an APTMS treated cover glass surface as before. The laser excitation wavelength was 785 nm, while the laser power used was 339.5 μW with a 10 second integration time. It can be seen that the signals for the Rh-800 molecule are much stronger than the signals for 4-mpy, even though a lower laser power is being used. This is most likely due to additional matching of the peak absorption of Rh-800 molecules with the plasmon resonance of the CSS NPs. The characteristic peaks of Rh-800 are also visible, with the strongest peak at 1660 cm^{-1} where the baseline to peak intensity is ~80000 a.u. Figure 4.5B plots the spectrum of Rh-800 molecules (85 μM sandwiched between two cover glass substrates) and shows that the fluorescence (~1380 cm^{-1}) dominates the spectrum. A very high laser power of 77.6 x 10^{3} μW with a 10 second integration time was used for this measurement. Using this data, and assuming complete coverage of the molecules on the CSS surface, the enhancement factor (EF) was calculated using the following equation:

$$EF = \frac{Intensity_{CSS} / N_{f,CSS}}{Intensity_{Raman} / N_{f,Raman}} \times \frac{laser\ power_{Raman}}{laser\ power_{CSS}} \times \frac{time\ of\ integration_{Raman}}{time\ of\ integration_{CSS}}$$

Here, $Intensity_{x}$ refers to the baseline to peak magnitude of the peak under consideration and $N_{f,x}$ refers to the total number of excited molecules under the laser beam. Using this equation, the EF was calculated to be 5.7 x 10^{5} for the CSS NPs.

Figure 4.6 shows the CARS spectra obtained for a sample with low density of CSS NPs. To prepare this sample, 5 μL of the CSS-Rh-800 colloid was dropped onto an O_2 plasma-treated cover glass substrate and blown away after 30 seconds with a N_2 gun. The laser conditions were chosen so as to keep the peak around 1650 cm^{-1} peak in the Raman

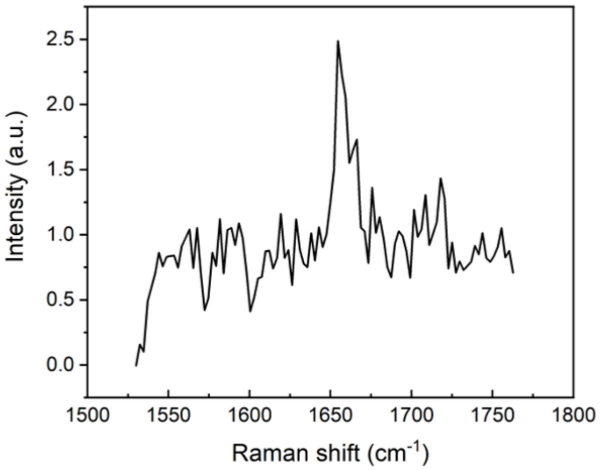

Figure 4.6: CARS spectra of Rh-800 molecules. Laser conditions were: pump-888 nm wavelength, 100 µW power; Stoke's-1040 nm wavelength, 100 µW power.

shift region. It can be seen that the 1650 cm^{-1} peak is visible in the spectrum, even at low powers of pump and probe ~100 µW. The acquisition time was still ~0.1 sec. This shows that CSS NPs have potential in providing fast bioimaging results due to their unique plasmon resonance. However, no signal could be obtained using CARS at lower densities, when working towards single particle imaging. This provides the necessity to explore other plasmonic nanostructures in order to achieve this goal.

Section Three: Plasmonic Nanoshells for fast sensing

The primary deterrent for CSS NPs is that they are primarily absorbing NPs, and imaging techniques like SERS and CARS require strong scattering particles. It has been shown previously that Nanoshells (NS) with a silica core and a Au outer shell are quite strong scatterers[165]. Additionally, by changing the dimensions of each of the layers involved, it is possible to push the plasmonic peaks to the NIR range. For this purpose, silica nanoparticles were synthesized using a modified Stöber method[185-186].

NH_4OH	**TEOS**	**Addition rate (TEOS)**	**Final diameter (nm)**
9.5 mL in 50 mL EtOH	5 mL + 30 mL EtOH	1 mL/min	1139 ± 63
9.5 mL in 50 mL EtOH	5 mL + 30 mL EtOH	2.5 mL/min	865 ± 41
9.5 mL in 50 mL EtOH	3 mL + 32 mL EtOH	1 mL/min	1036 ± 79
9.5 mL in 50 mL EtOH	1 mL + 34 mL EtOH	1 mL/min	806 ± 41
9.5 mL in 50 mL EtOH	0.5 mL + 34.5 mL EtOH	5 mL/min	400 ± 48
9.5 mL in 50 mL EtOH	0.3 mL + 34.7 mL EtOH	3 mL/min	208 ± 12
9.5 mL in 50 mL EtOH	0.1 mL + 34.9 mL EtOH	5 mL/min	123 ± 9

Table 4.1: Final diameters of the silica NPs formed as a function of the different parameters used.

First, 9.5 mL of NH_4OH was mixed with 50 mL of ethyl alcohol (EtOH). Then, depending on the desired dimension, different amounts of TEOS mixed with different volumes of ethyl alcohol was added to it. The ratio of TEOS/EtOH determines the size of the SiO_2 NPs formed as higher the ratio, larger the size of the particles. This is as the Gibb's free energy required to form nucleation centers is higher and the radius $R \propto e^{\frac{-\Delta G}{kT}}$. The rate of TEOS addition also determines the size of the NPs as it changes the density of the nucleation centers. Higher the rate is, smaller is the size of the NPs which are being formed. The reaction was allowed to continue under stirring for 20 hours. Table 4.1 gives the summary of the conditions used, and the subsequent sizes of the NPs formed. Figure 4.7A shows the SEM images of 200 nm SiO_2 NPs formed using this method.

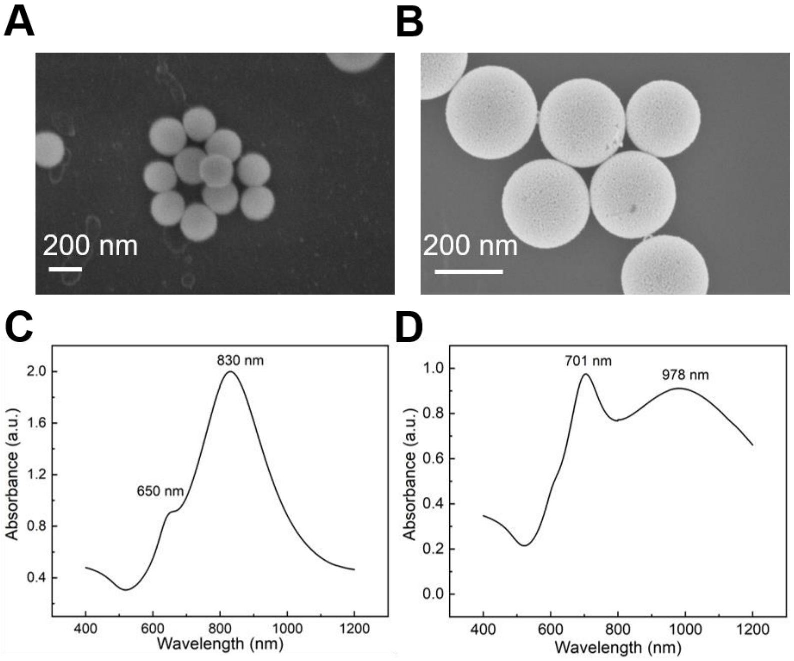

Figure 4.7: (A) SEM images of 100 nm radius silica NPs. (B) SEM image of NS with silica core of 100 nm radius and a 20 nm Au shell. (C) Absorbance of a NS with 60 nm core radius and 20 nm Au shell thickness. (D) Absorbance of a NS with 100 nm core radius and 20 nm thick Au shell.

Subsequently, Au shells were grown on the SiO_2 NPs using the Duff method as outlined in Chapter 3. The size of the shells formed were kept around 20 nm. Figure 4.7B shows the SEM images of the NS thus formed with a 200 nm core and a 20 nm thick shell. It can be seen that uniformly shaped and coated NS were formed using the above methods. The amount of $HAuCl_4$ added to the seeded SiO_2 NPs had to be adjusted in order to achieve this. For the purpose of the Raman measurements, two particular dimensions (r_1, t_2) were chosen where r_1 is the radius of the silica core and t_2 is the thickness of the Au shell: (60,20) nm and (100,20) nm. The rationale behind choosing these dimensions was based on the absorbance peaks shown in Figures 4.7C and 4.7D. The (60,20) NS shows an absorbance

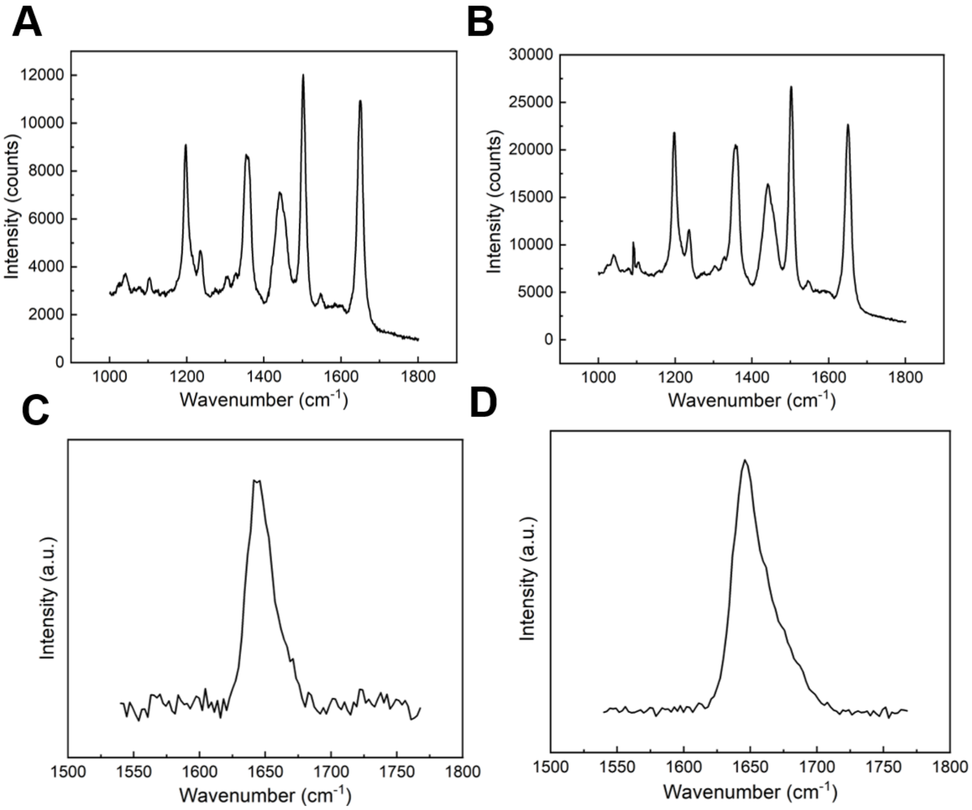

Figure 4.8: SERS spectra of (A) (60,20) NS and (B) (100,20) NS. Laser conditions were: Wavelength-785 nm, power-4.8 µW, integration time-10 s. CARS spectra of (C) (60,20) NS and (D) (100,20) NS. Laser conditions were: pump-888 nm wavelength,50 µW power; Stoke's-1040 nm wavelength, 50 µW power.

peak around 830 nm with a slight bump around 650 nm, while the (100,20) NS shows a broad peak at 978 nm, and a second peak at 701 nm. The rise of the 2nd peak with increase in size of the SiO_2 core is due to quadrupolar moment contributions which become more significant larger the core size is for a fixed shell size. As a result, there is a small bump for the (60,20) NS at 650 nm which becomes a full peak for the (100,20) NS. For the (60,20) NS, the plasmon resonance is near the laser excitation for SERS (785 nm), which makes it ideal for a strong SERS spectrum. The (100,20) NS on the other hand has a broad resonance peak at 978 nm which covers both the pump and Stoke's excitations, and the quadrupolar peak at 701 nm also matches the peak absorbance of Rh-800 molecules.

Figures 4.8A and 4.8B shows the SERS results of Rh-800 molecules mixed with the chosen NS. The samples were prepared by mixing 40 µL of NS with 10 µL of Rh-800 and allowing complete adsorption overnight at 4ºC. This was then centrifuged to remove excess Rh-800 and diluted to 50 µL. 5 µL of this solution was dropped 10 times onto a clean glass substrate and allowed to vacuum dry each time, to form a sample with high density of the NS. The laser excitation was at 785 nm wavelength with a power of 4.8 µW and an integration time of 10 seconds. It can be seen that the signal obtained from the (100,20) NS is stronger than the signal obtained from the (60,20) NS. This is most likely due to the matching of the Rh-800 peak with the quadrupolar peak for the (100,20) NS. The EF for the (60,20) and (100,20) NS were calculated to be 5.9×10^6 and 1.2×10^7 respectively. Figures 4.8C and 4.8D show the CARS spectra of the same NS samples. The laser conditions were chosen as before to center the 1650 cm^{-1} Raman peak, with a pump of wavelength 888 nm and a Stoke's of wavelength 1040 nm. The laser powers used for both were much smaller at 50 µW. Acquisition time was 0.1 s as before. It can be seen that the CARS signals obtained were much stronger than the ones seen for the CSS NPs, with the (100,20) NS providing a stronger signal compared to the (60,20) NS due to better matching with the laser excitations.

Subsequently, low density substrates were prepared with the objective of moving towards single particle imaging. For this purpose, the centrifuged solution prepared before was diluted 10 times and 5 µL of this solution was dropped onto a O_2 plasma treated cover

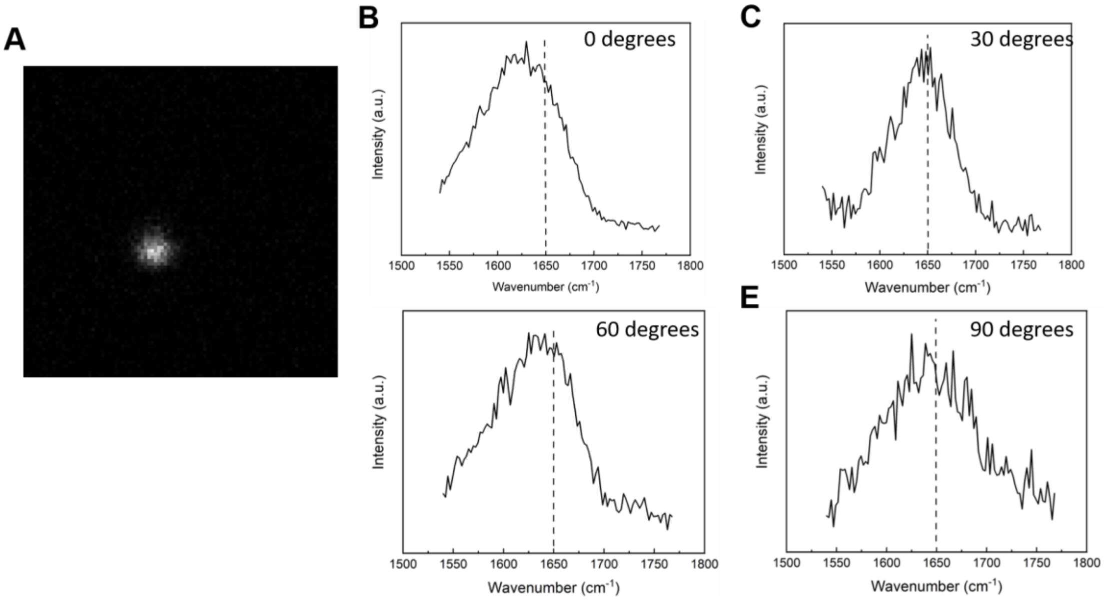

Figure 4.9: (A) Four wave mixing image of the particle whose spectrum is taken. (B)-(E) CARS spectra of the same particle with different polarizations of the incident light, as mentioned in the legend. Laser conditions were: pump-888 nm wavelength,100 μW power; Stoke's-1040 nm wavelength, 50 µW power.

glass substrate and blown off with a N_2 gun after 30 seconds. Figure 4.9 shows the CARS results obtained with the (100,20) NS. This NS was chosen due to better matching with the laser excitations used in CARS as well as the stronger results obtained. Figure 4.9A shows the four-wave mixed image of the NS whose data is being taken. As the diffraction limit is 500 nm and the size of the particle observed is also around that size (2x times the size of the NS), it was unsure whether the particle observed was single or a dimer. Figure 4.9B shows the CARS spectrum of the Rh-800 molecule, being centered around the 1650 cm^{-1} peak. To determine whether the particle is single or a dimer, different polarizations of the incident light were used with the objective that the signal would not depend on the polarization if it's a single particle. If it is a dimer, however, the signal will change depending on whether the exciting electric fields are along the line joining the two particle centers or perpendicular to this line. It was observed that when the polarization of the incident light was changed, the signal did change, with the most reliable peak observed being at a 30 degrees polarization. Thus, the particle being observed here is a dimer. Further testing of these NS always showed that signals obtained were usually from dimers, and not from single NS. This is most likely due to a gap enhanced plasmon resonance, which yields a very strong hot spot when a molecule is trapped between two plasmonic NPs. Thus, the NS is capable of producing CARS signals for the molecules when in a dimer configuration, and such a structure can be used for sensing.

CHAPTER FIVE: SUMMARY AND BROADER OUTLOOK

Section One: Summary

In conclusion, this dissertation provides a theoretical and experiment outlook of CMS NWs and CMS NPs and shows their benefits towards improving the performance of opto-electronic devices and sensing. Chapter 1 provides the motivation for the use of CMS nanostructures. It provides an outlook of nanoplasmonics and describes how plasmonics can be used to improve the optical performance of different devices. It also describes the advantage of using CS nanostructures with a core plasmonic layer and an outer semiconductor shell in order to improve optical properties of the semiconductor. It subsequently introduces the concept of plasmon hybridization in CSS nanostructures and the double resonance feature which can be used. It also introduces the concept of emerging plasmonic materials like TiN and ZrN, which can be used instead of the traditional plasmonic materials like Au and Ag.

Chapter 2 summarizes the theoretical outlook of using CMS NWs for improving opto-electronic device performance, specifically WLEDs and photodetectors, and also gives the methodology towards preparing such CMS NWs. In the first section, the methodology for computing the emission of CMS NWs was presented. A Green's function methodology to define the PF as a measure of emission was used. In section two, the absorption and scattering using a Mie formalism was presented. Section three showed the use of such CMS NWs for WLEDs. We show that both the emission and absorption of CS nanowires are significantly improved than those of bare semiconductor nanowires. The PF shows an improvement as high as 5 times for a CdSe based red phosphor, while the absorption efficiency shows a 55.7 times improvement for the CdSe based red phosphor. We have combined the PF and the absorption to define the EQE per dipole moment, which was used to determine the overall performance of these phosphors. The EQE of CS nanowires has been shown to have marked improvements over the bare semiconductor nanowire, with the maximum enhancement being 10.8 times for CdSe-based red-emitting nanowires, and as high as 15866 times for GaP-based green-emitting nanowires. We established the methodology combining the concept of CS structures and the tunability of their optical properties through varying of the dimensions of the different layers involved, and demonstrated the optimal performance through identifying best material combination and dimensions considering four different semiconductors (CdSe, CdTe, GaP, CdS) and Ce-doped YAG and four different plasmonic metals (Ag, Au, Al, Cu). We have also shown that CSS semiconductor-metal-semiconductor NWs show even better performances. For example, for CdSe-based CSS, 60% improvement is achieved over the best CS EQE value and for YAG-based CSS NWs, the improvement is 3 times larger over CS NWs. Particularly, we found that the optimal performance was not from CSS configurations with plasmon hybridization with the two resonant peaks overlapping the absorption and emission wavelengths, but from those configurations which had low enough inner shell thicknesses. The thin inner shells allowed the large fields at the core-inner shell interface to penetrate the shell and affect the fields in the outer shell. In section four, the use of CS nanostructures as a plasmonic cloak has been demonstrated. In particular, emerging plasmonic material ZrN has been shown to act as a plasmonic cloak, cancelling the scattering of a silicon nanowire. ZrN cloaks a silicon nanowire without substantially compromising the absorption, resulting in a less-intrusive, better performing silicon nanowire photosensor. Additionally, we have compared the performance to a traditional plasmonic material Au and have shown that ZrN cloaks far better in terms of scattering cancellation in the wavelength region of 400-500 nm, with the performance becoming comparable at 550 nm, where after a Au cloak performs better in the regime of 600-700 nm. We also observed, through absorption efficiency calculations, the absorption of the photosensor across the visible spectrum increases, while still maintaining high absorption in the silicon core to produce photocurrent, for both ZrN and Au cloaks. We used a figure of merit to incorporate both the absorption and scattering efficiencies and showed that a ZrN cloak has a higher FOM value than a Au cloak in the wavelength region of 400-500 nm, with the highest value being 2.95 at 500 nm. A Au cloak however performs better in the wavelength region of 600-700 nm, with the highest value being 17.69 at 650 nm. The dimensions and materials for the plasmonic cloaks have also been included for the wavelength region of 400-650 nm. In section five, the fabrication methodology for the CMS NWs has been described. A LPNE method for fabrication of the metal core, a ED method for formation of the semiconductor outer shell, and an ALD method for fabrication of a plasmonic TiN layer has been demonstrated here.

In Chapter 3, the use of plasmonic CSS NPs for improving the photocatalytic activity of hematite has been demonstrated. CSS NPs have been shown for the first time to be an efficient plasmonic system which can be used to improve the photocurrent response of hematite nanostructured photoanodes. We have shown that CSS NPs can substantially improve the hematite photocurrent density in two different architectures, one where the

NPs have been embedded in the hematite and the other where the NPs have been deposited on the top. Unique plasmonic properties of CSS NPs indicated by simulation provides rationales on why they can be strong candidates for improving semiconductor photoanodes for PEC water splitting. The simulation results demonstrate three unique features of CSS NPs. Firstly, the resonant wavelengths of the two plasmonic absorption peaks are highly tunable based on the dimensions. As a representative example, the higher wavelength resonance peak can be tuned from 600 nm to 1000 nm by changing the inner core radius from 10 nm to 60 nm while keeping the inner shell and outer shell thicknesses fixed at 20 nm. The lower wavelength resonance peak can vary between 540 nm and 700 nm under similar dimensional considerations. Secondly, by tuning the dimensions of each layer of the CSS NPs, the plasmonic peaks can be made to have strong scattering effects or strong absorption effects, thereby optimizing the optical and electrical contributions to the PEC activity of hematite, as mentioned earlier. Finally, spatially uniform electric field distributions of 20-25 nm from the outer surface of the CSS NPs offers potential to increase carrier generation when incorporated in a photoanode. We have shown two different architectures of NP-hematite heterostructure and have shown that in the top-down architecture, the CSS NPs improve the photocurrent density from the bare hematite by 0.6 mA/cm^2, whereas Au NPs can improve only by 0.36 mA/cm^2. However, the difference is much greater in the embedded architecture where the CSS NPs improve the performance of hematite, on an average, by a factor greater than 8 times when compared to Au NPs. Our best optimized embedded structure increases bare hematite photocurrent performance by over 3 times to a photocurrent of 3.0 mA/cm^2, a total increase of 2.18 mA/cm^2.

Additionally, we have demonstrated the versatility of the CSS NPs with other known methods for improvement in PEC performance by using a Co-Pi co-catalytic overlayer on the CSS/hematite heterostructures. We have achieved a photocurrent density value of 3.40 mA/cm^2 at 1.23 V vs RHE with the top-deposited architecture using a Co-Pi overlayer, which is an improvement of 1.81 mA/cm^2 from the bare hematite, and a photocurrent density value of 4.10 mA/cm^2 at 1.23 V vs RHE with the embedded architecture using a Co-Pi overlayer, which is an improvement of 2.83 mA/cm^2 from the bare hematite.

Finally, in Chapter 4, the use of plasmonic CSS NPs and NS for sensing has been shown. In particular, Raman spectroscopy was used as the guiding method for determining the feasibility of the plasmonic NPs as biosensors. The methodology for fabrication of the NS was described in detail. The EFs from SERS for the Rh-800 molecule using CSS NPs was determined to be ~10^5 while that for the NS was ~10^7. The greater EF for the NS was due to their stronger scattering/absorption ratio as compared to CSS NPs.This is for a high-density particle substrate. Moving towards single particle imaging, CARS was used due to the greater usefulness for bioimaging because of the faster acquisition times. It was found that though CSS NPs did not give a strong enough signal for single particles, a good signal was obtained for dimer NS. This shows the feasibility of use of such NS towards single particle ultra-fast sensing.

Section Two: Broader Outlook

We believe the concept of CS and CSS NWs and the tunability of its optical properties through varying the dimension can be used to improve the optical properties of the semiconductor in other nanowire based photonic devices, such as NW lasers. The optical enhancement conditions for the plasmonic component of the NW laser can be tuned to match the emission of the semiconductor material and subsequently a much greater optical gain can be achieved. Additionally, alternative plasmonic materials such as ZrN have the potential to be used as better plasmonic cloaks than traditional metals. Due to the tunability of the optical properties of these alternative materials the magnitude of the permittivity can be controlled to best match the desired to-be cloaked core to cancel scattering. Our data indicates that alternative plasmonic materials can be used to improve the measurements of near-field probing and nanoscopic imaging nanowire photosensors.

The novel CSS NPs have pushed the performance of hematite well beyond any previously reported system employing plasmonics. Our CSS-photoanode design can be potentially generalized for all the before mentioned semiconductors, making it a universal approach for optimizing photoanode performance and hence identifying the best performing design and combination. While Au@SiO2@Au is ideal for hematite, TiO_2, WO_3, and $BiVO_4$ can benefit from a Ag@SiO2@Ag or Au@SiO2@Ag design. Additionally, this design also allows us to test emerging plasmonic metamaterials such as Titanium Nitride (TiN) with the CSS-photoanode architecture. TiN has been shown to have favorable absorption in the visible range, with one TiN/Au/TiN planar architecture reporting broadband absorption from 400-800 nm. Given the tunability and unique field distributions of the CSS architecture, TiN@SiO2@TiN structures could be tuned to enhance most photoanode materials. The use of such plasmonic CMS NPs towards single particle sensing by varying the design of the structure (CSS vs NS, sharper features vs rounded features) has also been shown. Though single particle bioimaging could not be achieved here, we believe that further optimization and tuning can further enhance the optical performance of the NS presented, and as a result help in single particle imaging.

APPENDIX A: MATLAB CODE FOR COMPUTING LDOS OF CMS NWS

- **Main code:**

```
%%%%%NWldos.m%%%%%%%
clear all;
clc;
%%ver1.1 corrected for the weird curves
%%Code calculate the LDOS and Purcell Enhancement for Nanowires
%%Assumptions: cylinder is of infinite length; homogenous materials
%%The dipole source at 'rs' is moved along x axis for simplicity (i.e
beta
%%= 0). Due to azimuthal symmetry, dipole on x axis provides complete
%%information of the LDOS.
%%%%%%Constants%%%%%%%%%%%%%%%%%%%%%%%%%%%%%%%%%%%%%%%%%%
e_0=8.8542e-12; %permitivity of free space
u_0=1.2566e-6; %permeability of free space
c_light=1/sqrt(e_0*u_0);%speed of light
hbar=1.055e-34; %Planck's constant
kb=1.38e-23;%Boltzmann constant
%%%%%%%%%%%%%%%%%%%%%%%%%%%%%%%%%%%%%%%%%%%%%%%%%%%%%%

%%%%%%Optical Data for Si%%%%%%%%%%%%%%%%%%%%%%%%%%%%%%%%%%%%%%%%%%
%L=530;%wavelength of light
%L1=L*1e-9;

%w=2*pi*c_light./L1;
%e_1=e_0;
%e_2=e_0;
%Lambda=xlsread('nh-si.xlsx','A2:A62');
ersi=xlsread('nh-si.xlsx','B2:B62'); %real part of dielectric const
eisi=xlsread('nh-si.xlsx','C2:C62'); %imag part
%e_si=ersi+1i*eisi;
%%%%%%%%%%%%%%%%%%%%%%%%%%%%%%%%%%%%%%%%%%%%%%%%%%%%%%
% %%%%%%Optical Data for aSi%%%%%%%%%%%%%%%%%%%%%%%%%%%%%%%%%%%%%%%%%%
% erasi=xlsread('nh-asi.xlsx','B2:B31'); %real part of dielectric const
% eiasi=xlsread('nh-asi.xlsx','C2:C31'); %imag part
% e_asi=erasi+1i*eiasi;
% %%%%%%%%%%%%%%%%%%%%%%%%%%%%%%%%%%%%%%%%%%%%%%%%%%%%%%
% %%%%%%Optical Data for
Fe2O3%%%%%%%%%%%%%%%%%%%%%%%%%%%%%%%%%%%%%%%%%%
%erfe2o3=xlsread('fe2o3.xlsx','B2:B62'); %real part of dielectric const
%eife2o3=xlsread('fe2o3.xlsx','C2:C62'); %imag part
% e_fe2o3=erfe2o3+1i*eife2o3;
% %%%%%%%%%%%%%%%%%%%%%%%%%%%%%%%%%%%%%%%%%%%%%%%%%%%%%%
% %%%%%%Optical Data for Cu%%%%%%
 ercu=xlsread('nh-cu.xlsx','B2:B72'); %real part of dielectric const
 eicu=xlsread('nh-cu.xlsx','C2:C72'); %imag part
% e_cu=ercu+1i*eicu;
% %%%%%%%%%%%%%%%%%%
```

```
% %%%%%%Optical Data for Cu2o%%%%%%
% ercu2o=xlsread('nh-cu2o.xlsx','B2:B72'); %real part of dielectric
const
% eicu2o=xlsread('nh-cu2o.xlsx','C2:C72'); %imag part
% e_cu2o=ercu2o+1i*eicu2o;
% %%%%%%%%%%%%%%%%%
% %%%%%%Optical Data for TiO2%%%%%%%%%%%%%%%%%%%%%%%%%%%%%%%%%%%%%%%%%%
% ertio2=xlsread('nh-tio2.xlsx','B2:B72'); %real part of dielectric
const
% eitio2=xlsread('nh-tio2.xlsx','C2:C72'); %imag part
% e_tio2=ertio2+1i*eitio2;
% %%%%%%%%%%%%%%%%%%

%%%%%%%%%%%Optical Data for CdSe
ercdse=xlsread('nh-CdSe.xlsx','B12:B48'); %real part of dielectric
const
eicdse=xlsread('nh-CdSe.xlsx','C12:C48'); %imag part
% e_cdse=ercdse+1i*eicdse;
% % %%%%%%Optical Data for Ge%%%%%%%%%%%%%%%%%%%%%%%%%%%%%%%%%%%%%%%%%%
% % erge=xlsread('nh-ge.xlsx','B2:B72'); %real part of dielectric const
% % eige=xlsread('nh-ge.xlsx','C2:C72'); %imag part
% % e_ge=erge+1i*eige;
% % %%%%%%%%%%%%%%%%%%
%%%%%%Optical Data for Au%%%%%%%%%%%%%%%%%%%%%%%%%%%%%%%%%%%%%%%%%%
%Lambda=xlsread('nh-au.xlsx','A2:A72');
erau=xlsread('nh-au.xlsx','B12:B48'); %real part of dielectric const
eiau=xlsread('nh-au.xlsx','C12:C48'); %imag part
%Lambda=sort(Lambda);
%Lambda1=find(Lambda==L);

%e_1=(erau(Lambda1)+1i*eiau(Lambda1))*e_0;
%%%%%%%%%%%%%%%%%%
%%%%%%Optical Data for Ag%%%%%%%%%%%%%%%%%%%%%%%%%%%%%%%%%%%%%%%%%%
Lambda=xlsread('nh-ag.xlsx','A2:A72');
erag=xlsread('nh-ag.xlsx','B2:B72'); %real part of dielectric const
eiag=xlsread('nh-ag.xlsx','C2:C72'); %imag part

%%%%%%%%%%%%%%%%%%
%%%%%%Optical Data for Al%%%%%%%%%%%%%%%%%%%%%%%%%%%%%%%%%%%%%%%%%%
%eral=xlsread('nh-al.xlsx','B2:B172'); %real part of dielectric const
%eial=xlsread('nh-al.xlsx','C2:C172'); %imag part
%e_al=eral+1i*eial;
%%%%%%%%%%%%%%%%%%
% %%%%%%Optical Data for
CuInSe2%%%%%%%%%%%%%%%%%%%%%%%%%%%%%%%%%%%%%%%%%%
% ercuinse2_p=xlsread('cuinse2.xlsx','B2:B72'); %real part of
dielectric const for perpendicular
% eicuinse2_p=xlsread('cuinse2.xlsx','C2:C72'); %imag part
% e_cuinse2_p=ercuinse2_p+1i*eicuinse2_p;
% ercuinse2_l=xlsread('cuinse2.xlsx','D2:D72'); %real part of
dielectric const for perpendicular
% eicuinse2_l=xlsread('cuinse2.xlsx','E2:E72'); %imag part
% e_cuinse2_l=ercuinse2_l+1i*eicuinse2_l;
```

```
% %%%%%%%%%%%%%%%%%%
%%%%%%Optical Data for CdTe%%%%%%%%%%%%%%%%%%%%%%%%%%%%%%%%%%%%%%%%%%
ercdte=xlsread('nh-cdte.xlsx','B2:C72'); %real part of dielectric const
eicdte=xlsread('nh-cdte.xlsx','C2:C72'); %imag part
%e_cdte=ercdte+1i*eicdte;
%%%%%%Optical Data for YAG%%%%%%%%%%%%%%%%%%%%%%%%%%%%%%%%%%%%%%%%%%
eryag=xlsread('yag.xlsx','B12:B40'); %real part of dielectric const
eiyag=xlsread('yag.xlsx','C12:C40'); %imag part
%e_cdte=ercdte+1i*eicdte;

% %%%%%%Optical Data for Ni%%%%%%%%%%%%%%%%%%%%%%%%%%%%%%%%%%%%%%%%%%
% erni=xlsread('nh-ni.xlsx','B2:B32'); %real part of dielectric const
% eini=xlsread('nh-ni.xlsx','C2:C32'); %imag part
% e_ni=erni+1i*eini;
%%%%%%%%%%%%%%%%%%
% %%%%%%Optical Data for GaP%%%%%%%%%%%%%%%%%%%%%%%%%%%%%%%%%%%%%%%%%%
ergap=xlsread('nh-gap.xlsx','B2:B72'); %real part of dielectric const
eigap=xlsread('nh-gap.xlsx','C2:C72'); %imag part
e_gap=ergap+1i*eigap;
% %%%%%%%%%%%%%%%%%%
% %%%%%%Optical Data for
Silica%%%%%%%%%%%%%%%%%%%%%%%%%%%%%%%%%%%%%%%%%%
% n_silica=1.54*ones(71,1);
%e_silica=(3.9)*ones(71,1);
% %%%%%%%%%%%%%%%%%%
%%%%%%Optical Data for GaSb%%%%%%
% ergasb=xlsread('nh-gasb.xlsx','B2:B32'); %real part of dielectric
const
% eigasb=xlsread('nh-gasb.xlsx','C2:C32'); %imag part
% e_gasb=ergasb+1i*eigasb;
%%%%%%%%%%%%%%%%%%
%%%%%%Optical Data for ZnS%%%%%%
%erzns=xlsread('nh-ZnS.xlsx','B2:B102'); %real part of dielectric const
%eizns=xlsread('nh-ZnS.xlsx','C2:C102'); %imag part
% e_zns=erzns+1i*zns;
%%%%%%%%%%%%%%%%%%%%%%%%%%%%
%%%%%%Optical Data for ZnSe%%%%%%
%erznse=xlsread('nh-ZnSe.xlsx','B2:B102'); %real part of dielectric
const
%eiznse=xlsread('nh-ZnSe.xlsx','C2:C102'); %imag part
% e_zns=erzns+1i*zns;
%%%%%%%%%%%%%%%%%%
%e_al2o3=2.777*ones(31,1);
%%%%%%%%%%%%%%%%%%%%%%%%%%%%%%%%%%%%%%%%%%%%%%%%%%%%%%%%%%%%%%%%%%%%%%%
%
%%%%%Optical Data for 1.5G
Sun%%%%%%%%%%%%%%%%%%%%%%%%%%%%%%%%%%%%%%%%%%
% amL=xlsread('am15g.xlsx','A3:A900')*1e-9; %real part of dielectric
const
% amG=xlsread('am15g.xlsx','C3:C900'); %imag part
% for lcount=1:length(L)
% %     am15L(lcount)=amL(amL==L(lcount));
%     am15G(lcount)=amG(amL==L(lcount));
```

```
% end
% am15G=am15G';
%%%%%%%%%%%%%%%%%%%%%%%%%%%%%%%%%%%%%%%%%%%%%%%%%%%%%
%%%%%%%Defining dielectric layers and velocities%%%%%%%

eta0=sqrt(e_0/u_0);
%eta1=sqrt(e_1/u_0);
%eta2=sqrt(e_2/u_0);
%eta3=eta0;
%eta4=eta0;

vel0=sqrt(1/(e_0*u_0));
%vel1=sqrt(1/(e_1*u_0));
%vel2=sqrt(1/(e_2*u_0));
%vel3=vel0;
%vel4=vel0;

%%%%%Input variables; SourceDir defines direction of source, 1==x,
2==y,
%%%%%3==z;Radius gives an array of the number of layers from core
outwards,
%%%%%Eta gives the array for etas from core outwards%%%%%%%%%%%%

Type='1';%%%2 gives LDOS and Purcell Factor for varying dipole source
locations
         %%%3 plots LDOS and PF as a function of wavelength at a given
rs
         %%%4 plots the LDOS as a contour plot for varying R1 and R2
         %%%5 varies core and shell radii for a fixed rs and wavelength
         %%%6 varies wavelength and rs for a fixed radius%%%%%%%%
Radius=[25*1e-9];
Etafs=[eta0 eta0];%free space only
nb=[sqrt(e_0/e_0) sqrt(e_0/e_0)];%refractive index of background
nb_fs=[sqrt(e_0/e_0) sqrt(e_0/e_0)];
Epsilon_fs=[e_0 e_0];
%k_fs=[w/vel0 w/vel0];

M=length(Radius);%calculates number of layers

if strcmp(Type, '1')

    rs=26*1e-9:0.5e-9:126*1e-9;
    ldos=zeros(length(rs),1);
    ldosfs=zeros(length(rs),1);
    PF=zeros(length(rs),1);
    L=710;%wavelength of light
    L1=L*1e-9;
    Lambda1=find(Lambda==L);
    w=2*pi*c_light./L1;
    e_1=(erag(L==Lambda)+1i*eiag(L==Lambda))*e_0;
    %e_2=(erau(L==Lambda)+1i*eiau(L==Lambda))*e_0;
   % e_3=(ercdse(L==Lambda)+1i*eicdse(L==Lambda))*e_0;
```

```
    eta1=sqrt(e_1/u_0);
    %eta2=sqrt(e_2/u_0);
    %eta3=sqrt(e_3/u_0);
    Eta=[eta1 eta0];
    Vel=[1/sqrt(e_1*u_0) vel0];
    k=[w/Vel(1) w/Vel(2)];
    k_fs=[w/vel0 w/vel0];
    Epsilon=[e_1 e_0];


    for i=1:length(rs)

            ldos(i)=Qldos4(M,rs(i),Radius,Eta,k,w,c_light,Epsilon,nb);

ldosfs(i)=Qldos4(M,rs(i),Radius,Etafs,k_fs,w,c_light,Epsilon_fs,nb_fs);
            PF(i)=ldos(i)/ldosfs(i);

    end

    %%%%%%plot for LDOS%%%%%
    figure
    plot (rs*1e9,ldos)
    title('LDOS')
    xlabel('rs(nm)')
    ylabel('LDOS')

    %%%%%%%plot for Purcell Factor%%%%%
    figure
    plot (rs*1e9,PF)
    title('Purcell Factor')
    xlabel('rs(nm)')
    ylabel('PF')
%%%%%%%%%%%%%%%%%%%%%%%%%%%%%%%%%%%%%%%%%%%%%%%%%%%%%%%%%%%%%%%

elseif strcmp(Type,'2')
        L=400:10:760;%wavelength of light
        L1=L*1e-9;
        rs=10.1*1e-9:0.1*1e-9:25*1e-9;
        ldos=zeros(length(rs),1);
        dos=zeros(length(rs),1);
        ldosfs=zeros(length(rs),1);
        PF1=zeros(length(rs),1);
        PF=zeros(length(L1),1);
        Therm=zeros(length(L1),1);
        %e0=zeros(length(L1),1);
        e_1=zeros(length(L1),1);
        e_2=zeros(length(L1),1);
        %e_3=zeros(length(L1),1);
        %T=300;
        i=1;
```

```
        for L=400:10:760
            e_1(i)=(1i*eiau(L==Lambda))*e_0;
            e_2(i)=(ercdse(L==Lambda)+1i*eicdse(L==Lambda))*e_0;
            %e_3(i)=(ercdse(L==Lambda)+1i*eicdse(L==Lambda))*e_0;
            i=i+1;
        end

        for i=1:length(L1)
        for k1=1:length(rs)
            w=2*pi*c_light./L1(i);
            Vel=[1/sqrt((e_1(i))*u_0) 1/sqrt((e_2(i))*u_0) vel0];
            %k=[w(i)/Vel(1) w(i)/Vel(2)];
            Eta=[sqrt(e_1(i)/u_0) sqrt(e_2(i)/u_0) sqrt(e_0/u_0)];
            k=[w/Vel(1) w/Vel(2) w/Vel(3)];
            k_fs=[w/vel0 w/vel0 w/vel0];
            Epsilon=[e_1(i) e_2(i) e_0];

ldos(k1)=Qldos4(M,rs(k1),Radius,Eta,k,w,c_light,Epsilon,nb);
            dos(k1)=ldos(k1)*2*3.14159*rs(k1)*0.1*1e-9;

ldosfs(k1)=Qldos4(M,rs(k1),Radius,Etafs,k_fs,w,c_light,Epsilon_fs,nb_fs
);
            PF1(k1)=dos(k1)/(ldosfs(k1)*(3.14159*((Radius(2))^2-
(Radius(1))^2)));

        end
        PF(i)=sum(PF1);
        %Therm(i)=(sum(dos)*hbar*w/((exp(hbar*w/(T*kb)-
1)))*(4*3.1415));
        end

    %%%%%%plot for LDOS%%%%%
    %figure
    %plot (L1*1e9,ldos)
    %title('LDOS')
    %xlabel('L(nm)')
    %ylabel('LDOS')

    %%%%%%%plot for Purcell Factor%%%%%
    figure
    plot (L1*1e9,PF)
    title('Purcell Factor')
    xlabel('L(nm)')
    ylabel('PF')
%%%%%%%%%%%%%%%%%%%%%%%%%%%%%%%%%%%%%%%%%%%%%%%%%%%%%%%%%%%%%%%

elseif strcmp(Type,'3')

        L=300:10:730;%wavelength of light
        L1=L*1e-9;
        R1=10*1e-9:5*1e-9:80*1e-9;
        R2=zeros(length(R1),1);
```

```
        %rs=zeros(length(R1),1);
        %ldos=zeros(length(R1),length(L1));
        %ldosfs=zeros(length(R1),length(L1));
        PF=zeros(length(R1),length(L1));
        %e0=zeros(length(L1),1);
        e_1=zeros(length(L1),1);
        e_2=zeros(length(L1),1);
        i=1;



        for L=300:10:730
            e_1(i)=(erau(L==Lambda)+1i*eiau(L==Lambda))*e_0;
            e_2(i)=(ercdse(L==Lambda)+1i*eicdse(L==Lambda))*e_0;
            i=i+1;
        end
        for j=1:length(R1)
            R2(j)=R1(j)+50*1e-9;
            rs=R1(j)+1.5*1e-9:0.5*1e-9:(R2(j)-0.5*1e-9);
            PF1=zeros(length(rs),1);
            ldos=zeros(length(rs),1);
            ldosfs=zeros(length(rs),1);
            Radius=[R1(j) R2(j)];
            M=length(Radius);
         for i=1:length(L1)
            w=2*pi*c_light./L1(i);
            Vel=[1/sqrt((e_1(i))*u_0) 1/sqrt((e_2(i))*u_0) vel0];
            %k=[w(i)/Vel(1) w(i)/Vel(2)];
            Eta=[sqrt(e_1(i)/u_0) sqrt(e_2(i)/u_0) sqrt(e_0/u_0)];
            k=[w/Vel(1) w/Vel(2) w/Vel(3)];
            k_fs=[w/vel0 w/vel0 w/vel0];
            %k_fs=[w/vel0 w/vel0];
            Epsilon=[e_1(i) e_2(i) e_0];
            for k1=1:length(rs)
            ldos(k1)=Qldos4(M,rs(k1),[R1(j)
R2(j)],Eta,k,w,c_light,Epsilon,nb);
            ldosfs(k1)=Qldos4(M,rs(k1),[R1(j)
R2(j)],Etafs,k_fs,w,c_light,Epsilon_fs,nb_fs);
            PF1(k1)=(ldos(k1)/ldosfs(k1));
            end
             PF(j,i)=sum(PF1);
         end
        end
     %plot contour for ldos
     %figure, contourf(L1*1e9, R1*1e9,ldos, 200 ,'LineColor','none'),
colorbar;
     %set(gca,'FontWeight','bold','FontSize',14);
     %title('ldos');
     %xlabel('L(nm)')
     %ylabel('Core thickness(nm)')
     %plot contour for PF
     figure, contourf(L1*1e9, R1*1e9,PF, 200 ,'LineColor','none'),
colorbar;
     set(gca,'FontWeight','bold','FontSize',14);
```

```
     %caxis([0 100]);
     title('Purcell factor');
     xlabel('Wavelength(nm)')
     ylabel('Core thickness(nm)')

elseif strcmp(Type,'4')

    L=710;
    L1=L*1e-9;
    Radius=[0 0];
    M=length(Radius);
    R1=10*1e-9:5*1e-9:100*1e-9;
    R2=5*1e-9:5*1e-9:50*1e-9;
    ldos=zeros(length(R1),length(R2));
    ldosfs=zeros(length(R1),length(R2));
    PF=zeros(length(R1),length(R2));
    Lambda1=find(Lambda==L);
    w=2*pi*c_light./L1;
    e_1=(ercu(Lambda1)+1i*eicu(Lambda1))*e_0;
    e_2=(ercdse(Lambda1)+1i*eicdse(Lambda1))*e_0;
    Vel=[1/sqrt((e_1)*u_0) 1/sqrt((e_2)*u_0) vel0];
    Eta=[sqrt(e_1/u_0) sqrt(e_2/u_0) sqrt(e_0/u_0)];
    k=[w/Vel(1) w/Vel(2) w/Vel(3)];
    k_fs=[w/vel0 w/vel0 w/vel0];
    Epsilon=[e_1 e_2 e_0];

        for j=1:length(R1)
         for i=1:length(R2)
            Radius=[R1(j) R1(j)+R2(i)];
            ldos(j,i)=Qldos4(M,R1(j)+R2(i)-0.5*1e-
9,Radius,Eta,k,w,c_light,Epsilon,nb);
            ldosfs(j,i)=Qldos4(M,R1(j)+R2(i)-0.5*1e-
9,Radius,Etafs,k_fs,w,c_light,Epsilon_fs,nb_fs);
            PF(j,i)=ldos(j,i)/ldosfs(j,i);
         end
        end



    %plot contour for ldos
     %figure, contourf(R2*1e9, R1*1e9,ldos, 200 ,'LineColor','none'),
colorbar;
     %set(gca,'FontWeight','bold','FontSize',14);
     %title('ldos');
     %xlabel('Shell thickness(nm)')
     %ylabel('Core radius(nm)')
     %plot contour for PF
     figure, contourf(R2*1e9, R1*1e9,PF, 200 ,'LineColor','none'),
colorbar;
     set(gca,'FontWeight','bold','FontSize',14);
     title('Purcell factor');
     xlabel('Shell thickness(nm)')
     ylabel('Core radius(nm)')
```

```
    elseif strcmp(Type,'5')

        L=300:10:730;%wavelength of light
        L1=L*1e-9;
        rs=(Radius(1)+10*1e-9):1e-9:(Radius(2)+5*1e-9);
        ldos=zeros(length(rs),length(L1));
        ldosfs=zeros(length(rs),length(L1));
        PF=zeros(length(rs),length(L1));
        %e0=zeros(length(L1),1);
        e_1=zeros(length(L1),1);
        e_2=zeros(length(L1),1);
        i=1;



        for L=300:10:900
            e_1(i)=(erag(L==Lambda)+1i*eiag(L==Lambda))*e_0;
            e_2(i)=(ercdse(L==Lambda)+1i*eicdse(L==Lambda))*e_0;
            i=i+1;
        end

         for i=1:length(L1)
             for j=1:length(rs)
            w=2*pi*c_light./L1(i);
            Vel=[1/sqrt((e_1(i))*u_0) 1/sqrt((e_2(i))*u_0) vel0];
            %k=[w(i)/Vel(1) w(i)/Vel(2)];
            Eta=[sqrt(e_1(i)/u_0) sqrt(e_2(i)/u_0) sqrt(e_0/u_0)];
            k=[w/Vel(1) w/Vel(2) w/Vel(3)];
            k_fs=[w/vel0 w/vel0 w/vel0];
            %k_fs=[w/vel0 w/vel0];
            Epsilon=[e_1(i) e_2(i) e_0];

ldos(j,i)=Qldos4(M,rs(j),Radius,Eta,k,w,c_light,Epsilon,nb);

ldosfs(j,i)=Qldos4(M,rs(j),Radius,Etafs,k_fs,w,c_light,Epsilon_fs,nb_fs
);
            PF(j,i)=ldos(j,i)/ldosfs(j,i);
            end
        end
     %plot contour for ldos
     %figure, contourf(L1*1e9, R1*1e9,ldos, 200 ,'LineColor','none'),
colorbar;
     %set(gca,'FontWeight','bold','FontSize',14);
     %title('ldos');
     %xlabel('L(nm)')
     %ylabel('Core thickness(nm)')
     %plot contour for PF
     figure, contourf(L1*1e9, rs*1e9,PF, 200 ,'LineColor','none'),
colorbar;
     set(gca,'FontWeight','bold','FontSize',14);
     title('Purcell factor');
     xlabel('Wavelength(nm)')
     ylabel('Radial position(nm)')
```

```
end
```

➢ Function QLDOS4:

```
 function [ldos]=Qldos4(M,rs,Radius,Eta,k,w,c_light,Epsilon,nb)
%%%%%%function calculates PF and ldos; m=1 is core and m=2 is cs%%%%

%%%%%%Constants%%%%%%%%%%%%%%%%%%%%%%%%%%%%%%%%%%%%%%%%%%%
nmax=30;
u_0=1.2566e-6;

%%find layer which contains source%%
rtemp=[Radius rs];
rtemp=sort(rtemp);
taker=find(rtemp==rs);


if M==1 %Single NW

    Bz=0;
    Ez=0;
    Bxr=0;
    TExr=0;
    %Ex=0;
    Byp=0;
    TEyp=0;
    %Ey=0;

         if eq(taker,1)%source inside NW


                [Anx,Any,Anz]=GC3(w,u_0,M,Eta,taker,k,Radius,rs,nmax);

                for n=-nmax:nmax
                    %%Green's function calculation
                    %Bz=Bz+(1/4i).*besselh(n,1,k(1)*rs).*besselj(n,k(1)
.*rs);%r<rs
                    Bz = Bz-
(w*u_0/4).*besselj(n,k(1)*rs).*besselh(n,1,k(1).*rs);%r>rs

                end

                %Ez(r<=Radius(M))=Bz(r<=Radius(M));

                for n=-nmax:nmax
                    nc=n+nmax+1;
                    %%%%%%E%%%%%%%
                    Ez = Ez +Anz(nc,2).*besselj(n,k(1).*rs);
                    %Ez = Ez - Anz(nc,1).*besselh(n,k(2).*rs);
```

```
                end
                TM=(Ez+Bz)/(-1i.*w.*u_0);

                for n=-nmax:nmax
                    %%Green's function calculation
                    %Bx(r<=rs) =
Bx(r<=rs)+(1i*Eta(1)/8).*exp(1i*n*phi(r<=rs)).*(besselh(n-
1,k(1)*rs)+besselh(n+1,k(1)*rs)).*besselj(n,k(1).*r(r<=rs));%r<rs
                    %Bx= Bx+(1i*Eta(1)/8).*(besselj(n-
1,k(1)*rs)+besselj(n+1,k(1)*rs)).*besselh(n,1,k(1).*rs);%r>rs
                        %Bxr = Bxr+(1i*Eta(1)/8).*(besselh(n-
1,k(1)*rs)+besselh(n+1,k(1)*rs)).*besselj(n,k(1).*rs).*1i.*n;%r<rs
                        Bxr = Bxr+(k(1)/8).*(besselj(n-
1,k(1)*rs)+besselj(n+1,k(1)*rs)).*(besselh(n-
1,k(1).*rs)+besselh(n+1,k(1).*rs)).*0.5.*1i;%r>rs
                    %Bxp(r<=rs)=Bxp(r<=rs)-
(1i*Eta(1)/8).*exp(1i*n*phi(r<=rs)).*(besselh(n-
1,k(1)*rs)+besselh(n+1,k(1)*rs)).*0.5.*(besselj(n-1,k(1).*r(r<=rs))-
besselj(n+1,k(1).*r(r<=rs)));
                    %Bxp(r>rs)=Bxp(r>rs)-
(1i*Eta(1)/8).*exp(1i*n*phi(r>rs)).*(besselj(n-
1,k(1)*rs)+besselj(n+1,k(1)*rs)).*0.5.*(besselh(n-1,k(1).*r(r>rs))-
besselh(n+1,k(1).*r(r>rs)));
                end

                    %Ex(r<=Radius(M))=Bx(r<=Radius(M));
                    Bxr=Bxr.*(1i/(w.*Epsilon(1))).*k(1);
                    %TExp(r<=Radius(M))=Bxp(r<=Radius(M)).*1i./(w.*Eta(
1)).*k(1);

                    for n=-nmax:nmax
                        nc=n+nmax+1;

                        %Ex(r<=Radius(M)) = Ex(r<=Radius(M))
+Anx(nc,2).*besselj(n,k(1).*r(r<=Radius(M))).*exp(1i.*n.*phi(r<=Radius(
M)));
                        %Ex(r>Radius(M)) = Ex(r>Radius(M)) -
Anx(nc,1).*besselh(n,k(2).*r(r>Radius(M))).*exp(1i.*n.*phi(r>Radius(M))
);
                         %%%%%%%%%%%%Electric Fiedl%%%%%%%%%%%
                        TExr = TExr+Anx(nc,2).*(besselj(n-
1,k(1).*rs)+besselj(n+1,k(1).*rs)).*(1i/(w.*Epsilon(1))).*0.5.*1i.*k(1)
;
                        %TExr(r>Radius(M)) = TExr(r>Radius(M)) -
1i./(w.*Eta(2)).*Anx(nc,1).*besselh(n,k(2).*r(r>Radius(M))).*exp(1i.*n.
*phi(r>Radius(M))).*1i.*n./r(r>Radius(M));
                        %TExp(r<=Radius(M)) = TExp(r<=Radius(M))-
0.5*1i./(w.*Eta(1)).*Anx(nc,2).*(besselj(n-1,k(1).*r(r<=Radius(M)))-
besselj(n+1,k(1).*r(r<=Radius(M)))).*exp(1i.*n.*phi(r<=Radius(M)))*k(1)
;
                        %TExp(r>Radius(M)) =
TExp(r>Radius(M))+0.5*1i./(w.*Eta(2)).*Anx(nc,1).*(besselh(n-
```

```
1,k(2).*r(r>Radius(M)))-
besselh(n+1,k(2).*r(r>Radius(M)))).*exp(1i.*n.*phi(r>Radius(M)))*k(2);

                    end
                    TExx= (Bxr+TExr)/(-1i.*w.*u_0);
                    %TExy=sin(phi).*TExr+cos(phi).*TExp;

                    for n=-nmax:nmax
                    %%Green's function calculation
                    %By = By+(1*Eta(1)/8).*(besselh(n-1,k(1)*rs)-
besselh(n+1,k(1)*rs)).*besselj(n,k(1).*rs);%r<rs
                    %By(r>rs) =
By(r>rs)+(1*Eta(1)/8).*exp(1i*n*phi(r>rs)).*(besselj(n-1,k(1)*rs)-
besselj(n+1,k(1)*rs)).*besselh(n,1,k(1).*r(r>rs));%r>rs
                    %Byr = Byr+(1*Eta(1)/8).*(besselh(n-1,k(1)*rs)-
besselh(n+1,k(1)*rs)).*besselj(n,k(1).*rs).*1i.*n;%r<rs
                    %Byr(r>rs) =
By(r>rs)+(1*Eta(1)/8).*exp(1i*n*phi(r>rs)).*(besselj(n-1,k(1)*rs)-
besselj(n+1,k(1)*rs)).*besselh(n,1,k(1).*r(r>rs)).*1i.*n;%r>rs
                        Byp=Byp-(k(1)/8i).*(besselh(n-1,k(1)*rs)-
besselh(n+1,k(1)*rs)).*0.5.*(besselj(n-1,k(1).*rs)-
besselj(n+1,k(1).*rs));
                    %Byp(r>rs)=Byp(r>rs)-
(1*Eta(1)/8).*exp(1i*n*phi(r>rs)).*(besselj(n-1,k(1)*rs)-
besselj(n+1,k(1)*rs)).*0.5.*(besselh(n-1,k(1).*r(r>rs))-
besselh(n+1,k(1).*r(r>rs)));

                    end

                    %Ey(r<=Radius(M))=By(r<=Radius(M));
                    %TEyr=Byr.*(1i./(w.*Eta(1)))./rs;
                    Byp=Byp.*1i./(w.*Epsilon(1)).*k(1);

                    for n=-nmax:nmax
                        nc=n+nmax+1;

                        %Ey(r<=Radius(M)) = Ey(r<=Radius(M))
+Any(nc,2).*besselj(n,k(1).*r(r<=Radius(M))).*exp(1i.*n.*phi(r<=Radius(
M)));
                        %Ey(r>Radius(M)) = Ey(r>Radius(M)) -
Any(nc,1).*besselh(n,k(2).*r(r>Radius(M))).*exp(1i.*n.*phi(r>Radius(M))
);
                        %%%%%%Electric fields%%%%%%%
                        %TEyr = TEyr
+1i./(w.*Eta(1)).*Any(nc,2).*besselj(n,k(1).*rs).*1i.*n./rs;
                        %TEyr(r>Radius(M)) = TEyr(r>Radius(M)) -
1i./(w.*Eta(2)).*Any(nc,1).*besselh(n,k(2).*r(r>Radius(M))).*exp(1i.*n.
*phi(r>Radius(M))).*1i.*n./r(r>Radius(M));
                        TEyp = TEyp-
0.5*1i./(w.*Epsilon(1)).*Any(nc,2).*(besselj(n-1,k(1).*rs)-
besselj(n+1,k(1).*rs))*k(1);
```

```
                        %TEyp(r>Radius(M)) =
TEyp(r>Radius(M))+0.5*1i./(w.*Eta(2)).*Any(nc,1).*(besselh(n-
1,k(2).*r(r>Radius(M)))-
besselh(n+1,k(2).*r(r>Radius(M)))).*exp(1i.*n.*phi(r>Radius(M)))*k(2);

                    end
                    %TEyx=cos(phi).*TEyr-sin(phi).*TEyp;
                    TEyy=(TEyp+Byp)/(-1i.*w.*u_0);
                    ldos=-
2*w*nb(1)^2/(pi*c_light^2).*imag(TExx+TEyy+TM);

            else

                [Anx,Any,Anz]=GC3(w,u_0,M,Eta,taker,k,Radius,rs,nmax);

                for n=-nmax:nmax
                    %%Green's function calculation
                    %Bz=Bz+
(1/4i).*besselh(n,1,k(1)*rs).*besselj(n,k(1).*rs);%r<rs
                    Bz = Bz-
(w*u_0/4).*besselj(n,k(2)*rs).*besselh(n,1,k(2).*rs);%r>rs

                end

                %Ez(r<=Radius(M))=Bz(r<=Radius(M));

                for n=-nmax:nmax
                    nc=n+nmax+1;
                    %%%%%E%%%%%%%
                    %disp(Anz(nc,2));
                    %Ez = Ez +Anz(nc,2).*besselj(n,k(1).*rs);
                    Ez = Ez - Anz(nc,1).*besselh(n,k(2).*rs);

                end
                TM=(Ez+Bz)/(-1i.*w.*u_0);

                for n=-nmax:nmax
                    %%Green's function calculation
                    %Bx =
Bx(r<=rs)+(1i*Eta(2)/8).*exp(1i*n*phi(r<=rs)).*(besselh(n-
1,k(2)*rs)+besselh(n+1,k(2)*rs)).*besselj(n,k(2).*r(r<=rs));%r<rs
                    %Bx(r>rs) =
Bx(r>rs)+(1i*Eta(2)/8).*exp(1i*n*phi(r>rs)).*(besselj(n-
1,k(2)*rs)+besselj(n+1,k(2)*rs)).*besselh(n,1,k(2).*r(r>rs));%r>rs
                        Bxr = Bxr+(k(2)/8).*(besselh(n-
1,k(2)*rs)+besselh(n+1,k(2)*rs)).*(besselj(n-
1,k(2).*rs)+besselj(n+1,k(2).*rs)).*0.5.*1i;%r<rs
                    %Bxr(r>rs) =
Bx(r>rs)+(1i*Eta(2)/8).*exp(1i*n*phi(r>rs)).*(besselj(n-
1,k(2)*rs)+besselj(n+1,k(2)*rs)).*besselh(n,1,k(2).*r(r>rs)).*1i.*n;%r>
rs
```

```
                    %Bxp(r<=rs)=Bxp(r<=rs)-
(1i*Eta(2)/8).*exp(1i*n*phi(r<=rs)).*(besselh(n-
1,k(2)*rs)+besselh(n+1,k(2)*rs)).*0.5.*(besselj(n-1,k(2).*r(r<=rs))-
besselj(n+1,k(2).*r(r<=rs)));
                    %Bxp(r>rs)=Bxp(r>rs)-
(1i*Eta(2)/8).*exp(1i*n*phi(r>rs)).*(besselj(n-
1,k(2)*rs)+besselj(n+1,k(2)*rs)).*0.5.*(besselh(n-1,k(2).*r(r>rs))-
besselh(n+1,k(2).*r(r>rs)));

                end

                    %Ex(r>Radius(M))=Bx(r>Radius(M));
                    Bxr=Bxr.*(1i/(w.*Epsilon(2))).*k(2);
                    %TExp(r>Radius(M))=-
Bxp(r>Radius(M)).*1i./(w.*Eta(2)).*k(2);



                    for n=-nmax:nmax
                        nc=n+nmax+1;
                        %Ex(r<=Radius(M)) = Ex(r<=Radius(M))
+Anx(nc,2).*besselj(n,k(1).*r(r<=Radius(M))).*exp(1i.*n.*phi(r<=Radius(
M)));
                        %Ex(r>Radius(M)) = Ex(r>Radius(M)) -
Anx(nc,1).*besselh(n,k(2).*r(r>Radius(M))).*exp(1i.*n.*phi(r>Radius(M))
);
                         %%%%%%%%Electric FIeld%%%%%%%%%%%
                        %TExr(r<=Radius(M)& r>0) = TExr(r<=Radius(M)&
r>0)+1i./(w.*Eta(1)).*Anx(nc,2).*besselj(n,k(1).*r(r<=Radius(M)&
r>0)).*exp(1i.*n.*phi(r<=Radius(M)& r>0)).*1i.*n./r(r<=Radius(M)& r>0);
                            TExr = TExr-
(1i/(w.*Epsilon(2))).*Anx(nc,1).*(besselh(n-
1,k(2).*rs)+besselh(n+1,k(2).*rs)).*0.5.*1i.*k(2);
                        %TExp(r<=Radius(M)) = TExp(r<=Radius(M))-
0.5*1i./(w.*Eta(1)).*Anx(nc,2).*(besselj(n-1,k(1).*r(r<=Radius(M)))-
besselj(n+1,k(1).*r(r<=Radius(M)))).*exp(1i.*n.*phi(r<=Radius(M)))*k(1)
;
                        %TExp(r>Radius(M))=0.5*1i./(w.*Eta(2)).*Anx(nc,
1).*(besselh(n-1,k(2).*r(r>Radius(M)))-
besselh(n+1,k(2).*r(r>Radius(M)))).*exp(1i.*n.*phi(r>Radius(M)))*k(2);

                    end
                    TExx= (Bxr+TExr)/(-1i.*w.*u_0);
                    %TExy=sin(phi).*TExr+cos(phi).*TExp;

                for n=-nmax:nmax
                    %%Green's function calculation
                    %By(r<=rs) =
By(r<=rs)+(1*Eta(2)/8).*exp(1i*n*phi(r<=rs)).*(besselh(n-1,k(2)*rs)-
besselh(n+1,k(2)*rs)).*besselj(n,k(2).*r(r<=rs));%r<rs
                    %By(r>rs) =
By(r>rs)+(1*Eta(2)/8).*exp(1i*n*phi(r>rs)).*(besselj(n-1,k(2)*rs)-
besselj(n+1,k(2)*rs)).*besselh(n,1,k(2).*r(r>rs));%r>rs
```

```
                         %Byr = Byr+(1*Eta(1)/8).*(besselh(n-
1,k(1)*rs)-besselh(n+1,k(1)*rs)).*besselj(n,k(1).*rs).*1i.*n;%r<rs
                    %Byr(r>rs) =
By(r>rs)+(1*Eta(1)/8).*exp(1i*n*phi(r>rs)).*(besselj(n-1,k(1)*rs)-
besselj(n+1,k(1)*rs)).*besselh(n,1,k(1).*r(r>rs)).*1i.*n;%r>rs
                    %Byp(r<=rs)=Byp(r<=rs)-
(1*Eta(2)/8).*exp(1i*n*phi(r<=rs)).*(besselh(n-1,k(2)*rs)-
besselh(n+1,k(2)*rs)).*0.5.*(besselj(n-1,k(2).*r(r<=rs))-
besselj(n+1,k(2).*r(r<=rs)));
                        Byp=Byp-(k(2)/8i).*(besselj(n-1,k(2)*rs)-
besselj(n+1,k(2)*rs)).*0.5.*(besselh(n-1,k(2).*rs)-
besselh(n+1,k(2).*rs));

                end

                    %Ey(r>Radius(M))=By(r>Radius(M));
                    %TEyr=Byr.*(1i./(w.*Eta(1)))./rs;
                    Byp=Byp.*1i./(w.*Epsilon(2)).*k(2);
                    for n=-nmax:nmax
                        nc=n+nmax+1;

                        %Ey(r<=Radius(M)) = Ey(r<=Radius(M))
+Any(nc,2).*besselj(n,k(1).*r(r<=Radius(M))).*exp(1i.*n.*phi(r<=Radius(
M)));
                        %Ey(r>Radius(M)) = Ey(r>Radius(M)) -
Any(nc,1).*besselh(n,k(2).*r(r>Radius(M))).*exp(1i.*n.*phi(r>Radius(M))
);
                         %%%%%%%%%%Electric Field%%%%%%%%%%%%%
                        %TEyr(r<=Radius(M)& r>0) = TEyr(r<=Radius(M) &
r>0) +1i./(w.*Eta(1)).*Any(nc,2).*besselj(n,k(1).*r(r<=Radius(M) &
r>0)).*exp(1i.*n.*phi(r<=Radius(M) & r>0)).*1i.*n./r(r<=Radius(M)&
r>0);
                        %TEyr = TEyr(r>Radius(M)) -
1i./(w.*Eta(2)).*Any(nc,1).*besselh(n,k(2).*r).*1i.*n./rs;
                        %TEyp(r<=Radius(M)) = TEyp(r<=Radius(M))-
0.5*1i./(w.*Eta(1)).*Any(nc,2).*(besselj(n-1,k(1).*r(r<=Radius(M)))-
besselj(n+1,k(1).*r(r<=Radius(M)))).*exp(1i.*n.*phi(r<=Radius(M)))*k(1)
;
                        TEyp =
TEyp+0.5*1i./(w.*Epsilon(2)).*Any(nc,1).*(besselh(n-1,k(2).*rs)-
besselh(n+1,k(2).*rs))*k(2);

                    end
                    %TEyx=cos(phi).*TEyr-sin(phi).*TEyp;
                    TEyy=(TEyp+Byp)/(-1i.*w.*u_0);
                    %assignin('base', 'Anx', Anz)
                ldos=-2*w*nb(2)^2/(pi*c_light^2).*imag(TExx+TEyy+TM);
        end

      %%%%%%%%%%%%%%%%%%%%%%%%%%%%%%%%%%%%%%%%%%%%%%%%%%%%%%%%%%%%%%%
elseif M==2%CS structure
```

```
    Bz=0;
    Ez=0;
    Bxr=0;
    TExr=0;
    %Ex=0;
    Byp=0;
    TEyp=0;
    %Ey=0;

            if eq(taker,1)%source in core
                [Anx,Any,Anz]=GCS3(w,u_0,M,Eta,taker,k,Radius,rs,nmax);

                    for n=-nmax:nmax
                        %%Green's function calculation
                        Bz = Bz-
w*u_0/4.*besselh(n,1,k(1)*rs).*besselj(n,k(1).*rs);%r<rs
                        %Bz(r>rs) =
Bz(r>rs)+(1/4i).*exp(1i*n*phi(r>rs)).*besselj(n,k(1)*rs).*besselh(n,1,k
(1).*r(r>rs));%r>rs

                    end

                    %Ez(r<Radius(1))=Bz(r<Radius(1));

                    for n=-nmax:nmax
                        nc=n+nmax+1;
                        %%%%%%E%%%%%%%
                        Ez = Ez +Anz(nc,4).*besselj(n,k(1).*rs);
                        %Ez(r>=Radius(1)& r<=Radius(2)) =
Ez(r>=Radius(1)& r<=Radius(2)) +
(Anz(nc,2).*besselj(n,k(2).*r(r>=Radius(1)&
r<=Radius(2)))+Anz(nc,3).*besselh(n,k(2).*r(r>=Radius(1)&
r<=Radius(2)))).*exp(1i.*n.*phi(r>=Radius(1)& r<=Radius(2)));
                        %Ez(r>Radius(2))=Ez(r>Radius(2))-
Anz(nc,1).*besselh(n,k(3).*r(r>Radius(2))).*exp(1i.*n.*phi(r>Radius(2))
);
                    end
                    TM=(Ez+Bz)/(-1i.*w.*u_0);
                    for n=-nmax:nmax
                        %%Green's function calculation
                        %Bx(r<=rs) =
Bx(r<=rs)+(1i*Eta(1)/8).*exp(1i*n*phi(r<=rs)).*(besselh(n-
1,k(1)*rs)+besselh(n+1,k(1)*rs)).*besselj(n,k(1).*r(r<=rs));%r<rs
                        %Bx(r>rs) =
Bx(r>rs)+(1i*Eta(1)/8).*exp(1i*n*phi(r>rs)).*(besselj(n-
1,k(1)*rs)+besselj(n+1,k(1)*rs)).*besselh(n,1,k(1).*r(r>rs));%r>rs
                        %Bxr(r<=rs) =
Bx(r<=rs)+(1i*Eta(1)/8).*exp(1i*n*phi(r<=rs)).*(besselh(n-
1,k(1)*rs)+besselh(n+1,k(1)*rs)).*besselj(n,k(1).*r(r<=rs)).*1i.*n;%r<r
s
                        Bxr = Bxr+(k(1)/8).*(besselh(n-
1,k(1)*rs)+besselh(n+1,k(1)*rs)).*(besselj(n-
1,k(1).*rs)+besselj(n+1,k(1).*rs)).*0.5.*1i.*k(1);
```

```
                        %Bxp(r<=rs)=Bxp(r<=rs)-
(1i*Eta(1)/8).*exp(1i*n*phi(r<=rs)).*(besselh(n-
1,k(1)*rs)+besselh(n+1,k(1)*rs)).*0.5.*(besselj(n-1,k(1).*r(r<=rs))-
besselj(n+1,k(1).*r(r<=rs)));
                        %Bxp(r>rs)=Bxp(r>rs)-
(1i*Eta(1)/8).*exp(1i*n*phi(r>rs)).*(besselj(n-
1,k(1)*rs)+besselj(n+1,k(1)*rs)).*0.5.*(besselh(n-1,k(1).*r(r>rs))-
besselh(n+1,k(1).*r(r>rs)));
                    end

                    %Ex(r<Radius(1))=Bx(r<Radius(1));
                    %TExr(r<=Radius(1) & r>0)=Bx(r<=Radius(1) &
r>0).*(1i./(w.*Eta(1)))./r(r<=Radius(1) & r>0);
                    %TExp(r<=Radius(1))=Bxp(r<=Radius(1)).*1i./(w.*Eta(
1)).*k(1);
                    Bxr=Bxr.*(1i/(w.*Epsilon(1)));

                    for n=-nmax:nmax
                        nc=n+nmax+1;
                        %%%%%E%%%%%%%
                        %Ex(r<Radius(1)) = Ex(r<Radius(1))
+Anx(nc,4).*besselj(n,k(1).*r(r<Radius(1))).*exp(1i.*n.*phi(r<Radius(1)
));
                        %Ex(r>=Radius(1)& r<=Radius(2)) =
Ex(r>=Radius(1)& r<=Radius(2)) +
(Anx(nc,2).*besselj(n,k(2).*r(r>=Radius(1)&
r<=Radius(2)))+Anx(nc,3).*besselh(n,k(2).*r(r>=Radius(1)&
r<=Radius(2)))).*exp(1i.*n.*phi(r>=Radius(1)& r<=Radius(2)));
                        %Ex(r>Radius(2))=Ex(r>Radius(2))-
Anx(nc,1).*besselh(n,k(3).*r(r>Radius(2))).*exp(1i.*n.*phi(r>Radius(2))
);
                        %%%%%%%%%%Electric Field%%%%%%%%%
                        TExr = TExr+Anx(nc,4).*(besselj(n-
1,k(1).*rs)+besselj(n+1,k(1).*rs)).*(1i/(w.*Epsilon(1))).*0.5.*1i.*k(1)
;
                        %TExr(r>=Radius(1) & r<=Radius(2)) =
TExr(r>=Radius(1) & r<=Radius(2)) -
1i./(w.*Eta(2)).*(Anx(nc,2).*besselj(n,k(2).*r(r>=Radius(1) &
r<=Radius(2)))+Anx(nc,3).*besselh(n,k(2).*r(r>=Radius(1) &
r<=Radius(2)))).*exp(1i.*n.*phi(r>=Radius(1) &
r<=Radius(2))).*1i.*n./r(r>=Radius(1) & r<=Radius(2));
                        %TExr(r>Radius(2))=TExr(r>Radius(2))-
1i./(w.*Eta(3)).*Anx(nc,1).*besselh(n,k(3).*r(r>Radius(2))).*exp(1i.*n.
*phi(r>Radius(2))).*1i.*n./r(r>Radius(2));
                        %TExp(r<Radius(1)) = TExp(r<Radius(1))-
0.5*1i./(w.*Eta(1)).*Anx(nc,4).*(besselj(n-1,k(1).*r(r<Radius(1)))-
besselj(n+1,k(1).*r(r<Radius(1)))).*exp(1i.*n.*phi(r<Radius(1)))*k(1);
                        %TExp(r>=Radius(1) &
r<=Radius(2))=TExp(r>=Radius(1) & r<=Radius(2))-
0.5*1i./(w.*Eta(2)).*(Anx(nc,2).*(besselj(n-1,k(2).*r(r>=Radius(1) &
r<=Radius(2)))-besselj(n+1,k(2).*r(r>=Radius(1) &
r<=Radius(2))))+Anx(nc,3).*(besselh(n-1,k(2).*r(r>=Radius(1) &
```

```
r<=Radius(2)))-besselh(n+1,k(2).*r(r>=Radius(1) &
r<=Radius(2))))).*exp(1i.*n.*phi(r>=Radius(1) & r<=Radius(2)))*k(2);
                        %TExp(r>Radius(2)) =
TExp(r>Radius(2))+0.5*1i./(w.*Eta(3)).*Anx(nc,1).*(besselh(n-
1,k(2).*r(r>Radius(2)))-
besselh(n+1,k(3).*r(r>Radius(2)))).*exp(1i.*n.*phi(r>Radius(2)))*k(3);

                    end
                    TExx= (Bxr+TExr)/(-1i.*w.*u_0);

                    for n=-nmax:nmax
                        %%Green's function calculation
                        %By(r<=rs) =
By(r<=rs)+(1*Eta(1)/8).*exp(1i*n*phi(r<=rs)).*(besselh(n-1,k(1)*rs)-
besselh(n+1,k(1)*rs)).*besselj(n,k(1).*r(r<=rs));%r<rs
                        %By(r>rs) =
By(r>rs)+(1*Eta(1)/8).*exp(1i*n*phi(r>rs)).*(besselj(n-1,k(1)*rs)-
besselj(n+1,k(1)*rs)).*besselh(n,1,k(1).*r(r>rs));%r>rs
                        %Byr(r<=rs) =
By(r<=rs)+(1*Eta(1)/8).*exp(1i*n*phi(r<=rs)).*(besselh(n-1,k(1)*rs)-
besselh(n+1,k(1)*rs)).*besselj(n,k(1).*r(r<=rs)).*1i.*n;%r<rs
                        %Byr(r>rs) =
By(r>rs)+(1*Eta(1)/8).*exp(1i*n*phi(r>rs)).*(besselj(n-1,k(1)*rs)-
besselj(n+1,k(1)*rs)).*besselh(n,1,k(1).*r(r>rs)).*1i.*n;%r>rs
                        %Byp(r<=rs)=Byp(r<=rs)-
(1*Eta(1)/8).*exp(1i*n*phi(r<=rs)).*(besselh(n-1,k(1)*rs)-
besselh(n+1,k(1)*rs)).*0.5.*(besselj(n-1,k(1).*r(r<=rs))-
besselj(n+1,k(1).*r(r<=rs)));
                        Byp=Byp-(k(1)/8i).*(besselj(n-1,k(1)*rs)-
besselj(n+1,k(1)*rs)).*0.5.*(besselh(n-1,k(1).*rs)-
besselh(n+1,k(1).*rs));
                        %Byp(r>rs)=Byp(r>rs)-
(1*Eta(1)/8).*exp(1i*n*phi(r>rs)).*(besselj(n-1,k(1)*rs)-
besselj(n+1,k(1)*rs)).*0.5.*(besselh(n-1,k(1).*r(r>rs))-
besselh(n+1,k(1).*r(r>rs)));
                    end

                    %Ey(r<Radius(1))=By(r<Radius(1));
                    %TEyr(r<=Radius(1) & r>0)=Byr(r<=Radius(1) &
r>0).*(1i./(w.*Eta(1)))./r(r<=Radius(1) & r>0);
                    %TEyp(r<=Radius(1))=Byp(r<=Radius(1)).*1i./(w.*Eta(
1)).*k(1);
                    Byp=Byp.*1i/(w.*Epsilon(1)).*k(1);

                    for n=-nmax:nmax
                        nc=n+nmax+1;
                        %%%%%%E%%%%%%%%
                        %Ey(r<Radius(1)) = Ey(r<Radius(1))
+Any(nc,4).*besselj(n,k(1).*r(r<Radius(1))).*exp(1i.*n.*phi(r<Radius(1)
));
                        %Ey(r>=Radius(1)& r<=Radius(2)) =
Ey(r>=Radius(1)& r<=Radius(2)) +
(Any(nc,2).*besselj(n,k(2).*r(r>=Radius(1)&
```

```
r<=Radius(2)))+Any(nc,3).*besselh(n,k(2).*r(r>=Radius(1)&
r<=Radius(2)))).*exp(1i.*n.*phi(r>=Radius(1)& r<=Radius(2)));
                        %Ey(r>Radius(2))=Ey(r>Radius(2))-
Any(nc,1).*besselh(n,k(3).*r(r>Radius(2))).*exp(1i.*n.*phi(r>Radius(2))
);
                        %%%%%%%%%%%%%%%Electric
Field%%%%%%%%%%%%%%%%%%%
                        %TEyr(r<Radius(1) & r>0) = TEyr(r<Radius(1) &
r>0) +1i./(w.*Eta(1)).*Any(nc,4).*besselj(n,k(1).*r(r<Radius(1) &
r>0)).*exp(1i.*n.*phi(r<Radius(1) & r>0)).*1i.*n./r(r<Radius(1) & r>0);
                        %TEyr(r>=Radius(1) & r<=Radius(2)) =
TEyr(r>=Radius(1) & r<=Radius(2)) -
1i./(w.*Eta(2)).*(Any(nc,2).*besselj(n,k(2).*r(r>=Radius(1) &
r<=Radius(2)))+Any(nc,3).*besselh(n,k(2).*r(r>=Radius(1) &
r<=Radius(2)))).*exp(1i.*n.*phi(r>=Radius(1) &
r<=Radius(2))).*1i.*n./r(r>=Radius(1) & r<=Radius(2));
                        %TEyr(r>Radius(2))=TEyr(r>Radius(2))-
1i./(w.*Eta(3)).*Any(nc,1).*besselh(n,k(3).*r(r>Radius(2))).*exp(1i.*n.
*phi(r>Radius(2))).*1i.*n./r(r>Radius(2));
                        TEyp = TEyp-
0.5*1i./(w.*Epsilon(1)).*Any(nc,4).*(besselj(n-1,k(1).*rs)-
besselj(n+1,k(1).*rs)).*k(1);
                        %TEyp(r>=Radius(1) &
r<=Radius(2))=TEyp(r>=Radius(1) & r<=Radius(2))-
0.5*1i./(w.*Eta(2)).*(Any(nc,2).*(besselj(n-1,k(2).*r(r>=Radius(1) &
r<=Radius(2)))-besselj(n+1,k(2).*r(r>=Radius(1) &
r<=Radius(2))))+Any(nc,3).*(besselh(n-1,k(2).*r(r>=Radius(1) &
r<=Radius(2)))-besselh(n+1,k(2).*r(r>=Radius(1) &
r<=Radius(2))))).*exp(1i.*n.*phi(r>=Radius(1) & r<=Radius(2)))*k(2);
                        %TEyp(r>Radius(2)) =
TEyp(r>Radius(2))+0.5*1i./(w.*Eta(3)).*Any(nc,1).*(besselh(n-
1,k(2).*r(r>Radius(2)))-
besselh(n+1,k(3).*r(r>Radius(2)))).*exp(1i.*n.*phi(r>Radius(2)))*k(3);
                    end
                    TEyy=(Byp+TEyp)/(-1i.*w.*u_0);

                    ldos=-2*w*nb(1)^2/(pi*c_light^2).*imag(TM);



            elseif eq(taker,2)%source in shell

                [Anx,Any,Anz]=GCS3(w,u_0,M,Eta,taker,k,Radius,rs,nmax);

                    for n=-nmax:nmax
                        %%Green's function calculation
                        Bz = Bz-
(w*u_0/4).*besselh(n,1,k(2)*rs).*besselj(n,k(2).*rs);%r<rs
                        %Bz(r>rs) =
Bz(r>rs)+(1/4i).*exp(1i*n*phi(r>rs)).*besselj(n,k(2)*rs).*besselh(n,1,k
(2).*r(r>rs));%r>rs

                    end
```

```
                    %Ez(r>=Radius(1) & r<=Radius(2))=Bz(r>=Radius(1) &
r<=Radius(2));

                    for n=-nmax:nmax
                        nc=n+nmax+1;
                        %%%%%%E%%%%%%%
                        %Ez(r<Radius(1)) = Ez(r<Radius(1))
+Anz(nc,4).*besselj(n,k(1).*r(r<Radius(1))).*exp(1i.*n.*phi(r<Radius(1)
));
                        Ez= Ez +
(Anz(nc,2).*besselj(n,k(2).*rs)+Anz(nc,3).*besselh(n,k(2).*rs));
                        %Ez(r>Radius(2))=Ez(r>Radius(2))-
Anz(nc,1).*besselh(n,k(3).*r(r>Radius(2))).*exp(1i.*n.*phi(r>Radius(2))
);
                    end
                    TM=(Ez+Bz)/(-1i.*w.*u_0);

                    for n=-nmax:nmax
                        %%Green's function calculation
                        %Bx(r<=rs) =
Bx(r<=rs)+(1i*Eta(2)/8).*exp(1i*n*phi(r<=rs)).*(besselh(n-
1,k(2)*rs)+besselh(n+1,k(2)*rs)).*besselj(n,k(2).*r(r<=rs));%r<rs
                        %Bx(r>rs) =
Bx(r>rs)+(1i*Eta(2)/8).*exp(1i*n*phi(r>rs)).*(besselj(n-
1,k(2)*rs)+besselj(n+1,k(2)*rs)).*besselh(n,1,k(2).*r(r>rs));%r>rs
                        %Bxr(r<=rs) =
Bx(r<=rs)+(1i*Eta(2)/8).*exp(1i*n*phi(r<=rs)).*(besselh(n-
1,k(2)*rs)+besselh(n+1,k(2)*rs)).*besselj(n,k(2).*r(r<=rs)).*1i.*n;%r<r
s
                        Bxr = Bxr+(k(2)/8).*(besselh(n-
1,k(2)*rs)+besselh(n+1,k(2)*rs)).*(besselj(n-
1,k(2).*rs)+besselj(n+1,k(2).*rs)).*0.5.*1i.*k(2);
                        %Bxr(r>rs) =
Bx(r>rs)+(1i*Eta(2)/8).*exp(1i*n*phi(r>rs)).*(besselj(n-
1,k(2)*rs)+besselj(n+1,k(2)*rs)).*besselh(n,1,k(2).*r(r>rs)).*1i.*n;%r>
rs
                        %Bxp(r<=rs)=Bxp(r<=rs)-
(1i*Eta(2)/8).*exp(1i*n*phi(r<=rs)).*(besselh(n-
1,k(2)*rs)+besselh(n+1,k(2)*rs)).*0.5.*(besselj(n-1,k(2).*r(r<=rs))-
besselj(n+1,k(2).*r(r<=rs)));
                        %Bxp(r>rs)=Bxp(r>rs)-
(1i*Eta(2)/8).*exp(1i*n*phi(r>rs)).*(besselj(n-
1,k(2)*rs)+besselj(n+1,k(2)*rs)).*0.5.*(besselh(n-1,k(2).*r(r>rs))-
besselh(n+1,k(2).*r(r>rs)));

                    end

                    %Ex(r>=Radius(1) & r<=Radius(2))=Bx(r>=Radius(1) &
r<=Radius(2));
                    %TExr(r>=Radius(1) & r<=Radius(2))=Bx(r>=Radius(1)
& r<=Radius(2)).*(1i./(w.*Eta(2)))./r(r>=Radius(1) & r<=Radius(2));
```

```
                    %TExp(r>=Radius(1) & r<=Radius(2))=Bxp(r>=Radius(1)
& r<=Radius(2)).*1i./(w.*Eta(2)).*k(2);
                    Bxr=Bxr.*(1i/(w.*Epsilon(2)));
                    for n=-nmax:nmax
                        nc=n+nmax+1;
                        %%%%%%E%%%%%%%
                        %Ex(r<Radius(1)) = Ex(r<Radius(1))
+Anx(nc,4).*besselj(n,k(1).*r(r<Radius(1))).*exp(1i.*n.*phi(r<Radius(1)
));
                        %Ex(r>=Radius(1)& r<=Radius(2)) =
Ex(r>=Radius(1)& r<=Radius(2)) +
(Anx(nc,2).*besselj(n,k(2).*r(r>=Radius(1)&
r<=Radius(2)))+Anx(nc,3).*besselh(n,k(2).*r(r>=Radius(1)&
r<=Radius(2)))).*exp(1i.*n.*phi(r>=Radius(1)& r<=Radius(2)));
                        %Ex(r>Radius(2))=Ex(r>Radius(2))-
Anx(nc,1).*besselh(n,k(3).*r(r>Radius(2))).*exp(1i.*n.*phi(r>Radius(2))
);
                        %%%%%%%%%%%%Electric Field%%%%%%%
                        %TExr(r<Radius(1) & r>0) = TExr(r<Radius(1) &
r>0) +1i./(w.*Eta(1)).*Anx(nc,4).*besselj(n,k(1).*r(r<Radius(1) &
r>0)).*exp(1i.*n.*phi(r<Radius(1) & r>0)).*1i.*n./r(r<Radius(1) & r>0);
                        TExr = TExr+
1i./(w.*Epsilon(2)).*(Anx(nc,2).*(besselj(n-
1,k(2).*rs)+besselj(n+1,k(2).*rs))+Anx(nc,3).*(besselh(n-
1,k(2).*rs)+besselh(n+1,k(2).*rs))).*1i*0.5*k(2);
                        %TExr(r>Radius(2))=TExr(r>Radius(2))-
1i./(w.*Eta(3)).*Anx(nc,1).*besselh(n,k(3).*r(r>Radius(2))).*exp(1i.*n.
*phi(r>Radius(2))).*1i.*n./r(r>Radius(2));
                        %TExp(r<Radius(1)) = TExp(r<Radius(1))-
0.5*1i./(w.*Eta(1)).*Anx(nc,4).*(besselj(n-1,k(1).*r(r<Radius(1)))-
besselj(n+1,k(1).*r(r<Radius(1)))).*exp(1i.*n.*phi(r<Radius(1)))*k(1);
                        %TExp(r>=Radius(1) &
r<=Radius(2))=TExp(r>=Radius(1) & r<=Radius(2))-
0.5*1i./(w.*Eta(2)).*(Anx(nc,2).*(besselj(n-1,k(2).*r(r>=Radius(1) &
r<=Radius(2)))-besselj(n+1,k(2).*r(r>=Radius(1) &
r<=Radius(2))))+Anx(nc,3).*(besselh(n-1,k(2).*r(r>=Radius(1) &
r<=Radius(2)))-besselh(n+1,k(2).*r(r>=Radius(1) &
r<=Radius(2))))).*exp(1i.*n.*phi(r>=Radius(1) & r<=Radius(2)))*k(2);
                        %TExp(r>Radius(2)) =
TExp(r>Radius(2))+0.5*1i./(w.*Eta(3)).*Anx(nc,1).*(besselh(n-
1,k(2).*r(r>Radius(2)))-
besselh(n+1,k(3).*r(r>Radius(2)))).*exp(1i.*n.*phi(r>Radius(2)))*k(3);
                    end
                    TExx= (Bxr+TExr)/(-1i.*w.*u_0);

                    for n=-nmax:nmax
                        %%Green's function calculation
                        %By(r<=rs) =
By(r<=rs)+(1*Eta(1)/8).*exp(1i*n*phi(r<=rs)).*(besselh(n-1,k(1)*rs)-
besselh(n+1,k(1)*rs)).*besselj(n,k(1).*r(r<=rs));%r<rs
                        %By(r>rs) =
By(r>rs)+(1*Eta(1)/8).*exp(1i*n*phi(r>rs)).*(besselj(n-1,k(1)*rs)-
besselj(n+1,k(1)*rs)).*besselh(n,1,k(1).*r(r>rs));%r>rs
```

```
                        %Byr(r<=rs) =
By(r<=rs)+(1*Eta(1)/8).*exp(1i*n*phi(r<=rs)).*(besselh(n-1,k(1)*rs)-
besselh(n+1,k(1)*rs)).*besselj(n,k(1).*r(r<=rs)).*1i.*n;%r<rs
                        %Byr(r>rs) =
By(r>rs)+(1*Eta(1)/8).*exp(1i*n*phi(r>rs)).*(besselj(n-1,k(1)*rs)-
besselj(n+1,k(1)*rs)).*besselh(n,1,k(1).*r(r>rs)).*1i.*n;%r>rs
                        %Byp(r<=rs)=Byp(r<=rs)-
(1*Eta(1)/8).*exp(1i*n*phi(r<=rs)).*(besselh(n-1,k(1)*rs)-
besselh(n+1,k(1)*rs)).*0.5.*(besselj(n-1,k(1).*r(r<=rs))-
besselj(n+1,k(1).*r(r<=rs)));
                        Byp=Byp-(k(2)/8i).*(besselj(n-1,k(2)*rs)-
besselj(n+1,k(2)*rs)).*0.5.*(besselh(n-1,k(2).*rs)-
besselh(n+1,k(2).*rs));
                        %Byp(r>rs)=Byp(r>rs)-
(1*Eta(1)/8).*exp(1i*n*phi(r>rs)).*(besselj(n-1,k(1)*rs)-
besselj(n+1,k(1)*rs)).*0.5.*(besselh(n-1,k(1).*r(r>rs))-
besselh(n+1,k(1).*r(r>rs)));
                    end

                    %Ey(r<Radius(1))=By(r<Radius(1));
                    %TEyr(r<=Radius(1) & r>0)=Byr(r<=Radius(1) &
r>0).*(1i./(w.*Eta(1)))./r(r<=Radius(1) & r>0);
                    %TEyp(r<=Radius(1))=Byp(r<=Radius(1)).*1i./(w.*Eta(
1)).*k(1);
                    Byp=Byp.*1i/(w.*Epsilon(2)).*k(2);

                    for n=-nmax:nmax
                        nc=n+nmax+1;
                        %%%%%E%%%%%%
                        %Ey(r<Radius(1)) = Ey(r<Radius(1))
+Any(nc,4).*besselj(n,k(1).*r(r<Radius(1))).*exp(1i.*n.*phi(r<Radius(1)
));
                        %Ey(r>=Radius(1)& r<=Radius(2)) =
Ey(r>=Radius(1)& r<=Radius(2)) +
(Any(nc,2).*besselj(n,k(2).*r(r>=Radius(1)&
r<=Radius(2)))+Any(nc,3).*besselh(n,k(2).*r(r>=Radius(1)&
r<=Radius(2)))).*exp(1i.*n.*phi(r>=Radius(1)& r<=Radius(2)));
                        %Ey(r>Radius(2))=Ey(r>Radius(2))-
Any(nc,1).*besselh(n,k(3).*r(r>Radius(2))).*exp(1i.*n.*phi(r>Radius(2))
);
                        %%%%%%%%%%%%%%Electric
Field%%%%%%%%%%%%%%%%%%%
                        %TEyr(r<Radius(1) & r>0) = TEyr(r<Radius(1) &
r>0) +1i./(w.*Eta(1)).*Any(nc,4).*besselj(n,k(1).*r(r<Radius(1) &
r>0)).*exp(1i.*n.*phi(r<Radius(1) & r>0)).*1i.*n./r(r<Radius(1) & r>0);
                        %TEyr(r>=Radius(1) & r<=Radius(2)) =
TEyr(r>=Radius(1) & r<=Radius(2)) -
1i./(w.*Eta(2)).*(Any(nc,2).*besselj(n,k(2).*r(r>=Radius(1) &
r<=Radius(2)))+Any(nc,3).*besselh(n,k(2).*r(r>=Radius(1) &
r<=Radius(2)))).*exp(1i.*n.*phi(r>=Radius(1) &
r<=Radius(2))).*1i.*n./r(r>=Radius(1) & r<=Radius(2));
```

```
                        %TEyr(r>Radius(2))=TEyr(r>Radius(2))-
1i./(w.*Eta(3)).*Any(nc,1).*besselh(n,k(3).*r(r>Radius(2))).*exp(1i.*n.
*phi(r>Radius(2))).*1i.*n./r(r>Radius(2));
                        TEyp=TEyp-
0.5*1i./(w.*Epsilon(2)).*(Any(nc,2).*(besselj(n-1,k(2).*rs))-
besselj(n+1,k(2).*rs)+Any(nc,3).*(besselh(n-1,k(2).*rs)-
besselh(n+1,k(2).*rs)))*k(2);
                        %TEyp(r>Radius(2)) =
TEyp(r>Radius(2))+0.5*1i./(w.*Eta(3)).*Any(nc,1).*(besselh(n-
1,k(2).*r(r>Radius(2)))-
besselh(n+1,k(3).*r(r>Radius(2)))).*exp(1i.*n.*phi(r>Radius(2)))*k(3);
                    end
                    TEyy=(Byp+TEyp)/(-1i.*w.*u_0);

                    ldos=-2*w*nb(2)^2/(pi*c_light^2).*imag(TM);
            else

                [Anx,Any,Anz]=GCS3(w,u_0,M,Eta,taker,k,Radius,rs,nmax);

                    for n=-nmax:nmax
                        %%Green's function calculation
                        Bz = Bz-
w*u_0/4.*besselh(n,1,k(3)*rs).*besselj(n,k(3).*rs);%r<rs
                        %Bz(r>rs) =
Bz(r>rs)+(1/4i).*exp(1i*n*phi(r>rs)).*besselj(n,k(3)*rs).*besselh(n,1,k
(3).*r(r>rs));%r>rs

                    end

                    %Ez(r>Radius(2))=Bz(r>Radius(2));

                    for n=-nmax:nmax
                        nc=n+nmax+1;
                        %%%%%%E%%%%%%%
                        %Ez(r<Radius(1)) = Ez(r<Radius(1))
+Anz(nc,4).*besselj(n,k(1).*r(r<Radius(1))).*exp(1i.*n.*phi(r<Radius(1)
));
                        %Ez(r>=Radius(1)& r<=Radius(2)) =
Ez(r>=Radius(1)& r<=Radius(2)) +
(Anz(nc,2).*besselj(n,k(2).*r(r>=Radius(1)&
r<=Radius(2)))+Anz(nc,3).*besselh(n,k(2).*r(r>=Radius(1)&
r<=Radius(2)))).*exp(1i.*n.*phi(r>=Radius(1)& r<=Radius(2)));
                        Ez=Ez-Anz(nc,1).*besselh(n,k(3).*rs);
                    end
                    TM=(Ez+Bz)/(-1i.*w.*u_0);

                    for n=-nmax:nmax
                        %%Green's function calculation
                        %Bx(r<=rs) =
Bx(r<=rs)+(1i*Eta(2)/8).*exp(1i*n*phi(r<=rs)).*(besselh(n-
1,k(2)*rs)+besselh(n+1,k(2)*rs)).*besselj(n,k(2).*r(r<=rs));%r<rs
```

```
                        %Bx(r>rs) =
Bx(r>rs)+(1i*Eta(2)/8).*exp(1i*n*phi(r>rs)).*(besselj(n-
1,k(2)*rs)+besselj(n+1,k(2)*rs)).*besselh(n,1,k(2).*r(r>rs));%r>rs
                        %Bxr(r<=rs) =
Bx(r<=rs)+(1i*Eta(2)/8).*exp(1i*n*phi(r<=rs)).*(besselh(n-
1,k(2)*rs)+besselh(n+1,k(2)*rs)).*besselj(n,k(2).*r(r<=rs)).*1i.*n;%r<r
s
                        Bxr = Bxr+(k(3)/8).*(besselh(n-
1,k(3)*rs)+besselh(n+1,k(3)*rs)).*(besselj(n-
1,k(3).*rs)+besselj(n+1,k(3).*rs)).*0.5.*1i.*k(3);
                        %Bxr(r>rs) =
Bx(r>rs)+(1i*Eta(2)/8).*exp(1i*n*phi(r>rs)).*(besselj(n-
1,k(2)*rs)+besselj(n+1,k(2)*rs)).*besselh(n,1,k(2).*r(r>rs)).*1i.*n;%r>
rs
                        %Bxp(r<=rs)=Bxp(r<=rs)-
(1i*Eta(2)/8).*exp(1i*n*phi(r<=rs)).*(besselh(n-
1,k(2)*rs)+besselh(n+1,k(2)*rs)).*0.5.*(besselj(n-1,k(2).*r(r<=rs))-
besselj(n+1,k(2).*r(r<=rs)));
                        %Bxp(r>rs)=Bxp(r>rs)-
(1i*Eta(2)/8).*exp(1i*n*phi(r>rs)).*(besselj(n-
1,k(2)*rs)+besselj(n+1,k(2)*rs)).*0.5.*(besselh(n-1,k(2).*r(r>rs))-
besselh(n+1,k(2).*r(r>rs)));

                    end

                    %Ex(r>=Radius(1) & r<=Radius(2))=Bx(r>=Radius(1) &
r<=Radius(2));
                    %TExr(r>=Radius(1) & r<=Radius(2))=Bx(r>=Radius(1)
& r<=Radius(2)).*(1i./(w.*Eta(2)))./r(r>=Radius(1) & r<=Radius(2));
                    %TExp(r>=Radius(1) & r<=Radius(2))=Bxp(r>=Radius(1)
& r<=Radius(2)).*1i./(w.*Eta(2)).*k(2);
                    Bxr=Bxr.*(1i/(w.*Epsilon(3)));
                    for n=-nmax:nmax
                        nc=n+nmax+1;
                        %%%%%E%%%%%%%
                        %Ex(r<Radius(1)) = Ex(r<Radius(1))
+Anx(nc,4).*besselj(n,k(1).*r(r<Radius(1))).*exp(1i.*n.*phi(r<Radius(1)
));
                        %Ex(r>=Radius(1)& r<=Radius(2)) =
Ex(r>=Radius(1)& r<=Radius(2)) +
(Anx(nc,2).*besselj(n,k(2).*r(r>=Radius(1)&
r<=Radius(2)))+Anx(nc,3).*besselh(n,k(2).*r(r>=Radius(1)&
r<=Radius(2)))).*exp(1i.*n.*phi(r>=Radius(1)& r<=Radius(2)));
                        %Ex(r>Radius(2))=Ex(r>Radius(2))-
Anx(nc,1).*besselh(n,k(3).*r(r>Radius(2))).*exp(1i.*n.*phi(r>Radius(2))
);
                        %%%%%%%%%%%Electric Field%%%%%%%
                        %TExr(r<Radius(1) & r>0) = TExr(r<Radius(1) &
r>0) +1i./(w.*Eta(1)).*Anx(nc,4).*besselj(n,k(1).*r(r<Radius(1) &
r>0)).*exp(1i.*n.*phi(r<Radius(1) & r>0)).*1i.*n./r(r<Radius(1) & r>0);
                        %TExr = TExr+
1i./(w.*Epsilon(3)).*(Anx(nc,2).*(besselj(n-
```

```
1,k(3).*rs)+besselj(n+1,k(3).*rs))+Anx(nc,3).*(besselh(n-
1,k(2).*rs)+besselh(n+1,k(2).*rs))).*1i*0.5*k(2);
                        TExr=TExr-
1i./(w.*Epsilon(3)).*Anx(nc,1).*besselh(n,k(3).*rs).*1i.*n./rs;
                        %TExp(r<Radius(1)) = TExp(r<Radius(1))-
0.5*1i./(w.*Eta(1)).*Anx(nc,4).*(besselj(n-1,k(1).*r(r<Radius(1)))-
besselj(n+1,k(1).*r(r<Radius(1)))).*exp(1i.*n.*phi(r<Radius(1)))*k(1);
                        %TExp(r>=Radius(1) &
r<=Radius(2))=TExp(r>=Radius(1) & r<=Radius(2))-
0.5*1i./(w.*Eta(2)).*(Anx(nc,2).*(besselj(n-1,k(2).*r(r>=Radius(1) &
r<=Radius(2)))-besselj(n+1,k(2).*r(r>=Radius(1) &
r<=Radius(2))))+Anx(nc,3).*(besselh(n-1,k(2).*r(r>=Radius(1) &
r<=Radius(2)))-besselh(n+1,k(2).*r(r>=Radius(1) &
r<=Radius(2))))).*exp(1i.*n.*phi(r>=Radius(1) & r<=Radius(2)))*k(2);
                        %TExp(r>Radius(2)) =
TExp(r>Radius(2))+0.5*1i./(w.*Eta(3)).*Anx(nc,1).*(besselh(n-
1,k(2).*r(r>Radius(2)))-
besselh(n+1,k(3).*r(r>Radius(2)))).*exp(1i.*n.*phi(r>Radius(2)))*k(3);
                    end
                    TExx= (Bxr+TExr)/(-1i.*w.*u_0);
                    for n=-nmax:nmax
                        %%Green's function calculation
                        %By(r<=rs) =
By(r<=rs)+(1*Eta(3)/8).*exp(1i*n*phi(r<=rs)).*(besselh(n-1,k(3)*rs)-
besselh(n+1,k(3)*rs)).*besselj(n,k(3).*r(r<=rs));%r<rs
                        %By(r>rs) =
By(r>rs)+(1*Eta(3)/8).*exp(1i*n*phi(r>rs)).*(besselj(n-1,k(3)*rs)-
besselj(n+1,k(3)*rs)).*besselh(n,1,k(3).*r(r>rs));%r>rs
                        %Byr(r<=rs) =
By(r<=rs)+(1*Eta(3)/8).*exp(1i*n*phi(r<=rs)).*(besselh(n-1,k(3)*rs)-
besselh(n+1,k(3)*rs)).*besselj(n,k(1).*r(r<=rs)).*1i.*n;%r<rs
                        %Byr(r>rs) =
By(r>rs)+(1*Eta(3)/8).*exp(1i*n*phi(r>rs)).*(besselj(n-1,k(3)*rs)-
besselj(n+1,k(3)*rs)).*besselh(n,1,k(1).*r(r>rs)).*1i.*n;%r>rs
                        %Byp(r<=rs)=Byp(r<=rs)-
(1*Eta(3)/8).*exp(1i*n*phi(r<=rs)).*(besselh(n-1,k(3)*rs)-
besselh(n+1,k(3)*rs)).*0.5.*(besselj(n-1,k(3).*r(r<=rs))-
besselj(n+1,k(3).*r(r<=rs)));
                        Byp=Byp-(k(3)/8i).*(besselh(n-1,k(3)*rs)-
besselh(n+1,k(3)*rs)).*0.5.*(besselj(n-1,k(3).*rs)-
besselj(n+1,k(3).*rs));
                        %Byp(r>rs)=Byp(r>rs)-
(1*Eta(3)/8).*exp(1i*n*phi(r>rs)).*(besselj(n-1,k(3)*rs)-
besselj(n+1,k(3)*rs)).*0.5.*(besselh(n-1,k(3).*r(r>rs))-
besselh(n+1,k(3).*r(r>rs)));
                    end


                    %Ey(r>Radius(2))=By(r>Radius(2));
                    %TEyr(r>Radius(2))=Byr(r>Radius(2)).*(1i./(w.*Eta(3
)))./r(r>Radius(2));
                    Byp=Byp.*1i./(w.*Epsilon(3)).*k(3);

                    for n=-nmax:nmax
```

```
                        nc=n+nmax+1;
                        %%%%%%E%%%%%%%
                        %Ey(r<Radius(1)) = Ey(r<Radius(1))
+Any(nc,4).*besselj(n,k(1).*r(r<Radius(1))).*exp(1i.*n.*phi(r<Radius(1)
));
                        %Ey(r>=Radius(1)& r<=Radius(2)) =
Ey(r>=Radius(1)& r<=Radius(2)) +
(Any(nc,2).*besselj(n,k(2).*r(r>=Radius(1)&
r<=Radius(2)))+Any(nc,3).*besselh(n,k(2).*r(r>=Radius(1)&
r<=Radius(2)))).*exp(1i.*n.*phi(r>=Radius(1)& r<=Radius(2)));
                        %Ey(r>Radius(2))=Ey(r>Radius(2))-
Any(nc,1).*besselh(n,k(3).*r(r>Radius(2))).*exp(1i.*n.*phi(r>Radius(2))
);
                        %%%%%%%%%%%%%%%Electric
Field%%%%%%%%%%%%%%%%%%%%
                        %TEyr(r<Radius(1) & r>0) = TEyr(r<Radius(1) &
r>0) +1i./(w.*Eta(1)).*Any(nc,4).*besselj(n,k(1).*r(r<Radius(1) &
r>0)).*exp(1i.*n.*phi(r<Radius(1) & r>0)).*1i.*n./r(r<Radius(1) & r>0);
                        %TEyr(r>=Radius(1) & r<=Radius(2)) =
TEyr(r>=Radius(1) & r<=Radius(2)) -
1i./(w.*Eta(2)).*(Any(nc,2).*besselj(n,k(2).*r(r>=Radius(1) &
r<=Radius(2)))+Any(nc,3).*besselh(n,k(2).*r(r>=Radius(1) &
r<=Radius(2)))).*exp(1i.*n.*phi(r>=Radius(1) &
r<=Radius(2))).*1i.*n./r(r>=Radius(1) & r<=Radius(2));
                        %TEyr(r>Radius(2))=TEyr(r>Radius(2))-
1i./(w.*Eta(3)).*Any(nc,1).*besselh(n,k(3).*r(r>Radius(2))).*exp(1i.*n.
*phi(r>Radius(2))).*1i.*n./r(r>Radius(2));
                        %TEyp(r<Radius(1)) = TEyp(r<Radius(1))-
0.5*1i./(w.*Eta(1)).*Any(nc,4).*(besselj(n-1,k(1).*r(r<Radius(1)))-
besselj(n+1,k(1).*r(r<Radius(1)))).*exp(1i.*n.*phi(r<Radius(1)))*k(1);
                        %TEyp(r>=Radius(1) &
r<=Radius(2))=TEyp(r>=Radius(1) & r<=Radius(2))-
0.5*1i./(w.*Eta(2)).*(Any(nc,2).*(besselj(n-1,k(2).*r(r>=Radius(1) &
r<=Radius(2)))-besselj(n+1,k(2).*r(r>=Radius(1) &
r<=Radius(2))))+Any(nc,3).*(besselh(n-1,k(2).*r(r>=Radius(1) &
r<=Radius(2)))-besselh(n+1,k(2).*r(r>=Radius(1) &
r<=Radius(2))))).*exp(1i.*n.*phi(r>=Radius(1) & r<=Radius(2)))*k(2);
                        TEyp =
TEyp+0.5*1i./(w.*Epsilon(3)).*Any(nc,1).*(besselh(n-1,k(3).*rs)-
besselh(n+1,k(3).*rs)).*k(3);
                    end
                    TEyy=(Byp+TEyp)/(-1i.*w.*u_0);
                    ldos=-2*w*nb(3)^2/(pi*c_light^2).*imag(TM);
            end
elseif M==3%CSS structure
    Bz=0;
    Ez=0;
    Bxr=0;
    TExr=0;
    %Ex=0;
    Byp=0;
    TEyp=0;
    %Ey=0;
```

```
            if eq(taker,1)%source in core
                [Anx,Any,Anz]=GCSS(w,u_0,M,Eta,taker,k,Radius,rs,nmax);

                    for n=-nmax:nmax
                        %%Green's function calculation
                        Bz = Bz-
w*u_0/4.*besselh(n,1,k(1)*rs).*besselj(n,k(1).*rs);%r<rs
                        %Bz(r>rs) =
Bz(r>rs)+(1/4i).*exp(1i*n*phi(r>rs)).*besselj(n,k(1)*rs).*besselh(n,1,k
(1).*r(r>rs));%r>rs

                    end

                    %Ez(r<Radius(1))=Bz(r<Radius(1));

                    for n=-nmax:nmax
                        nc=n+nmax+1;
                        %%%%%%E%%%%%%%
                        Ez = Ez +Anz(nc,6).*besselj(n,k(1).*rs);
                        %Ez(r>=Radius(1)& r<=Radius(2)) =
Ez(r>=Radius(1)& r<=Radius(2)) +
(Anz(nc,2).*besselj(n,k(2).*r(r>=Radius(1)&
r<=Radius(2)))+Anz(nc,3).*besselh(n,k(2).*r(r>=Radius(1)&
r<=Radius(2)))).*exp(1i.*n.*phi(r>=Radius(1)& r<=Radius(2)));
                        %Ez(r>Radius(2))=Ez(r>Radius(2))-
Anz(nc,1).*besselh(n,k(3).*r(r>Radius(2))).*exp(1i.*n.*phi(r>Radius(2))
);
                    end
                    TM=(Ez+Bz)/(-1i.*w.*u_0);
                    for n=-nmax:nmax
                        %%Green's function calculation
                        %Bx(r<=rs) =
Bx(r<=rs)+(1i*Eta(1)/8).*exp(1i*n*phi(r<=rs)).*(besselh(n-
1,k(1)*rs)+besselh(n+1,k(1)*rs)).*besselj(n,k(1).*r(r<=rs));%r<rs
                        %Bx(r>rs) =
Bx(r>rs)+(1i*Eta(1)/8).*exp(1i*n*phi(r>rs)).*(besselj(n-
1,k(1)*rs)+besselj(n+1,k(1)*rs)).*besselh(n,1,k(1).*r(r>rs));%r>rs
                        %Bxr(r<=rs) =
Bx(r<=rs)+(1i*Eta(1)/8).*exp(1i*n*phi(r<=rs)).*(besselh(n-
1,k(1)*rs)+besselh(n+1,k(1)*rs)).*besselj(n,k(1).*r(r<=rs)).*1i.*n;%r<r
s
                        Bxr = Bxr+(k(1)/8).*(besselh(n-
1,k(1)*rs)+besselh(n+1,k(1)*rs)).*(besselj(n-
1,k(1).*rs)+besselj(n+1,k(1).*rs)).*0.5.*1i.*k(1);
                        %Bxp(r<=rs)=Bxp(r<=rs)-
(1i*Eta(1)/8).*exp(1i*n*phi(r<=rs)).*(besselh(n-
1,k(1)*rs)+besselh(n+1,k(1)*rs)).*0.5.*(besselj(n-1,k(1).*r(r<=rs))-
besselj(n+1,k(1).*r(r<=rs)));
                        %Bxp(r>rs)=Bxp(r>rs)-
(1i*Eta(1)/8).*exp(1i*n*phi(r>rs)).*(besselj(n-
1,k(1)*rs)+besselj(n+1,k(1)*rs)).*0.5.*(besselh(n-1,k(1).*r(r>rs))-
besselh(n+1,k(1).*r(r>rs)));
```

```
                    end

                    %Ex(r<Radius(1))=Bx(r<Radius(1));
                    %TExr(r<=Radius(1) & r>0)=Bx(r<=Radius(1) &
r>0).*(1i./(w.*Eta(1)))./r(r<=Radius(1) & r>0);
                    %TExp(r<=Radius(1))=Bxp(r<=Radius(1)).*1i./(w.*Eta(
1)).*k(1);
                    Bxr=Bxr.*(1i/(w.*Epsilon(1)));

                    for n=-nmax:nmax
                        nc=n+nmax+1;
                        %%%%%%E%%%%%%%
                        %Ex(r<Radius(1)) = Ex(r<Radius(1))
+Anx(nc,4).*besselj(n,k(1).*r(r<Radius(1))).*exp(1i.*n.*phi(r<Radius(1)
));
                        %Ex(r>=Radius(1)& r<=Radius(2)) =
Ex(r>=Radius(1)& r<=Radius(2)) +
(Anx(nc,2).*besselj(n,k(2).*r(r>=Radius(1)&
r<=Radius(2)))+Anx(nc,3).*besselh(n,k(2).*r(r>=Radius(1)&
r<=Radius(2)))).*exp(1i.*n.*phi(r>=Radius(1)& r<=Radius(2)));
                        %Ex(r>Radius(2))=Ex(r>Radius(2))-
Anx(nc,1).*besselh(n,k(3).*r(r>Radius(2))).*exp(1i.*n.*phi(r>Radius(2))
);
                        %%%%%%%%%%%Electric Field%%%%%%%%%
                        TExr = TExr+Anx(nc,6).*(besselj(n-
1,k(1).*rs)+besselj(n+1,k(1).*rs)).*(1i/(w.*Epsilon(1))).*0.5.*1i.*k(1)
;
                        %TExr(r>=Radius(1) & r<=Radius(2)) =
TExr(r>=Radius(1) & r<=Radius(2)) -
1i./(w.*Eta(2)).*(Anx(nc,2).*besselj(n,k(2).*r(r>=Radius(1) &
r<=Radius(2)))+Anx(nc,3).*besselh(n,k(2).*r(r>=Radius(1) &
r<=Radius(2)))).*exp(1i.*n.*phi(r>=Radius(1) &
r<=Radius(2))).*1i.*n./r(r>=Radius(1) & r<=Radius(2));
                        %TExr(r>Radius(2))=TExr(r>Radius(2))-
1i./(w.*Eta(3)).*Anx(nc,1).*besselh(n,k(3).*r(r>Radius(2))).*exp(1i.*n.
*phi(r>Radius(2))).*1i.*n./r(r>Radius(2));
                        %TExp(r<Radius(1)) = TExp(r<Radius(1))-
0.5*1i./(w.*Eta(1)).*Anx(nc,4).*(besselj(n-1,k(1).*r(r<Radius(1)))-
besselj(n+1,k(1).*r(r<Radius(1)))).*exp(1i.*n.*phi(r<Radius(1)))*k(1);
                        %TExp(r>=Radius(1) &
r<=Radius(2))=TExp(r>=Radius(1) & r<=Radius(2))-
0.5*1i./(w.*Eta(2)).*(Anx(nc,2).*(besselj(n-1,k(2).*r(r>=Radius(1) &
r<=Radius(2)))-besselj(n+1,k(2).*r(r>=Radius(1) &
r<=Radius(2))))+Anx(nc,3).*(besselh(n-1,k(2).*r(r>=Radius(1) &
r<=Radius(2)))-besselh(n+1,k(2).*r(r>=Radius(1) &
r<=Radius(2))))).*exp(1i.*n.*phi(r>=Radius(1) & r<=Radius(2)))*k(2);
                        %TExp(r>Radius(2)) =
TExp(r>Radius(2))+0.5*1i./(w.*Eta(3)).*Anx(nc,1).*(besselh(n-
1,k(2).*r(r>Radius(2)))-
besselh(n+1,k(3).*r(r>Radius(2)))).*exp(1i.*n.*phi(r>Radius(2)))*k(3);

                    end
                    TExx= (Bxr+TExr)/(-1i.*w.*u_0);
```

```
                    for n=-nmax:nmax
                        %%Green's function calculation
                        %By(r<=rs) =
By(r<=rs)+(1*Eta(1)/8).*exp(1i*n*phi(r<=rs)).*(besselh(n-1,k(1)*rs)-
besselh(n+1,k(1)*rs)).*besselj(n,k(1).*r(r<=rs));%r<rs
                        %By(r>rs) =
By(r>rs)+(1*Eta(1)/8).*exp(1i*n*phi(r>rs)).*(besselj(n-1,k(1)*rs)-
besselj(n+1,k(1)*rs)).*besselh(n,1,k(1).*r(r>rs));%r>rs
                        %Byr(r<=rs) =
By(r<=rs)+(1*Eta(1)/8).*exp(1i*n*phi(r<=rs)).*(besselh(n-1,k(1)*rs)-
besselh(n+1,k(1)*rs)).*besselj(n,k(1).*r(r<=rs)).*1i.*n;%r<rs
                        %Byr(r>rs) =
By(r>rs)+(1*Eta(1)/8).*exp(1i*n*phi(r>rs)).*(besselj(n-1,k(1)*rs)-
besselj(n+1,k(1)*rs)).*besselh(n,1,k(1).*r(r>rs)).*1i.*n;%r>rs
                        %Byp(r<=rs)=Byp(r<=rs)-
(1*Eta(1)/8).*exp(1i*n*phi(r<=rs)).*(besselh(n-1,k(1)*rs)-
besselh(n+1,k(1)*rs)).*0.5.*(besselj(n-1,k(1).*r(r<=rs))-
besselj(n+1,k(1).*r(r<=rs)));
                        Byp=Byp-(k(1)/8i).*(besselj(n-1,k(1)*rs)-
besselj(n+1,k(1)*rs)).*0.5.*(besselh(n-1,k(1).*rs)-
besselh(n+1,k(1).*rs));
                        %Byp(r>rs)=Byp(r>rs)-
(1*Eta(1)/8).*exp(1i*n*phi(r>rs)).*(besselj(n-1,k(1)*rs)-
besselj(n+1,k(1)*rs)).*0.5.*(besselh(n-1,k(1).*r(r>rs))-
besselh(n+1,k(1).*r(r>rs)));
                    end

                    %Ey(r<Radius(1))=By(r<Radius(1));
                    %TEyr(r<=Radius(1) & r>0)=Byr(r<=Radius(1) &
r>0).*(1i./(w.*Eta(1)))./r(r<=Radius(1) & r>0);
                    %TEyp(r<=Radius(1))=Byp(r<=Radius(1)).*1i./(w.*Eta(
1)).*k(1);
                    Byp=Byp.*1i/(w.*Epsilon(1)).*k(1);

                    for n=-nmax:nmax
                        nc=n+nmax+1;
                        %%%%%%E%%%%%%%
                        %Ey(r<Radius(1)) = Ey(r<Radius(1))
+Any(nc,4).*besselj(n,k(1).*r(r<Radius(1))).*exp(1i.*n.*phi(r<Radius(1)
));
                        %Ey(r>=Radius(1)& r<=Radius(2)) =
Ey(r>=Radius(1)& r<=Radius(2)) +
(Any(nc,2).*besselj(n,k(2).*r(r>=Radius(1)&
r<=Radius(2)))+Any(nc,3).*besselh(n,k(2).*r(r>=Radius(1)&
r<=Radius(2)))).*exp(1i.*n.*phi(r>=Radius(1)& r<=Radius(2)));
                        %Ey(r>Radius(2))=Ey(r>Radius(2))-
Any(nc,1).*besselh(n,k(3).*r(r>Radius(2))).*exp(1i.*n.*phi(r>Radius(2))
);
                        %%%%%%%%%%%%%%%Electric
Field%%%%%%%%%%%%%%%%%%%
```

```
                         %TEyr(r<Radius(1) & r>0) = TEyr(r<Radius(1) &
r>0) +1i./(w.*Eta(1)).*Any(nc,4).*besselj(n,k(1).*r(r<Radius(1) &
r>0)).*exp(1i.*n.*phi(r<Radius(1) & r>0)).*1i.*n./r(r<Radius(1) & r>0);
                         %TEyr(r>=Radius(1) & r<=Radius(2)) =
TEyr(r>=Radius(1) & r<=Radius(2)) -
1i./(w.*Eta(2)).*(Any(nc,2).*besselj(n,k(2).*r(r>=Radius(1) &
r<=Radius(2)))+Any(nc,3).*besselh(n,k(2).*r(r>=Radius(1) &
r<=Radius(2)))).*exp(1i.*n.*phi(r>=Radius(1) &
r<=Radius(2))).*1i.*n./r(r>=Radius(1) & r<=Radius(2));
                         %TEyr(r>Radius(2))=TEyr(r>Radius(2))-
1i./(w.*Eta(3)).*Any(nc,1).*besselh(n,k(3).*r(r>Radius(2))).*exp(1i.*n.
*phi(r>Radius(2))).*1i.*n./r(r>Radius(2));
                         TEyp = TEyp-
0.5*1i./(w.*Epsilon(1)).*Any(nc,6).*(besselj(n-1,k(1).*rs)-
besselj(n+1,k(1).*rs)).*k(1);
                         %TEyp(r>=Radius(1) &
r<=Radius(2))=TEyp(r>=Radius(1) & r<=Radius(2))-
0.5*1i./(w.*Eta(2)).*(Any(nc,2).*(besselj(n-1,k(2).*r(r>=Radius(1) &
r<=Radius(2)))-besselj(n+1,k(2).*r(r>=Radius(1) &
r<=Radius(2))))+Any(nc,3).*(besselh(n-1,k(2).*r(r>=Radius(1) &
r<=Radius(2)))-besselh(n+1,k(2).*r(r>=Radius(1) &
r<=Radius(2))))).*exp(1i.*n.*phi(r>=Radius(1) & r<=Radius(2)))*k(2);
                         %TEyp(r>Radius(2)) =
TEyp(r>Radius(2))+0.5*1i./(w.*Eta(3)).*Any(nc,1).*(besselh(n-
1,k(2).*r(r>Radius(2)))-
besselh(n+1,k(3).*r(r>Radius(2)))).*exp(1i.*n.*phi(r>Radius(2)))*k(3);
                     end
                     TEyy=(Byp+TEyp)/(-1i.*w.*u_0);

                     ldos=-
2*w*nb(1)^2/(pi*c_light^2).*imag(TM+TExx+TEyy);



             elseif eq(taker,2)%source in shell

                 [Anx,Any,Anz]=GCSS(w,u_0,M,Eta,taker,k,Radius,rs,nmax);

                     for n=-nmax:nmax
                         %%Green's function calculation
                         Bz = Bz-
(w*u_0/4).*besselh(n,1,k(2)*rs).*besselj(n,k(2).*rs);%r<rs
                         %Bz(r>rs) =
Bz(r>rs)+(1/4i).*exp(1i*n*phi(r>rs)).*besselj(n,k(2)*rs).*besselh(n,1,k
(2).*r(r>rs));%r>rs

                     end

                     %Ez(r>=Radius(1) & r<=Radius(2))=Bz(r>=Radius(1) &
r<=Radius(2));

                     for n=-nmax:nmax
                         nc=n+nmax+1;
```

```
                        %%%%%%E%%%%%%%
                        %Ez(r<Radius(1)) = Ez(r<Radius(1))
+Anz(nc,4).*besselj(n,k(1).*r(r<Radius(1))).*exp(1i.*n.*phi(r<Radius(1)
));
                        Ez= Ez +
(Anz(nc,4).*besselj(n,k(2).*rs)+Anz(nc,5).*besselh(n,k(2).*rs));
                        %Ez(r>Radius(2))=Ez(r>Radius(2))-
Anz(nc,1).*besselh(n,k(3).*r(r>Radius(2))).*exp(1i.*n.*phi(r>Radius(2))
);
                    end
                    TM=(Ez+Bz)/(-1i.*w.*u_0);

                    for n=-nmax:nmax
                        %%Green's function calculation
                        %Bx(r<=rs) =
Bx(r<=rs)+(1i*Eta(2)/8).*exp(1i*n*phi(r<=rs)).*(besselh(n-
1,k(2)*rs)+besselh(n+1,k(2)*rs)).*besselj(n,k(2).*r(r<=rs));%r<rs
                        %Bx(r>rs) =
Bx(r>rs)+(1i*Eta(2)/8).*exp(1i*n*phi(r>rs)).*(besselj(n-
1,k(2)*rs)+besselj(n+1,k(2)*rs)).*besselh(n,1,k(2).*r(r>rs));%r>rs
                        %Bxr(r<=rs) =
Bx(r<=rs)+(1i*Eta(2)/8).*exp(1i*n*phi(r<=rs)).*(besselh(n-
1,k(2)*rs)+besselh(n+1,k(2)*rs)).*besselj(n,k(2).*r(r<=rs)).*1i.*n;%r<r
s
                        Bxr = Bxr+(k(2)/8).*(besselh(n-
1,k(2)*rs)+besselh(n+1,k(2)*rs)).*(besselj(n-
1,k(2).*rs)+besselj(n+1,k(2).*rs)).*0.5.*1i.*k(2);
                        %Bxr(r>rs) =
Bx(r>rs)+(1i*Eta(2)/8).*exp(1i*n*phi(r>rs)).*(besselj(n-
1,k(2)*rs)+besselj(n+1,k(2)*rs)).*besselh(n,1,k(2).*r(r>rs)).*1i.*n;%r>
rs
                        %Bxp(r<=rs)=Bxp(r<=rs)-
(1i*Eta(2)/8).*exp(1i*n*phi(r<=rs)).*(besselh(n-
1,k(2)*rs)+besselh(n+1,k(2)*rs)).*0.5.*(besselj(n-1,k(2).*r(r<=rs))-
besselj(n+1,k(2).*r(r<=rs)));
                        %Bxp(r>rs)=Bxp(r>rs)-
(1i*Eta(2)/8).*exp(1i*n*phi(r>rs)).*(besselj(n-
1,k(2)*rs)+besselj(n+1,k(2)*rs)).*0.5.*(besselh(n-1,k(2).*r(r>rs))-
besselh(n+1,k(2).*r(r>rs)));

                    end

                    %Ex(r>=Radius(1) & r<=Radius(2))=Bx(r>=Radius(1) &
r<=Radius(2));
                    %TExr(r>=Radius(1) & r<=Radius(2))=Bx(r>=Radius(1)
& r<=Radius(2)).*(1i./(w.*Eta(2)))./r(r>=Radius(1) & r<=Radius(2));
                    %TExp(r>=Radius(1) & r<=Radius(2))=Bxp(r>=Radius(1)
& r<=Radius(2)).*1i./(w.*Eta(2)).*k(2);
                    Bxr=Bxr.*(1i/(w.*Epsilon(2)));
                    for n=-nmax:nmax
                        nc=n+nmax+1;
                        %%%%%%E%%%%%%%
```

```
                        %Ex(r<Radius(1)) = Ex(r<Radius(1))
+Anx(nc,4).*besselj(n,k(1).*r(r<Radius(1))).*exp(1i.*n.*phi(r<Radius(1)
));
                        %Ex(r>=Radius(1)& r<=Radius(2)) =
Ex(r>=Radius(1)& r<=Radius(2)) +
(Anx(nc,2).*besselj(n,k(2).*r(r>=Radius(1)&
r<=Radius(2)))+Anx(nc,3).*besselh(n,k(2).*r(r>=Radius(1)&
r<=Radius(2)))).*exp(1i.*n.*phi(r>=Radius(1)& r<=Radius(2)));
                        %Ex(r>Radius(2))=Ex(r>Radius(2))-
Anx(nc,1).*besselh(n,k(3).*r(r>Radius(2))).*exp(1i.*n.*phi(r>Radius(2))
);
                        %%%%%%%%%%%%Electric Field%%%%%%%
                        %TExr(r<Radius(1) & r>0) = TExr(r<Radius(1) &
r>0) +1i./(w.*Eta(1)).*Anx(nc,4).*besselj(n,k(1).*r(r<Radius(1) &
r>0)).*exp(1i.*n.*phi(r<Radius(1) & r>0)).*1i.*n./r(r<Radius(1) & r>0);
                        TExr = TExr+
1i./(w.*Epsilon(2)).*(Anx(nc,4).*(besselj(n-
1,k(2).*rs)+besselj(n+1,k(2).*rs))+Anx(nc,5).*(besselh(n-
1,k(2).*rs)+besselh(n+1,k(2).*rs))).*1i*0.5*k(2);
                        %TExr(r>Radius(2))=TExr(r>Radius(2))-
1i./(w.*Eta(3)).*Anx(nc,1).*besselh(n,k(3).*r(r>Radius(2))).*exp(1i.*n.
*phi(r>Radius(2))).*1i.*n./r(r>Radius(2));
                        %TExp(r<Radius(1)) = TExp(r<Radius(1))-
0.5*1i./(w.*Eta(1)).*Anx(nc,4).*(besselj(n-1,k(1).*r(r<Radius(1)))-
besselj(n+1,k(1).*r(r<Radius(1)))).*exp(1i.*n.*phi(r<Radius(1)))*k(1);
                        %TExp(r>=Radius(1) &
r<=Radius(2))=TExp(r>=Radius(1) & r<=Radius(2))-
0.5*1i./(w.*Eta(2)).*(Anx(nc,2).*(besselj(n-1,k(2).*r(r>=Radius(1) &
r<=Radius(2)))-besselj(n+1,k(2).*r(r>=Radius(1) &
r<=Radius(2))))+Anx(nc,3).*(besselh(n-1,k(2).*r(r>=Radius(1) &
r<=Radius(2)))-besselh(n+1,k(2).*r(r>=Radius(1) &
r<=Radius(2))))).*exp(1i.*n.*phi(r>=Radius(1) & r<=Radius(2)))*k(2);
                        %TExp(r>Radius(2)) =
TExp(r>Radius(2))+0.5*1i./(w.*Eta(3)).*Anx(nc,1).*(besselh(n-
1,k(2).*r(r>Radius(2)))-
besselh(n+1,k(3).*r(r>Radius(2)))).*exp(1i.*n.*phi(r>Radius(2)))*k(3);
                    end
                    TExx= (Bxr+TExr)/(-1i.*w.*u_0);

                    for n=-nmax:nmax
                        %%Green's function calculation
                        %By(r<=rs) =
By(r<=rs)+(1*Eta(1)/8).*exp(1i*n*phi(r<=rs)).*(besselh(n-1,k(1)*rs)-
besselh(n+1,k(1)*rs)).*besselj(n,k(1).*r(r<=rs));%r<rs
                        %By(r>rs) =
By(r>rs)+(1*Eta(1)/8).*exp(1i*n*phi(r>rs)).*(besselj(n-1,k(1)*rs)-
besselj(n+1,k(1)*rs)).*besselh(n,1,k(1).*r(r>rs));%r>rs
                        %Byr(r<=rs) =
By(r<=rs)+(1*Eta(1)/8).*exp(1i*n*phi(r<=rs)).*(besselh(n-1,k(1)*rs)-
besselh(n+1,k(1)*rs)).*besselj(n,k(1).*r(r<=rs)).*1i.*n;%r<rs
                        %Byr(r>rs) =
By(r>rs)+(1*Eta(1)/8).*exp(1i*n*phi(r>rs)).*(besselj(n-1,k(1)*rs)-
besselj(n+1,k(1)*rs)).*besselh(n,1,k(1).*r(r>rs)).*1i.*n;%r>rs
```

```
                        %Byp(r<=rs)=Byp(r<=rs)-
(1*Eta(1)/8).*exp(1i*n*phi(r<=rs)).*(besselh(n-1,k(1)*rs)-
besselh(n+1,k(1)*rs)).*0.5.*(besselj(n-1,k(1).*r(r<=rs))-
besselj(n+1,k(1).*r(r<=rs)));
                        Byp=Byp-(k(2)/8i).*(besselj(n-1,k(2)*rs)-
besselj(n+1,k(2)*rs)).*0.5.*(besselh(n-1,k(2).*rs)-
besselh(n+1,k(2).*rs));
                        %Byp(r>rs)=Byp(r>rs)-
(1*Eta(1)/8).*exp(1i*n*phi(r>rs)).*(besselj(n-1,k(1)*rs)-
besselj(n+1,k(1)*rs)).*0.5.*(besselh(n-1,k(1).*r(r>rs))-
besselh(n+1,k(1).*r(r>rs)));
                    end

                    %Ey(r<Radius(1))=By(r<Radius(1));
                    %TEyr(r<=Radius(1) & r>0)=Byr(r<=Radius(1) &
r>0).*(1i./(w.*Eta(1)))./r(r<=Radius(1) & r>0);
                    %TEyp(r<=Radius(1))=Byp(r<=Radius(1)).*1i./(w.*Eta(
1)).*k(1);
                    Byp=Byp.*1i/(w.*Epsilon(2)).*k(2);

                    for n=-nmax:nmax
                        nc=n+nmax+1;
                        %%%%%%E%%%%%%%
                        %Ey(r<Radius(1)) = Ey(r<Radius(1))
+Any(nc,4).*besselj(n,k(1).*r(r<Radius(1))).*exp(1i.*n.*phi(r<Radius(1)
));
                        %Ey(r>=Radius(1)& r<=Radius(2)) =
Ey(r>=Radius(1)& r<=Radius(2)) +
(Any(nc,2).*besselj(n,k(2).*r(r>=Radius(1)&
r<=Radius(2)))+Any(nc,3).*besselh(n,k(2).*r(r>=Radius(1)&
r<=Radius(2)))).*exp(1i.*n.*phi(r>=Radius(1)& r<=Radius(2)));
                        %Ey(r>Radius(2))=Ey(r>Radius(2))-
Any(nc,1).*besselh(n,k(3).*r(r>Radius(2))).*exp(1i.*n.*phi(r>Radius(2))
);
                        %%%%%%%%%%%%%%Electric
Field%%%%%%%%%%%%%%%%%%%%
                        %TEyr(r<Radius(1) & r>0) = TEyr(r<Radius(1) &
r>0) +1i./(w.*Eta(1)).*Any(nc,4).*besselj(n,k(1).*r(r<Radius(1) &
r>0)).*exp(1i.*n.*phi(r<Radius(1) & r>0)).*1i.*n./r(r<Radius(1) & r>0);
                        %TEyr(r>=Radius(1) & r<=Radius(2)) =
TEyr(r>=Radius(1) & r<=Radius(2)) -
1i./(w.*Eta(2)).*(Any(nc,2).*besselj(n,k(2).*r(r>=Radius(1) &
r<=Radius(2)))+Any(nc,3).*besselh(n,k(2).*r(r>=Radius(1) &
r<=Radius(2)))).*exp(1i.*n.*phi(r>=Radius(1) &
r<=Radius(2))).*1i.*n./r(r>=Radius(1) & r<=Radius(2));
                        %TEyr(r>Radius(2))=TEyr(r>Radius(2))-
1i./(w.*Eta(3)).*Any(nc,1).*besselh(n,k(3).*r(r>Radius(2))).*exp(1i.*n.
*phi(r>Radius(2))).*1i.*n./r(r>Radius(2));
                        TEyp=TEyp-
0.5*1i./(w.*Epsilon(2)).*(Any(nc,4).*(besselj(n-1,k(2).*rs))-
besselj(n+1,k(2).*rs)+Any(nc,5).*(besselh(n-1,k(2).*rs)-
besselh(n+1,k(2).*rs)))*k(2);
```

```
                        %TEyp(r>Radius(2)) =
TEyp(r>Radius(2))+0.5*1i./(w.*Eta(3)).*Any(nc,1).*(besselh(n-
1,k(2).*r(r>Radius(2)))-
besselh(n+1,k(3).*r(r>Radius(2)))).*exp(1i.*n.*phi(r>Radius(2)))*k(3);
                    end
                    TEyy=(Byp+TEyp)/(-1i.*w.*u_0);

                    ldos=-
2*w*nb(2)^2/(pi*c_light^2).*imag(TM+TExx+TEyy);
            elseif eq(taker,3)

                [Anx,Any,Anz]=GCSS(w,u_0,M,Eta,taker,k,Radius,rs,nmax);

                    for n=-nmax:nmax
                        %%Green's function calculation
                        Bz = Bz-
(w*u_0/4).*besselh(n,1,k(3)*rs).*besselj(n,k(3).*rs);%r<rs
                        %Bz(r>rs) =
Bz(r>rs)+(1/4i).*exp(1i*n*phi(r>rs)).*besselj(n,k(2)*rs).*besselh(n,1,k
(2).*r(r>rs));%r>rs

                    end

                    %Ez(r>=Radius(1) & r<=Radius(2))=Bz(r>=Radius(1) &
r<=Radius(2));

                    for n=-nmax:nmax
                        nc=n+nmax+1;
                        %%%%%%E%%%%%%%
                        %Ez(r<Radius(1)) = Ez(r<Radius(1))
+Anz(nc,4).*besselj(n,k(1).*r(r<Radius(1))).*exp(1i.*n.*phi(r<Radius(1)
));
                        Ez= Ez +
(Anz(nc,2).*besselj(n,k(3).*rs)+Anz(nc,3).*besselh(n,k(3).*rs));
                        %Ez(r>Radius(2))=Ez(r>Radius(2))-
Anz(nc,1).*besselh(n,k(3).*r(r>Radius(2))).*exp(1i.*n.*phi(r>Radius(2))
);
                    end
                    TM=(Ez+Bz)/(-1i.*w.*u_0);

                    for n=-nmax:nmax
                        %%Green's function calculation
                        %Bx(r<=rs) =
Bx(r<=rs)+(1i*Eta(2)/8).*exp(1i*n*phi(r<=rs)).*(besselh(n-
1,k(2)*rs)+besselh(n+1,k(2)*rs)).*besselj(n,k(2).*r(r<=rs));%r<rs
                        %Bx(r>rs) =
Bx(r>rs)+(1i*Eta(2)/8).*exp(1i*n*phi(r>rs)).*(besselj(n-
1,k(2)*rs)+besselj(n+1,k(2)*rs)).*besselh(n,1,k(2).*r(r>rs));%r>rs
                        %Bxr(r<=rs) =
Bx(r<=rs)+(1i*Eta(2)/8).*exp(1i*n*phi(r<=rs)).*(besselh(n-
1,k(2)*rs)+besselh(n+1,k(2)*rs)).*besselj(n,k(2).*r(r<=rs)).*1i.*n;%r<r
s
```

```
                        Bxr = Bxr+(k(3)/8).*(besselh(n-
1,k(3)*rs)+besselh(n+1,k(3)*rs)).*(besselj(n-
1,k(3).*rs)+besselj(n+1,k(3).*rs)).*0.5.*1i.*k(3);
                        %Bxr(r>rs) =
Bx(r>rs)+(1i*Eta(2)/8).*exp(1i*n*phi(r>rs)).*(besselj(n-
1,k(2)*rs)+besselj(n+1,k(2)*rs)).*besselh(n,1,k(2).*r(r>rs)).*1i.*n;%r>
rs
                        %Bxp(r<=rs)=Bxp(r<=rs)-
(1i*Eta(2)/8).*exp(1i*n*phi(r<=rs)).*(besselh(n-
1,k(2)*rs)+besselh(n+1,k(2)*rs)).*0.5.*(besselj(n-1,k(2).*r(r<=rs))-
besselj(n+1,k(2).*r(r<=rs)));
                        %Bxp(r>rs)=Bxp(r>rs)-
(1i*Eta(2)/8).*exp(1i*n*phi(r>rs)).*(besselj(n-
1,k(2)*rs)+besselj(n+1,k(2)*rs)).*0.5.*(besselh(n-1,k(2).*r(r>rs))-
besselh(n+1,k(2).*r(r>rs)));

                    end

                    %Ex(r>=Radius(1) & r<=Radius(2))=Bx(r>=Radius(1) &
r<=Radius(2));
                    %TExr(r>=Radius(1) & r<=Radius(2))=Bx(r>=Radius(1)
& r<=Radius(2)).*(1i./(w.*Eta(2)))./r(r>=Radius(1) & r<=Radius(2));
                    %TExp(r>=Radius(1) & r<=Radius(2))=Bxp(r>=Radius(1)
& r<=Radius(2)).*1i./(w.*Eta(2)).*k(2);
                    Bxr=Bxr.*(1i/(w.*Epsilon(3)));
                    for n=-nmax:nmax
                        nc=n+nmax+1;
                        %%%%%%E%%%%%%%
                        %Ex(r<Radius(1)) = Ex(r<Radius(1))
+Anx(nc,4).*besselj(n,k(1).*r(r<Radius(1))).*exp(1i.*n.*phi(r<Radius(1)
));
                        %Ex(r>=Radius(1)& r<=Radius(2)) =
Ex(r>=Radius(1)& r<=Radius(2)) +
(Anx(nc,2).*besselj(n,k(2).*r(r>=Radius(1)&
r<=Radius(2)))+Anx(nc,3).*besselh(n,k(2).*r(r>=Radius(1)&
r<=Radius(2)))).*exp(1i.*n.*phi(r>=Radius(1)& r<=Radius(2)));
                        %Ex(r>Radius(2))=Ex(r>Radius(2))-
Anx(nc,1).*besselh(n,k(3).*r(r>Radius(2))).*exp(1i.*n.*phi(r>Radius(2))
);
                        %%%%%%%%%%%%Electric Field%%%%%%%
                        %TExr(r<Radius(1) & r>0) = TExr(r<Radius(1) &
r>0) +1i./(w.*Eta(1)).*Anx(nc,4).*besselj(n,k(1).*r(r<Radius(1) &
r>0)).*exp(1i.*n.*phi(r<Radius(1) & r>0)).*1i.*n./r(r<Radius(1) & r>0);
                        TExr = TExr+
1i./(w.*Epsilon(3)).*(Anx(nc,2).*(besselj(n-
1,k(3).*rs)+besselj(n+1,k(3).*rs))+Anx(nc,3).*(besselh(n-
1,k(3).*rs)+besselh(n+1,k(3).*rs))).*1i*0.5*k(3);
                        %TExr(r>Radius(2))=TExr(r>Radius(2))-
1i./(w.*Eta(3)).*Anx(nc,1).*besselh(n,k(3).*r(r>Radius(2))).*exp(1i.*n.
*phi(r>Radius(2))).*1i.*n./r(r>Radius(2));
                        %TExp(r<Radius(1)) = TExp(r<Radius(1))-
0.5*1i./(w.*Eta(1)).*Anx(nc,4).*(besselj(n-1,k(1).*r(r<Radius(1)))-
besselj(n+1,k(1).*r(r<Radius(1)))).*exp(1i.*n.*phi(r<Radius(1)))*k(1);
```

```
                        %TExp(r>=Radius(1) &
r<=Radius(2))=TExp(r>=Radius(1) & r<=Radius(2))-
0.5*1i./(w.*Eta(2)).*(Anx(nc,2).*(besselj(n-1,k(2).*r(r>=Radius(1) &
r<=Radius(2)))-besselj(n+1,k(2).*r(r>=Radius(1) &
r<=Radius(2))))+Anx(nc,3).*(besselh(n-1,k(2).*r(r>=Radius(1) &
r<=Radius(2)))-besselh(n+1,k(2).*r(r>=Radius(1) &
r<=Radius(2))))).*exp(1i.*n.*phi(r>=Radius(1) & r<=Radius(2)))*k(2);
                        %TExp(r>Radius(2)) =
TExp(r>Radius(2))+0.5*1i./(w.*Eta(3)).*Anx(nc,1).*(besselh(n-
1,k(2).*r(r>Radius(2)))-
besselh(n+1,k(3).*r(r>Radius(2)))).*exp(1i.*n.*phi(r>Radius(2)))*k(3);
                    end
                    TExx= (Bxr+TExr)/(-1i.*w.*u_0);

                    for n=-nmax:nmax
                        %%Green's function calculation
                        %By(r<=rs) =
By(r<=rs)+(1*Eta(1)/8).*exp(1i*n*phi(r<=rs)).*(besselh(n-1,k(1)*rs)-
besselh(n+1,k(1)*rs)).*besselj(n,k(1).*r(r<=rs));%r<rs
                        %By(r>rs) =
By(r>rs)+(1*Eta(1)/8).*exp(1i*n*phi(r>rs)).*(besselj(n-1,k(1)*rs)-
besselj(n+1,k(1)*rs)).*besselh(n,1,k(1).*r(r>rs));%r>rs
                        %Byr(r<=rs) =
By(r<=rs)+(1*Eta(1)/8).*exp(1i*n*phi(r<=rs)).*(besselh(n-1,k(1)*rs)-
besselh(n+1,k(1)*rs)).*besselj(n,k(1).*r(r<=rs)).*1i.*n;%r<rs
                        %Byr(r>rs) =
By(r>rs)+(1*Eta(1)/8).*exp(1i*n*phi(r>rs)).*(besselj(n-1,k(1)*rs)-
besselj(n+1,k(1)*rs)).*besselh(n,1,k(1).*r(r>rs)).*1i.*n;%r>rs
                        %Byp(r<=rs)=Byp(r<=rs)-
(1*Eta(1)/8).*exp(1i*n*phi(r<=rs)).*(besselh(n-1,k(1)*rs)-
besselh(n+1,k(1)*rs)).*0.5.*(besselj(n-1,k(1).*r(r<=rs))-
besselj(n+1,k(1).*r(r<=rs)));
                        Byp=Byp-(k(3)/8i).*(besselj(n-1,k(3)*rs)-
besselj(n+1,k(3)*rs)).*0.5.*(besselh(n-1,k(3).*rs)-
besselh(n+1,k(3).*rs));
                        %Byp(r>rs)=Byp(r>rs)-
(1*Eta(1)/8).*exp(1i*n*phi(r>rs)).*(besselj(n-1,k(1)*rs)-
besselj(n+1,k(1)*rs)).*0.5.*(besselh(n-1,k(1).*r(r>rs))-
besselh(n+1,k(1).*r(r>rs)));
                    end

                    %Ey(r<Radius(1))=By(r<Radius(1));
                    %TEyr(r<=Radius(1) & r>0)=Byr(r<=Radius(1) &
r>0).*(1i./(w.*Eta(1)))./r(r<=Radius(1) & r>0);
                    %TEyp(r<=Radius(1))=Byp(r<=Radius(1)).*1i./(w.*Eta(
1)).*k(1);
                    Byp=Byp.*1i/(w.*Epsilon(3)).*k(3);

                    for n=-nmax:nmax
                        nc=n+nmax+1;
                        %%%%%%E%%%%%%%
```

```
                        %Ey(r<Radius(1)) = Ey(r<Radius(1))
+Any(nc,4).*besselj(n,k(1).*r(r<Radius(1))).*exp(1i.*n.*phi(r<Radius(1)
));
                        %Ey(r>=Radius(1)& r<=Radius(2)) =
Ey(r>=Radius(1)& r<=Radius(2)) +
(Any(nc,2).*besselj(n,k(2).*r(r>=Radius(1)&
r<=Radius(2)))+Any(nc,3).*besselh(n,k(2).*r(r>=Radius(1)&
r<=Radius(2)))).*exp(1i.*n.*phi(r>=Radius(1)& r<=Radius(2)));
                        %Ey(r>Radius(2))=Ey(r>Radius(2))-
Any(nc,1).*besselh(n,k(3).*r(r>Radius(2))).*exp(1i.*n.*phi(r>Radius(2))
);
                        %%%%%%%%%%%%%%%Electric
Field%%%%%%%%%%%%%%%%%%%%
                        %TEyr(r<Radius(1) & r>0) = TEyr(r<Radius(1) &
r>0) +1i./(w.*Eta(1)).*Any(nc,4).*besselj(n,k(1).*r(r<Radius(1) &
r>0)).*exp(1i.*n.*phi(r<Radius(1) & r>0)).*1i.*n./r(r<Radius(1) & r>0);
                        %TEyr(r>=Radius(1) & r<=Radius(2)) =
TEyr(r>=Radius(1) & r<=Radius(2)) -
1i./(w.*Eta(2)).*(Any(nc,2).*besselj(n,k(2).*r(r>=Radius(1) &
r<=Radius(2)))+Any(nc,3).*besselh(n,k(2).*r(r>=Radius(1) &
r<=Radius(2)))).*exp(1i.*n.*phi(r>=Radius(1) &
r<=Radius(2))).*1i.*n./r(r>=Radius(1) & r<=Radius(2));
                        %TEyr(r>Radius(2))=TEyr(r>Radius(2))-
1i./(w.*Eta(3)).*Any(nc,1).*besselh(n,k(3).*r(r>Radius(2))).*exp(1i.*n.
*phi(r>Radius(2))).*1i.*n./r(r>Radius(2));
                        TEyp=TEyp-
0.5*1i./(w.*Epsilon(3)).*(Any(nc,2).*(besselj(n-1,k(3).*rs))-
besselj(n+1,k(3).*rs)+Any(nc,3).*(besselh(n-1,k(3).*rs)-
besselh(n+1,k(3).*rs)))*k(3);
                        %TEyp(r>Radius(2)) =
TEyp(r>Radius(2))+0.5*1i./(w.*Eta(3)).*Any(nc,1).*(besselh(n-
1,k(2).*r(r>Radius(2)))-
besselh(n+1,k(3).*r(r>Radius(2)))).*exp(1i.*n.*phi(r>Radius(2)))*k(3);
                    end
                    TEyy=(Byp+TEyp)/(-1i.*w.*u_0);

                    ldos=-
2*w*nb(3)^2/(pi*c_light^2).*imag(TM+TExx+TEyy);


            else

                [Anx,Any,Anz]=GCSS(w,u_0,M,Eta,taker,k,Radius,rs,nmax);

                    for n=-nmax:nmax
                        %%Green's function calculation
                        Bz = Bz-
w*u_0/4.*besselh(n,1,k(4)*rs).*besselj(n,k(4).*rs);%r<rs
                        %Bz(r>rs) =
Bz(r>rs)+(1/4i).*exp(1i*n*phi(r>rs)).*besselj(n,k(3)*rs).*besselh(n,1,k
(3).*r(r>rs));%r>rs

                    end
```

```
                    %Ez(r>Radius(2))=Bz(r>Radius(2));

                    for n=-nmax:nmax
                        nc=n+nmax+1;
                        %%%%%%E%%%%%%%
                        %Ez(r<Radius(1)) = Ez(r<Radius(1))
+Anz(nc,4).*besselj(n,k(1).*r(r<Radius(1))).*exp(1i.*n.*phi(r<Radius(1)
));
                        %Ez(r>=Radius(1)& r<=Radius(2)) =
Ez(r>=Radius(1)& r<=Radius(2)) +
(Anz(nc,2).*besselj(n,k(2).*r(r>=Radius(1)&
r<=Radius(2)))+Anz(nc,3).*besselh(n,k(2).*r(r>=Radius(1)&
r<=Radius(2)))).*exp(1i.*n.*phi(r>=Radius(1)& r<=Radius(2)));
                        Ez=Ez-Anz(nc,1).*besselh(n,k(4).*rs);
                    end
                    TM=(Ez+Bz)/(-1i.*w.*u_0);

                    for n=-nmax:nmax
                        %%Green's function calculation
                        %Bx(r<=rs) =
Bx(r<=rs)+(1i*Eta(2)/8).*exp(1i*n*phi(r<=rs)).*(besselh(n-
1,k(2)*rs)+besselh(n+1,k(2)*rs)).*besselj(n,k(2).*r(r<=rs));%r<rs
                        %Bx(r>rs) =
Bx(r>rs)+(1i*Eta(2)/8).*exp(1i*n*phi(r>rs)).*(besselj(n-
1,k(2)*rs)+besselj(n+1,k(2)*rs)).*besselh(n,1,k(2).*r(r>rs));%r>rs
                        %Bxr(r<=rs) =
Bx(r<=rs)+(1i*Eta(2)/8).*exp(1i*n*phi(r<=rs)).*(besselh(n-
1,k(2)*rs)+besselh(n+1,k(2)*rs)).*besselj(n,k(2).*r(r<=rs)).*1i.*n;%r<r
s
                        Bxr = Bxr+(k(4)/8).*(besselh(n-
1,k(4)*rs)+besselh(n+1,k(4)*rs)).*(besselj(n-
1,k(4).*rs)+besselj(n+1,k(4).*rs)).*0.5.*1i.*k(4);
                        %Bxr(r>rs) =
Bx(r>rs)+(1i*Eta(2)/8).*exp(1i*n*phi(r>rs)).*(besselj(n-
1,k(2)*rs)+besselj(n+1,k(2)*rs)).*besselh(n,1,k(2).*r(r>rs)).*1i.*n;%r>
rs
                        %Bxp(r<=rs)=Bxp(r<=rs)-
(1i*Eta(2)/8).*exp(1i*n*phi(r<=rs)).*(besselh(n-
1,k(2)*rs)+besselh(n+1,k(2)*rs)).*0.5.*(besselj(n-1,k(2).*r(r<=rs))-
besselj(n+1,k(2).*r(r<=rs)));
                        %Bxp(r>rs)=Bxp(r>rs)-
(1i*Eta(2)/8).*exp(1i*n*phi(r>rs)).*(besselj(n-
1,k(2)*rs)+besselj(n+1,k(2)*rs)).*0.5.*(besselh(n-1,k(2).*r(r>rs))-
besselh(n+1,k(2).*r(r>rs)));

                    end

                    %Ex(r>=Radius(1) & r<=Radius(2))=Bx(r>=Radius(1) &
r<=Radius(2));
                    %TExr(r>=Radius(1) & r<=Radius(2))=Bx(r>=Radius(1)
& r<=Radius(2)).*(1i./(w.*Eta(2)))./r(r>=Radius(1) & r<=Radius(2));
```

```
                    %TExp(r>=Radius(1) & r<=Radius(2))=Bxp(r>=Radius(1)
& r<=Radius(2)).*1i./(w.*Eta(2)).*k(2);
                    Bxr=Bxr.*(1i/(w.*Epsilon(4)));
                    for n=-nmax:nmax
                        nc=n+nmax+1;
                        %%%%%%E%%%%%%%
                        %Ex(r<Radius(1)) = Ex(r<Radius(1))
+Anx(nc,4).*besselj(n,k(1).*r(r<Radius(1))).*exp(1i.*n.*phi(r<Radius(1)
));
                        %Ex(r>=Radius(1)& r<=Radius(2)) =
Ex(r>=Radius(1)& r<=Radius(2)) +
(Anx(nc,2).*besselj(n,k(2).*r(r>=Radius(1)&
r<=Radius(2)))+Anx(nc,3).*besselh(n,k(2).*r(r>=Radius(1)&
r<=Radius(2)))).*exp(1i.*n.*phi(r>=Radius(1)& r<=Radius(2)));
                        %Ex(r>Radius(2))=Ex(r>Radius(2))-
Anx(nc,1).*besselh(n,k(3).*r(r>Radius(2))).*exp(1i.*n.*phi(r>Radius(2))
);
                        %%%%%%%%%%%Electric Field%%%%%%%
                        %TExr(r<Radius(1) & r>0) = TExr(r<Radius(1) &
r>0) +1i./(w.*Eta(1)).*Anx(nc,4).*besselj(n,k(1).*r(r<Radius(1) &
r>0)).*exp(1i.*n.*phi(r<Radius(1) & r>0)).*1i.*n./r(r<Radius(1) & r>0);
                        %TExr = TExr+
1i./(w.*Epsilon(3)).*(Anx(nc,2).*(besselj(n-
1,k(3).*rs)+besselj(n+1,k(3).*rs))+Anx(nc,3).*(besselh(n-
1,k(2).*rs)+besselh(n+1,k(2).*rs))).*1i*0.5*k(2);
                        TExr=TExr-
1i./(w.*Epsilon(4)).*Anx(nc,1).*besselh(n,k(4).*rs).*1i.*n./rs;
                        %TExp(r<Radius(1)) = TExp(r<Radius(1))-
0.5*1i./(w.*Eta(1)).*Anx(nc,4).*(besselj(n-1,k(1).*r(r<Radius(1)))-
besselj(n+1,k(1).*r(r<Radius(1)))).*exp(1i.*n.*phi(r<Radius(1)))*k(1);
                        %TExp(r>=Radius(1) &
r<=Radius(2))=TExp(r>=Radius(1) & r<=Radius(2))-
0.5*1i./(w.*Eta(2)).*(Anx(nc,2).*(besselj(n-1,k(2).*r(r>=Radius(1) &
r<=Radius(2)))-besselj(n+1,k(2).*r(r>=Radius(1) &
r<=Radius(2))))+Anx(nc,3).*(besselh(n-1,k(2).*r(r>=Radius(1) &
r<=Radius(2)))-besselh(n+1,k(2).*r(r>=Radius(1) &
r<=Radius(2))))).*exp(1i.*n.*phi(r>=Radius(1) & r<=Radius(2)))*k(2);
                        %TExp(r>Radius(2)) =
TExp(r>Radius(2))+0.5*1i./(w.*Eta(3)).*Anx(nc,1).*(besselh(n-
1,k(2).*r(r>Radius(2)))-
besselh(n+1,k(3).*r(r>Radius(2)))).*exp(1i.*n.*phi(r>Radius(2)))*k(3);
                    end
                    TExx= (Bxr+TExr)/(-1i.*w.*u_0);
                    for n=-nmax:nmax
                        %%Green's function calculation
                        %By(r<=rs) =
By(r<=rs)+(1*Eta(3)/8).*exp(1i*n*phi(r<=rs)).*(besselh(n-1,k(3)*rs)-
besselh(n+1,k(3)*rs)).*besselj(n,k(3).*r(r<=rs));%r<rs
                        %By(r>rs) =
By(r>rs)+(1*Eta(3)/8).*exp(1i*n*phi(r>rs)).*(besselj(n-1,k(3)*rs)-
besselj(n+1,k(3)*rs)).*besselh(n,1,k(3).*r(r>rs));%r>rs
                        %Byr(r<=rs) =
By(r<=rs)+(1*Eta(3)/8).*exp(1i*n*phi(r<=rs)).*(besselh(n-1,k(3)*rs)-
besselh(n+1,k(3)*rs)).*besselj(n,k(1).*r(r<=rs)).*1i.*n;%r<rs
```

```
                        %Byr(r>rs) =
By(r>rs)+(1*Eta(3)/8).*exp(1i*n*phi(r>rs)).*(besselj(n-1,k(3)*rs)-
besselj(n+1,k(3)*rs)).*besselh(n,1,k(1).*r(r>rs)).*1i.*n;%r>rs
                        %Byp(r<=rs)=Byp(r<=rs)-
(1*Eta(3)/8).*exp(1i*n*phi(r<=rs)).*(besselh(n-1,k(3)*rs)-
besselh(n+1,k(3)*rs)).*0.5.*(besselj(n-1,k(3).*r(r<=rs))-
besselj(n+1,k(3).*r(r<=rs)));
                        Byp=Byp-(k(4)/8i).*(besselh(n-1,k(4)*rs)-
besselh(n+1,k(4)*rs)).*0.5.*(besselj(n-1,k(4).*rs)-
besselj(n+1,k(4).*rs));
                        %Byp(r>rs)=Byp(r>rs)-
(1*Eta(3)/8).*exp(1i*n*phi(r>rs)).*(besselj(n-1,k(3)*rs)-
besselj(n+1,k(3)*rs)).*0.5.*(besselh(n-1,k(3).*r(r>rs))-
besselh(n+1,k(3).*r(r>rs)));
                    end

                    %Ey(r>Radius(2))=By(r>Radius(2));
                    %TEyr(r>Radius(2))=Byr(r>Radius(2)).*(1i./(w.*Eta(3
))))./r(r>Radius(2));
                    Byp=Byp.*1i./(w.*Epsilon(4)).*k(4);

                    for n=-nmax:nmax
                        nc=n+nmax+1;
                        %%%%%%E%%%%%%%
                        %Ey(r<Radius(1)) = Ey(r<Radius(1))
+Any(nc,4).*besselj(n,k(1).*r(r<Radius(1))).*exp(1i.*n.*phi(r<Radius(1)
));
                        %Ey(r>=Radius(1)& r<=Radius(2)) =
Ey(r>=Radius(1)& r<=Radius(2)) +
(Any(nc,2).*besselj(n,k(2).*r(r>=Radius(1)&
r<=Radius(2)))+Any(nc,3).*besselh(n,k(2).*r(r>=Radius(1)&
r<=Radius(2)))).*exp(1i.*n.*phi(r>=Radius(1)& r<=Radius(2)));
                        %Ey(r>Radius(2))=Ey(r>Radius(2))-
Any(nc,1).*besselh(n,k(3).*r(r>Radius(2))).*exp(1i.*n.*phi(r>Radius(2))
);
                        %%%%%%%%%%%%%%Electric
Field%%%%%%%%%%%%%%%%%%%
                        %TEyr(r<Radius(1) & r>0) = TEyr(r<Radius(1) &
r>0) +1i./(w.*Eta(1)).*Any(nc,4).*besselj(n,k(1).*r(r<Radius(1) &
r>0)).*exp(1i.*n.*phi(r<Radius(1) & r>0)).*1i.*n./r(r<Radius(1) & r>0);
                        %TEyr(r>=Radius(1) & r<=Radius(2)) =
TEyr(r>=Radius(1) & r<=Radius(2)) -
1i./(w.*Eta(2)).*(Any(nc,2).*besselj(n,k(2).*r(r>=Radius(1) &
r<=Radius(2)))+Any(nc,3).*besselh(n,k(2).*r(r>=Radius(1) &
r<=Radius(2)))).*exp(1i.*n.*phi(r>=Radius(1) &
r<=Radius(2))).*1i.*n./r(r>=Radius(1) & r<=Radius(2));
                        %TEyr(r>Radius(2))=TEyr(r>Radius(2))-
1i./(w.*Eta(3)).*Any(nc,1).*besselh(n,k(3).*r(r>Radius(2))).*exp(1i.*n.
*phi(r>Radius(2))).*1i.*n./r(r>Radius(2));
                        %TEyp(r<Radius(1)) = TEyp(r<Radius(1))-
0.5*1i./(w.*Eta(1)).*Any(nc,4).*(besselj(n-1,k(1).*r(r<Radius(1)))-
besselj(n+1,k(1).*r(r<Radius(1)))).*exp(1i.*n.*phi(r<Radius(1)))*k(1);
```

```
                        %TEyp(r>=Radius(1) &
r<=Radius(2))=TEyp(r>=Radius(1) & r<=Radius(2))-
0.5*1i./(w.*Eta(2)).*(Any(nc,2).*(besselj(n-1,k(2).*r(r>=Radius(1) &
r<=Radius(2)))-besselj(n+1,k(2).*r(r>=Radius(1) &
r<=Radius(2))))+Any(nc,3).*(besselh(n-1,k(2).*r(r>=Radius(1) &
r<=Radius(2)))-besselh(n+1,k(2).*r(r>=Radius(1) &
r<=Radius(2))))).*exp(1i.*n.*phi(r>=Radius(1) & r<=Radius(2)))*k(2);
                        TEyp =
TEyp+0.5*1i./(w.*Epsilon(4)).*Any(nc,1).*(besselh(n-1,k(4).*rs)-
besselh(n+1,k(4).*rs)).*k(4);
                    end
                    TEyy=(Byp+TEyp)/(-1i.*w.*u_0);
                    ldos=-
2*w*nb(4)^2/(pi*c_light^2).*imag(TM+TExx+TEyy);
            end
end
```

- **Function QCSS:**

```
function
[bn,an]=QCSS(a,b,c,k_0,k_1,k_2,k_3,eta_0,eta_1,eta_2,eta_3,nmax)
%returns the Mie coefficients. For TM - bn(wavelength,n,:)
bn=zeros(2*nmax+1,6);
an=zeros(2*nmax+1,6);
    for n=-nmax:nmax
        nl=n+nmax+1;
        Z_1=[besselj(n,k_3*c), bessely(n,k_3*c), besselh(n,k_0*c), 0,
0, 0];
        Z_2=[(0.5/eta_3)*(besselj(n-1,k_3*c)-besselj(n+1,k_3*c)),
(0.5/eta_3)*(bessely(n-1,k_3*c)-bessely(n+1,k_3*c)),
(0.5/eta_0)*(besselh(n-1,k_0*c)-besselh(n+1,k_0*c)), 0, 0, 0];
        Z_3=[besselj(n,k_3*b), bessely(n,k_3*b), 0, -besselj(n,k_2*b),
-bessely(n,k_2*b), 0];
        Z_4=[(0.5/eta_3)*(besselj(n-1,k_3*b)-besselj(n+1,k_3*b)),
(0.5/eta_3)*(bessely(n-1,k_3*b)-bessely(n+1,k_3*b)), 0, (-
0.5/eta_2)*(besselj(n-1,k_2*b)-besselj(n+1,k_2*b)), (-
0.5/eta_2)*(bessely(n-1,k_2*b)-bessely(n+1,k_2*b)), 0];
        Z_5=[0, 0, 0, besselj(n,k_2*a), bessely(n,k_2*a), -
besselj(n,k_1*a)];
        Z_6=[0, 0, 0, (0.5/eta_2)*(besselj(n-1,k_2*a)-
besselj(n+1,k_2*a)), (0.5/eta_2)*(bessely(n-1,k_2*a)-
bessely(n+1,k_2*a)), (-0.5/eta_1)*(besselj(n-1,k_1*a)-
besselj(n+1,k_1*a))];
        Z=[Z_1; Z_2; Z_3; Z_4; Z_5; Z_6];

        A=[besselj(n,k_0*c); (0.5/eta_0)*(besselj(n-1,k_0*c)-
besselj(n+1,k_0*c)); 0; 0; 0; 0];
        bn(nl,:)=Z\A;



        Z_1=[besselj(n,k_3*c), bessely(n,k_3*c), besselh(n,k_0*c), 0,
0, 0];
```

```
        Z_2=[(0.5*eta_3)*(besselj(n-1,k_3*c)-besselj(n+1,k_3*c)),
(0.5*eta_3)*(bessely(n-1,k_3*c)-bessely(n+1,k_3*c)),
(0.5*eta_0)*(besselh(n-1,k_0*c)-besselh(n+1,k_0*c)), 0, 0, 0];
        Z_3=[besselj(n,k_3*b), bessely(n,k_3*b), 0, -besselj(n,k_2*b),
-bessely(n,k_2*b), 0];
        Z_4=[(0.5*eta_3)*(besselj(n-1,k_3*b)-besselj(n+1,k_3*b)),
(0.5*eta_3)*(bessely(n-1,k_3*b)-bessely(n+1,k_3*b)), 0, (-
0.5*eta_2)*(besselj(n-1,k_2*b)-besselj(n+1,k_2*b)), (-
0.5*eta_2)*(bessely(n-1,k_2*b)-bessely(n+1,k_2*b)), 0];
        Z_5=[0, 0, 0, besselj(n,k_2*a), bessely(n,k_2*a), -
besselj(n,k_1*a)];
        Z_6=[0, 0, 0, (0.5*eta_2)*(besselj(n-1,k_2*a)-
besselj(n+1,k_2*a)), (0.5*eta_2)*(bessely(n-1,k_2*a)-
bessely(n+1,k_2*a)), (-0.5*eta_1)*(besselj(n-1,k_1*a)-
besselj(n+1,k_1*a))];
        Z=[Z_1; Z_2; Z_3; Z_4; Z_5; Z_6];

        A=[besselj(n,k_0*c); (0.5*eta_0)*(besselj(n-1,k_0*c)-
besselj(n+1,k_0*c)); 0; 0; 0; 0];
        an(nl,:)=Z\A;
    end
end
```

- **Function QCS:**

```
function [bn,an]=QCS(a,b,k_0,k_1,k_2,eta_0,eta_1,eta_2,nmax)
%returns the Mie coefficients. For TM - bn(wavelength,n,:)
bn=zeros(2*nmax,4);
an=zeros(2*nmax,4);
nl=1;
    for n=-1:2:1
        %nl=n+nmax+1;
        Z_1=[besselj(n,k_2*b), bessely(n,k_2*b), besselh(n,k_0*b), 0];
        Z_2=[(0.5/eta_2)*(besselj(n-1,k_2*b)-besselj(n+1,k_2*b)),
(0.5/eta_2)*(bessely(n-1,k_2*b)-bessely(n+1,k_2*b)),
(0.5/eta_0)*(besselh(n-1,k_0*b)-besselh(n+1,k_0*b)), 0];
        Z_3=[besselj(n,k_2*a), bessely(n,k_2*a), 0, -besselj(n,k_1*a)];
        Z_4=[(0.5/eta_2)*(besselj(n-1,k_2*a)-besselj(n+1,k_2*a)),
(0.5/eta_2)*(bessely(n-1,k_2*a)-bessely(n+1,k_2*a)), 0, (-
0.5/eta_1)*(besselj(n-1,k_1*a)-besselj(n+1,k_1*a))];
        Z=[Z_1; Z_2; Z_3; Z_4];

        A=[besselj(n,k_0*b); (0.5/eta_0)*(besselj(n-1,k_0*b)-
besselj(n+1,k_0*b)); 0; 0];

        bn(nl,:)=Z\A;

        Z_1=[besselj(n,k_2*b), bessely(n,k_2*b), besselh(n,k_0*b), 0];
        Z_2=[(0.5*eta_2)*(besselj(n-1,k_2*b)-besselj(n+1,k_2*b)),
(0.5*eta_2)*(bessely(n-1,k_2*b)-bessely(n+1,k_2*b)),
(0.5*eta_0)*(besselh(n-1,k_0*b)-besselh(n+1,k_0*b)), 0];
        Z_3=[besselj(n,k_2*a), bessely(n,k_2*a), 0, -besselj(n,k_1*a)];
```

```
        Z_4=[(0.5*eta_2)*(besselj(n-1,k_2*a)-besselj(n+1,k_2*a)),
(0.5*eta_2)*(bessely(n-1,k_2*a)-bessely(n+1,k_2*a)), 0, (-
0.5*eta_1)*(besselj(n-1,k_1*a)-besselj(n+1,k_1*a))];
        Z=[Z_1; Z_2; Z_3; Z_4];

        A=[besselj(n,k_0*b); (0.5*eta_0)*(besselj(n-1,k_0*b)-
besselj(n+1,k_0*b)); 0; 0];

        an(nl,:)=Z\A;
       nl=nl+1;
    end
end
```

BIBLIOGRAPHY

1. Bao, Q. L.; Loh, K. P., Graphene Photonics, Plasmonics, and Broadband Optoelectronic Devices. *ACS Nano* **2012,** *6* (5), 3677-3694.
2. Brolo, A. G., Plasmonics for future biosensors. *Nature Photonics* **2012,** *6* (11), 709-713.
3. Cetin, A. E.; Coskun, A. F.; Galarreta, B. C.; Huang, M.; Herman, D.; Ozcan, A.; Altug, H., Handheld high-throughput plasmonic biosensor using computational on-chip imaging. *Ligh, Science & Applications* **2014,** *3*.
4. Liang, Z. Q.; Sun, J.; Jiang, Y. Y.; Jiang, L.; Chen, X. D., Plasmonic Enhanced Optoelectronic Devices. *Plasmonics* **2014,** *9* (4), 859-866.
5. Purkayastha, A.; Srivastava, T.; Jha, R., Ultrasensitive THz - Plasmonics gaseous sensor using doped graphene. *Sensors and Actuators B-Chemical* **2016,** *227*, 291-295.
6. Zheng, B. Y.; Wang, Y. M.; Nordlander, P.; Halas, N. J., Color-Selective and CMOS-Compatible Photodetection Based on Aluminum Plasmonics. *Advanced Materials* **2014,** *26* (36), 6318-6323.
7. Zhan, C.; Chen, X. J.; Yi, J.; Li, J. F.; Wu, D. Y.; Tian, Z. Q., From plasmon-enhanced molecular spectroscopy to plasmon-mediated chemical reactions. *Nature Reviews. Chemistry* **2018,** *2* (9), 216-230.
8. Ramadurgam, S.; Lin, T.; Yang, C., Aluminum Plasmonics for Enhanced Visible Light Absorption and High Efficiency Water Splitting in Core-Multishell

Nanowire Photoelectrodes with Ultrathin Hematite Shells. *Nano Letters* **2014,** *14* (8), 4517-4522.

9. Bohn, J.; Bucher, T.; Chong, K. E.; Komar, A.; Choi, D. Y.; Neshev, D. N.; Kivshar, Y. S.; Pertsch, T.; Staude, I., Active Tuning of Spontaneous Emission by Mie-Resonant Dielectric Metasurfaces. *Nano Letters* **2018,** *18* (6), 3461-3465.
10. Kelly, K. L.; Coronado, E.; Zhao, L. L.; Schatz, G. C., The optical properties of metal nanoparticles: The influence of size, shape, and dielectric environment. *Journal of Physical Chemistry B* **2003,** *107* (3), 668-677.
11. Miller, M. M.; Lazarides, A. A., Sensitivity of metal nanoparticle surface plasmon resonance to the dielectric environment. *Journal of Physical Chemistry B* **2005,** *109* (46), 21556-21565.
12. Miller, M. M.; Lazarides, A. A., Sensitivity of metal nanoparticle plasmon resonance band position to the dielectric environment as observed in scattering. *Journal of Optics A: Pure and Applied Optics* **2006,** *8* (4), S239-S249.
13. Wu, D. J.; Liu, X. J.; Li, B., Localized surface plasmon resonance properties of two-layered gold nanowire: Effects of geometry, incidence angle, and polarization. *Journal of Applied Physics* **2011,** *109* (8).
14. Lozano, G.; Louwers, D. J.; Rodriguez, S. R. K.; Murai, S.; Jansen, O. T. A.; Verschuuren, M. A.; Rivas, J. G., Plasmonics for solid-state lighting: enhanced excitation and directional emission of highly efficient light sources. *Light, Science & Applications* **2013,** *2*.

15. Gan, Q. Q.; Bartoli, F. J.; Kafafi, Z. H., Plasmonic-Enhanced Organic Photovoltaics: Breaking the 10% Efficiency Barrier. *Advanced Materials* **2013,** *25* (17), 2385-2396.

16. Muench, J. E.; Ruocco, A.; Giambra, M. A.; Miseikis, V.; Zhang, D. K.; Wang, J. J.; Watson, H. F. Y.; Park, G. C.; Akhavan, S.; Sorianello, V.; Midrio, M.; Tomadin, A.; Coletti, C.; Romagnoli, M.; Ferrari, A. C.; Goykhman, I., Waveguide-Integrated, Plasmonic Enhanced Graphene Photodetectors. *Nano Letters* **2019,** *19* (11), 7632-7644.

17. Jiang, C. Y., Controlled syntheses of gold nanostars for stronger surface enhanced Raman scattering. *Abstracts of Papers – American Chemical Society* **2018,** *255*.

18. Khoury, C. G.; Vo-Dinh, T., Gold Nanostars For Surface-Enhanced Raman Scattering: Synthesis, Characterization and Optimization. *Journal of Physical Chemistry C* **2008,** *112* (48), 18849-18859.

19. Lee, Y.; Nam, K. T., Size-controllable and uniform gold bumpy nanocubes for single-particle-level surface enhanced Raman scattering sensitivity. *Abstracts of Papers – American Chemical Society* **2019,** *258*.

20. Park, J. E.; Lee, Y.; Nam, J. M., Precisely Shaped, Uniformly Formed Gold Nanocubes with Ultrahigh Reproducibility in Single-Particle Scattering and Surface-Enhanced Raman Scattering (vol 18, pg 6475, 2018). *Nano Letters* **2018,** *18* (11), 7419-7419.

21. Bhatia, P.; Verma, S. S.; Sinha, M. M., Tuning the optical properties of Fe-Au core-shell nanoparticles with spherical and spheroidal nanostructures. *Physics Letters. A* **2019,** *383* (21), 2542-2550.

22. Nekic, N.; Sancho-Parramon, J.; Bogdanovic-Radovic, I.; Grenzer, J.; Hubner, R.; Bernstorff, S.; Ivanda, M.; Buljan, M., Ge/Si core/shell quantum dots in alumina: tuning the optical absorption by the core and shell size. *Nanophotonics-Berlin* **2017,** *6* (5), 1055-1062.

23. Sugawa, K.; Sakai, T.; Tanaka, D.; Akiyama, T., Tuning Optical Properties of Two-Dimensional Ordered Arrays of Silica/Gold and Silver Core/Shell Structured Nanoparticles in Near-Infrared Region. *Japanese Journal of Applied Physics* **2012,** *51* (4).

24. Naik, G. V.; Kim, J.; Boltasseva, A., Oxides and nitrides as alternative plasmonic materials in the optical range. *Optical Materials Express* **2011,** *1* (6), 1090-1099.

25. Naik, G. V.; Schroeder, J. L.; Ni, X.; Kildishev, A. V.; Sands, T. D.; Boltasseva, A., Titanium nitride as a plasmonic material for visible and near-infrared wavelengths. *Optical Materials Express* **2012,** *2* (4), 478-489.

26. Lalisse, A.; Tessier, G.; Plain, J.; Baffou, G., Plasmonic efficiencies of nanoparticles made of metal nitrides (TiN, ZrN) compared with gold. *Scientific Reports* **2016,** *6*, 38647.

27. Dutta, A.; Ramadurgam, S.; Yang, C., Plasmonic Core–Multishell Nanowire Phosphors for Light-Emitting Diodes. *ACS Photonics* **2018,** *5*(5), 1853-1862.

28. Novotny, L.; Hecht, B., *Principles of Nano-Optics*. Cambridge University Press: 2012.

29. Economou, E. N., *Green Functions in Quantum Physics*. 1983.

30. Asatryan, A.; Fabre, S.; Busch, K.; McPhedran, R.; Botten, L.; de Sterke, C.; Nicorovici, N., Two-dimensional local density of states in two-dimensional photonic crystals. *Optics Express* **2001,** *8* (3), 191-196.

31. Hummer, T.; Garcia-Vidal, F. J.; Martin-Moreno, L.; Zueco, D., Weak and strong coupling regimes in plasmonic QED. *Physical Review. B* **2013,** *87* (11).

32. Ni, X.; Liu, Z.; Kildishey, A. *PhotonicsDB: Optical Constants*, 2010.

33. Ramadurgam, S.; Lin, T. G.; Yang, C., Aluminum plasmonics for enhanced visible light absorption and high efficiency water splitting in core-multishell nanowire photoelectrodes with ultrathin hematite shells. *Nano Letters* **2014,** *14* (8), 4517-22.

34. Frezza, F.; Mangini, F.; Tedeschi, N., Introduction to electromagnetic scattering: tutorial. *Journal of the Optical Society of America. A* **2018,** *35* (1), 163-173.

35. Lawrence, N.; Dal Negro, L., Light scattering, field localization and local density of states in co-axial plasmonic nanowires. *Optics Express* **2010,** *18* (15), 16120-16132.

36. Narukawa, Y.; Narita, J.; Sakamoto, T.; Yamada, T.; Narimatsu, H.; Sano, M.; Mukai, T., Recent progress of high efficiency white LEDs. *Physica Status Solidi a-Applications and Materials Science* **2007,** *204* (6), 2087-2093.

37. Jang, E.; Jun, S.; Jang, H.; Llim, J.; Kim, B.; Kim, Y., White-Light-Emitting Diodes with Quantum Dot Color Converters for Display Backlights. *Advanced Materials* **2010,** *22* (28), 3076-3080.

38. Ho, H.; Wu, S.; Yang, M.; Cheung, A., Application of white light-emitting diode to surface plasmon resonance sensors. *Sensors and Actuators B-Chemical* **2001,** *80* (2), 89-94.

39. Elgala, H.; Mesleh, R.; Haas, H., Indoor Optical Wireless Communication: Potential and State-of-the-Art. *IEEE Communications Magazine* **2011,** *49* (9), 56-62.

40. Sheu, J.; Chang, S.; Kuo, C.; Su, Y.; Wu, L.; Lin, Y.; Lai, W.; Tsai, J.; Chi, G.; Wu, R., White-light emission from near UV InGaN-GaN LED chip precoated with blue/green/red phosphors. *IEEE Photonics Technology Letters* **2003,** *15* (1), 18-20.

41. Jang, H.; Bin Im, W.; Lee, D.; Jeon, D.; Kim, S., Enhancement of red spectral emission intensity of Y3Al5O12 : Ce3+ phosphor via Pr co-doping and Tb substitution for the application to white LEDs. *Journal of Luminescence* **2007,** *126* (2), 371-377.

42. Kim, J.; Jeon, P.; Choi, J.; Park, H.; Mho, S.; Kim, G., Warm-white-light emitting diode utilizing a single-phase full-color Ba3MgSi2O8 : Eu2+, Mn2+ phosphor. *Applied Physics Letters* **2004,** *84* (15), 2931-2933.

43. Schlotter, P.; Schmidt, R.; Schneider, J., Luminescence conversion of blue light emitting diodes. *Applied Physics A-Materials Science & Processing* **1997,** *64* (4), 417-418.

44. Tamura, T.; Setomoto, T.; Taguchi, T., Illumination characteristics of lighting array using 10 candela-class white LEDs under AC 100 V operation. *Journal of Luminescence* **2000,** *87-9*, 1180-1182.

45. Moustakas, T.; Paiella, R., Optoelectronic device physics and technology of nitride semiconductors from the UV to the terahertz. *Reports on Progress in Physics* **2017,** *80* (10).

46. Brodrick, J. *DOE SSL Program, "R&D Plan"*.

47. Jang, H.; Yang, H.; Kim, S.; Han, J.; Lee, S.; Jeon, D., White light-emitting diodes with excellent color rendering based on organically capped CdSe quantum dots and Sr3SiO5 : Ce3+, Li+ phosphors. *Advanced Materials* **2008,** *20* (14), 2696-+.

48. Nizamoglu, S.; Zengin, G.; Demir, H., Color-converting combinations of nanocrystal emitters for warm-white light generation with high color rendering index. *Applied Physics Letters* **2008,** *92* (3).

49. Sapra, S.; Mayilo, S.; Klar, T.; Rogach, A.; Feldmann, J., Bright white-light emission from semiconductor nanocrystals: by chance and by design. *Advanced Materials* **2007,** *19* (4), 569-+.

50. Vasudevan, D.; Gaddam, R.; Trinchi, A.; Cole, I., Core-shell quantum dots: Properties and applications. *Journal of Alloys and Compounds* **2015,** *636*, 395-404.

51. Lin, Q.; Song, B.; Wang, H.; Zhang, F.; Chen, F.; Wang, L.; Li, L.; Guo, F.; Shen, H., High-efficiency deep-red quantum-dot light-emitting diodes with type-II CdSe/CdTe core/shell quantum dots as emissive layers. *Journal of Materials Chemistry C* **2016,** *4* (30), 7223-7229.

52. Shen, H.; Cao, W.; Shewmon, N.; Yang, C.; Li, L.; Xue, J., High-Efficiency, Low Turn-on Voltage Blue-Violet Quantum-Dot-Based Light-Emitting Diodes. *Nano Letters* **2015,** *15* (2), 1211-1216.

53. Landes, C.; Braun, M.; Burda, C.; El-Sayed, M., Observation of large changes in the band gap absorption energy of small CdSe nanoparticles induced by the adsorption of a strong hole acceptor. *Nano Letters* **2001,** *1* (11), 667-670.

54. Rogach, A.; Kornowski, A.; Gao, M.; Eychmuller, A.; Weller, H., Synthesis and characterization of a size series of extremely small thiol-stabilized CdSe nanocrystals. *Journal of Physical Chemistry B* **1999,** *103* (16), 3065-3069.

55. Gaigalas, A.; DeRose, P.; Wang, L.; Zhang, Y., Optical Properties of CdSe/ZnS Nanocrystals. *Journal of Research of the National Institute of Standards and Technology* **2014,** *119,* 610-628.

56. Giblin, J.; Kuno, M., Nanostructure Absorption: A Comparative Study of Nanowire and Colloidal Quantum Dot Absorption Cross Sections. *Journal of Physical Chemistry Letters* **2010,** *1* (23), 3340-3348.

57. Boriskina, S. V.; Tong, J. K.; Hsu, W. C.; Liao, B. L.; Huang, Y.; Chiloyan, V.; Chen, G., Heat meets light on the nanoscale. *Nanophotonics-Berlin* **2016,** *5* (1), 134-160.

58. Chance, R. R.; Prock, A.; Silbey, R., Comments on Classical Theory of Energy-Transfer. *Journal of Chemical Physics* **1975,** *62* (6), 2245-2253.

59. Yoshikawa, A.; Kobayashi, M.; Tokita, S., Surface-Reaction Mechanism in Mombe-Ale of Znse and Cdse as Determined by a New in-Situ Optical Probing Method. *Applied Surface Science* **1994,** *82-3*, 316-321.

60. Canneson, D.; Mallek-Zouari, I.; Buil, S.; Quelin, X.; Javaux, C.; Mahler, B.; Dubertret, B.; Hermier, J., Strong Purcell effect observed in single thick-shell CdSe/CdS nanocrystals coupled to localized surface plasmons. *Physical Review B* **2011,** *84* (24).

61. Lee, H. M.; Cheng, C. C.; Huang, C. Y., The synthesis and optical property of solid-state-prepared YAG:Ce phosphor by a spray-drying method. *Materials Research Bulletin* **2009,** *44* (5), 1081-1085.

62. Chao, W. H.; Wu, R. J.; Tsai, C. S.; Wu, T. B., Surface plasmon-enhanced emission from Ag-coated Ce doped Y3Al5O12 thin films phosphor capped with a dielectric layer of SiO2. *Journal of Applied Physics* **2010,** *107* (1).

63. Ramadurgam, S.; Yang, C., Semiconductor-Metal-Semiconductor Core-Multishell Nanowires as Negative-Index Metamaterial in Visible Domain. *Scientific Reports* **2014,** *4*.

64. Prodan, E.; Radloff, C.; Halas, N.; Nordlander, P., A hybridization model for the plasmon response of complex nanostructures. *Science* **2003,** *302* (5644), 419-422.

65. Li, L. S.; Alivisatos, A. P., Origin and scaling of the permanent dipole moment in CdSe nanorods. *Physical Review Letters* **2003,** *90* (9).

66. Kim, J. Y.; Han, M. G.; Lien, M. B.; Magonov, S.; Zhu, Y. M.; George, H.; Norris, T. B.; Kotov, N. A., Dipole-like electrostatic asymmetry of gold nanorods. *Science Advances* **2018,** *4* (2).

67. Henneghien, A. L.; Tourbot, G.; Daudin, B.; Lartigue, O.; Desieres, Y.; Gerard, J. M., Optical anisotropy and light extraction efficiency of MBE grown GaN nanowires epilayers. *Optics Express* **2011,** *19* (2), 527-539.

68. Versteegh, M. A. M.; Reimer, M. E.; Jons, K. D.; Dalacu, D.; Poole, P. J.; Gulinatti, A.; Giudice, A.; Zwiller, V., Observation of strongly entangled photon pairs from a nanowire quantum dot. *Nature Communications* **2014,** *5*.

69. Henneghien, A. L.; Gayral, B.; Desieres, Y.; Gerard, J. M., Simulation of waveguiding and emitting properties of semiconductor nanowires with hexagonal or circular sections. *Journal of the Optical Society of America. B* **2009,** *26* (12), 2396-2403.

70. Soer, W., High luminance LEDs: LED- and luminaire-level performance. *DOE SSL Technology Development Workshop* **2017**.

71. Hansen, K.; Dutta, A.; Cardona, M.; Yang, C., Zirconium Nitride for Plasmonic Cloaking of Visible Nanowire Photodetectors. *Plasmonics* **2020,** *15* (5), 1231-1241.

72. Cansizoglu, H.; Cansizoglu, M. F.; Watanabe, F.; Karabacak, T., Enhanced photocurrent and dynamic response in vertically aligned In(2)S(3)/Ag core/shell nanorod array photoconductive devices. *ACS Applied Materials & Interfaces* **2014,** *6* (11), 8673-8682.

73. Vj, L.; Oh, J.; Nayak, A. P.; Katzenmeyer, A. M.; Gilchrist, K. H.; Grego, S.; Kobayashi, N. P.; Wang, S.-Y.; Talin, A. A.; Dhar, N. K.; Islam, M. S., A Perspective on Nanowire Photodetectors: Current Status, Future Challenges, and Opportunities. *IEEE Journal of Selected Topics in Quantum Electronics* **2011,** *17* (4), 1002-1032.

74. Soci, C.; Zhang, A.; Bao, X.-Y.; Kim, H.; Lo, Y.; Wang, D., Nanowire Photodetectors. *Journal of Nanoscience and Nanotechnology* **2010,** *10* (3), 1430-1449.

75. Guo, Z.; Zhao, D.; Liu, Y.; Shen, D.; Zhang, J.; Li, B., Visible and ultraviolet light alternative photodetector based on ZnO nanowire/n-Si heterojunction. *Applied Physics Letters* **2008,** *93* (16).

76. Park, H.; Crozier, K. B., Vertically Stacked Photodetector Devices Containing Silicon Nanowires with Engineered Absorption Spectra. *ACS Photonics* **2015,** *2* (4), 544-549.

77. Alu, A.; Engheta, N., Cloaking a sensor. *Physical Review Letters* **2009,** *102* (23), 233901.

78. Zou, Y. S.; Steinvurzel, P.; Yang, T.; Crozier, K. B., Surface plasmon resonances of optical antenna atomic force microscope tips. *Applied Physics Letters* **2009,** *94* (17).

79. Fleury, R.; Alù, A., cloaking and invisibility - a review. In *Forum for Electromagnetic Research Methods and Application Technologies (FERMAT)*, 2014; Vol. 1.

80. Soric, J. C.; Fleury, R.; Monti, A.; Toscano, A.; Bilotti, F.; Alu, A., Controlling Scattering and Absorption With Metamaterial Covers. *IEEE Transactions on Antennas and Propagation* **2014,** *62* (8), 4220-4229.

81. Alu, A.; Engheta, N., Achieving Transparency with Plasmonic and Metamaterial Coatings. *Physical Review E* **2005,** *72*, 016623.

82. Alu, A.; Rainwater, D.; Kerkhoff, A., Plasmonic cloaking of cylinders: finite length, oblique illumination and cross-polarization coupling. *New Journal of Physics* **2010,** *12*.

83. Chen, P. Y.; Soric, J.; Alu, A., Invisibility and cloaking based on scattering cancellation. *Advanced Materials* **2012,** *24* (44), OP281-304.

84. Alù, A.; Engheta, N., Plasmonic materials in transparency and cloaking problems- mechanism, robustness, and physical insights. *Optics Express* **2007,** *15* (6), 3318-3332.

85. Monticone, F.; Argyropoulos, C.; Alu, A., Layered plasmonic cloaks to tailor the optical scattering at the nanoscale. *Scientific Reports* **2012,** *2*, 912.

86. Fan, P.; Chettiar, U. K.; Cao, L.; Afshinmanesh, F.; Engheta, N.; Brongersma, M. L., An invisible metal–semiconductor photodetector. *Nature Photonics* **2012,** *6* (6), 380-385.

87. Muneshwar, T.; Cadien, K., Low temperature plasma enhanced atomic layer deposition of conducting zirconium nitride films using tetrakis (dimethylamido) zirconium and forming gas (5% H-2+95% N-2) plasma. *Journal of Vacuum Science & Technology. A* **2015,** *33* (3).

88. Naik, G. V.; Kim, J.; Boltasseva, A., Oxides and nitrides as alternative plasmonic materials in the optical range [Invited]. *Optical Materials Express* **2011,** *1* (6), 1090-1099.

89. Lalisse, A.; Tessier, G.; Plain, J.; Baffou, G., Quantifying the Efficiency of Plasmonic Materials for Near-Field Enhancement and Photothermal Conversion. *Journal of Physical Chemistry. C* **2015,** *119* (45), 25518-25528.

90. Wiecha, P. R.; Cuche, A.; Arbouet, A.; Girard, C.; des Francs, G. C.; Lecestre, A.; Larrieu, G.; Fournel, F.; Larrey, V.; Baron, T.; Paillard, V., Strongly Directional Scattering from Dielectric Nanowires. *ACS Photonics* **2017,** *4* (8), 2036-2046.

91. Golshani, N.; Mohammadi, V.; Schellevis, H.; Beenakker, C. I. M.; Ishihara, R., Research Update: Reactively sputtered nanometer-thin ZrN film as a diffusion barrier between Al and boron layers for radiation detector applications. *APL Materials* **2014,** *2* (10).

92. Ghosh, P. K.; Debu, D. T.; French, D. A.; Herzog, J. B., Calculated thickness dependent plasmonic properties of gold nanobars in the visible to near-infrared light regime. *PLoS One* **2017,** *12* (5).

93. Massa, E.; Maier, S. A.; Giannini, V., An analytical approach to light scattering from small cubic and rectangular cuboidal nanoantennas. *New Journal of Physics* **2013,** *15*.

94. Zhu, J., Theoretical study of the light scattering from gold nanotubes: Effects of wall thickness. *Materials Science & Engineering. A, Structural Materials* **2007,** *454*, 685-689.

95. Fleury, R.; Soric, J.; Alu, A., Physical Bounds on Absorption and Scattering for Cloaked Sensors. *Physical Review. B* **2014,** *89*, 045122.

96. Xiang, C. X.; Yang, Y. G.; Penner, R. M., Cheating the diffraction limit: electrodeposited nanowires patterned by photolithography. *Chemical Communications* **2009,** (8), 859-873.

97. Chung, S. H.; Ramadurgam, S.; Yang, C., Effect of Dopants on Epitaxial Growth of Silicon Nanowires. *Nanomaterials and Nanotechnology* **2014,** *4*.

98. Hansen, K.; Cardona, M.; Dutta, A.; Yang, C., Plasma Enhanced Atomic Layer Deposition of Plasmonic TiN Ultrathin Films Using TDMATi and NH3. *Materials* **2020,** *13* (5).

99. Musschoot, J.; Xie, Q.; Deduytsche, D.; Van den Berghe, S.; Van Meirhaeghe, R. L.; Detavernier, C., Atomic layer deposition of titanium nitride from TDMAT precursor. *Microelectronic Engineering* **2009,** *86* (1), 72-77.

100. Briggs, J. A.; Naik, G. V.; Petach, T. A.; Baum, B. K.; Goldhaber-Gordon, D.; Dionne, J. A., Fully CMOS-compatible titanium nitride nanoantennas. *Applied Physics Letters* **2016,** *108* (5), 051110.

101. Schramke, K. S.; Qin, Y.; Held, J. T.; Mkhoyan, K. A.; Kortshagen, U. R., Nonthermal Plasma Synthesis of Titanium Nitride Nanocrystals with Plasmon Resonances at Near-Infrared Wavelengths Relevant to Photothermal Therapy. *ACS Applied Nano Materials* **2018,** *1* (6), 2869-2876.

102. Shah, D.; Reddy, H.; Kinsey, N.; Shalaev, V. M.; Boltasseva, A., Optical Properties of Plasmonic Ultrathin TiN Films. *Advanced Optical Materials* **2017,** *5* (13), 1700065.

103. Sharma, A. K.; Kvit, A.; Narayan, J., Growth of single crystal MgO on TiN/Si heterostructure by pulsed laser deposition. *Journal of Vacuum Science & Technology A-Vacuum Surfaces and Films* **1999,** *17* (6), 3393-3396.

104. Sasinska, A.; Ritschel, D.; Czympiel, L.; Mathur, S., Metallic Copper Thin Films Grown by Plasma-Enhanced Atomic Layer Deposition of Air Stable Precursors. *Advanced Engineering Materials* **2016,** *19* (2), 1600593.

105. Wang, Y.; Capretti, A.; Dal Negro, L., Wide tuning of the optical and structural properties of alternative plasmonic materials. *Optical Materials Express* **2015,** *5* (11), 2415-2430.

106. Yu, I.-S.; Cheng, H.-E.; Chang, C.-C.; Lin, Y.-W.; Chen, H.-T.; Wang, Y.-C.; Yang, Z.-P., Substrate-insensitive atomic layer deposition of plasmonic titanium nitride films. *Optical Materials Express* **2017,** *7* (3), 777-784.

107. Patsalas, P.; Kalfagiannis, N.; Kassavetis, S., Optical Properties and Plasmonic Performance of Titanium Nitride. *Materials* **2015,** *8* (6), 3128.

108. Zgrabik, C. M.; Hu, E. L., Optimization of sputtered titanium nitride as a tunable metal for plasmonic applications. *Optical Materials Express* **2015,** *5* (12), 2786-2797.

109. Braic, L.; Vasilantonakis, N.; Mihai, A.; Villar Garcia, I. J.; Fearn, S.; Zou, B.; Alford, N. M.; Doiron, B.; Oulton, R. F.; Maier, S. A.; Zayats, A. V.; Petrov, P. K.,

Titanium Oxynitride Thin Films with Tunable Double Epsilon-Near-Zero Behavior for Nanophotonic Applications. *ACS Applied Materials & Interfaces* **2017,** *9* (35), 29857-29862.

110. Muradov, N. Z.; Veziroglu, T. N., "Green" path from fossil-based to hydrogen economy: An overview of carbon-neutral technologies. *Int J Hydrogen Energ* **2008,** *33* (23), 6804-6839.

111. Lee, D. H.; Hung, C. P., Toward a clean energy economy: With discussion on role of hydrogen sectors. *International Journal of Hydrogen Energy* **2012,** *37* (20), 15753-15765.

112. Chen, X. B.; Shen, S. H.; Guo, L. J.; Mao, S. S., Semiconductor-based Photocatalytic Hydrogen Generation. *Chemical Reviews* **2010,** *110* (11), 6503-6570.

113. Abe, R., Recent progress on photocatalytic and photoelectrochemical water splitting under visible light irradiation. *Journal of Photochemistry and Photobiology C* **2010,** *11* (4), 179-209.

114. Chen, Z.; Dinh, H. N.; Miller, E., *Photoelectrochemical Water Splitting*. Springer: 2013.

115. Sivula, K.; van de Krol, R., Semiconducting materials for photoelectrochemical energy conversion. *Nature Reviews. Materials* **2016,** *1* (2).

116. Ling, Y.; Li, Y., Review of Sn-Doped Hematite Nanostructures for Photoelectrochemical Water Splitting. *Particle and Particle Systems Characterization* **2014,** *31* (11), 1113-1121.

117. Naldoni, A.; Guler, U.; Wang, Z.; Marelli, M.; Malara, F.; Meng, X.; Besteiro, L. V.; Govorov, A. O.; Kildishev, A. V.; Boltasseva, A.; Shalaev, V. M., Broadband Hot Electron Collection for Solar Water Splitting with Plasmonic Titanium Nitride. *Advanced Optical Materials* **2017**, *5* (15), 1601031.

118. Primc, D.; Bärtsch, M.; Barreca, D.; Carraro, G.; Maccato, C.; Sada, C.; Niederberger, M., Doping of TiO2 as a tool to optimize the water splitting efficiencies of titania–hematite photoanodes. *Sustainable Energy & Fuels* **2017,** *1* (1), 199-206.

119. Xu, K.; Chatzitakis, A.; Norby, T., Solid-state photoelectrochemical cell with TiO2 nanotubes for water splitting. *Photochemical & Photobiological Sciences* **2017,** *16* (1), 10-16.

120. Ye, K.-H.; Li, H.; Huang, D.; Xiao, S.; Qiu, W.; Li, M.; Hu, Y.; Mai, W.; Ji, H.; Yang, S., Enhancing photoelectrochemical water splitting by combining work function tuning and heterojunction engineering. *Nature Communications* **2019,** *10* (1).

121. Meng, Q.; Zhang, B.; Fan, L.; Liu, H.; Valvo, M.; Edström, K.; Cuartero, M.; Marco, R.; Crespo, G. A.; Sun, L., Efficient BiVO 4 Photoanodes by Postsynthetic Treatment: Remarkable Improvements in Photoelectrochemical Performance from Facile Borate Modification. *Angewandte Chemie* **2019,** *58* (52), 19027–19033.

122. Zhang, L.; Herrmann, L. O.; Baumberg, J. J., Size Dependent Plasmonic Effect on BiVO4 Photoanodes for Solar Water Splitting. *Scientific Reports* **2015,** *5* (1), 16660.

123. Wang, S.; Chen, H.; Gao, G.; Butburee, T.; Lyu, M.; Thaweesak, S.; Yun, J.-H.; Du, A.; Liu, G.; Wang, L., Synergistic crystal facet engineering and structural control of WO3 films exhibiting unprecedented photoelectrochemical performance. *Nano Energy* **2016,** *24*, 94-102.

124. Zhang, T.; Zhu, Z.; Chen, H.; Bai, Y.; Xiao, S.; Zheng, X.; Xue, Q.; Yang, S., Iron-doping-enhanced photoelectrochemical water splitting performance of nanostructured WO 3 : a combined experimental and theoretical study. *Nanoscale* **2015,** *7* (7), 2933-2940.

125. Wu, P.; Liu, Z.; Chen, D.; Zhou, M.; Wei, J., Flake-like NiO/WO 3 p-n heterojunction photocathode for photoelectrochemical water splitting. *Applied Surface Science* **2018,** *440*, 1101-1106.

126. Feng, J.; Luo, W.; Fang, T.; Lv, H.; Wang, Z.; Gao, J.; Liu, W.; Yu, T.; Li, Z.; Zou, Z., Highly Photo-Responsive LaTiO2N Photoanodes by Improvement of Charge Carrier Transport among Film Particles. *Advanced Functional Materials* **2014,** *24* (23), 3535-3542.

127. Akiyama, S.; Nakabayashi, M.; Shibata, N.; Minegishi, T.; Asakura, Y.; Abdulla-Al-Mamun, M.; Hisatomi, T.; Nishiyama, H.; Katayama, M.; Yamada, T.; Domen, K., Highly Efficient Water Oxidation Photoanode Made of Surface Modified LaTiO2N Particles. *Small* **2016,** *12* (39), 5468-5476.

128. Abdulla-Al-Mamun, M.; Rahman, M. M.; Shamsuddin, S. M., Dual cocatalysts induced photocurrent enhancement of LaTiO2N photoanode. *Materials Letters* **2019,** *245*, 147-150.

129. Hou, J.; Cheng, H.; Takeda, O.; Zhu, H., Unique 3D heterojunction photoanode design to harness charge transfer for efficient and stable photoelectrochemical water splitting. *Energy & Environmental Science* **2015,** *8* (4), 1348-1357.

130. Pei, L.; Xu, Z.; Yan, S.; Zou, Z., Temperature-controlled evolution of microstructures that promote charge separation in a TaON photoanode for enhanced solar energy conversion. *Journal of Materials Chemistry A* **2017,** *5* (25), 12848-12855.

131. Higashi, M.; Tomita, O.; Abe, R., Porous TaON Photoanodes Loaded with Cobalt-Based Cocatalysts for Efficient and Stable Water Oxidation Under Visible Light. *Topics in Catalysis* **2016,** *59* (8-9), 740-749.

132. Seo, J.; Nakabayashi, M.; Hisatomi, T.; Shibata, N.; Minegishi, T.; Domen, K., Solar-Driven Water Splitting over a BaTaO2N Photoanode Enhanced by Annealing in Argon. *ACS Applied Energy Materials* **2019,** *2* (8), 5777–5784.

133. Wang, C.; Hisatomi, T.; Minegishi, T.; Wang, Q.; Zhong, M.; Katayama, M.; Kubota, J.; Domen, K., Synthesis of Nanostructured BaTaO 2 N Thin Films as Photoanodes for Solar Water Splitting. *Journal of Physical Chemistry. C* **2016,** *120* (29), 15758–15764.

134. Zhang, H.; Wei, S.; Xu, X., Mg modified BaTaO2N as an efficient visible-light-active photocatalyst for water oxidation. *Journal of Catalysis* **2020,** *383,* 135-143.

135. Tamirat, A. G.; Rick, J.; Dubale, A. A.; Su, W.-N.; Hwang, B.-J., Using hematite for photoelectrochemical water splitting: a review of current progress and challenges. *Nanoscale Horizons* **2016,** *1* (4), 243-267.

136. Bora, D. K.; Braun, A.; Constable, E. C., “In rust we trust”. Hematite – the prospective inorganic backbone for artificial photosynthesis. *Energy & Environmental Science* **2013,** *6* (2), 407-425.

137. Shen, S. H.; Lindley, S. A.; Chen, X. Y.; Zhang, J. Z., Hematite heterostructures for photoelectrochemical water splitting: rational materials design and charge carrier dynamics. *Energy & Environmental Science* **2016,** *9* (9), 2744-2775.

138. Dias, P.; Vilanova, A.; Lopes, T.; Andrade, L.; Mendes, A., Extremely stable bare hematite photoanode for solar water splitting. *Nano Energy* **2016,** *23,* 70-79.

139. Steier, L.; Herraiz-Cardona, I.; Gimenez, S.; Fabregat-Santiago, F.; Bisquert, J.; Tilley, S. D.; Gratzel, M., Understanding the Role of Underlayers and Overlayers in Thin Film Hematite Photoanodes. *Advanced Functional Materials* **2014,** *24* (48), 7681-7688.

140. Barroso, M.; Pendlebury, S. R.; Cowan, A. J.; Durrant, J. R., Charge carrier trapping, recombination and transfer in hematite (alpha-Fe2O3) water splitting photoanodes. *Chemical Science* **2013,** *4* (7), 2724-2734.

141. Dotan, H.; Sivula, K.; Gratzel, M.; Rothschild, A.; Warren, S. C., Probing the photoelectrochemical properties of hematite (alpha-Fe2O3) electrodes using hydrogen peroxide as a hole scavenger. *Energy & Environmental Science* **2011,** *4* (3), 958-964.

142. Peerakiatkhajohn, P.; Yun, J.-H.; Chen, H.; Lyu, M.; Butburee, T.; Wang, L., Stable Hematite Nanosheet Photoanodes for Enhanced Photoelectrochemical Water Splitting. *Advanced Materials* **2016,** *28* (30), 6405-6410.

143. Jeon, T. H.; Moon, G.-H.; Park, H.; Choi, W., Ultra-efficient and durable photoelectrochemical water oxidation using elaborately designed hematite nanorod arrays. *Nano Energy* **2017,** *39*, 211-218.

144. Li, M.; Yang, Y.; Ling, Y.; Qiu, W.; Wang, F.; Liu, T.; Song, Y.; Liu, X.; Fang, P.; Tong, Y.; Li, Y., Morphology and Doping Engineering of Sn-Doped Hematite Nanowire Photoanodes. *Nano Letters* **2017,** *17* (4), 2490-2495.

145. Tang, P.; Xie, H.; Ros, C.; Han, L.; Biset-Peiró, M.; He, Y.; Kramer, W.; Rodríguez, A. P.; Saucedo, E.; Galán-Mascarós, J. R.; Andreu, T.; Morante, J. R.; Arbiol, J., Enhanced photoelectrochemical water splitting of hematite multilayer nanowire photoanodes by tuning the surface state via bottom-up interfacial engineering. *Energy & Environmental Science* **2017,** *10* (10), 2124-2136.

146. Kwon, J.; Yeo, J.; Hong, S.; Suh, Y. D.; Lee, H.; Choi, J.-H.; Lee, S. S.; Ko, S. H., Photoreduction Synthesis of Hierarchical Hematite/Silver Nanostructures for Photoelectrochemical Water Splitting. *Energy Technology* **2016,** *4* (2), 271-277.

147. Wang, X.; Peng, K.-Q.; Hu, Y.; Zhang, F.-Q.; Hu, B.; Li, L.; Wang, M.; Meng, X.-M.; Lee, S.-T., Silicon/Hematite Core/Shell Nanowire Array Decorated with Gold Nanoparticles for Unbiased Solar Water Oxidation. *Nano Letters* **2014,** *14* (1), 18-23.

148. Lei Wang, Y. Y., Yajun Zhang, Qiang Rui, Beibei Zhang, Zhiqiang Shen and Yingpu Bi, One-dimensional hematite photoanodes with spatially separated Pt and FeOOH nanolayers for efficient solar water splitting. *Journal of Materials Chemistry A* **2017,** *5* (32), 17056–17063. https://doi.org/10.1039/C7TA05318E.

149. Zheng, Z.; Xie, W.; Huang, B.; Dai, Y., Plasmon‐Enhanced Solar Water Splitting on Metal‐Semiconductor Photocatalysts. *Chemistry – A European Journal* **2018,** *24* (69), 18322-18333.

150. Zhang, Q.; Thrithamarassery Gangadharan, D.; Liu, Y.; Xu, Z.; Chaker, M.; Ma, D., Recent advancements in plasmon-enhanced visible light-driven water splitting. *Journal of Materiomics* **2017,** *3* (1), 33-50.

151. Ingram, D. B.; Linic, S., Water Splitting on Composite Plasmonic-Metal/Semiconductor Photoelectrodes: Evidence for Selective Plasmon-Induced Formation of Charge Carriers near the Semiconductor Surface. *Journal of the American Chemical Society* **2011,** *133* (14), 5202-5205.

152. Cole, J. R.; Halas, N. J., Optimized plasmonic nanoparticle distributions for solar spectrum harvesting. *Applied Physics Letters* **2006,** *89* (15), 153120.

153. Wang, L.; Zhou, X.; Nguyen, N. T.; Schmuki, P., Plasmon-Enhanced Photoelectrochemical Water Splitting Using Au Nanoparticles Decorated on Hematite Nanoflake Arrays. *ChemSusChem* **2015,** *8* (4), 618-622.

154. Lei, F.; Liu, H.; Yu, J.; Tang, Z.; Xie, J.; Hao, P.; Cui, G.; Tang, B., Promoted water splitting by efficient electron transfer between Au nanoparticles and hematite nanoplates: a theoretical and experimental study. *Physical Chemistry Chemical Physics* **2019,** *21* (3), 1478-1483.

155. Wang, L.; Nakajima, T.; Zhang, Y., Simultaneous reduction of surface, bulk, and interface recombination for Au nanoparticle-embedded hematite nanorod

photoanodes toward efficient water splitting. *Journal of Materials Chemistry A* **2019,** *7* (10), 5258-5265.

156. Ayala-Orozco, C.; Urban, C.; Knight, M. W.; Urban, A. S.; Neumann, O.; Bishnoi, S. W.; Mukherjee, S.; Goodman, A. M.; Charron, H.; Mitchell, T.; Shea, M.; Roy, R.; Nanda, S.; Schiff, R.; Halas, N. J.; Joshi, A., Au Nanomatryoshkas as Efficient Near-Infrared Photothermal Transducers for Cancer Treatment: Benchmarking against Nanoshells. *ACS Nano* **2014,** *8* (6), 6372-6381.

157. Schlather, A. E.; Manjavacas, A.; Lauchner, A.; Marangoni, V. S.; Desantis, C. J.; Nordlander, P.; Halas, N. J., Hot Hole Photoelectrochemistry on Au@SiO2@Au Nanoparticles. *The Journal of Physical Chemistry Letters* **2017**, 2060-2067.

158. Chen, Y. Y.; Dal Negro, L., Pole-zero analysis of scattering resonances of multilayered nanospheres. *Physical Review B* **2018,** *98* (23).

159. Ling, Y. C.; Wang, G. M.; Wheeler, D. A.; Zhang, J. Z.; Li, Y., Sn-Doped Hematite Nanostructures for Photoelectrochemical Water Splitting. *Nano Letters* **2011,** *11* (5), 2119-2125.

160. Wang, G. M.; Ling, Y. C.; Wheeler, D. A.; George, K. E. N.; Horsley, K.; Heske, C.; Zhang, J. Z.; Li, Y., Facile Synthesis of Highly Photoactive alpha-Fe2O3-Based Films for Water Oxidation. *Nano Letters* **2011,** *11* (8), 3503-3509.

161. Ling, Y.; Wang, G.; Wheeler, D. A.; Zhang, J. Z.; Li, Y., Sn-Doped Hematite Nanostructures for Photoelectrochemical Water Splitting. *Nano Letters* **2011,** *11* (5), 2119-2125.

162. Morrish, R.; Rahman, M.; Macelroy, J. M. D.; Wolden, C. A., Activation of Hematite Nanorod Arrays for Photoelectrochemical Water Splitting. *ChemSusChem* **2011,** *4* (4), 474-479.

163. Duff, D. G.; Baiker, A.; Edwards, P. P., A New Hydrosol of Gold Clusters. *Journal of the Chemical Society. Chemical Communications* **1993,** (1), 96-98.

164. M. Luty-Blocho, K. P., W. Jaworski, B. Streszewski, K. Fitzner, Kinetic Studies of Gold Nanoparticles Formation in the Batch and in the Flow Microreactor System. In *Trends in Colloid and Interface Science XXIV*, Springer-Verlag Berlin Heidelberg 2011: 2011.

165. Hogan, N. J.; Urban, A. S.; Ayala-Orozco, C.; Pimpinelli, A.; Nordlander, P.; Halas, N. J., Nanoparticles Heat through Light Localization. *Nano Letters* **2014,** *14* (8), 4640-4645.

166. A.R. Shafiqa, A. Abdul Aziz and B. Mehrdel, Nanoparticle Optical Properties: Size Dependence of a Single Gold Spherical Nanoparticle. In *Journal of Physics: Conference Series*, 2018; Vol. 1083.

167. Peerakiatkhajohn, P.; Yun, J. H.; Chen, H. J.; Lyu, M. Q.; Butburee, T.; Wang, L. Z., Stable Hematite Nanosheet Photoanodes for Enhanced Photoelectrochemical Water Splitting. *Advanced Materials* **2016,** *28* (30), 6405-+.

168. Kim, J. Y.; Magesh, G.; Youn, D. H.; Jang, J. W.; Kubota, J.; Domen, K.; Lee, J. S., Single-crystalline, wormlike hematite photoanodes for efficient solar water splitting. *Scientific Reports* **2013,** *3*.

169. Anker, J. N.; Hall, W. P.; Lyandres, O.; Shah, N. C.; Zhao, J.; Van Duyne, R. P., Biosensing with plasmonic nanosensors. *Nature Materials* **2008,** *7* (6), 442-453.

170. SadAbadi, H.; Badilescu, S.; Packirisamy, M.; Wuthrich, R., Integration of gold nanoparticles in PDMS microfluidics for lab-on-a-chip plasmonic biosensing of growth hormones. *Biosensors & Bioelectronics* **2013,** *44,* 77-84.

171. Toma, M.; Cho, K.; Wood, J. B.; Corn, R. M., Gold Nanoring Arrays for Near Infrared Plasmonic Biosensing. *Plasmonics* **2014,** *9* (4), 765-772.

172. Liedberg, B.; Nylander, C.; Lundstrom, I., Surface-Plasmon Resonance for Gas-Detection and Biosensing. *Sensor Actuator* **1983,** *4* (2), 299-304.

173. Nylander, C.; Liedberg, B.; Lind, T., Gas-Detection by Means of Surface-Plasmon Resonance. *Sensors and Actuators* **1982,** *3* (1), 79-88.

174. Wang, Y. Y.; Zhou, J. H.; Li, J. H., Construction of Plasmonic Nano-Biosensor-Based Devices for Point-of-Care Testing. *Small Methods* **2017,** *1* (11).

175. Zhou, J. Y.; Tao, F.; Zhu, J. F.; Lin, S. W.; Wang, Z. Y.; Wang, X.; Ou, J. Y.; Li, Y.; Liu, Q. H., Portable tumor biosensing of serum by plasmonic biochips in combination with nanoimprint and microfluidics. *Nanophotonics-Berlin* **2019,** *8* (2), 307-316.

176. Soler, M.; Huertas, C. S.; Lechuga, L. M., Label-free plasmonic biosensors for point-of-care diagnostics: a review. *Expert Review of Molecular Diagnostics* **2019,** *19* (1), 71-81.

177. Caldwell, J. D.; Glembocki, O.; Bezares, F. J.; Bassim, N. D.; Rendell, R. W.; Feygelson, M.; Ukaegbu, M.; Kasica, R.; Shirey, L.; Hosten, C., Plasmonic

Nanopillar Arrays for Large-Area, High-Enhancement Surface-Enhanced Raman Scattering Sensors. *ACS Nano* **2011,** *5* (5), 4046-4055.

178. Park, J. E.; Yonet-Tanyeri, N.; Vander Ende, E.; Henry, A. I.; White, B. E. P.; Mrksich, M.; Van Duyne, R. P., Plasmonic Microneedle Arrays for in Situ Sensing with Surface Enhanced Raman Spectroscopy (SERS). *Nano Letters* **2019,** *19* (10), 6862-6868.

179. Ashley, M. J.; Bourgeois, M. R.; Murthy, R. R.; Laramy, C. R.; Ross, M. B.; Naik, R. R.; Schatz, G. C.; Mirkin, C. A., Shape and Size Control of Substrate-Grown Gold Nanoparticles for Surface-Enhanced Raman Spectroscopy Detection of Chemical Analytes. *Journal of Physical Chemistry C* **2018,** *122* (4), 2307-2314.

180. Singh, P.; Konig, T. A. F.; Jaiswal, A., NIR-Active Plasmonic Gold Nanocapsules Synthesized Using Thermally Induced Seed Twinning for Surface-Enhanced Raman Scattering Applications. *ACS Applied Materials & Interfaces* **2018,** *10* (45), 39380-39390.

181. Fast, A.; Potma, E. O., Coherent Raman scattering with plasmonic antennas. *Nanophotonics-Berlin* **2019,** *8* (6), 991-1021.

182. Camp, C. H.; Cicerone, M. T., Chemically sensitive bioimaging with coherent Raman scattering. *Nature Photonics* **2015,** *9* (5), 295-305.

183. Cicerone, M., Molecular imaging with CARS micro-spectroscopy. *Current Opinion in Chemical Biology* **2016,** *33*, 179-185.

184. Kumar, S.; Kamali, T.; Levitte, J. M.; Katz, O.; Hermann, B.; Werkmeister, R.; Povazay, B.; Drexler, W.; Unterhuber, A.; Silberberg, Y., Single-pulse CARS

based multimodal nonlinear optical microscope for bioimaging. *Optics Express* **2015,** *23* (10), 13082-13098.

185. Rossi, L. M.; Shi, L. F.; Quina, F. H.; Rosenzweig, Z., Stober synthesis of monodispersed luminescent silica nanoparticles for bioanalytical assays. *Langmuir* **2005,** *21* (10), 4277-4280.

186. Tadanaga, K.; Morita, K.; Mori, K.; Tatsumisago, M., Synthesis of monodispersed silica nanoparticles with high concentration by the Stober process. *Journal of Sol-Gel Science and Technology* **2013,** *68* (2), 341-345.

CURRICULUM VITAE

[redacted]

[redacted]

[redacted]

[redacted]